Development and application of a transparent µECoG array and optrode microdrive for combined electrophysiology and optophysiology

Thesis

for the degree of

doctor rerum naturalium (Dr. rer. nat.)

approved by the Faculty of Natural Sciences of Otto von Guericke University Magdeburg

by M. Sc. Marcel Brosch

born on 10.11.1991 in Ilmenau, Germany

Examiner: Prof. Dr. Frank Ohl
Prof. Dr. sc. Nat. Christoph Kayser

submitted on: 22.09.2021
defended on: 27.04.2022

“For instance, on the planet Earth, man had always assumed that he was more intelligent than dolphins because he had achieved so much — the wheel, New York, wars and so on — whilst all the dolphins had ever done was muck about in the water having a good time. But conversely, the dolphins had always believed that they were far more intelligent than man — for precisely the same reasons.”

– Douglas Adams, The Hitchhiker's Guide to the Galaxy

Abstract

Conventional extracellular *in vivo* electrophysiology has advanced our understanding of brain function. Thereby, improvements in electrode design and materials have led to new recoding possibilities. Previously, recordings of exclusively isolated single neurons had led to the neuron doctrine in which the neuron is the structural and functional unit. The development of multielectrode devices allowed to record single-neuron ensembles and distributed mesoscopic population activity. Thus, the provided evidence shifted the perspective towards neural networks as functional units creating behavior and cognition. Nevertheless, our understanding of the nervous system is still limited, and the measuring tools' capabilities restrict new insights. Improving neural recording devices but also making them more easily available would facilitate new knowledge.

The general limitations of chronic *in vivo* electrophysiology are device stability and signal stability. The mechanical mismatch of electrode and brain tissue results in an acute and chronic inflammatory response. Neural signal quality degrades over time through electrode movements and the encapsulation by a glial sheath. This suggests that current neural implants require additional innovations that improve chronic recording stability. Advancements in optogenetic tools to manipulate neural activity require neural devices that incorporate simultaneous electrophysiological recordings and optophysiological modulation.

In this dissertation, I focus on improving mesoscopic electrocorticography (ECoG) recordings and microscopic single-unit recordings. The main aim is to improve recording devices that are still widely used: platinum µECoG arrays and tetrode microdrives. I aim to improve ECoG signal stability by increasing the structural biocompatibility of the device. Single-unit stability should be achieved by both stable tetrode positions over sessions and precisely advanced tetrodes. Both devices should combine electrophysiological recordings and simultaneous optical modulation or imaging.

Over the last years, many new neural recording devices incorporating optical methods were proposed. However, due to complicated manufacturing, they have often not yet found a widespread application. Thus, the aim is to build neural recording devices that can be easily fabricated and used and, therefore, find widespread use.

The complexity and fragility of current transparent µECoG arrays made from indium tin oxide (ITO) and graphene have limited their widespread use. I tested a transparent µECoG array which allowed simultaneous cortical recordings with optical manipulation and imaging. I successfully tested a polyimide (PI)-based array using metal traces instead of transparent electrodes. Therefore, reducing the complexity and fragility of previous transparent µECoG arrays. The reduced thickness of the PI allowed increased transparency and a better conformability to the cortical surface. The µECoG array is nearly immune against the photovoltaic artifact, long-term stable, and biocompatible. ECoG activity is recorded over months without a significant reduction in peak-to-peak amplitude. High-resolution auditory cortex tonotopy can be mapped chronically for up to a week but vanishes in chronic recordings. Overall, the µECoG array is simple to manufacture, robust, and offers chronic stability that has not been demonstrated in previous opto-electrode µECoG arrays.

The second device advancement features an open-source multi-tetrode microdrive – the TetrODrive. Just like the µECoG array, it enables combined *in vivo* electrophysiology and optophysiology. Existing microdrives have limited stability and drive precision, high costs, complex assembly, and excessive weight. In contrast, the TetrODrive is 3D-printed, has only two main components, and short assembly time. The drive is developed for mice and has a small footprint and weight.

Recording stability is improved by mechanically decoupling the drive mechanism from the plugging force of electrical and optical connectors. The microdrive allowed chronic recordings of many different cells by slowly driving electrodes through the area of interest. However, single units were also stable if electrodes were kept chronically at a stationary position.

I tested the microdrive *in vivo* and evaluated dopaminergic single units and calcium signals in the ventral tegmental area (VTA) during classical conditioning. Additionally, I built the necessary setup for research of the reward prediction error (RPE). During recordings, some single units did not follow the classic RPE theory but can be explained by contributions of movement initiation responses and a diverse set of dopaminergic subpopulations. Optogenetic tagging allowed to successfully identify dopaminergic neurons in the VTA. The microdrive's movable optical fiber allowed imaging of population activity via fiber photometry. This imaging revealed a more uniform signal following the RPE theory. The microdrive's open-source, lightweight, simple, and affordable design can significantly expand the use of microdrives in mouse preparations.

Zusammenfassung

Die konventionelle extrazelluläre *in vivo* Elektrophysiologie hat unser Verständnis von der Funktion des Gehirns verbessert. Dabei haben vor allem Verbesserungen im Elektrodendesign und Material neue Möglichkeiten hervorgebracht, die Aktivität von Neuronen aufzuzeichnen. Zuerst hatten Ableitungen von ausschließlich wenigen Neuronen zur Neuronentheorie geführt, in welcher das Neuron die strukturelle und funktionelle Einheit darstellt. Die Entwicklung von Messungen mit einer erhöhten Anzahl an Elektroden ermöglichte die Aufzeichnung von Neuron Ensembles und mesoskopischer neuronaler Populationsaktivität. Das ermöglichte die Perspektive zu ändern und neuronale Netzwerke anstatt einzelner Neurone als funktionelle Einheiten für Verhalten und Kognition zu sehen. Dennoch ist unser Verständnis des Nervensystems nach wie vor begrenzt, und die Einschränkungen der Messgeräte schränken den Gewinn neuer neurobiologischer Erkenntnisse zu einem gewissen Maße ein. Eine Verbesserung der Messgeräte, aber auch deren erleichterte Verfügbarkeit würden der Gewinnung neuen neurobiologischen Wissens beitragen.

Die häufigsten Einschränkungen für erfolgreiche chronische *in vivo* Elektrophysiologie sind die eingeschränkte Langlebigkeit der Elektroden und zeitlich abnehmende Signalqualität. Die Diskrepanz der mechanischen Eigenschaften von harten Elektroden und weichem Hirngewebe führt zu einer akuten und chronischen Entzündungsreaktion des Gewebes um die Elektrode herum. Dadurch verschlechtert sich im Laufe der Zeit die Qualität der neuronalen Signale. Die Entzündungsreaktion resultiert im Wachstum einer Gliazellen-Hülle um die Elektrode. Dies zeigt, dass die derzeitigen neuronalen Implantate zusätzliche Innovationen erfordern, um chronische neuronale Aufzeichnungen mit guter Signalqualität zu ermöglichen. Die Fortschritte in der Optogenetik erlauben eine Beeinflussung der neuronalen Aktivität durch Lichtsignale. Neuronale Geräte benötigen Funktionen, die gleichzeitige elektrophysiologische Aufzeichnungen und optophysiologische Modulation ermöglichen.

In dieser Dissertation konzentriere ich mich auf die Verbesserung von neuronalen Ableitungsgeräten, die zwei verschiedener neuronaler Signaltypen aufnehmen: mesoskopische Electrocorticography (ECoG, deutsch: Elektrokortikographie) und mikroskopischer Ableitungen von individuellen Neuronen. Das Hauptziel ist die Verbesserung von neuronalen Ableitungsgeräten, die weit verbreitet sind: µECoG Elektroden-Array aus Platin und Tetroden Mikroelektroden Antrieb (Microdrive). Ich möchte die Stabilität des ECoG-Signals verbessern, indem die strukturelle Biokompatibilität des Elektroden-Arrays verbessert wird. Die Aufnahme guter Signale von einzelnen Neuronen soll sowohl möglich sein, wenn die Tetroden stationär an der gleichen Stelle verweilen als auch wenn sie präzise neu positioniert werden. Beide Geräte sollten die Kombination von elektrophysiologischen Aufzeichnungen und gleichzeitige optische Modulation und Bildgebung ermöglichen.

In den letzten Jahren wurden viele neue neuronale Aufzeichnungsgeräte vorgeschlagen, die auch mit optischen Methoden kombinierbar sind. Aufgrund der komplizierten Herstellung haben sie jedoch oft noch keine breite Anwendung gefunden. Ziel ist es daher, neuronale Aufzeichnungsgeräte

zu bauen, die einfach herzustellen und zu verwenden sind und daher eine breite Anwendung finden können.

Die Komplexität und Brüchigkeit der derzeitigen transparenten µECoG Elektroden-Arrays aus Indiumzinnoxid und Graphen limitieren deren breite Anwendung. Ich habe ein transparentes µECoG-Array getestet, das gleichzeitige elektrische kortikale Aufzeichnungen mit optischer Manipulation und Bildgebung ermöglicht. Die Komplexität und Zerbrechlichkeit sind gegenüber der derzeitigen transparenten Elektroden-Arrays verringert. Das Array besteht aus Polyimid mit Elektroden aus Metall anstelle der üblichen transparenten Elektroden. Die geringere Schichtdicke des Polyimid ermöglicht eine höhere Transparenz und eine bessere Anpassungsfähigkeit an die Oberfläche des Kortex als vorherige Arrays aus Polyimid. Das µECoG-Array ist nahezu resistent gegenüber dem photovoltaischen Artefakt, langzeitstabil und biokompatibel. Die ECoG-Aktivität kann über Monate hinweg aufgezeichnet werden, ohne dass es zu einer signifikanten Verringerung der Signalamplitude kommt. Die hochauflösende Tonotopie des auditorischen Kortex kann bis zu einer Woche lang chronisch aufgezeichnet werden. Bei längeren Aufzeichnungen nimmt die Auflösung der Tonotopie jedoch signifikant ab. Allgemein ist das µECoG-Array einfach herzustellen, robust und erlaubt chronische Aufzeichnungen neuronaler Aktivität. Es hat Eigenschaften, die andere transparenten µECoG-Arrays nicht nachweißen konnten.

Das zweite neuronale Aufnahmegerät ist ein Open-Source Multitetroden-Microdrive – das TetrODrive. Genau wie das µECoG Elektroden-Array ermöglicht es die Kombination von *in vivo* Elektrophysiologie und Optophysiologie. Existierende Microdrives haben eine begrenzte Signalstabilität und ungenaue Präzision der beweglichen Elektroden, hohe Kosten, eine komplexe Montage und ein hohes Gewicht. Im Gegensatz dazu ist der TetrODrive 3D-gedruckt, hat nur zwei Hauptkomponenten und eine kurze Montagezeit. Das Microdrive wurde für Mäuse entwickelt und hat daher eine kleine Größe und ein geringes Gewicht.

Die Stabilität der neuronalen Signale wird verbessert durch die mechanische Entkopplung der beweglichen Elektroden und der Kraft, die beim Anschließen der elektrischen und optischen Anschlüsse entsteht. Das Microdrive ermöglichte chronische Aufzeichnungen vieler verschiedener Neurone, indem die Elektroden langsam durch das Gewebe gefahren werden. Individuelle Neurone können jedoch auch stabil über einen längeren Zeitraum aufgenommen werden, wenn die Elektroden in einer stationären Position gehalten werden.

Ich habe den Microdrive *in vivo* getestet und dopaminerge Neurone sowohl elektrisch als auch optisch in der Area tegmentalis ventralis (VTA) während einer klassischen Konditionierung abgeleitet. Außerdem konstruierte ich den notwendigen Verhaltensaufbau für die Untersuchung des Belohnungssystems (speziell des reward prediction error: RPE) in Mäusen. Während der Ableitung zeigten einzelne Neurone Signale, die nicht zur klassischen RPE-Theorie passen. Diese veränderten Signale lassen sich z. B. durch neuronale Signale generiert durch Bewegungsinitiierung und verschiedener dopaminerge Subpopulationen erklären. Durch optogenetische Markierung konnten dopaminerge Neurone in der VTA erfolgreich identifiziert werden. Die bewegliche optische Faser des Microdrives ermöglichte die Aufnahme von Populationsaktivität mittels Faserphotometrie. Diese

Art von Bildgebung ergab vorwiegend ein Signal, welches in Bezug auf die RPE-Theorie zu erwarten wäre. Das Microdrive Design ist Open-Source, leicht, einfache und kostengünstig. Dadurch kann es für eine Vielzahl von Anwendungen in Maus Experimenten verwendet werden.

Contents

List of Figures

Introduction

µECoG array

Multi-tetrode microdrive

List of Abbreviations

A1	primary auditory cortex
AAF	anterior auditory field
ChR2	Channelrhodopsin-2
CMOS	Complementary metal-oxide-semiconductor
CS	conditioned stimulus
CSF	cerebrospinal fluid
DAT	dopamine transporter
ECoG	electrocorticography
EEG	electroencephalography
EIB	electric interface board
ERP	event-related potential
FDM	fused deposition modeling
GABA	gamma-aminobutyric acid
GFAP	glial fibrillary acidic protein
GUI	graphical user interface
Iba1	ionized calcium-binding adaptor molecule 1
ITO	indium tin oxide
LFP	local field potential
NA	numerical aperture
NAc	nucleus accumbens
PBS	phosphate-buffered saline
PDMS	polydimethylsiloxane
PEDOT	poly(3,4-ethylenedioxythiophene)
PET	polyethylene terephthalate
PI	polyimide
PSS	polystyrene sulfonate
RMS	root mean square
ROI	region of interest
RPE	reward prediction error
SNc	substantia nigra pars compacta
SNR	signal-to-noise ratio
TH	tyrosine hydroxylase
TTL	transistor-transistor logic
US	unconditioned stimulus
V1	primary visual cortex
VSD	voltage-sensitive dye
VTA	ventral tegmental area

1. INTRODUCTION

1.1. Extracellular recordings

The neuronal transmembrane currents give rise to a voltage potential within the extracellular space. Electrodes placed in the close vicinity of neurons can record this extracellular activity with sub-millisecond resolution. They either penetrate the neural tissue or are placed on the cortical surface. Extracellular electrodes do not puncture the neuron. Thus, extracellular recordings can be kept stable for longer periods than intracellular ones. However, the disadvantage is a lower signal amplitude in the range of µV to a few mV. In contrast, intracellularly recorded signals are in the range of tens of mV. Filtering dissociates the extracellular signal into two components. The first component consists of high-frequency spikes (action potentials) of nearby neurons. The second component consists of low-frequency local field potentials (LFPs) from collective neuronal activity. Cortical surface electrodes record only mesoscopic activity because of their larger surface area and distance from the neural tissue. The signal recorded from electrode arrays placed on the dura mater consists of synchronized postsynaptic potentials called electrocorticogram.

Brain activity and processes range from millisecond spikes but also involve plastic changes over months and years. Neural devices must capture these various temporal dynamics. Spatial scales must address the nanometer and micrometer scale of neurons. Coordinated processes of higher cognitive functions include multiple ensembles of neurons of different brain areas. Thus, neural recording and imaging technologies need a resolution from microscopic single neurons to macroscopic brain-wide activity. Traditionally, the various spatiotemporal scales of brain activity must be recorded with different techniques, each tailored to a specific spatial scale and temporal precision. A collaboration of neuroscientists and neural engineers might allow dealing with such challenges. Devices could, for instance, combine electrophysiological recordings and optical neural modulation.

The following introductory chapter describes the historical development and advancement of extracellular recording techniques. These include penetrating electrodes, microdrives, and non-penetrating surface electrodes. Further, abiotic and biotic factors that influence the recorded signal quality are described.

1.2. Penetrating depth electrodes

1.2.1. Origins and current approaches

Traditional wire and silicon neural probes

In the first isolated microelectrode applications, a glass capillary insulated silver wire was used (Weale, 1951). Hubel (1957) developed tungsten microwires. The manufacturing process allowed the production of sharp tungsten electrode tips with micrometer diameter. Those resulted in the discovery of receptive fields in the visual cortex (Hubel and Wiesel, 1959, 1962), hippocampal place cells (O'Keefe and Dostrovsky, 1971), and the reward response in midbrain dopamine neurons (Schultz, 1986). The reduction in electrode size significantly advanced recordings. Earlier approaches with larger electrodes were performed in acute giant squid axon recordings (Hodgkin and Huxley, 1939). Microwires instead recorded small mammalian neurons for up to an hour. Thus, insulated thin single metal microwires have been the primary electrode type for a long time.

Single wires were later arranged in an electrode array. This method improved neural mapping and was first performed with five tungsten microwires by Marg and Adams (1967). This development was followed by advanced multi-electrode probes: Michigan array (Wise et al., 1970), stereotrodes (McNaughton et al., 1983), four twisted wires forming a tetrode (Reece and O'Keefe, 1989), and the Utah array (Campbell et al., 1990). Both Michigan and Utah arrays were produced from metallic electrodes on a semiconducting silicon substrate. Silicon probes are passive electrodes. They do not incorporate any circuitry for amplification or digitization. The increased channel count is based on advancements in semiconductor microfabrication. These include silicon etching and photolithography. Photolithography uses light to pattern materials onto a substrate with nanometer precision (Szostak et al., 2017). Therefore, it creates precise electrode geometries needed for 2D and 3D devices.

2D Michigan arrays are built from electrodes along the length of a linear shank. Compared to wires recording only at the tip, they enable cortical laminar recordings. Michigan-type probes are produced by commercial suppliers like Neuronexus (Berényi et al., 2014) or Cambridge Neurotech (Jiang et al., 2017).

3D Utah arrays consist of many conductive silicon needles, which record only at the platinum-coated electrode tip. Utah arrays were mainly used in non-human primate studies (Barrese et al., 2013). Later they started to be used for human brain-computer interfaces (Maynard et al., 1997; Hochberg et al., 2006). The recording depth is limited to 1.5 mm (Rousche and Normann, 1998).

High channel count neural probes

Changes in the previously mentioned probes have been made mainly through changes in device geometry and electrical impedance. Nowadays, neural implants are fabricated with a higher channel count while keeping the device dimensions reasonable. Moore's law describes the doubling of circuit transistor numbers every two years (Khan et al., 2018). In neuroscience, Moore's law is mimicked

by the number of recorded cells. Recording yield by a higher channel count has exponential growth doubling almost every seven years (Stevenson and Kording, 2011).

The traditional Utah and Michigan arrays have inspired the development of future semiconductor-based generations of electrode designs. Complementary metal-oxide-semiconductor (CMOS) technologies allowed smaller packing of silicon-based electrode devices. Neuropixels (Jun et al., 2017) and NeuroSeeker (Raducanu et al., 2017) are Michigan-type designs that allow laminar recordings along the shank surface. Channel counts are close to 1000 with on-site amplification/digitization. The newest development –Neuropixels 2.0– has a miniaturized headstage and a probe with four shanks of 5120 channels in total (Steinmetz et al., 2021). In total, 768 channels can record simultaneously. As an alternative to stiff silicon devices, flexible polyimide (PI) encapsulated electrodes have been developed (Cheung et al., 2007).

1.2.2. Continuous improvements of wire recordings

Metal microwires were continuously improved. Initially, only acute recordings were possible. Later electrode probe designs allowed chronic recordings with improved unit yield. Increased longevity enables improved brain-machine interfaces. Improvements are related to material aspects like wire size, conductor, and insulation. Glass insulators are rigid and fragile (Salcman and Bak, 1973). Teflon and PI are flexible and suitable for chronic implantations (Im and Seo, 2016). Wires got progressively thinner, requiring coatings to reduce impedance and increase biocompatibility (Polikov et al., 2005).

The electrode geometry plays an essential role in the successful detection of single units. High-impedance single wires traditionally recorded single-unit activity, which is recorded only from the nearest neurons. Single wire recordings do not allow reliable sorting of individually recorded spikes into different units. Single wire spike sorting requires a unique amplitude and waveform specific for each neuron's action potential. However, this is not true for brain areas with a high density of neurons. High firing rates and burst firing results, for instance, in varying amplitudes.

Tetrodes have four tightly twisted wires. The first tetrode was tested *in vivo* for hippocampal recordings (Wilson and McNaughton, 1993). Spikes get picked up by all four electrodes. Triangulation allows improved identification of the spike's neuronal source. The amplitude of a spike is different on each electrode and depends on the distance of the neuron to individual electrode tips. This additional information is ideally unique for each active neuron. Thus, spike clustering with varying spike amplitudes and waveforms is more reliable. Noise and background activity (multi-unit activity) are distributed more evenly across all electrodes. Thus, background activity can be easily distinguished. Usually, tetrodes have low impedances. This allows recording from more neurons than high impedances wires.

The advantage of tetrodes over single wires can be shown in a simple experiment. Spike sorting results can be compared using the four contacts of a tetrode against one selected contact. Single contact recording results in doubled spike sorting errors compared to tetrodes (Harris et al., 2000). Errors in spike sorting occur if spikes from different neurons are clustered together (false positive). Spikes from one neuron can also be missed (false negative).

1.2.3. Importance of tetrodes for recordings in ventral tegmental area

A chapter of the dissertation focuses on single-unit recordings with tetrodes in the VTA in the context of the reward prediction error (RPE). Therefore, this subsection introduces dopamine neurons, the RPE, and methodological recording aspects.

This subsection first introduces the dopaminergic VTA neurons and the RPE signaling in the first paragraph. The following paragraph introduces the limitations of silicon probes compared to tetrodes for recordings in deep brain areas like the VTA. Therefore, it introduces reasons for our choice of electrodes. Recent major scientific findings of the RPE acquired by tetrodes are presented in the last paragraph. This highlights the predominant use of flexible thin tetrodes for deep brain VTA recordings. The last paragraph introduces the diversity of dopaminergic neuron signaling, which contrasts with a previous more homogeneous recorded activity.

Dopaminergic neurons in the ventral tegmental area

Midbrain dopamine neurons are concentrated in two adjacent regions, the VTA and the substantia nigra pars compacta (SNc). The VTA consists of dopaminergic neurons (≈ 70%), gamma-aminobutyric acid (GABA) neurons (≈ 30%), and glutamatergic neurons (≈ 2-3%, Nair-Roberts et al., 2008; Ungless and Grace, 2012). Activity is modulated by input from many and diverse brain areas (Watabe-Uchida et al., 2012; Morales and Margolis, 2017, Figure 1a). VTA dopamine neurons project to mainly four areas: the medial prefrontal cortex, two nucleus accumbens (NAc) subdivisions (medial shell, lateral shell), and amygdala (Beier et al., 2015).

Dopaminergic phasic, slow, or tonic activity patterns serve multiple functions, like prediction error, movement, attention, and motivation (Bromberg-Martin et al., 2010; Roeper, 2013; Schultz et al., 2017). Dopaminergic neurons' activity is mainly researched in relation to reinforcement learning and motor activity (Wise, 2004; Redgrave and Gurney, 2006; Ikemoto, 2007; Schultz, 2007; Cohen et al., 2012).

Midbrain dopamine neurons encode the RPE during Pavlovian conditioning (Schultz et al., 1993), which is the difference between a received reward and the predicted reward (Figure 1b). Those *in vivo* signals were compatible with earlier proposed theoretical approaches like the Rescorla-Wagner model (Rescorla and Wagner, 1972) and the temporal difference reinforcement learning (Sutton and Barto, 1981).

The RPE acts as a teaching signal and updates future actions. Unpredicted rewards induce a positive RPE and strengthen cue-reward associations. Already predicted rewards do not generate a prediction error. Therefore, no further learning occurs. After conditioning, a cue-reward association

is built. Dopamine neurons respond to the cue. However, if the predicted outcome is worse than expected, a negative RPE occurs. The result is the extinction of learned behavior.

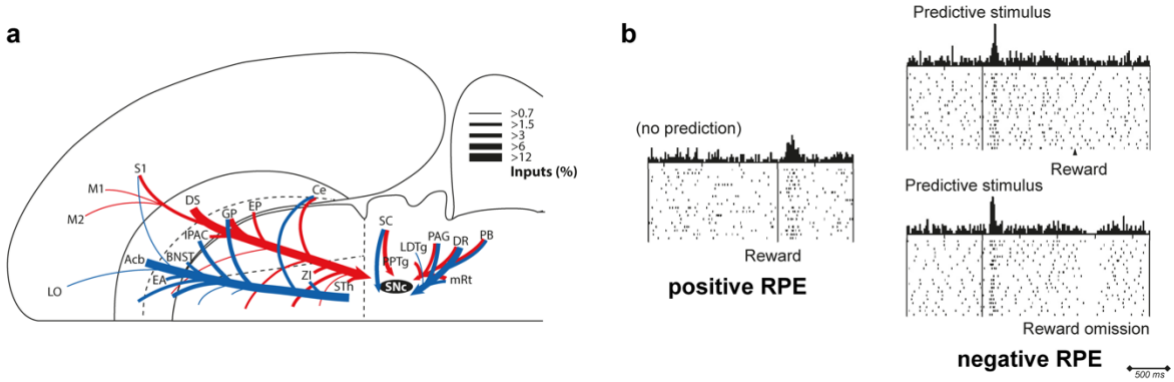

Figure 1 | Midbrain dopamine neurons

a, Schematic illustration of the monosynaptic inputs to VTA and SNc dopamine neurons. Input tracing via retrograde rabies virus. Line thickness indicates the percentage of total input neurons. Adapted from Watabe-Uchida et al. (2017). **b**, Dopamine prediction error responses. Unpredicted rewards elicit a positive RPE. Fully predicted rewards have no prediction error but a response at the predictive stimulus. Omission of predicted reward results in a negative RPE. Adapted from Schultz et al. (1997).

Multi-tetrode microdrives compared to silicon probes

This paragraph describes why tetrodes compared to silicon microelectrode probes are still superior for deep brain recordings. Although this paragraph and the following subsection (1.2.4. Tetrode efficiency) highlight the limitations of high-density silicone probes, their development and advancement are crucial for new scientific findings.

CMOS-based probes like Neuropixels or NeuroSeeker allow high-density recordings along the dorsoventral axis. However, they induce increased neural damage. They generate heat through the incorporated electronics directly on the electrode shaft, thereby changing neural activity and damaging neural tissue (Steinmetz et al., 2018). Further, the tissue damage is increased by the increased volume and silicon stiffness. Silicon probes, unlike tetrodes, are rigid in the transverse direction. Therefore, the electrode drifts introduced through respiration- and cardiac-related movements are higher for silicon probes.

Silicon probe bending stiffness is lower than metal microwires (Hong and Lieber, 2019). Wire flexibility is advantageous to prevent vascular damage. Individual drivable and flexible microwires are advantageous in deep brain structures. Ventricles and major veins often obstruct deep brain structures.

These limitations result in a reduced chronic recording capability. Microwire recordings revealed chronic stable recordings of single-units for months up to years in primates (Krüger et al., 2010; McMahon et al., 2014) or rodents (Williams et al., 1999). High-density silicon probes allowed limited chronic recording times from eight weeks up to a maximum of 150 days (Jun et al., 2017; Juavinett et al., 2019). Systematic studies to characterize the chronic recording ability of Neuropixels in different brain regions are needed (Luo et al., 2020).

Scientific findings of VTA tetrode recordings

The following publications report dopaminergic VTA single-unit activity recorded mainly with tetrodes and thus, highlight the importance of wire electrode recordings for such a deep brain area. This paragraph also introduces divergent findings from the RPE, which will be addressed later again in the discussion of recorded data. Specifically, the heterogeneity of dopamine signals plays a role in one section of the dissertation.

The scientific novelty does not exclusively rely on conventional electrophysiology but its combination with optical methods. That is of particular importance to ensure cell selectivity of the recorded single units. Important new insights of midbrain dopaminergic neurons are also often performed via optical imaging methods like fiber photometry and two-photon imaging (Howe and Dombeck, 2016; Parker et al., 2016; Menegas et al., 2017; Saunders et al., 2018).

Initially, studies reported a homogeneous and simple RPE signal. However, it is not clear if every dopamine neuron calculates the same RPE signal. Alternatively, different specialized cells could show different computations. Eshel et al. (2016) found that dopamine neurons' responses to predicted and unpredicted rewards follow the same function, only the individual scaling is different. Therefore, dopamine neurons have a homogenous output response.

The reinforcement theory states that the received reward is subtracted from the predicted reward. However, this assumption was never investigated *in vivo.* Alternatively, dopamine neurons' responses can be a result of a division. Calculation based on division is also a common computation within brain circuits (Carandini and Heeger, 2011). It was shown that dopamine neurons calculation is mediated by the subtracted signal from GABA neurons within the VTA (Eshel et al., 2015). GABA neurons inhibit reward signaling of predicted rewards.

So far, the dopamine signal seems to be based on simple calculations and homogeneity. However, dopamine neurons show more complex behaviors. This is already reported in a review by Bromberg-Martin et al. (Bromberg-Martin et al., 2010) more than ten years ago. More descriptions of dopamine diversity followed (e.g., Roeper, 2013; Lammel et al., 2014).

The following summary highlights three examples in which the dopamine signal deviates from the classical RPE theory. A complete overview would go beyond the scope of this dissertation.

In the context of classical conditioning, it is known that dopaminergic neurons typically change their firing sensitivity from phasic excitation by the unconditioned stimulus (US) in the initial stage of conditioning to phasic excitation towards the presence of the conditioned stimulus (CS) as learning progresses. This gradual shift of dopaminergic firing rate occurs typically over hundreds of conditioning trials. Cohen et al. (2012) observed such firing rate shifts in many neurons. However, they also observed neurons excited exclusively by the US or the CS after prolonged conditioning. Other neurons were equally excited by the presentation of both the CS and US.

Dopaminergic neurons respond to stimuli that are not rewarding or predict future rewards. Such stimuli include, for instance, aversive stimuli. Inhibition of midbrain dopamine neurons causes aversion, whereas excitation induced place preference as observed during an operant place preference task (Ilango et al., 2014). The RPE model states that unpredicted adverse outcomes reduce firing. Thus, aversive stimuli in the first exposures should reduce dopaminergic firing. Generally, the effect of aversive stimuli on VTA and SNc showed populations of inhibited and excited dopamine neurons-(Ilango et al., 2012). The fact that dopamine neurons also showed increased firing to aversive stimuli (Joshua et al., 2009; Fiorillo et al., 2013b), points to a motivational salience response rather than an actual value calculation (Watabe-Uchida et al., 2017). It could also be that individual dopaminergic functional subpopulations could signal either reward or aversion (Verharen et al., 2020). During aversive outcomes, often a phasic excitation occurs before a general inhibition. This phasic excitation can be independent of the aversive outcome. Instead, it can be explained by the animals being trained in a high-reward context (Cohen et al., 2012; Tian and Uchida, 2015).

Dopamine activity is not exclusively driven by sensory cue-related signals but also by movement initiation signals (Coddington and Dudman, 2019). Thereby, the distinction of tonic dopamine activity for movement and phasic activity for the RPE has been challenged.
Dopaminergic neurons revealed phasic excitation during voluntary movement onset and offset (Wang and Tsien, 2011). New behavioral tracking possibilities allow the alignment of movement initiation and electrophysiology on a sub-millisecond timescale. In freely moving mice, phasic midbrain dopamine modulation has been recorded before self-paced movement initiation (Da Silva et al., 2018). Interestingly, dopamine neurons seem to encode movement when the animal is engaged in a self-paced operant task. In contrast, non-dopaminergic neurons in the VTA code for motor information without strong task engagement of the animal (Kremer et al., 2020). Overall, movement initiation signals become more important in reinforcement learning models.

1.2.4. Tetrode efficiency

The dissertation focuses in one chapter on tetrode recordings. This subsection makes a comparison of the relative yield between tetrodes and high-density silicone probes.

Efficiency of new high-density electrode devices

High-density silicon probes sample a large neural volume with many more contacts than wire electrodes. Therefore, the total amount of acquired single units is higher. It is, however, unclear if the relative yield (single units per electrode) is also increased compared to wire electrodes. Tetrodes make use of the differential spike amplitudes across four contacts. High-density electrode arrays have multiple closely placed contacts. In theory, this should allow an even better spike sorting yield.

A tetrode can record simultaneously from 5 to 20 neurons in the hippocampus (Reece and O'Keefe, 1989; Wilson and McNaughton, 1993). The yield depends on the recorded brain area. In general, an average of approximately 10 single units per tetrode in many different brain areas is

realistic (Harris et al., 2000; Voigts et al., 2013). With this number of single units, the relative efficiency is 2.5 single units/electrode. If the absolute minimum of 5 units per tetrode is used, the relative yield is 1.25 single units/electrode.

Neuropixels recordings in mice were performed in different laboratories and showed being able to isolate 20-200 single units per brain area (cortex, hippocampus, striatum, thalamus, and others) with an average of 79 single units $\pm$ 55.5. Relative single unit efficiency depends on the brain area and is estimated to be on average 0.64 $\pm$ 0.32 single units/electrode (Figure 2b, Jun et al., 2017). Juavinett et al. (2019) showed 60-100 single units recorded with a Neuropixels probe in freely moving mice over two weeks. The relative efficiency is approximately 0.26 single units per electrode (Figure 2c). This result indicates that the relative yield for high-density probes is comparable to tetrodes. However, tetrodes perform slightly better.

However, recording yield must be analyzed with caution. The same probe design in the same animal can reveal significantly different yields. The yield highly depends on multiple factors. These include induced neuronal damage, material biocompatibility, device geometry, recording area, model organism, acute vs. chronic recording timescale, freely moving vs. head-fixed setup, and many more. Single units do not have an exact ubiquitous definition. Additionally, differences in spike sorting algorithms lead to detection variations and sorting errors.

Explanations for a good relative yield of tetrodes

One explanation could be the distortion of the action potential's waveform in the extracellular space. Harris et al. (2000) showed that an extracellular waveform greatly varies with distance from the soma. Extracellular potentials are a sum of somatic and dendritic currents. Figure 2d shows a linear hexatrode recording with a significantly varying waveform between four to six channels. Therefore, a few channels are sufficient to capture amplitude differences. Further added channels do not contribute more information on the neuron's spatial location. This can explain the efficiency of tetrodes, despite their low electrode number.

Another explanation is the electrode geometry. The center-to-center distance of tetrode wires can be as close as 10 µm. Electrodes are distributed in the horizontal plane. The center-to-center distance for Neuropixels 1.0 is 20 µm. Electrodes are distributed in the vertical plane (Figure 2a). Pyramidal neurons are oriented perpendicular to the brain surface. Thus, Neuropixels record highly distorted waveforms along the somatodendritic axis. The horizontal geometry of tetrodes could, in part, explain the better efficiency. However, this depends on the brain area.

Other factors for a different relative yield include neuronal damage. Neuropixels silicon probes are stiffer compared to flexible thin wires. This fact also plays a role in chronic unit yield. New recording probes would optimally increase neuronal yield by not simply adding more electrodes and sampling a larger neural volume but increasing the yield in a defined volume.

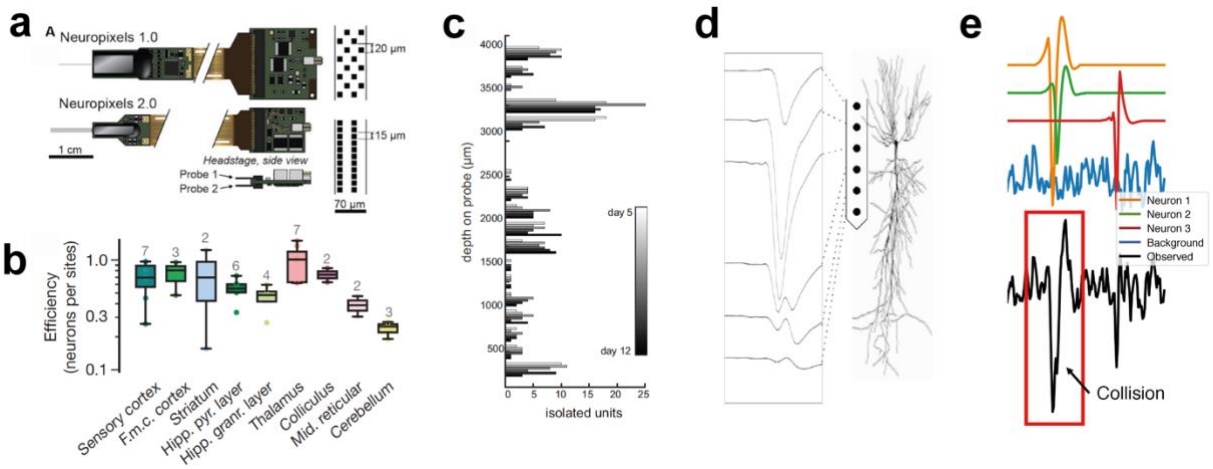

Figure 2 | Yield efficiency (neurons/electrode) in high-density silicon probes

a, Channel arrangement in Neuropixels 1.0 and 2.0. Adapted from Steinmetz et al., 2020. **b**, Neuropixels recording from different brain-structures in awake head-fixed animals: total numbers of recorded neurons divided by the number of electrode contacts. Adapted from Jun et al., 2017. **c**, Histogram single units across the ventromedial extent of a Neuropixels probe for an exemplary mouse over several recording days. Adapted from Juavinett et al., 2019. **d**, Waveforms from a pyramidal cell recorded with a linear hexatrode. The overlay shows the positioning of the probe along the somatodendritic axis. Adapted from Harris et al. (2000). **e**, Temporal superposition of two spikes from different neurons (orange and green trace) resulted in a collided spike (black trace). Spike sorting cannot differentiate the origin of two different neurons. Adapted from Carlson and Carin (2019).

1.2.5. Spike sorting algorithms

After data acquisition, data analysis is the next critical step. Enormous datasets from high-density silicon probes possess analysis challenges. This subchapter introduces spike sorting and new generation spike sorting in the example of Kilosort., which is a software used in this dissertation. It also highlights a possible advantage of silicon probes during spike sorting and shows how new spike sorting software developed for such large datasets can also benefit tetrode acquired data. The last paragraph highlights general limitations of spike sorting.

Semi-automated spike sorting generally consists of four steps: 1.) High-pass filtering of the raw data and spike detection using threshold crossings of the electric potential; 2.) Extracting spatiotemporal features of the detected spikes, usually by principal component analysis; 3.) Assigning similar spikes into clusters by, for instance, template matching; 4.) Automated and manual cluster evaluation that includes observing violations in auto-correlograms or cross-correlograms.

Automated clustering algorithms are challenging to implement since neither the number of neurons in the recording nor the cluster waveform shape is initially known. The main problems of spike sorting are electrode drift, overlapping spikes, and waveform changes during bursting activity (Harris et al., 2001; Quirk et al., 2001).

Spike sorting of high-density probes

The relative unit yield of Neuropixels silicon probes seems to be not increased compared to tetrode recordings. However, the additional information of temporal coherence across many electrodes can help during spike sorting. Simultaneous firing of two spikes from different neurons results in a collision. The result is a single recorded spike (Figure 2e). This temporal overlap can be better resolved by high-density probes (Sauer et al., 2015; Rossant et al., 2016).

Naturally, overlapping spikes will also occur more often in large and dense electrode arrays. For these dense silicon arrays, spike sorting needs to be improved. Newer algorithms use improved template-matching algorithms (Ekanadham et al., 2014; Pachitariu et al., 2016b; Stringer et al., 2019). Those are needed to resolve temporally overlapping spikes (Lefebvre et al., 2016). Additionally, they reduce the computational workload of the simultaneous integration of many hundred channels.

Spike sorting: Kilosort

Modern sorting algorithms, like Kilosort, use graphics processing unit computations and can handle increased amounts of data (Pachitariu et al., 2016a). Such algorithms also correct electrode drifts, which are often observed in silicon probes (Kilosort 2.0: Stringer et al., 2019; Steinmetz et al., 2020). These algorithms reduce manual curation by automated detection of well-isolated units (Kilosort 2.0: Stringer et al., 2019, Klustakwik: Rossant et al., 2016) and introduce quantitative criteria to curate the clusters isolation quality (Schmitzer-Torbert et al., 2005; Hill et al., 2011). However, a manual human operator assessment based on, for instance, waveform shape is often inevitable. Newer spike sorting algorithms are also useful for multi-tetrode recordings. The reduction in false-negative and false-positive errors and quantitative measures of sorting efficiency is an advantage.

Spike sorting limitations

At a closer look, error-free spike sorting is difficult (Buzsáki, 2004). Amplitudes and waveforms of extracellular spikes from the same neuron are highly variable. Membrane potential changes are state-dependent (Buzsáki et al., 1996; Quirk et al., 2001). Electrophysiological markers, like spike duration and firing rate, are often variable (Margolis et al., 2006; Ungless and Grace, 2012).

This high variability of amplitudes and waveforms has many causes. One reason is that neurons are defined as a point source (McNaughton et al., 1983; Gray et al., 1995). A point source shows an apparent amplitude variation based on the distance of the neurons to each electrode contact. However, neurons are biophysically not a point source: action potentials can also be generated along the neuronal membrane (Llinás, 1988).

Another reason is signal backpropagation. Extracellular recorded potentials cannot distinguish between soma and dendritic regions and are, therefore, a sum of both. Backpropagating signals from the somatic region towards the dendrites have an impact on the spike waveform and amplitude. Backpropagation largely varies depending on excitatory and inhibitory afferents (Stuart et al., 1997).

Finally, also the refractory period has an impact. The refractory period of neurons results in drastic variations of spike amplitudes during burst firing (Harris et al., 2001; Quirk et al., 2001).

1.2.6. Combining optophysiology with tetrodes

A focus of the dissertation are devices that combine electrophysiology and optophysiology. Exemplary penetrating electrode devices and methods combining both technologies are introduced here.

Optrode

Simultaneous neural recording and optical modulation allow new possibilities in the field of systems neuroscience. Electric stimulation induces significant artifacts, which are reduced for optical stimulation. Genetically encoded opsins or calcium indicators offer a high cell specificity.

Light scatters and gets absorbed within the neural tissue. Thus, optical waveguides need to be closely implanted along the recording electrodes. Combined electric and optic devices are referred to as optrodes. Tetrode optrodes allowed, for instance, to optically deconstruct the parkinsonian neural circuity (Gradinaru et al., 2009). Michigan-type single- and multi-shank silicon optrodes allowed to examine the contribution of excitatory and inhibitory neurons on high-frequency hippocampal ripple oscillations (Stark et al., 2014).

Optrodes also allowed combined extracellular recordings and imaging of fluorescent calcium indicators. Fiber photometry uses genetically encoded calcium indicators, allowing to image cell-type-specific population activity (Adelsberger et al., 2005; Cui et al., 2014; Kim et al., 2016). A recently developed sensor for dopaminergic midbrain neurons, called dLight1, has improved temporal characteristics and a high affinity (Patriarchi et al., 2018).

Optogenetic tagging

Extracellular electrophysiological recordings do not allow identifying the type of the recorded neuron. The VTA, for instance, is composed of different neuronal subpopulations: dopaminergic, GABAergic, and glutamatergic neurons (Nair-Roberts et al., 2008; Ungless and Grace, 2012). Midbrain dopamine neurons have diverse electrophysiological characteristics (Margolis et al., 2006; Ungless and Grace, 2012). Therefore, electrophysiological markers are insufficient to characterize a neuron's identity.

Optogenetic tagging (optotagging) is used to confirm the identity of a recorded single unit (Lima et al., 2009; Cohen et al., 2012; Chen et al., 2017a; Mohebi et al., 2019). Optotagging combines electrophysiology and cell-specific optogenetics. The Cre-LoxP system allows producing genetically engineered mouse lines (Nagy, 2000). The opsin sequence is flanked by Lox sites and, for instance, packed in an adeno-associated virus. Injection of the virus results in cell-specific ChR2 expression because only Cre recombinase can invert the lox sites and allow opsin expression. Many mouse lines exist in which the Cre recombinase is only present in a specific cell type. Cell type specificity can be, for instance, reached by Cre expression targeted to gene promotors that are unique to a certain cell type. Dopamine neurons can be targeted by the dopamine transport (DAT) promotor or tyrosine hydroxylase (TH) promotor (Pupe and Wallén-Mackenzie, 2015).

Overall, Cre-dependent channelrhodopsin-2 (ChR2) is expressed only in dopaminergic neurons. Light illumination of the recording site depolarizes neurons exclusively expressing the light-sensitive ChR2 and are, therefore, identified as dopaminergic.

1.3. Microdrives

One chapter of the dissertation covers the development of a tetrode microdrive. The following section introduces and compares different aspects of microdrives for extracellular *in vivo* electrophysiology.

1.3.1. The benefit of movable microelectrodes

Acute anesthetized *in vivo* experiments with stereotactic micromanipulators allow repositioning of the electrodes (Hubel and Wiesel, 1962; Seshagiri and Delgutte, 2007). However, the quality of single units with static implanted electrodes in chronic awake recordings is determined by the initial implantation accuracy (Schultz, 1986; Nicolelis et al., 2003).

Some factors make movable electrodes advantageous over static ones. Due to electrode micromovements, single units can be lost permanently over time. An extracellular action potential above background noise can only be recorded if the neuron is not further than ≈50-100 µm away (Henze et al., 2000; Seshagiri and Delgutte, 2007; Mechler et al., 2011). A higher distance results in multi-unit activity. The mismatch of the stiff electrode and the soft brain tissue causes a change in the electrode's position. Movements further than ≈50-100 will cause a loss of the previously separatable single units.

This mechanical mismatch of the stiff electrode and soft brain tissue causes a neuroinflammatory response. Ultimately a glial sheath forms and prevents single-unit detection (Dickey et al., 2009; Muthuswamy et al., 2011). The glial sheath encapsulation of the electrodes starts as early as one day after implantation (Fujita et al., 1998). This concept is further introduced in section: 1.6. Biotic properties of signal quality, subsection: 1.6.1 Foreign body response.

Driving the electrodes in continuous small steps over time through the brain can circumvent the described difficulties. This is performed by head-mounted microelectrode drives (microdrives). Microdrives allow head-fixed or freely moving recordings in awake animals. Microdrives also increase the yield by acquiring new single units with every depth adjustment.

A microdrive provides post-surgery adjustment if electrodes were implanted too dorsal. Electrophysiological markers during surgery can be misleading since anesthesia affects neural activity (Pachitariu et al., 2015; Deane et al., 2020).

Implanting electrodes several hundred micrometers above the desired recording area can improve recording quality. A successive advancement in small steps allows tissue adaption. It is shown that microdrive micromotions induce a force approximately ten times less than the initial full-depth electrode penetration force (Sridharan et al., 2013). However, the tissue response to a movable electrode needs further investigation (Buzsáki et al., 2015).

1.3.2. Rodent microdrive designs

Light-weight implants for mice

The first microdrives were designed for rats and mainly hippocampal recordings. This paragraph describes the impact of two early microdrive designs. A microdrive with 12 individual adjustable tetrodes was arranged in a circular shape. This microdrive simultaneously records many hippocampal place cells in rats (Wilson et al., 1991). The drive facilitated recordings of the neural ensemble that allowed to decode place cell activity and predict the animal's location for the first time (Wilson and McNaughton, 1993). Gothard et al. (1996) made advancements to that initial design. It was then used in the 1988 Neurolab Space Shuttle mission. They explored hippocampal place cells and thalamic head direction cells of rats in microgravity (Knierim et al., 2000). Hippocampal isotropic and circular place fields were found in rats by walking on an orthogonal surface just like on earth. Place fields were found, although the information about the head direction and the landmarks in zero gravity do not match. Despite three-dimensional navigation being challenged, place fields are comparable to recordings made on earth. The microdrive designs mentioned here were bulky and heavy. Therefore, they could only be used in rats.

Microdrives for mice are more challenging to design. Head implants can disturb the natural behavior of a mouse. Thus, the head implant's weight should be < 10% of the animal's weight (Buzsáki et al., 2015). Dimensions must be small to enable a low point of gravity. Post-surgery recovery can be severely impaired when the mouse cannot raise the head for eating and drinking. A pulley system to aid head lifting can only be used during experimental procedures but not in the homecage. Not many microdrives are explicitly designed for mice, and downscaling complex rat designs for the usage in mice resulted in bulky and heavy microdrives (McHugh et al., 1996). Simpler and lightweight microdrives for mice are necessary. Mice are the primary model species because of their diverse pool of genetically modified lines (Kim et al., 2017), such as different Cre driver lines that allow cell-specific opsin expression (Lammel et al., 2015).

Different microdrive designs

Tetrode microdrives have to design categories: single-carrier microdrives and hyperdrives.

Single-carrier microdrives consist of one drivable electrode carrier. In a single-carrier microdrive, all electrodes are driven simultaneously with a single screw (Korshunov, 2006; Anikeeva et al., 2012; Delcasso et al., 2018; Kim et al., 2020). Thus, they are used in preparations in which the position of the tetrodes and fiber can be pre-defined. Electrode arrangements can be flexible. Later adjustments of the relative position of single electrodes are not possible. Such a mechanism can be built with a vented screw and tetrodes fixed to an optical fiber (Figure 3a).

Another possibility is a sliding electrode carrier with tetrodes fixed inside guide tubes (Figure 3b). The weight limitations for mice can be fulfilled with such designs. Single-carrier microdrives have a small footprint and are easily fabricated. Therefore, such designs allow the implantations of several microdrives (Headley et al., 2015).

Hyperdrives consist of an assembly of drive units in a concentric arrangement. Hyperdrives allow driving each electrode independently. Such a design is beneficial, for example, in targeting thin cell layers like the hippocampus. Several drive units are often arranged in a cone shape. Electrodes are fixed inside guide cannulas that funnel them to the exit (Figure 3c, Wilson et al., 1991; Siegle et al., 2011; Freedman et al., 2016; Liang et al., 2017). Hyperdrives host a larger number of tetrodes compared to single carrier microdrives. Recent hyperdrives accommodate up to 16 tetrodes for mice and 64 tetrodes for rats (Liang et al., 2017; Voigts et al., 2020). Such complexity increases weight, costs, and fabrication time significantly.

The manual fabrication of tetrodes is already time-consuming. Additionally, assembly and loading of hyperdrives can take days. Reliable manufacturing of most hyperdrive designs often needs experienced experimenters. In comparison, single-carrier microdrive fabrication takes less than a day. Hyperdrives have a fixed electrode spacing and spatial arrangement. The concentric arrangement reduces the flexibility of electrode positioning. Some hyperdrives, like the flexDrive, allow higher flexibility (Voigts et al., 2013, 2020). The concentric arrangement and tetrode bending within the guide tube result in friction (Figure 3c). This friction force can corrupt the tetrode isolation layer.

Overall, single-carrier designs offer higher flexibility, low weight, reduced costs, and less time investment. Hyperdrives are necessary for experiments where individually drivable electrodes are needed.

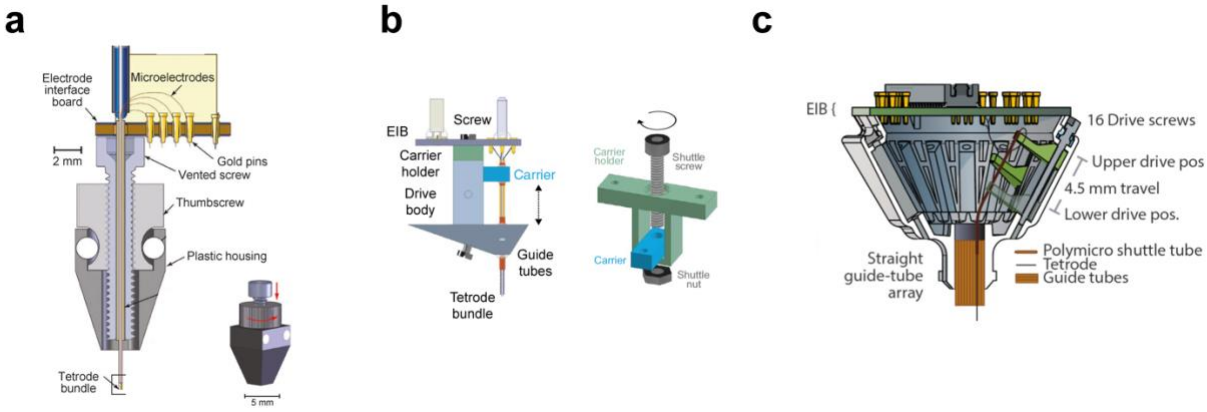

Figure 3 | Cross-sections of microdrive designs (examples for mice)

a, **b**, Single-carrier microdrive designs. **c**, Hyperdrive cone-shaped design. **a**, Optetrode: A vented screw contains the tetrodes and enters a thumbscrew and plastic housing. Thumbscrew rotations drive the screw with the tetrodes down. The head of the screw is fixated to the EIB. Adapted from Anikeeva et al. (2012). **b**, The DMCdrive: Tetrodes are moved vertically by inserting them into guide tubes (orange) that are fixated to a tetrode carrier (blue) and the drive body (gray). A shuttle screw moves the tetrode carrier up and down inside a carrier holder (green). The EIB is fixated on top of the carrier holder. Adapted from Kim et al. (2020). **c**, Shuttledrive: Individually movable tetrodes are fixated in a cone shape drive. The EIB is fixated on top. Each shuttle (green) holds a tetrode and is moved up and down by a screw. Tetrodes are inserted into a shuttle tube, which then enters a guide tube. Adapted from Voigts et al. (2020). **a**, **b**, and **c** allow the integration of an optical fiber.

1.3.3. Single-carrier microdrives for mice

Important microdrive developments in the past 20 years

One project of this dissertation is the development of a single-carrier microdrive for mice. Many different customized single-carrier microdrives have been proposed over the past 20 years (Figure 4). A historical evaluation helps to understand the advantages and disadvantages of the past microdrives.

Microdrives have been adapted and specialized for various probe designs: first for single wires (violet), later for tetrodes (red), and more recently for silicon probes (yellow, Figure 4). This development of high channel count recordings goes in hand with improved data acquisition systems. A single high-impedance wire recording allowed simple microdrives and headstages. In contrast, multi-electrode tetrodes need more lightweight and compact multi-contact electrode interface boards and headstages.

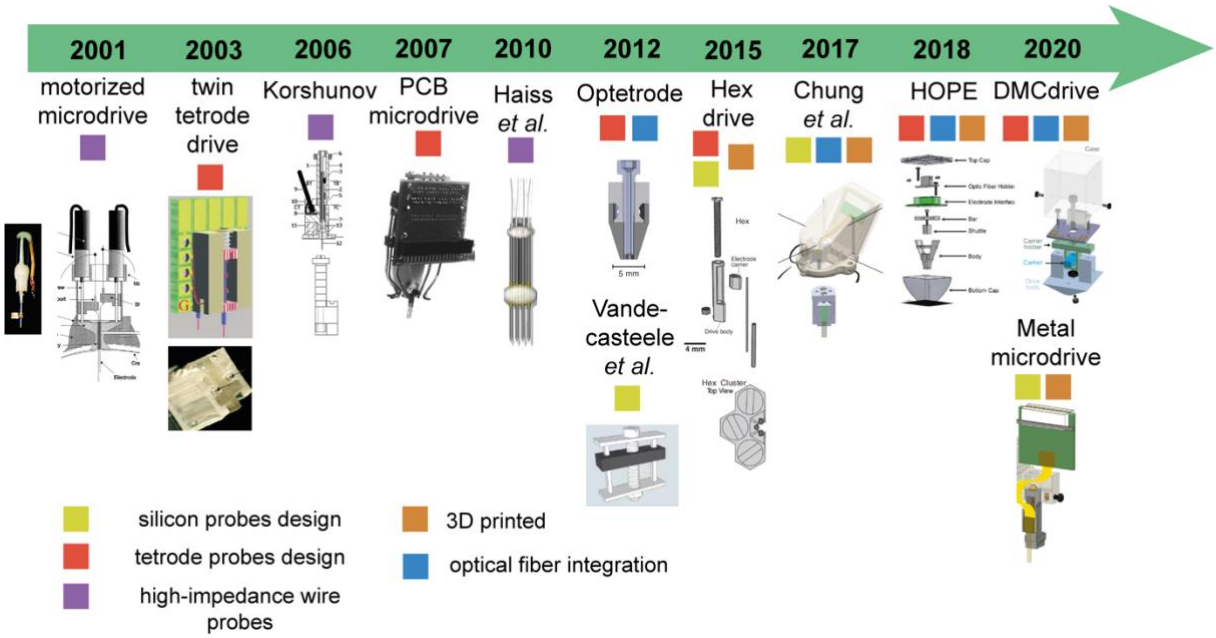

Figure 4 | Timeline of custom-build single-carrier driven microdrives used in mice

Designs underwent steady improvements in the past 20 years. Reproducibility and channel count increased. The fabrication process became easier. Here, only specialized drive papers are included. Custom drives that do not include a fabrication process description are not included. Figures adapted from the following publications (left to right): Fee and Leonardo (2001), Jeantet and Cho, (2003), Korshunov (2006), Tóth et al. (2007), Haiss et al. (2010), Anikeeva et al. (2012), Headley et al. (2015), Chung et al. (2017), Delcasso et al. (2018), Kim et al. (2020), Vöröslakos et al. (2021).

Early designs were made from heavy materials or required specialized workshop equipment. Often the given instructions for fabrication are incomplete or vague. Their fabrication was inconsistent and their practical use, therefore, limited. With the advent of optogenetics, it was necessary to integrate optical silica fibers into microdrives. Optrodes combine electrophysiology and optogenetic manipulation. The first microdrive for mice incorporating electrodes and an optical fiber was the so-called Optetrode (Figure 3a, Figure 4, Anikeeva et al., 2012). The electrical and optical connectors are directly coupled to the electrode probe. Connecting the headstage and optical fiber for recordings induces plugging forces. Such forces could result in micromovements of the attached tetrodes. The

result is a loss of previously recorded units. Repeated plugging forces could also interfere with the precision of the drive mechanism.

Other designs included only a stationary fiber (HOPE and DMCdrive, Figure 4). If tetrodes are advanced beyond the light penetration depth, high laser power must be used. The heat generated by increased laser power damages the neural tissue. At some point, the electrodes are inevitably moved out of the light cone from the stationary fiber.

The complexity of all microdrives increased by incorporating an optical fiber (Anikeeva et al., 2012; Delcasso et al., 2018; Kim et al., 2020). A simple solution that also does not increase weight has not been found.

3D printable microdrives

Only in recent years have 3D printed microdrives become available (Figure 4). The used materials reduce the microdrive's weight significantly. It further allows the fabrication of high quantities in an automated and reliable process. 3D printing is cost-effective. Earlier microdrives were expensive and could only be produced in limited amounts. Therefore, microdrives were only implanted in a limited number of animals that had already shown good learning performance during pre-training of a behavioral task. The design of 3D parts can be easily customized without the need for specialized parts or tools. The metal microdrive design in Figure 3a needs a machined modification process for its drive mechanism (Anikeeva et al., 2012).

Two types of 3D printers are used: FDM (fused deposition modeling) and stereolithography printers. FDM printing has a lower precision and is more often used for larger objects. Stereolithography printers have a higher precision, which is beneficial for small parts.
In both types, layers are successively added to build a complete object. 3D printing software does not need specialized knowledge and suggests optimal settings like layer thickness. The biocompatibility of 3D printing materials is not certified. However, the material does not come in direct contact with living tissue.

Previous 3D printed designs used less accurate FDM printers, leading to difficulties with small microdrive parts (Ma et al., 2019; Kim et al., 2020). Other 3D printed microdrives have an immovable fiber (Kim et al., 2020) or a complicated assembly process and increased weight (Delcasso et al., 2018).

A single-carrier microdrive design is missing that incorporates an optical fiber but is easily customizable, lightweight, prevents plugging forces, is cost-effective, and easy to replicate.

Commercial microdrives

Commercial microdrives lack the flexibility to customize the design for various experimental approaches. They are much more expensive than custom microdrives. The cost of a single commercial microdrive can exceed the costs of a desktop 3D printer. The VersaDrive-8 Optical from Neuralynx, for example, costs more than 250 € (Hardung et al., 2017). A custom 3D-printed hyperdrive with an integrated optical fiber costs less than 50 € (Voigts et al., 2013).

There are almost no single-carrier commercial microdrives that also incorporate optical fibers. Printing costs for a 3D printed single-carrier microdrive design are <1 €. The total costs, including tetrodes, electric connectors, and optical fibers, are typically <50 € (Delcasso et al., 2018; Kim et al., 2020).

Commercial vendors also use 3D printing (e.g., Halo microdrive, Neuralynx). 3D printed guide channels promote the linear motion of tetrodes. In contrast, earlier designs needed manual insertion of guide channels. The same principle is used in the custom open-source Shuttledrive (Open Ephys) depicted in Figure 3c (Voigts et al., 2020). This example shows how the open-source community produces top-notch microdrives which are on par with commercial suppliers.

1.3.4. An open-source single-carrier microdrive

One project in this dissertation is the development of an open-source microdrive and a behavioral setup, which is based on an open-source Arduino platform. Therefore, this subsection introduces the open-source neuroscience movement.

Neuroscientists in the field of systems neuroscience are, in part, engineers and developers themselves. Recording hardware like microdrives or non-standardized behavioral setups are not commercially available or require modifications. Therefore, many advancements are made inside the laboratory. However, most of the methodological knowledge stays within the laboratory. The result is a patchwork rug of neuroscientific equipment and software. Currently, this trend shifts towards a unified framework of neuroscientific hard- and software.

Several developments caused the emergence of unified science community-driven hard- and software.

a) Neuroscience laboratories are emerging around the world and need affordable scientific equipment. This is of high importance in countries with low scientific funding capabilities. However, it is also relevant for countries with high funding competition.
b) Nowadays, a scientific question is investigated with many different techniques. A laboratory that previously specialized in one technique must expand its methodological repertoire. New techniques must be established in a short time window and without decades of experience.
c) Hard- and software needs customization. Additionally, upgrading to new developments should be cost-effective.

A unified framework can assist the reproducibility crisis. Instead of different systems in every laboratory, unified open-source systems increase comparability. Additionally, open-access publications, data availability, and shared analysis scripts exist. Altogether, they increase reproducibility and accessibility.

Different open-source hard- and software already exist. Open-source software packages include DeepLabCut and Kilosort. DeepLabCut is a markerless behavior pose estimation software that uses deep neural networks (Mathis et al., 2018). Kilosort is a fast and fully automated spike sorting software. It uses fast graphics processing unit computing with drift correction (Pachitariu et al., 2016a, 2016b).

Open-source hardware includes data acquisition systems, miniature microscopes, and microdrives. The Miniscope was developed at the University of California, Los Angeles. It is a wide-field fluorescence miniature head-fixed microscope for mice (Cai et al., 2016; Shuman et al., 2020). OpenEphys is a multichannel data acquisition system (Siegle et al., 2017). The flexDrive is a hyperdrive that incorporates up to 16 individual drivable tetrodes (Voigts et al., 2013). The design was recently updated to the so-called shuttledrive, allowing 3D printing (Voigts et al., 2020). However, a single-carrier open-source 3D printed microdrive that also incorporates a movable optical fiber is still missing.

Here, only a few examples are mentioned. Further projects can be found at OpenBehavior, a centralized repository for open-source behavioral neuroscience. To some extent, the open-source movement has democratized the science community. It allows every scientist to contribute new developments and use tools that are otherwise inaccessible.

1.3.5. Comparison of tetrode electrophysiology and calcium imaging

In vivo recordings of neural activity can be performed with a variety of methods. This subsection highlights some limitations of newer calcium imaging techniques. It does not aim to prove that one method is better than the other but rather that the combination of optophysiology and electrophysiology is more advantageous than each method separately. This perspective follows this dissertation's focus on combining both modalities in neural recording devices.

Optical methods include two-photon fluorescence microscopy (Denk et al., 1990; Denk and Svoboda, 1997) and single-photon head-mounted miniature microscopes (Aharoni and Hoogland, 2019; de Groot et al., 2020). Such optical methods compete with conventional electric recording technologies such as tetrodes and can often visualize a larger number of individual neurons with high cell specificity and image for long time periods over months.

The major limitation of optical calcium imaging is the slow kinetics of the indicators. Additionally, calcium signal interpretations are complex. Electrophysiological recordings allow measuring the extracellular potential instead of an indirect calcium signal. The calcium signal is an indirect signal of neural activity. A direct correlation with spiking activity is difficult for several reasons (Theis et al., 2016).

The relationship between spikes and calcium indicator fluorescence is non-linear. Non-linearity arises, for instance, through multiple cooperative calcium-binding sites (Rose et al., 2014). Additional difficulties arise from variations of the calcium signal in neuron types, exogenous ion concentration, and burst activities (Harris et al., 2016). The imaged cells are contaminated with activity from the

neuropil. This effect makes signal interpretations in densely packed regions like the hippocampus difficult (Harris et al., 2016; Yang et al., 2016).

The correct calcium indicator expression is crucial but difficult to achieve. Chronic imaging or high-intensity light causes bleaching of the fluorescent calcium indicators (Kuzum et al., 2014). Viral overexpression interferes with the neuron's calcium buffer capability. Overexpression also leads to a nuclear filling with the calcium indicator. These cytotoxic phenomena lead to cell death (Grienberger and Konnerth, 2012), whereas low expression of the viral construct results in a low imaging yield (Resendez et al., 2016).

Devices that incorporate the fast temporal features of direct extracellular potential recordings combined with the cell specificity and high yield of calcium imaging can yield unique insights into neuronal processing. Optimally one would electrically and optically record from the same neuronal cells to counterbalance individual technique-related limitations. This potential can be facilitated with the upcoming rise of genetically encoded voltage sensors that have much faster temporal kinetics (Bando et al., 2019; Zhu et al., 2021). However, this type of sensor also needs imaging hardware with higher frame rates.

1.4. Non-penetrating cortical surface electrodes

1.4.1. Origins and current approaches

One chapter of the dissertation focuses on the advancement of a µECoG array. This subsection introduces the origins of these devices.

ECoG signal origin and analysis

Planar cortical surface electrodes record the synchronized neural activity of functionally linked neocortical neurons. Electrodes are placed epidural or subdural and therefore record activity from mainly superficial layers. However, the extracellular medium is conductive. The current spreads from distant neural sources, which is a process termed volume conduction. Therefore, the ECoG signal contains activity from deeper brain areas as well (Ojemann et al., 2013; Richner et al., 2019). The ECoG signal depicts mesoscopic activity patterns: the level of cell assemblies and cortical columns (Ohl et al., 2001; Ceballo et al., 2019).

ECoG signals are processed in multiple ways to extract different properties. Spectral analysis reveals oscillatory patterns such as alpha, beta, gamma, delta, and theta oscillations that give rise to various cognitive states (Jacobs and Kahana, 2010; Wang, 2010). Functional coupling of separate brain areas is assessed via cross-correlations or coherency (Nolte et al., 2004; Schulz et al., 2016). Granger causality is used to infer the directionality of functional coupling (Kamiński et al., 2001; Brovelli et al., 2004).

The development of µECoG arrays

ECoG surface arrays are less invasive than penetrating electrodes. Therefore, they are essential for clinical research. ECoG recordings are also promising devices for brain-computer interfaces (Hill et al., 2006; Minev et al., 2015).

ECoG recordings were first used in the 1940s for epilepsy screening (Penfield and Steelman, 1947). They bypassed the signal reduction, an inherent hurdle of electroencephalography (EEG). Early electrodes were rudimentary ball electrodes. Those were later replaced by platinum-iridium planar electrodes embedded in a silicone elastomer. The technology was approved by the U.S. Food and Drug Administration. The device was the first extensively used clinical ECoG array. It allowed to successfully localize epileptogenic foci (Goldring and Gregorie, 1984), which was previously only possible using invasive depth electrodes.

ECoG array applications for clinical usage have been growing continuously in the past decades. Applications in small mammalian brains need significant miniaturization. In the late 2000s, the modern photolithography microfabrication process allowed the fabrication of small µECoG arrays. Photolithography precisely patterns different layers of the µECoG array on an initial sacrifice layer. At the end of fabrication, photolithography is used to encapsulate the device with an insulating substrate. Electrode contacts are left uninsulated. The inter-electrode spacing of µECoG arrays is in the range of hundreds of micrometers (Kim et al., 2007).

These advancements in manufacturing processes gave rise to many different µECoG arrays designs. Rubehn et al. (2009) developed the first PI-based µECoG arrays for Rhesus monkeys. Small Parylene C-based arrays were later developed for use in rats (Ledochowitsch et al., 2011a). The NeuroGrid allowed to not only record ECoG signals but simultaneously acquire single units. This was possible through small electrodes with a poly(3,4-ethylenedioxythiophene):polystyrene sulfonate (PEDOT:PSS) modification (Khodagholy et al., 2015). Subdural cortical spike recordings allow future µECoG-based brain-computer/brain-machine interfaces (Khodagholy et al., 2015; Bockhorst et al., 2018).

Another µECoG array improvement concerns insulator thickness. Many µECoG arrays were too thick. Thus, not allowing flexibility and transparency. Thin-film insulators allow high flexibility. Such thin insulator films also conform to the curvature of the brain surface. Thin PI insulators have been a promising solution (Yeager et al., 2008; Zátonyi et al., 2018b). However, they lack the transparency needed for simultaneous optogenetics and optical imaging methods.

1.4.2. Combining optophysiology with µECoG arrays

The usage of transparent insulators was the first step in allowing optical imaging and stimulation through an µECoG array. Many devices additionally incorporated optical transparency of the electrode surface area, which was possible through using indium tin oxide (ITO) and graphene.

Ledochowitsch et al. (2011b) developed one of the first rodent transparent electrode ITO µECoG arrays. In a later approach, the electrode and the conducting traces to the electric interface board (EIB) were made of ITO. This enabled complete transparency of the array. This transparency allowed voltage-sensitive dye (VSD) imaging of sensory-evoked activity through the array (Kunori and Takashima, 2015). Integrated LEDs above the transparent ITO electrodes were also demonstrated (Kwon et al., 2013). A recently developed ITO array confirmed longevity only *in vitro* (soaked in phosphate-buffered saline (PBS) with increased room temperature for four days, Zátonyi et al., 2020). However, none of the published ITO arrays showed chronic *in vivo* recording capabilities.

Graphene is an alternative transparent electrode material. Rodent graphene µECoG arrays show higher transmittance and better electrical parameters than ITO (Kuzum et al., 2014; Park et al., 2018). Graphene is chemically stable, has a high transmittance, and is flexible (Geim and Novoselov, 2007; Lee et al., 2008). However, graphene arrays are used mainly in acute *in vivo* recordings (Kuzum et al., 2014; Thunemann et al., 2018). Chronic recordings for up to 70 days were possible in one graphene array design (Park et al., 2014). Graphene transparency requires a one-atom thick layer. The thin layer results in high sheet resistance, mechanical instability, and high electrode impedance. Full transparency of insulators and ITO or graphene electrodes can be useful for wide-field two-photon imaging (Lu et al., 2018b; Thunemann et al., 2018).

1.4.3. µECoG applications: Tonotopic auditory cortex mapping

A newly developed µECoG array will be tested *in vivo* in one chapter of the dissertation. Thereby, the mapping of the auditory cortex is going to play a major role. Relevant aspects are introduced in this subsection.

The auditory system is in large parts tonotopically organized. Tone frequency separation starts in the basilar membrane in the inner ear and continues along the brainstem. Frequency separation is preserved along the pathway towards the auditory cortex. Thus, the primary auditory cortex (A1) has a gradient of auditory frequency bands. In that gradient, some neurons preferentially respond to low frequencies and others to higher frequencies. Topographically organized maps exist in multiple species (Hackett, 2011). They are used to evaluate sensory-evoked neural plasticity.

A1 is not only a pure stimulus analyzer. Tonotopic maps can undergo plastic changes throughout the whole lifespan. The auditory cortex is involved in learning and showed reshaping of tuning properties (Ohl and Scheich, 1996; Weinberger, 2007). The following examples highlight A1 map plasticity. Simultaneously VTA stimulation and tone presentation increased the cortical area of the specific tone frequency (Bao et al., 2001). The area of neighboring frequencies decreased. A similar tonotopic map reorganization was observed during nucleus basalis stimulation (Kilgard and Merzenich, 1998). Tonotopic map reorganization was also observed during reinforcement tasks. Bieszczad and Weinberger (2012) revealed an increase of the tonotopic field for the tone frequency predicting a reward. Behavioral extinction reversed this effect.

Mapping the reorganization of the tonotopy has one primary confinement. Recording techniques do not allow continuous *in vivo* tonotopy mapping. However, complete tonotopic maps can only be recorded in one terminal recording. Anesthetized animals are recorded from middle cortical layers with dense multi-wire arrays. Single- and multi-unit threshold frequency tunings are interpolated with Voronoi tessellation (Yarrow et al., 2014). Multiple tessellated polygons across the cortex resemble the tonotopic map. Cortical microelectrode penetrations sites can reach up to 100 penetration sites (Polley et al., 2006). This magnitude of electrode insertion impacts neuronal functions and induces severe neural damage.

All auditory map plasticity studies use between-group comparisons (Heil and Irvine, 1998; Kilgard and Merzenich, 1998; Bao et al., 2001; Hui et al., 2009; Hackett et al., 2011; Bieszczad and Weinberger, 2012). Thereby, tonotopic maps of single terminal recordings in naïve animals are compared to single terminal recordings of trained animals.

Our understanding of topographic maps is exclusively based on one limited methodology: multi-wire recordings of cortical layer IV/V in anesthetized animals. Interpretations might suffer from the used methodology. µECoG recordings could allow continuous chronic tonotopy mapping and enable comparing map plasticity changes within the same animal. Due to the epidural placement, neuronal damage would be reduced.

1.5. Abiotic properties of signal quality

This section introduces several material-dependent aspects that need to be considered for neural device advancements. It introduces concepts that are important for developing and testing the two neural devices in this dissertation: a transparent µECoG array and a multi-tetrode microdrive.

1.5.1. Choice of electrodes and insulators

This subsection provides an overview of electrode and insulation materials. An ideal neural implant would cause low inflammation and minimal neuronal damage; additionally, it should be flexible but stable against mechanical stress and biochemical degradation. The dissertation's focus is not on engineering. Therefore, only a short overview of materials and fabrication processes is presented.

ECoG electrode materials

Planar cortical surface electrodes are made from gold, copper, platinum, silver, titanium, tungsten, ITO, and graphene. The toxicity of copper and silver makes them unusable. Platinum and titanium are regularly used in medical implants. They are highly biocompatible. Platinum has high electrochemical stability and corrosion resistance (White and Gross, 1974). It is regularly used in cochlear implants, DBS electrodes, and retinal implants. Additionally, platinum and other metals can be easily used in standard microfabrication processes (Negi et al., 2010).

New electrode materials like graphene and ITO are transparent. However, ITO suffers from poor insulator adhesion and cracking (Chen et al., 2001; Alzoubi et al., 2011). Graphene shows limited chronic recording capabilities (Park et al., 2014; Thunemann et al., 2018). Platinum electrodes are therefore advantageous for chronic ECoG *in vivo* recordings.

ECoG insulator materials

Typical µECoG array isolators are flexible polymers. Typically used polymer substrates include Parylene C, PI, SU-8, polydimethylsiloxane (PDMS), PET (polyethylene terephthalate), and liquid crystal polymers. Important insulator properties are flexibility, biocompatibility, robustness, and transparency. PI and Parylene C are the most common insulators for µECoG arrays (Shokoueinejad et al., 2019).

Parylene C is long-term stable, biocompatible, colorless, transparent, and has good barrier properties (U.S. Food and Drug Administration approved, Hassler et al., 2011). However, it shows adhesion problems to metal conductors. It is fragile in flexible thin devices (Schmidt et al., 1988). Its limited thermal stability complicates device fabrication (Von Metzen and Stieglitz, 2013; Li et al., 2019). During handling Parylene C is more fragile compared to PI sheets (Hassler et al., 2011).

PI is thermostable, has high mechanical strength and electrical resistance. PI device fabrication does not need complicated processes and is, therefore, cost-efficient. PI µECoG arrays showed chronic *in vivo* reliability for months (Yeager et al., 2008; Rubehn et al., 2009). Its biocompatibility

has been proven (Lago et al., 2005; Stieglitz, 2009; Rubehn and Stieglitz, 2010). PI's main disadvantage is its lower blue-light transmittance compared to Parylene C (Hassler et al., 2011).

Tetrode wires

Wire electrodes have a small footprint and high flexibility. Thus, wires allow access to deep brain structures with minimal impact. Their fabrication is inexpensive and straightforward. Tetrodes consist of four twisted insulated metal wires. Recordings are performed at the insulation-free wire tip. The sharp electrode tip is produced by a clean cut of the wire end.

Wires are made from pure metals like tungsten, platinum, iridium, stainless steel, or alloys of metals like platinum-iridium, platinum-gold, nickel-chromium (nichrome). These materials are biocompatible, have a low impedance, and have good charge storage capacity. Wire diameters range within 10-200 µm. Center-to-center spacing in a tetrode configuration can be as low as 10 µm. Greater diameters allow an easier insertion. They are more rigid and ease linear motion. However, their rigidity increases tissue damage (Thelin et al., 2011).

Tetrode wire insulation

Biocompatibility and biochemical resistance are important properties for an insulator in chronic electrophysiology. Additionally, insulator surface friction must allow smooth gliding through the brain tissue. Common wire insulators are polytetrafluoroethylene (so-called Teflon), Parylene C, PI, formvar, epoxy, and glass. Teflon and PI are often used insulators (World Precision Instruments, Californian Fine Wire Co.). On top of a base insulating polymer layer, a thermoplastic PI can be used. This thermoplastic PI allows heat bonding of the four tetrode wires, preventing wire unwinding.

1.5.2. Biomechanical properties

Neural device flexibility largely depends on two physical properties: Young's modulus and bending stiffness. Young's modulus is an intrinsic material property that describes how much the material can resist longitudinal changes towards a tensile strength (Hassler et al., 2011). The bending stiffness is defined by the force required to achieve a bending deformation. It depends on Young's modulus and the geometry of the material.

The Young's modulus of metal wires and Michigan-type silicon probes is in the gigapascal range. Polymers have a reduced Young's modulus in the megapascal range. These values are still much higher than the brain's Young's modulus, which is in the range of pascal – kilopascal (Hong and Lieber, 2019). The biomechanical mismatch between the device and brain tissue results in chronic signal degradation and neuroinflammation. Thus, single units of penetrating electrodes can be lost over time. Cortical µECoG arrays are less invasive than penetrating electrodes. Nevertheless, cortical deformation and cortical layer thinning through stiff µECoG arrays are common issues (Minev et al., 2015; Vomero et al., 2020).

Two general approaches can decrease the mechanical mismatch. One approach is the usage of materials with a lower Young's modulus. µECoG arrays use polymer insulators materials like PDMS, PI, Parylene C, SU-8, and liquid crystal polymers. Penetrating depth electrodes make use of metal electrodes isolated by flexible polymers like PI (Rousche et al., 2001; Chung et al., 2019), the usage of carbon fibers (Yoshida Kozai et al., 2012; Guitchounts et al., 2013), or soft elastomer approaches (Minev et al., 2015). Using lower Young's modulus devices has several challenges. The Young's modulus of polymers, carbon probes, and elastomers is still several magnitudes larger than the soft brain tissue. Additionally, low Young's modulus materials show high fragility, making device failures like cracking and delamination are more likely (see subsection: 1.5.3 Neural probe failures).

An alternative approach is the reduction of bending stiffness. This is achieved by reducing material thickness. The bending stiffness is defined as an applied force (F) that is required to induce material deflection (d):

$$\kappa = \frac{F}{d}$$

For a rectangular probe, the bending stiffness is calculated as:

$$\kappa_{rectangular} = \frac{4\,E\,w\,t^3}{L^3}$$

with E = Young's modulus, w = width, t = thickness, and L = length of the electrode probe (Chen et al., 2017b). The bending stiffness scales cubically with the material thickness. Therefore, a slightly thinner rectangular µECoG array is significantly more flexible.

The bending stiffness of a cylindrical probe is calculated as:

$$\kappa_{radial} = \frac{3\,\pi\,E\,d^4}{64\,L^3}$$

with d = cross-sectional diameter (Shi and Fang, 2018). The thickness of a wire has a major impact on bending stiffness. It scales with the fourth power of the cross-sectional diameter.

Material thinning reduces bending stiffness. This creates flexible probes suitable for chronic experiments. Materials keep a rigid microstructure that is resistant to cracking and delamination. Both formulas also show that the material length defines bending stiffness. However, the electrode length for *in vivo* rodent electrodes changes only marginally.

A Michigan probe has a bending stiffness of ≈10^2 N/m. A meta-analysis revealed that inflammation and neuronal death significantly decreased if the bending stiffness is around ≈10^{-1} to 10^{-2} N/m (Stiller et al., 2018). By the reduction of the Michigan probe thickness from 50 µm to 10 µm, the bending stiffness was decreased in order to reduce neuroinflammation significantly.

1.5.3. Neural probe failures

Thin surface electrode arrays and intracortical electrodes can have multiple causes of failure. Chronic failures are related to the wet ionic environment of the brain. Delamination of the electrode insulator is often observed. (Figure 5, Pommersheim et al., 1995; Hämmerle et al., 2002). Intracranial bleedings result in oxidative stress, degrading the insulation layer (Prasad et al., 2014; Kozai et al., 2015).

Flexible polymers like PDMS and Parylene C are incompatible with high-temperature manufacturing processes (Scholten and Meng, 2015). Thus, delamination is more likely. Polymers are susceptible to increased water absorption. The resulting polymer volume increase can cause brain tissue compression (Kozai et al., 2015).

During implantation procedures, the electrode device can be damaged. Manual handling of the device through forceps is a major issue of electrode failure (Kozai et al., 2015). Sharp craniotomy edges cause another possibility of breakage (Cole et al., 2011).

The manufacturing process itself can induce device defects like cracking of the insulation layers (Prasad et al., 2014). Exposed and largely bent multi-electrode interconnections often become brittle. Parts of the EIB can break (Barrese et al., 2013). Electrode corrosion can occur over a time scale of weeks to months (Figure 5, Patrick et al. 2011)

The electrode device's robustness can be tested before usage. Evaluations include repeated bending tests, impedance measurements of electrodes soaked in PBS, and scanning electron microscopy (Yeager et al., 2008; Kwon et al., 2013). High temperatures in a PBS soak test accelerate the hydrolytic and oxidative processes and, thus, mimic *in vivo* aging.

In vivo impedance

Raw electrophysiological signal fluctuations are an indicator of electrode performance. *In vivo* electrochemical impedance measurements allow a more precise estimation of the electrode performance. Impedance can also provide give rough estimates of the electrode-tissue interface.

Impedance values can vary greatly. A continuous decline in impedance is often the result of an increased surface area. Electric leakage pathways can form on a cracked or delaminated neural probe insulation (Kane et al., 2013). Coatings like gold, PEDOT, platinum black increased the electrode surface area and reduced its impedance. An increase of impedance values can result from damage to the applied coating.

Protein deposition and immune cell adhesion on the electrode results in increased impedance (Aregueta-Robles et al., 2020). This fibrotic and gliotic encapsulation not only isolates spiking neurons from the electrode. It also but limits ion flow (Polikov et al., 2005). This ultimately can be observed in a rapid increase in impedance (Ludwig et al., 2006; Leach et al., 2010). A low impedance is generally preferred to keep noise levels down. The following subsection introduces the idea that extremely low impedance is not as important.

1.5.4. Noise: Impedance reduction

This subsection highlights a general misconception in neuroscience research: reducing impedance with all possible means improves signal quality significantly. However, this perspective ignores the physical properties of the data acquisition system. Therefore, this subsection highlights why the main focus of the device advancement in this dissertation is not impedance reduction with complicated processes.

Neural recording noise is removed by referencing. A reference signal is recorded away from the target region and subtracted from the recording signal in the target region. However, specifics of the recording hardware and biological factors can introduce additional noise. Noise can be divided into three different categories.

- First, biological noise that originates from background cell activity. In single-unit recordings, biological noise originates from distant neurons. Recorded activity from these neurons does not have the typical action potential resolution. This activity is visible in smaller signal oscillations that depend on the neurons firing properties.

- A second noise source is the preamplifier, also named headstage. It amplifies, filters, and digitizes the recorded signal before it is sent to the acquisition board. Such a headstage typically has a low noise level. However, it can pick up, for instance, 50 Hz interference of the power line. This is a common noise source in less well-grounded recording setups.

- The third noise source is often paid the most attention: electrode-electrolyte interface noise. Thermal noise as the primary source is characterized as:

$$v_\eta = \sqrt{4 \times k \times T \times Re(Z_e') \times \Delta f}$$

  With k (Boltzmann constant), T (temperature), Δf (noise bandwidth). $Re(Z_e')$ depicts the real part of the electrode impedance. Therefore, thermal noise is proportional to the square root of the electrode impedance. This is true only if the electrode is resistive but not in capacitive conditions. Most electrode modifications aim to decrease the impedance significantly. Thereby, thermal noise should be reduced, and the signal-to-noise ratio (SNR) improved. The following explanations question this assumption.

The electrode impedance Z_e' is connected in series with the headstage impedance Z_a', creating a voltage divider. A voltage divider in electronics is used to turn a larger input voltage into a smaller output voltage. The calculation of the output voltage is based on Ohm's law and can be calculated as:

$$V_{out} = \frac{V_{in} \times Z_a'}{Z_e' + Z_a'}$$

Thus, the output voltage is proportional to the ratio of the electrode (Z_e') and headstage (Z_a') impedances. The headstage has a high input impedance. This prevents connecting the electrode to the ground and limits its influence on the measured voltage. For example, the Intan RHD headstage has an input impedance of 13 MΩ at 1 kHz. If an electrode impedance is 2 MΩ and the recorded voltage is 1 V the output voltage is:

$$V_{out} = \frac{1\,V \times 13\,\mathrm{M\Omega}}{2\,\mathrm{M\Omega} + 13\,\mathrm{M\Omega}} = 0.87\,V$$

A relatively high electrode impedance of 2 MΩ results in a 13 % loss of the input voltage. Fortunately, most electrodes have impedances lower than 1 MΩ, which would result in a voltage loss of <7 %.

Electrode impedances are usually targeted to tens of kΩ with often complicated coating processes. Simple metal-based coatings are platinum/gold (Battaglia et al., 2009; Ferguson et al., 2009), platinum black (Desai et al., 2010), or iridium oxide (Meyer et al., 2001). Nanostructure coatings include platinum nanopillars (Xie et al., 2012) or gold nanoflakes (Kim et al., 2010).
In practice, this reduction in impedance would only concern a few µV of signal increase. Electrode impedance reduction significantly below the headstage impedance is sufficient.

Interestingly, biological noise has a more significant impact on signal quality than thermal noise. This is demonstrated in the following example. Spike amplitudes were recorded with two different electrodes from the same neurons (Neto et al., 2018). Coated low impedance electrodes (0.01 MΩ) and non-coated high impedance electrodes (2 MΩ) show different noise levels if recorded in saline solution. *In vivo* recorded signals are similar for both electrode types. Therefore, thermal noise reduction is masked by biological noise.

In wire electrodes, the low impedance is important. The capacitance along the thin insulated wire and the surrounding neuronal electrolyte results in a capacitive shunt loss. The result is a ground connection, which reduces the effective headstage impedance. The longer the wire, the higher the shunt capacitance. Signal loss can be minimized by further reducing electrode impedance.

1.5.5. Light-induced artifacts and damage

Light scattering and absorption in the neural tissue require the implantation of optical fibers. Optical fibers guide the light to the target region. However, light causes several types of artifacts.

The dissertation includes electrodes exposed to light. Light-induced artifacts play a role in both devices developed in this dissertation. Therefore, this subsection introduces several possible origins of them.

Photovoltaic- / Becquerel-effect artifacts

The photovoltaic effect, also known as the Becquerel effect, results from light exposure of metal electrodes positioned in the light beam center (Becquerel, 1839; Cardin et al., 2010; Khurram and Seymour, 2013). Loosely bound electrons in the metal are excited by absorbed photons and reach a higher energy state. The transition of many electrons' energy states results in a significant voltage change and the photovoltaic artifact. An often-used alternative term, photoelectric effect, describes a different process in which electrons are released from the material by light.The light-induced artifact interferes with LFPs and single units. Light-induced oscillations are not distinguishable from neural oscillations (Mikulovic et al., 2016).

Light-induced artifacts can be reduced or removed. Different electrode materials are differently susceptible to photovoltaic artifacts. The orientation of optical fiber and electrode impacts the photovoltaic artifact amplitude (Cardin et al., 2010). Photovoltaic artifacts can be filtered *post hoc*. LFPs are low-frequency oscillations. A low-pass filter preserves the LFP signal but filters out high-frequency short light pulses. Single units are in the high-frequency range. Low-frequency long ramp-up light pulses can be filtered out with a high pass filter (>600 Hz, Kozai and Vazquez, 2015).
However, filtering changes single-unit waveforms (Ungless and Grace, 2012). Bandpass filtered LFPs produce artifact spikes (Mikulovic et al., 2016). Such artifact spikes result in mistakes during spike sorting and false data interpretations. Photovoltaic artifacts themselves can have a waveform similar to single-unit spikes and lead to spike sorting errors.

Tissue heating artifacts

The photovoltaic artifact appears exclusively during light on- and offset. Constant light exposure results in an equilibrium of higher energy level electrons and low energy level electrons (Kozai and Vazquez, 2015). Therefore, continuous light exposure does not result in a change of net charge. Long-duration squared light pulses could be a solution to prevent artifacts. However, they cause significant brain heating. Low intensity (5 mW, 200 µm fiber, 0.22 numerical aperture (NA)) blue light stimulation (450 nm) of even short durations (500 ms) causes cortical heating of ≈2 °C (Arias-Gil et al., 2016). Cortical heating results in physiological changes of neural activity and acute inflammation. Even modest brain heating (0.1 °C) suppresses spiking activity (Owen et al., 2019). A temperature increase of >5 °C results in tissue damage (Deng et al., 2014).

ChR2 current artifacts

One type of artifact looks similar to a photovoltaic artifact but is physiological in origin. Light-gated cation channels open with a very short latency to light exposure. This ChR2 opening results in a rapid influx of cations, creating a sink. Thus, it appears as a short latency high amplitude negative peak in the recorded LFP. This opsin current appears before the actual neuronal postsynaptic activity.

Most literature characterizes this negative peak as a photovoltaic artifact and does not mention the contribution of the direct opsin current. The opsin current is mainly dependent on the opsin type and the light-activated neuronal cell type. Long pyramidal cells with their uniform orientation exhibit larger opsin currents than distributed small interneurons. Xiong et al. (2015) characterized the direct opsin current. In their study, the opsin current was observed as a strong artifact on the LFP activity. It could be ruled out that this artifact was of photovoltaic origin: it does not exist in the absence of opsin expression. The artifact is tetrodotoxin-insensitive, which excludes the artifact's origin in voltage-gated cation channels.

1.6. Biotic properties of signal quality

Abiotic and biotic factors play together, and the immune response is, therefore, multifactorial. The insertion of neural devices causes a cascade of neuroinflammation processes, degrading signal quality. This section highlights aspects that must be considered during the *in vivo* testing of the neural devices developed in this dissertation.

1.6.1. Foreign body response

The spike amplitude of ≈100 neurons around a tetrode in the hippocampus is theoretically large enough to be recorded and sorted into single units (Buzsáki, 2004). Nevertheless, tetrode recordings revealed typically less than 10 single units. Tetrode penetration induces neuronal damage and inflammation, decreasing neuronal cell yield.

This subsection provides a general overview. Detailed signaling pathways and activated cell types are summarized in several literature reviews (Polikov et al., 2005; Gulino et al., 2019).

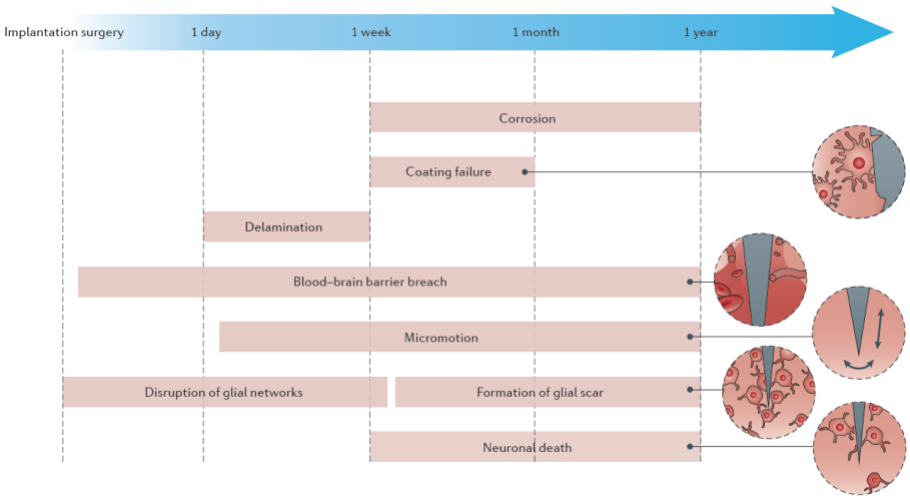

Figure 5 | Timescale of abiotic and biotic properties leading to signal degradation
Abiotic material failures like delamination of the insulation layers, coating failure, and corrosion can be improved by advancements in device design. Biotic signal degradation appears from continuous micromotions resulting in a blood-brain barrier disruption. A glial sheath forms around the electrode. Continuous damage leads to neural death. Adapted from Chen et al. (2017b).

Acute electrode insertion damage

Electrode insertion results in initial damage. A larger probe volume induces more significant neuronal damage. A consensus about electrode insertion speed and induced damage does not exist. Electrode insertion speed varies between 10 µm/s up to several mm/s. Rapid insertion of sharp and stiff electrodes allows cutting through the tissue and prevents tissue compression (Maynard et al., 2000). This can be advantageous if electrodes are inserted through an intact dura and pia mater. On the other hand, a slow insertion of electrodes allows tissue adaptation rather than damage. Without a systematic investigation, a clear statement cannot be made. It was, however, shown that slow ventral advancements are beneficial if deep brain regions are targeted, especially while using large diameter optical fibers (Bakhurin et al., 2020).

Damage occurs mainly at endothelial vessels where electrodes disrupt the blood-brain barrier function (Figure 5, Kozai et al., 2015). Increased hemoglobin levels result in reactive oxygen and reactive nitrogen species (Dávalos et al., 2000), which oxidize proteins, activate inflammatory cytokines, and recruit immune cells (Abdul-Muneer et al., 2015; Hermann et al., 2018). Within minutes and hours, the blood-brain barrier dysfunction results in ischemia and hypoxia. Hemorrhages and vasogenic edema increase intracranial pressure (Kozai et al., 2015). The brain edema leads to secondary ischemic injuries reaching beyond the insertion site. Bleeding correlates with the probe size in a sigmoidal function. A wire diameter <25 µm significantly reduces bleeding (Obaid et al., 2020).

Electrode insertion mechanically perforates neurons. Cell membrane destruction results in an increased calcium influx (Wolf et al., 2001; Williams et al., 2014). Opened calcium channels and release of intracellular calcium storages contribute as well. Prolonged elevated calcium levels lead to neuronal degeneration and cell death. Eles et al. (2018) show that neurons with an increased calcium level can be observed up to 150 µm away from the electrode. A high calcium concentration activates enzymes like calpain. Calpain disrupts the structure of microtubules, which leads to axonal transport deficits. This results in pathologically swollen axonal regions (axonal blebbing, Maxwell et al., 1997; Tang-Schomer et al., 2012).

Acute inflammation

The acute insertion damage causes cytokine accumulation. Cytokines activate first microglia (macrophages of the brain) and over days astrocytes (Kozai et al., 2012; Saxena et al., 2013; Jorfi et al., 2015). Microglia exist as pro- and anti-inflammatory types and, if activated, become amoeboid (Figure 6a, Polikov et al., 2005). Pro-inflammatory microglia recruit other immune cells and facilitate neuronal degeneration. Anti-inflammatory microglia act as a repair mechanism and clear cell debris via phagocytosis (Gulino et al., 2019). Within the first hour after implantation, activated microglia form a lamellipodia sheet around the electrode (Kozai et al., 2012). It takes up to 24 hours for more distant microglia to get motile and migrate towards the electrode.

Chronic inflammation

Resting astrocytes become reactive. In this state, they migrate faster, proliferate and produce inflammatory factors (Polikov et al., 2005). Astrocytes are most active in the first week after electrode implantation. Within several weeks, they form a glial sheath together with microglia and extracellular matrix proteins (Figure 5, Xie et al., 2014; Chen et al., 2017b). Thereby, the direct contact of neurons and electrodes is disrupted (Figure 6a). The glial sheath formation is accompanied by a significant impedance increase (Prasad et al., 2014).

Neuronal cell loss in the vicinity of the electrode occurs within several weeks after implantation (Figure 6a, Biran et al., 2005; McConnell et al., 2009). Evidence also shows that neurons actively migrate away from the electrode site (McConnell et al., 2009). Chronic signal quality is reduced because of the glial sheath and neuronal loss. Additionally, collagen encapsulation of neural devices

reduces signal quality. Destruction of the meninges during implantation results in a regrowth of collagenous scar tissue encapsulating the device (Schendel et al., 2014, Figure 6d)

Another observed phenomenon is a change in neurons' excitability. Neurons become hypoexcitable during chronic implantations (Ding et al., 2011; Vezzani and Viviani, 2015). This can be mediated by a progressive increase in potassium channels and a loss of sodium channel expression (Salatino et al., 2019).

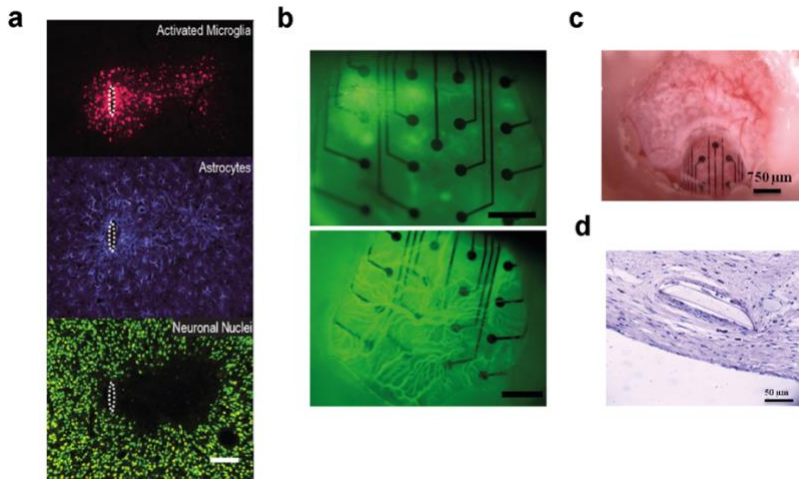

Figure 6 | Foreign body response

a, Fluorescence microscopy of immunohistologically processed brain slices of an intracortical electrode. Activated microglia travel towards the electrode, releasing pro-inflammatory cytokines. Astrocytes follow and encapsulate the electrode. Neuronal cells die in the vicinity of the electrode. Scalebar= 100 µm. Adapted from Jorfi et al. (2015). **b**, In vivo vascular growth around an epidural µECoG array (5 days and 24 days after implantation). Visualized via fluorescein isothiocyanate-dextran injections. Scalebar= 750 µm, Adapted from Schendel et al. (2013). **c**, In vivo opaque tissue growth around a µECoG array (28 days after implantation). **d**, Brain slice depicting collagen tissue surrounding a piece of an µECoG device. **c** and **d** adapted from Schendel et al. (2014).

1.6.2. µECoG array craniotomy and durotomy

The implantation of µECoG arrays requires slightly different steps than penetrating depth electrodes. The different aspects are introduced in this subsection.

The advantage of cortical µECoG arrays compared to penetrating electrodes is reduced parenchyma and blood-brain barrier damage (Schendel et al., 2014; Jorfi et al., 2015). The disadvantage is an increased size of the craniotomy: a large craniotomy window increases surgical-induced damage, brain edemas, and the risk of infections.

Drilling of the skull causes vibrations, a rise in cortical temperature, and bleeding. Therefore, drilling must be performed carefully to prevent damage to the underlying meninges and brain tissue. The thickness of the mouse cranium is only about 300 µm which makes drilling difficult. Additional holes for grounding, reference electrode, and stabilization screws need to be drilled. Drilling results in a skull surface temperature increase ranging from 3 °C to 21 °C (Shoffstall et al., 2018). The generated heat damages the blood-brain barrier. The traditional cooling procedure of saline irrigation shows an inconsistent cooling effect. The meningeal blood vessels are irritated by contact with debris

or edges of the craniotomy, which leads to micro-hematomas and edema (Schendel et al., 2013). The brain pulsation enforces this effect.

Brain edemas force the brain out of the craniotomy window causing damage on sharp edges. Immediate craniotomy sealing increases intracranial pressure. Thus, cortical blood vessels are compressed. This vessel pinching reduces blood perfusion and can lead to ischemic injuries (Kozai et al., 2015). Increased intracranial pressure can result in cortical depression (Vomero et al., 2020). The craniotomy without the implantation of the µECoG arrays already has a considerable impact. A craniotomy alone results in significant activation of microglia and astrocytes (Xu et al., 2007). Tissue growth and hematomas are apparent in solely craniotomy surgeries (Schendel et al., 2013, 2014).

Epidurally placed arrays are less invasive and are potentially more successful for long-term implantations. Generally, blood vessels start growing within days after array implantation. Vascular outgrowth stabilizes at ≈24 days after implantation (Figure 6b, Schendel et al., 2013). Subdurally placed µECoG arrays increase signal quality (Khodagholy et al., 2015). Dura removal results in cerebrospinal fluid (CSF) leakage, a high risk for infections, and increased brain edema. The dura mater grows back within several weeks. The regrown dura has an almost 4-fold thickness increase (Nunamaker and Kipke, 2010). Thickening of the dura mater was also observed as fibrous outgrowth within one month post-implantation of epidurally placed arrays (Figure 6c, d Schendel et al., 2013, 2014).

1.7. Advancing *in vivo* electrophysiology

New neuroscientific methods allowed us to move away from seeing the functional units of the brain as single neurons (neuron doctrine) towards the importance of neural networks.

Previously, single unit only approaches have led to a viewpoint in which individual neurons are seen as the building block of the nervous system. Research on receptive fields revealed that a single neuron coded for stimulus orientation and another neuron for a different modality (Hubel & Wiesel, 1962). The interpretation was that single neurons are not just the building blocks of the nervous system but that individual neurons mediate perception and behavior (Barlow, 1972). However, assessing the function of a neuron within a whole circuit by only observing its independent response to a sensory stimulus leads to limitations. It does not allow the understanding of how the brain computes complex processes like behavior.

The development of multi-electrode devices changes this view. Recording devices such as tetrodes, µECoG multi-electrode arrays, and high-density electrode silicon probes allow recording large neuronal populations, thus making conclusions about the functional connectivity of different neurons and brain areas.

Additionally, the revolution of optical recordings has changed our understanding of neuronal network activity. We are able to not only record but manipulate specific neural activity. Optical imaging started with the development of VSDs (Grinvald et al., 1987; Grinvald & Hildesheim, 2004) towards nowadays more widely used genetically encoded indicators (Miyawaki et al., 1997; Chen et al., 2013). *In vivo* calcium imaging like two-photon microscopy (Yuste & Denk, 1995; Svoboda et al., 1997), one-photon micro-endoscopes (Barretto & Schnitzer, 2012; Ziv et al., 2013), and fiber photometry (Adelsberger et al., 2005; Cui et al., 2014; Kim et al., 2016), allowed to image many hundred cells.

Understanding neural circuits require the integration of different neural readouts. Both the analysis of microscopic single-unit activity and mesoscopic LFP/ECoG activity is of importance. Optical methods add additional readouts. The challenge of current recording techniques lies in the combination of classical electrophysiological and newer optophysiological methods. This dissertation aims to advance devices that combine both modalities.

Current neural recording and imaging methods can be depicted figuratively as follows.
We are watching a movie. The goal is to understand the main storyline and the main characters' relationship to each other. Our vision allows only to see few 100 pixels of the screen simultaneously. It is challenging to observe those pixels continuously and certainly not for the entire length of the movie. If we also turn on the audio signal, interferences occur on the video signal. The audio signal is additionally translated from its original language. Therefore, its meaning is slightly changed. Available methods are limited and allow us to reveal only a fraction of the complex circuitry. A continuous advancement contributes to an ever better understanding.

1.8. Aim of this study

The dissertation's main aim is the improvement of rodent extracellular recordings. The focus lies on mesoscopic recordings with µECoG arrays and multiple single-unit recordings with microdrives.

Despite the development of numerous electrode probes in the past decades, few of them have found widespread use. Existing transparent µECoG arrays use graphene and ITO. These materials require complex manufacturing processes and are chronically fragile. The here presented approach makes use of non-transparent electrodes. The aim is to improve the transparency of the array's insulator. Using classical metal electrodes should improve longevity, recording quality and still allow the application of optical methods.

Existing multi-tetrode microdrives are expensive, heavy, and complex to assemble. Further, they often show limited unit stability and precision of the drive mechanism. In this dissertation, a newly developed microdrive should overcome these limitations.

Within this dissertation, I tested the usability of a newly developed transparent µECoG array and microdrive. Using simple solutions, we aim to enable widespread use.

Both devices aim for:

I.) Ease of production and practical use

II.) Chronic device and signal reliability

III.) The combination of electrophysiology and optophysiology

1.) The first part focuses on *in vivo* application of a custom-developed µECoG array. This project is performed in collaboration with the engineers from the Otto-von-Guericke University Magdeburg (M. Deckert, Prof. B. Schmidt) who fabricated the µECoG device and are responsible for the technical aspects.

The focus lies on chronic recordings of the auditory cortex tonotopy. High-resolution tonotopic maps are traditionally recorded with invasive penetrating wire electrodes. This method induces damage that limits chronic tonotopy resolution. I investigate whether a flexible thin-film µECoG array allows chronic recordings with a high tonotopy resolution. I will compare the chronic stability of event-related potentials (ERPs) and device functioning to other transparent µECoG devices.

2.) The second objective focuses on optical applications of the µECoG array. The µECoG array incorporates opaque electrodes instead of transparent ones. Optical imaging and optogenetic stimulation will be performed through the transparent insulator. Comparisons with transparent electrode arrays will focus on light-induced artifacts. Additionally, I focus on testing the transparent array during cortical imaging.

3.) The third objective is the development and establishment of a behavioral task employing positive reinforcement for the mouse. I concentrate on an appetitive classical conditioning task. This

behavioral task is used to investigate the RPE of VTA dopamine neurons. An additional aim of this part is the establishment of an operant task, which is used by colleagues in future projects. The construction of the setup and software centered around an Arduino microcontroller aims for easy modifiability in the future.

4.) The fourth objective is the development of an open-source 3D printed microdrive. The aim is to develop a microdrive that can be easily replicated in other laboratories. One difficulty is the incorporation of an optical fiber without increasing the complexity and weight of the microdrive.

5.) The fifth objective is the *in vivo* application of the microdrive. I aim to identify dopaminergic single units via optogenetic tagging. Drivable tetrodes and an optical fiber are necessary to find optotagged neurons.

The development of the RPE during behavioral training has never been recorded continuously in stable single units. I aim for an optimal condition where it is possible to track identified cells over the whole course of conditioning. However, the use of the microdrive allows readjustments if optotagged single units are lost over time.

2. *Part 1:* AN OPTICALLY TRANSPARENT µECOG ARRAY FOR COMBINED ELECTROPHYSIOLOGY AND OPTOPHYSIOLOGY

Parts of this µECoG multi-electrode array chapter are published in the journal of neural engineering (Brosch et al., 2020) and extended by a more detailed description of acute and chronic recordings of auditory cortex tonotopy.

2.1. Materials and methods

2.1.1. Electrode fabrication and packaging

The here developed µECoG arrays are based on PI (PI-2611, HD MicroSystems), a biocompatible and robust polymer. Fabrication was performed on 4" silicon wafers. PI-2611 precursor is spun on the wafers resulting in a homogeneous layer thickness of 4.15 ± 0.2 µm after curing in a nitrogen atmosphere at 350°C for one hour. A sacrifice layer was not used because it was not beneficial in our manufacturing process and added unnecessary complexity of removing this layer later. A critical step to achieve the long-term stable probes described here is surface activation through reactive ion etching for 30 s at an etch rate of 1.4 ± 0.01 µm/min. This etching leads to micro-roughness, enhancing layer binding. Following etching, metal patterns are created using a standard lift-off process (photoresist: TI-35 ES, MicroChemicals). The metal was deposited using direct-current sputtering. First, 50 nm of chrome was deposited, followed by 300 nm of gold and 100 nm of platinum. Chrome functions as an adhesion layer for the highly conductive gold traces. Platinum was used as the surface layer because of its biocompatibility, favorable electrode characteristics, and high blue light reflectivity. After metal deposition and patterning, the second layer of 2.5 ± 0.2 µm PI was spun on and cured as described above. Electrode sites and holes were opened by photolithography followed by aluminum hard-masking, lift-off, and dry etching as described above. This process also served to create the outer shape of the array. The finished arrays were then delaminated from the silicon wafer. The distal part of the electrode array was connected to a custom EIB using a novel, highly reliable soldering process (Deckert et al., 2017). As electrical connectors, we selected the Hirose DF12 and DF30 series, which allow a sufficient number of plugging cycles for long-term chronic experiments.

2.1.2. Animals

All experiments were conducted according to the guidelines of the European Community (EUVD 6 86/609/EEC) and approved by a local ethics commission of the State of Sachsen-Anhalt. We used eight male adult Mongolian gerbils (Meriones unguiculatus) and one male adult Wistar rat. Four gerbils were used for the chronic recording of auditory ECoG, two were used for acute auditory ECoG

recordings, one gerbil was used for combined optogenetic stimulation and recording, and one gerbil was used for a cortical window surgery to evaluate tissue reaction and bone regrowth. The rat was used for simultaneous ECoG recording and VSD imaging. Animals were housed under a twelve-hour light/dark cycle (light on at 6:00 AM). Food and water provided *ad libitum*.

2.1.3. Auditory cortex craniotomy

Anesthesia was induced by 3% Isoflurane vaporized in air, followed by an intraperitoneal injection of sodium pentobarbital (60 mg kg^{-1}). Local anesthesia at the surgery site was provided by bupivacaine hydrochloride injection (0.25%, 0.2 ml). After skin incision and cleaning the dorsal skull surface, a plastic head holder was fixated to the frontal bone. This allowed the fixation of the head in a stereotactic frame without damage to the eardrums resulting from ear bars. The temporal muscle was gently displaced ventrally, and a craniotomy on the temporal bone above the right auditory cortex was performed. On the exposed dura, we positioned one µECoG array (rectangular design, 250 µm spacing, Figure 7b) above A1, as determined by anatomical landmarks. We then mapped the responses to pure tones (125 Hz, 1 kHz, 4 kHz, 10 kHz, 200 ms duration, 5 ms linear ramp, 50-100 repetitions each) through the array and repositioned it according to the tonotopic gradient to cover A1. The craniotomy was sealed by either the original bone flap (n=2) or a silicone gel (n=2; Smooth-On BodyDouble Fast). Since no differences between bone and silicon cranioplasty on long-term signal quality were found, we pooled the animals for analysis. Chlorinated silver wires served as reference and ground electrodes. Dental cement was used to seal the surgical opening and secure the electrode connector in place.

2.1.4. Auditory stimulus generation and electrophysiological recordings

In subsequent recording sessions, stimuli consisted of 9 different pure tones (60 dB, 1-octave steps: 125 Hz – 8 kHz, followed by 12 kHz and 24 kHz, 200 ms duration, 5 ms onset/offset ramp, 150 randomized repetitions for each frequency, 1.5 s ± 0.5 s intertrial interval) and were delivered free-field to the awake, head-fixed animals. Tones were generated by a custom LabVIEW program and National Instruments data acquisition card and amplified by a Dynavox MT-50 pre-amplifier connected to a loudspeaker (Tannoy Mercury V1i). Animals were recorded at least once a week in a sound-attenuated and electrically shielded chamber. Neural responses from the µECoG array were recorded using a standard biosignal acquisition system (Intan RHD2000, RHD2132 headstage, recording bandwidth: 1 Hz-0.3 kHz, 1 kS s^{-1}). *In vivo* electrode impedance was measured after each session through the headstage at 1 kHz.

2.1.5. Optogenetic stimulation

The gerbil was anesthetized as described above, and a 1 mm diameter hole was drilled above the left visual cortex (anterior-posterior 0 mm, medial-lateral 4.5 mm relative to λ). A pulled glass pipette was lowered to three depths (300, 800, 1300 µm relative to the dura mater) at a 20° angle. At each depth, starting at 1300 µm, 250 nl virus solution (rAAV5/CAMKIIα-hChR2(H134R)-eYFP-WPRE-pA, $3x10^{12}$ gc ml^{-1}, University of North Carolina at Chapel Hill vector core) were injected into the tissue

at a rate of 50 nl min^{-1}. After 5 min diffusion time, the pipette was elevated to the next level. After injection, the skull was closed with bone wax and the skin sutured. The animal was given four weeks to recover and express sufficient opsin.

For the following acute experiment, the animal was anesthetized as described above, and a 4x3 mm craniotomy was performed bilaterally above the visual cortex. A µECoG array (quadratic design, 500 µm spacing) was placed over the visual cortex, and an optic fiber was placed directly above it, at the midpoint of four contacts (core 105 µm, 0.22 NA, Thorlabs FG105UCA). One recording was done at the site of opsin expression, and one recording on the contralateral hemisphere lacking opsin. Blue laser light was used to activate the opsins through the transparent array (473 nm, 20 mW mm^{-2}, 10 ms, 100 repetitions, interstimulus interval 1 s ± 0.5 s). Neural responses were recorded with the Intan system as described above. Reference and ground electrodes (chlorinated silver wires) were gently placed at the edge of the contralateral craniotomy window. At the end of the experiment, the animal was perfused with a 4% formaldehyde solution for histological analysis.

We investigated light-induced artifacts in vitro with the same µECoG array used in the in vivo optogenetic experiment. The electrode was placed in PBS, and fiber-coupled blue laser light (473 nm, 10 ms) was directed towards an electrode site or between electrode sites through the substrate. Light intensities were varied between 1-50 mW mm^{-2}, and 50 pulse repetitions were measured for each intensity.

2.1.6. Voltage-sensitive dye imaging

Anesthesia of the rat was induced by 3% Isoflurane vaporized in air followed by intraperitoneal injection of urethane (2 g kg^{-1}). The animal was fixed in a stereotaxic frame and a heating pad was used to control body temperature. The protocol for VSD imaging has been described previously (Lippert et al., 2007). Briefly, a cranial window was drilled above the left visual cortex (bregma -4 to -10 mm and lateral 1 to 7 mm). The dye RH-1691 (2mg ml^{-1}; Optical Imaging) was dissolved in saline and the cortex was stained for 60 min, followed by 20 min washing with saline. To fit the visual field of the imaging system, a quadratic electrode array (800 µm spacing) was placed over the visual cortex. Reference and ground electrodes (chlorinated silver wire) were placed over the frontal cortex. Neural responses were recorded as described before. The signal was filtered at 2-100 Hz (Butterworth filter, 6^{th} order). The average signal of the four electrode sites surrounding the VSD region of interest (ROI) was calculated.

VSD signal was imaged using a CMOS camera (MiCam02-CMOS, 92x80 pixels, 4 mm field of view, 1.7 kHz frame rate). Visual stimulation was provided by a polymer optic fiber (core: 1 mm) placed in front of the contralateral eye and coupled to a white LED. The electrocardiogram was recorded together with electrophysiological and optical signals and used for heartbeat artifact reduction (Lippert et al., 2007). After the experiment, the animal was killed.

VSD data were analyzed using custom scripts written in MATLAB (MathWorks). For the time course of the VSD signal, a ROI (17x11 pixels) was chosen in the transparent region of the array. Individual trials (n=168) were median filtered (201 samples) and averaged. Individual frames were extracted from the median-filtered traces and normalized for the background fluorescence (ΔF/F) to display the spatial distribution.

2.1.7. Electrophysiology data analysis

ECoG signals were bandpass-filtered using a 2-100 Hz, 6th order Butterworth filter. All data processing was performed in MATLAB (MathWorks). Trials with apparent movement artifacts were excluded from the analysis.

For each of the nine tone frequencies, 50 to 100 trials per session were averaged for event-related potential (ERP) calculation. Spatial tonotopy mapping was done by plotting the P1 and N1 peak amplitudes as the maximum of each channel in the respective time window (P1 window: 20-40 ms, N1 window: 40-80 ms). The tone frequency, which gave the highest amplitude for each channel, i.e., the best frequency, was used to plot the tonotopic gradient map. To assess the long-term stability of the signals, we measured the response to 1 kHz tones over 12 weeks. For these evoked responses, the P1 to N1 peak amplitude difference was normalized to the first week post-surgery of each animal to show the amplitude changes over time and across animals. The 200 ms time interval before stimulus presentation was used to calculate root mean square (RMS) baseline activity for each session across the long-term recording experiments.

Impedance was measured at 1 kHz before implantation in saline (NanoZ, Multichannelsystems) and later *in vivo* with the RHD2000 system (Intan Technology). Channels with impedance magnitude over 1 MΩ were considered non-working and excluded from the analysis. Due to connector damage in a single case, 13 channels were lost after implantation from one animal. Those channels were excluded from further analysis.

2.1.8. Histology

At the end of the experiment, animals were killed with pentobarbital and perfused with formaldehyde in PBS (4%). The brains were extracted and cryo-sectioned into 50 µm coronal slices. For the optogenetically transduced brain, slices were mounted in polyvinyl alcohol solution (Mowiol®), and fluorescence images of the visual cortex were taken.

For assessing long-term histological changes, slices from two animals were stained for glial fibrillary acidic protein (GFAP) and ionized calcium-binding adaptor molecule 1 (Iba1, animal 1: 28 weeks post-implantation, animal 2: 31 weeks post-implantation). We included only two out of four animals from the chronic experiment since the arrays did not cause any visible damage to the cortical surface and only in these two animals the exact location of the array above A1 could be reconstructed from the observed tonotopic pattern and matched to the atlas. Consecutive slices were alternatingly incubated with the primary antibodies against either GFAP (1:1000, Anti-GFAP ab7260, Abcam; dilution in blocking solution from Zytomed Systems at 4°C, incubation overnight) or Iba1 (1:2000, Anti-Iba1, ab178846, Abcam). Additionally, some slices were Nissl stained. Primary antibodies were fluorescence-tagged with secondary antibodies (1:200, Alexa Fluor 546 or Alexa Fluor 488, ThermoFisher Scientific). Slices were incubated for two hours at room temperature in this solution. Finally, slices of the auditory areas were mounted with Mowiol®. We confirmed astrocytes and microglia morphology through confocal laser scanning microscopy (Leica TCS SP5). Fluorescence images were taken with a standard upright fluorescence microscope (Axioscope, Zeiss).

Photographs of 4 representative slices of the auditory cortex and control hemisphere were taken for each animal (Bregma ≈ -1.65 mm till ≈ -4.10 mm). A gerbil brain atlas was used to identify the auditory cortex in every slice (Radtke-Schuller et al., 2016). The mean fluorescence intensity was evaluated in rectangle ROIs of the A1 covering 800 µm ventral to dorsal and 500 µm (Iba1) or 200 µm (GFAP) in depth from the cortex surface using ImageJ (NIH, USA, version 1.51j). The fluorescence of the hemisphere with the previously implanted electrode was normalized to the animal's contralateral auditory cortex without any intervention.

2.2. Results

2.2.1. Design and fabrication of optically transparent µECoG array

The initial design and fabrication originated in collaboration with Prof. Bertram Schmidt and Martin Deckert from the micro- and sensor systems institute of the Otto-von-Guericke University Magdeburg. The final design, as described in the following, was reached after multiple iterations of improvements. Those improvements were performed after initial *in vivo* testing and consisted of changes in the used material, thickness, and roughening step of the PI layers. In this section, we tested the optical parameters of the PI and electric parameters of the electrodes. Before using the array *in vivo,* bending tests and PBS soak test would reveal failures due to mechanical failures or delamination. Optical assessment and handling of different PI layer thicknesses allow assessing the optimal thickness of the material.

The focus of this dissertation work is distinctly on the neuroscientific evaluation of the µECoG array, while the µECoG array fabrication is the expertise of the engineering team within this multidisciplinary project. The summarized fabrication processes are nonetheless described in the methods section and illustrated in Figure 7e. The technical evaluation, including measurements of sheet resistance, impedance spectroscopy, cyclic voltammetry, light transmittance, and *in vitro* array stability tests, are still part of my work.

We designed a portfolio of several different µECoG arrays for electrophysiological and optogenetic applications (Figure 7b). All arrays are based on a PI-metal sandwich structure (Figure 7e) and differ in electrode site spacing (250 µm, 500 µm, and 800 µm) or electrode arrangement (rectangular, quadratic). Circular active electrode sites are 50 µm in diameter and feeding conductor paths are 10 µm in width and pitch. The final thickness of the PI film was 6.45 ± 0.13 µm, resulting in high transmittance of blue light as required for many optogenetic and calcium imaging applications (83 ± 5% between 450 to 500 nm, Figure 7c). Impedance spectroscopy and cyclic voltammetry were used to characterize the electrochemical properties of the array (Figure 7d). The sheet resistance of the metal layer was measured at 0.49 ± 0.03 Ω/sq.

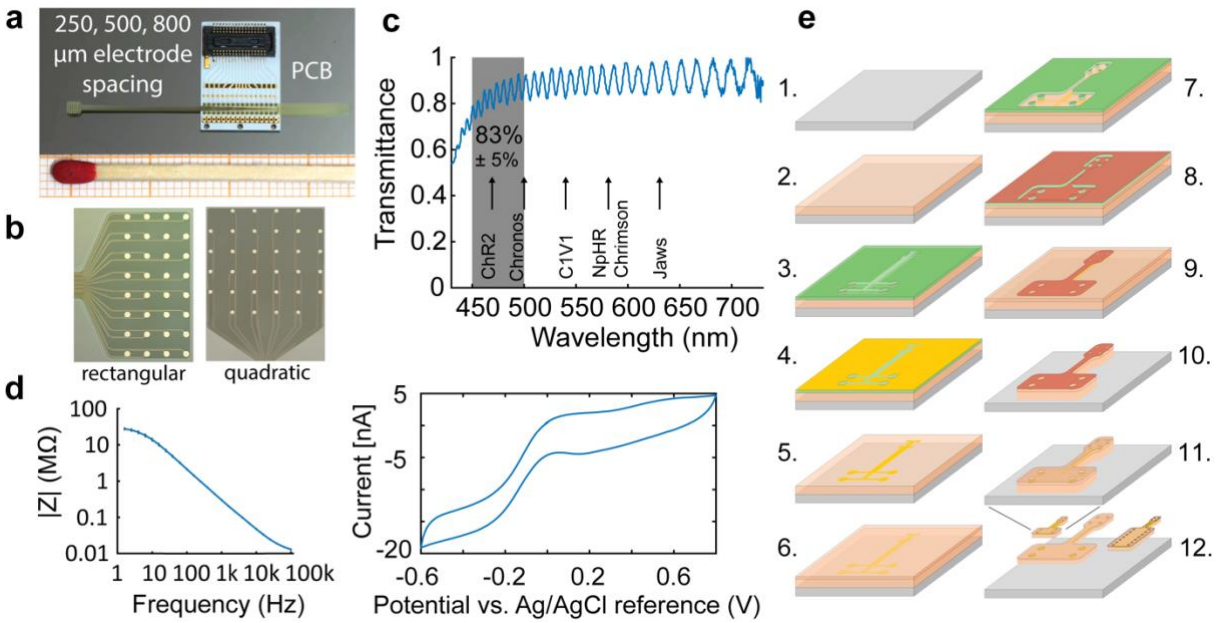

Figure 7 | µECoG array characterization and fabrication process

a, µECoG array flip-chip bonding on printed circuit board (PCB). Three different inter-electrode spacings were fabricated (250, 500, 800 µm). **b**, Different µECoG array designs (rectangular, quadratic) suited for different rodents (mice, gerbils, rats) and cortical areas (visual and auditory cortex). **c**, Transmittance for commonly used opsins at their specific wavelength. Transmittance through the µECoG array for blue light-gated opsins reaches 83 % (450-500 nm). **d**, Impedance spectroscopy (left) and cyclic voltammetry (right). **e**, Fabrication and assembly process: 1: Surface preparation, 2: PI-2611 deposition, 3: Photolithography, 4: Metal sputtering, 5: Lift-Off, 6: PI-2611 deposition, 7: Photolithography, 8: Hardmask sputtering, 9: Lift-Off, 10: Dry etching, 11: Hardmask Removal, 12: Delamination. Adapted from Brosch et al. (2020).

We tested thinner substrate materials, but they had significantly reduced handling properties, particularly regarding wrinkling (Figure 8a). In addition, transmittance would increase slightly with reduced material thickness but become more wavelength-dependent through thin-film interference (Figure 8c). Due to the low thickness of the PI, interference effects are, to some degree, present at all tested material thicknesses. However, this effect can be used to further optimize transparency with a narrowband light source, such as a laser. By selecting a wavelength at a transmission peak, over 90% transmission can be achieved. The interference bands could be used to achieve very high transmission at particular monochromatic wavelengths (e.g., 473 nm for 6.5 µm material).

A further advantage of the substrate thinness is the reduced risk of broader cortical damage from stiff implants. Upon contact with the wet brain, our arrays adhesively conform to the brain surface without any required external force. We performed a bend test to document resistance to 200 bend cycles at a 5 mm bend radius. 5 mm radius tube matches the range of the natural curvature of the mouse cortex (Thunemann et al., 2018). Bending did not influence the electrical characteristics of the array (Figure 8b). An *in vitro* PBS soak test revealed no significant impedance changes over time and therefore revealed array stability in a wet environment (Figure 8b). A small initial increase in impedance in PBS on day 3 relative to the first measurement in saline results from measurements in solutions with slightly different ion concertation and is similar to what is observed during the initial stage *in vivo* (Figure 12c).

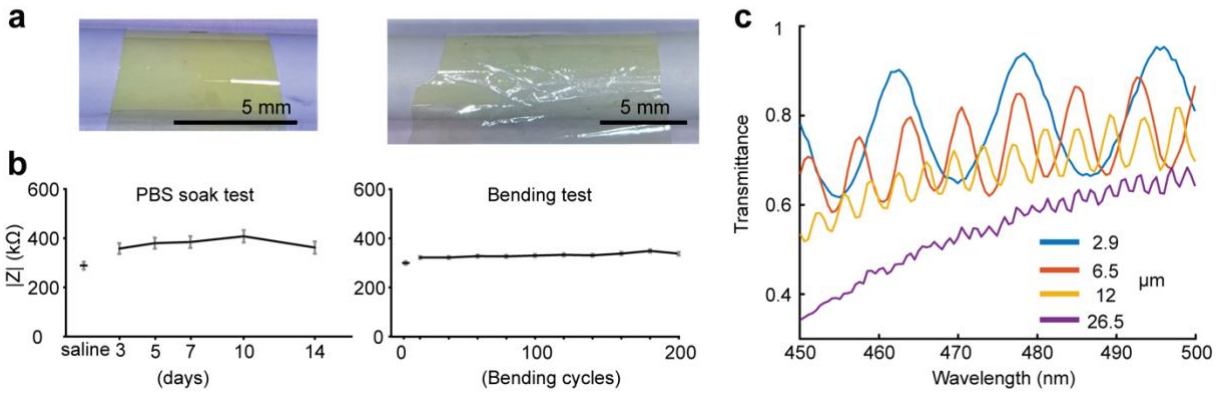

Figure 8 | Optimal PI foil thickness and stability test

a, Handling test and bending around a 5 mm radius tube. Left: The µECoG array originally used thickness of 6.5 µm PI adheres to the tube and can be easily handled with forceps. Right: A thinner 2 µm PI foil develops wrinkles from handling and limited adherence to the surface. **b**, In vitro test revealed µECoG array stability. Left: The µECoG array aged in a PBS soak test (20 °C) for 14 days without significant impedance changes (at 1 kHz) and therefore without major device failures. Right: Stable impedance after repeatedly bending the µECoG array around a 5 mm radius tube revealed mechanical stability. **c**, Transmittance spectrum for the blue light wavelengths (450-55 nm) of different PI foil thicknesses. Similar transparency is observed for PI thicknesses between 2.9 µm and 12 µm. Prominent thin-film interference bands are visible. For thicker PI foils, (26.5 µm) transparency is considerably reduced, as also inference effects. Adapted from Brosch et al. (2020).

2.2.2. µECoG array recordings of primary auditory cortex tonotopy

We tested the acute and chronic recording quality of the µECoG array by assessing auditory cortex tonotopy resolution. These results reveal if the array design and fabrication are suitable for recording distinct signals alongside the fine spatial extent of the rodent cortex. We can evaluate by these recordings the possible advantage of the conformable thin-film array compared to previous stiff µECoG arrays. Here the focus is not on the overall signal amplitude but rather the resolution of topographic maps exemplary shown by different tonotopic frequency bands. Additionally, we tested if the µECoG array could substitute established tonotopy recording techniques with penetrating electrodes.

Typically, single- and multi-unit activity, recorded via penetrating microelectrodes in anesthetized animals, has been used to map the spatial distribution of frequency representations—or tonotopy—in the cortex. Because of tissue damage, this tonotopic mapping recording technique is limited to one terminal recording per animal, as described in the introductory section: 1.4. Non-penetrating cortical surface electrodes, subsection: 1.4.3. µECoG applications: Tonotopic auditory cortex mapping. Here, we recorded multichannel signals of cortical tonotopy with epidurally placed µECoG arrays, reducing tissue damage.

From the design portfolio of our arrays, we selected rectangular probes with an inter-electrode spacing of 250 µm, approximating the known tonotopy resolution in the gerbil A1 at 200 µm/octave for frequencies above 1 kHz (Scheich et al., 1993; Thomas et al., 1993; Ohl et al., 2000a). Each channel of the µECoG array exhibited a different absolute P1 and N1 peak amplitude in response to

auditory pure tone stimulation (Figure 9b). Electrode contacts above a cortical area tuned to a specific stimulus frequency show higher P1 and N1 peak amplitudes (Figure 9b). Generally, contacts tuned to low frequencies were located more caudally than those tuned to high frequencies (Figure 9c, d); this observation agrees with the known caudorostral tonotopic gradient of the gerbil A1 (Figure 9a, Thomas et al., 1993). The 32 contacts were used to visualize the best frequency map, illustrating the tonotopy gradient (Figure 9d). Tonotopic maps computed from the N1 and P1 components of the ERP were similar (Figure 9c).

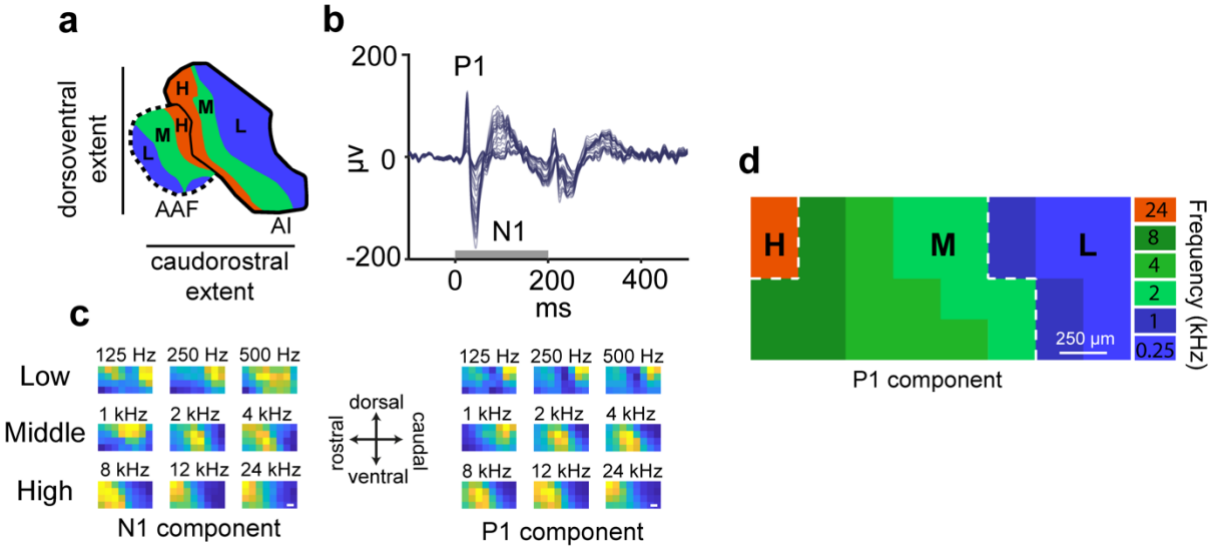

Figure 9 | High-resolution tonotopic recordings

a, Electrophysiological map of the two main auditory fields of the Mongolian gerbil showing low (L, 0.125 kHz -1 kHz), middle (M, 2 kHz -10 kHz), high (H, 12-30 kHz, wideband activity) frequency representations in the primary auditory cortex (A1, solid line) and anterior auditory field (AAF, dashed line). A1 and AAF show a reversed order of frequency representations in caudorostral orientation. Adopted from Budinger et al. (2000). **b**, Tone evoked single channel (n=32) ERPs (gray bar: pure tone stimulation, 200 ms, 12 kHz, 60 dB sound pressure level). Each channel shows different P1 and N1 peak amplitudes. **c**, Spatial representation of the N1 (left) and P1 (right) peak amplitudes in A1 cortex for 9 different pure tone stimulations. Brighter colors represent high positive P1 and negative N1 peak amplitudes. **d**, Best frequency tonotopic gradient of the P1 amplitude. The best frequency at a given channel transitions from low frequencies (L, caudal) to middle frequencies (M) and more rostral to high frequencies (H). Data in **b**, **c**, and **d** were recorded in the awake animal one day post-surgery. Scale bars: 250 µm. (n=1, rectangular array, 250 µm spacing). Adapted from Brosch et al. (2020).

The µECoG array allows simple cortical mapping with reduced neuronal damage. The array was placed on different locations within the cranial window on the temporal cortex without additional damage. Epidural recordings during surgery allowed to characterize tonotopic subfields (Figure 10). The 250 µm inter-electrode spacing µECoG array allowed to differentiate between A1 and anterior auditory field (AAF) with reversed caudorostral tonotopic gradients (Figure 10a: 3. position, c). Cortical mapping with a 500 µm inter-electrode spacing allowed to find auditory fields but not to characterize frequency-specific areas or auditory sub-fields (Figure 10b).

The mapping can be performed independently of anatomical markers that change with the animal's age, weight, and genetic background. Our experience showed that the typical anatomical landmarks and vascular pattern of the inferior cerebral vein as guidance for A1 localization were loosely correlated with the position of A1 and can only be used as general guidance to localize the

auditory receptive field. The cortical mapping time with four tone frequencies (200 ms duration, varying inter-trial-interval with average of 1.5 s) and approximately 100 repetitions for each tone does not exceed a maximum of 12 min. Therefore, the 250 µm spacing array allows mapping a cortical area of 1 mm x 2 mm in 32 locations simultaneously with short mapping times and immediate relocation possibilities. The recording area fits the size of A1 in gerbils (Figure 9, Figure 10). The location of the A1 and AAF or frequency specific sub-fields can be helpful, for instance, during viral opsin injections that are aimed at a specific location.

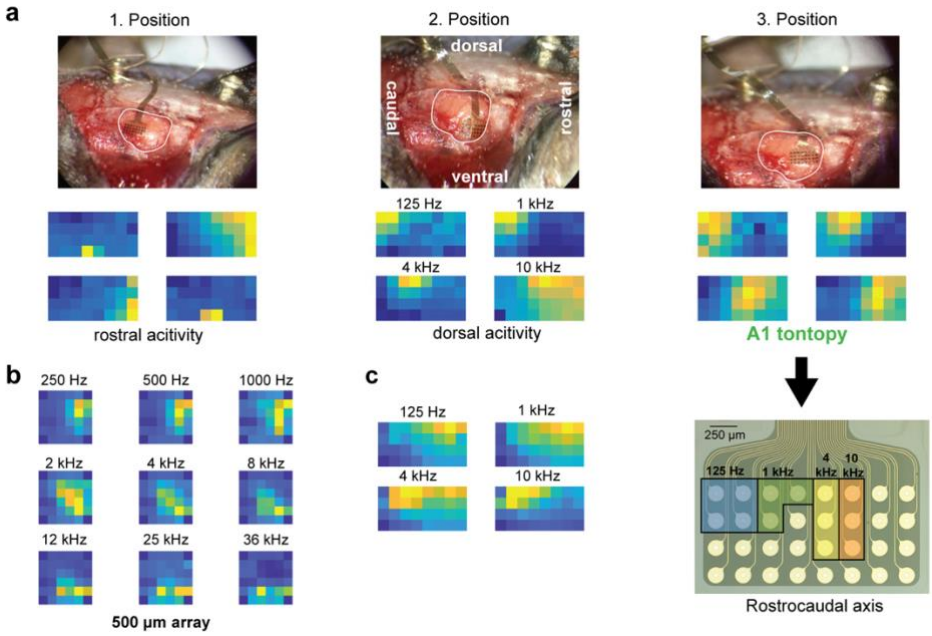

Figure 10 | µECoG array assisted localization of primary auditory cortex during surgery

a, Three different positions of the µECoG array (250 µm electrode spacing) on a craniotomy window of the temporal lobe and the respective spatial map of the ERPs N1 component. Four different pure tone frequencies with less than 100 stimulus repetitions allowed the subsequent rearrangement of the µECoG array (1. + 2. position) until localization of the primary auditory cortex (A1) was successful (3. position). Bottom right: Photograph µECoG array and overlay of the channels with highest amplitudes for a specific stimulus frequency (3. position). **b**, Exemplary recording of µECoG array with 500 µm inter-electrode spacing, allowed to localize auditory fields. Spatial resolution is not high enough to differentiate auditory sub-fields. **c**, Surgical tonotopic mapping of the anterior auditory field (AAF) with a reversed caudorostral extent (low frequencies rostral, high frequencies caudal) as depicted in the illustration in Figure 9a (250 µm electrode spacing).

Chronic tonotopic recordings were performed to assess µECoG array's suitability for auditory learning experiments, in which the tonotopic frequency gradients are typically reorganized over more extended periods. Therefore, we recorded chronic tonotopic maps during passive free-field auditory stimulation in awake, head-fixed animals. Distinguishable frequency areas as recorded during surgery were visible in the first days after implantation (Figure 11). Because of the progressive signal amplitude decrease, a uniform scaling of the spatial maps from different recording days resulted in a progressive vanishing of the separated frequency bands. (Figure 11a, b, c; uniform scaling). However, individual scaling of the spatial map of each recording day allowed a separation of the frequency-specific areas for more extended periods (Figure 11a, b, c; discrete scaling). For most frequency bands and animals, the clear tonotopic gradient disappeared within the first week after implantation (Figure 11), with some exceptions of up to approximately ten days (Figure 11b). If

analyzed closely, the activity shifted over time generally towards high-frequency areas (right site in each spatial map in Figure 11). The tonotopy degraded for all frequencies and animals, independent of the cranioplasty approach (original bone flap vs. silicone).

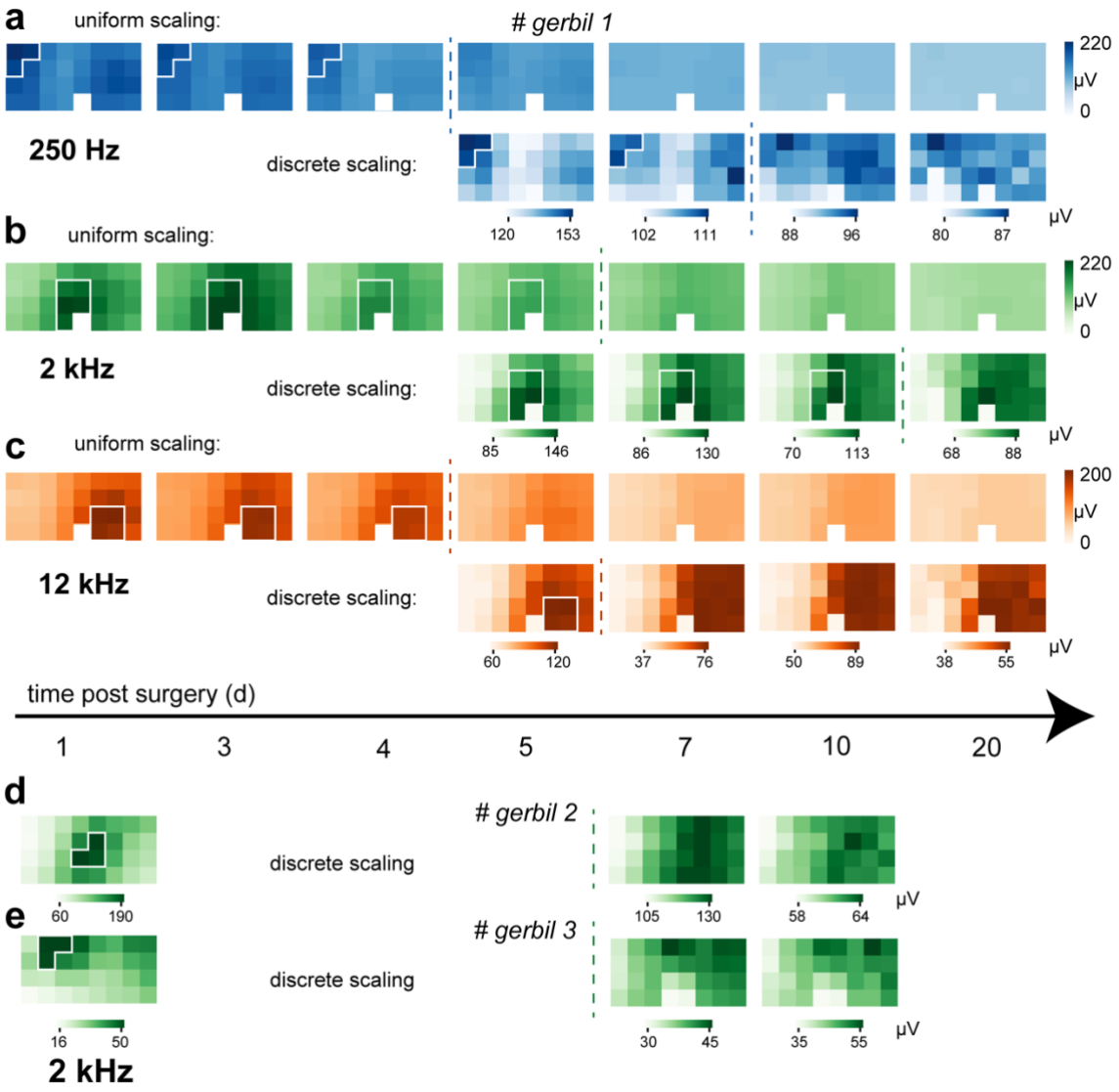

Figure 11 | Chronic tonotopic maps

a-**c** Tonotopic map degradation over time (1-20 days) for all frequencies. Spatial distribution of ECoG peak amplitudes of an awake, head-fixed animal for three exemplary stimuli: **a**, 250 Hz **b**, 2 kHz and **c**, 12 kHz pure tone stimulus presentations at different days post-surgery. Top row: uniform scaling of all spatial maps, bottom row: individual scaling of each spatial map. White rectangle: broken channel of the µECoG array. **d** and **e**, Two different animals also show tonotopic degradation. For simplicity, only 2 kHz stimulus presentations and discrete scaling is shown. **a**, **b**, **c**, **d**, **e**, White solid line marked area in spatial maps = distinguishable µECoG channels with highest amplitudes and, therefore, the approximate cortical representation of tone frequency. Dotted colored line: time threshold after which distinguishable frequency tonotopic area has vanished.

2.2.3. Long-term electrode characterization *in vivo*

While the recording resolution of topographic maps can be time-limited, the overall chronic signal amplitude and *in vivo* electrode performance can be different. Therefore, we measured the stability of spontaneous and tone-evoked responses across twelve weeks. Additionally, we assessed *in vivo* electrode performance and electrode-tissue interaction by chronic impedance measurements. The chronic stability of the implanted electrode array is critical if it is used for long-term behavioral learning experiments.

The chronic electrophysiological signal quality changes also depending on the foreign body response. Therefore, we looked at tissue growth and glial activation. This allows to assess the extent of neural tissue disruption and further contributes to possible explanations of signal degradation that are independent of electrode failures.

We found the power of pre-stimulus baseline activity to be stable over this time frame (Figure 12b), RMS: 5.36 ± 0.73 µV, median ± median absolute deviation). Further, we measured ERP auditory responses to pure tones. We quantified the amplitude difference between the first major positive (P1) and negative deflection (N1, Figure 12a, d: red lines) to measure total evoked activity. Over time, we found a modest decrease in this parameter. After one month, the P1-N1 amplitude difference still exceeded 75% percent of the initial value and stabilized around 68% percent at three months (Figure 12a). The curve shape of the response was generally conserved but showed a progressive attenuation of later components (Figure 12d). P1 and N1 peak latencies remained constant at 30 ms and 60 ms post-stimulus onset, respectively.

We further quantified long-term stability by *in vivo* electrode impedance measurements at a frequency of 1 kHz (Figure 12c). Immediate post-surgery impedance was 524 kΩ ± 39.26 (mean ± S.E.M), slightly higher than impedance in saline before implantation 397 kΩ ± 48.75 (mean ± S.E.M). Within the first days, impedance values dropped to 302 kΩ ± 89.32 (mean ± S.E.M, day 7, Figure 12c) and after five weeks to 200 kΩ. After explantation, the *ex vivo* impedance climbed back to 282 kΩ ± 43.33 (mean ± S.E.M). As a control experiment for the observed *in vivo* impedance changes, we performed an *in vitro* soak test in PBS over two weeks. We observed, besides the initial increase (saline to first days), no impedance changes (Figure 8b, left).

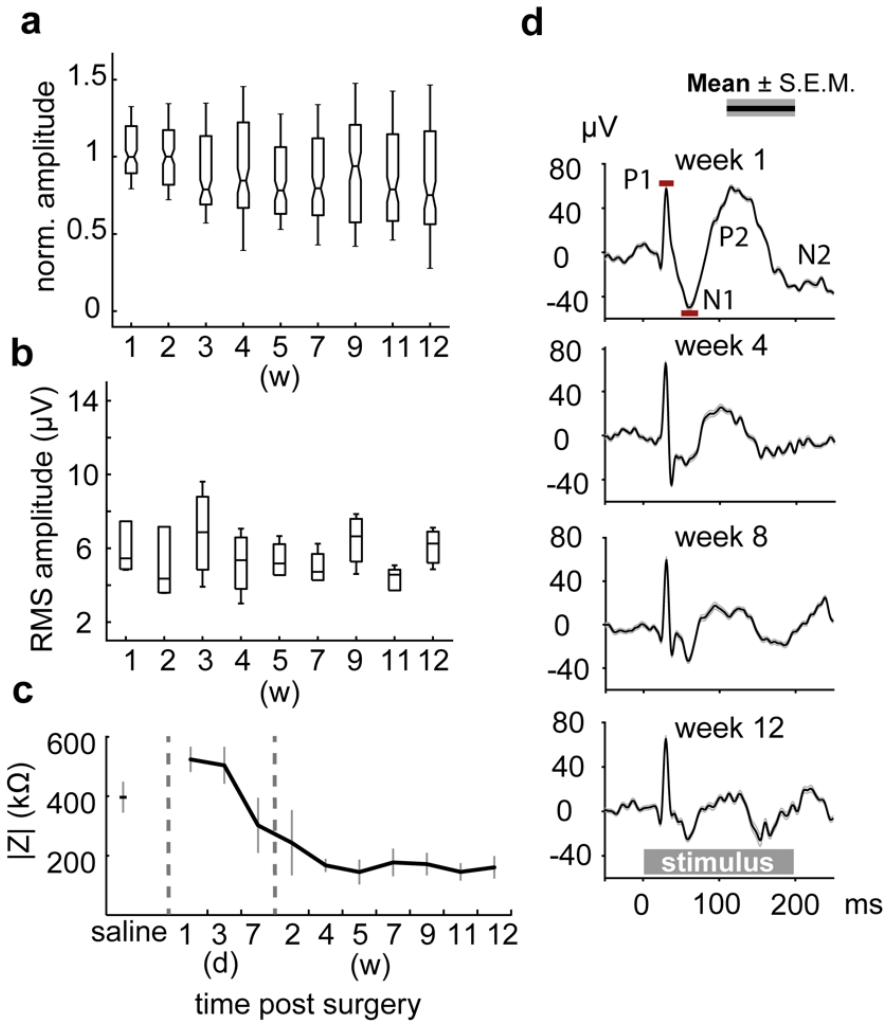

Figure 12 | Characterization of chronically implanted *in vivo* µECoG arrays

a, Normalized awake auditory ECoG peak-to-peak (P1-N1) amplitudes for 1 kHz pure tone stimulation. Peak-to-peak amplitudes decreased slowly over time. The P1-N1 amplitude after 12 weeks of surgery is still more than half of the initial amplitudes. **b**, Baseline activity voltage. The RMS voltage was calculated from one channel in a 200 ms time window before the stimulus. RMS voltage shows consistency over time (animals=4). **c**, Magnitude impedance of working channels before implantation, measured at 1 kHz in saline and *in vivo* measurements over time for the first 7 days (day 1, 3, 7) and subsequent weeks (n=4, rectangular array, 250 µm inter-electrode spacing). **d**, Mean ERPs from a representative animal over months, showing changes in P1, N1, P2, and N2 components (gray bar: 1 kHz pure tone 200 ms, channels=32). Adapted from Brosch et al. (2020).

We used individual channel impedances to quantify the fraction of working channels, where a channel was considered working if its impedance at 1 kHz was below 1 MΩ. All electrode sites of the implanted arrays remained working for three months post-surgery. After even longer implantation in additional animals, channels from the edge of the craniotomy start to exceed the threshold impedance. A cranial window implanted in one additional animal allowed evaluating the epidural µECoG array and the tissue reaction around it (Figure 13). We observed micro-hematomas and the overgrowth of the array by dural and bony tissue. After explantation, the impedance of the electrodes returned to pre-implantation values, indicating bone tissue overgrowth as the limiting factor instead of electrode failure. A light-microscopic inspection of the explanted electrodes showed no signs of degradation, such as delamination, even after extended implantation periods.

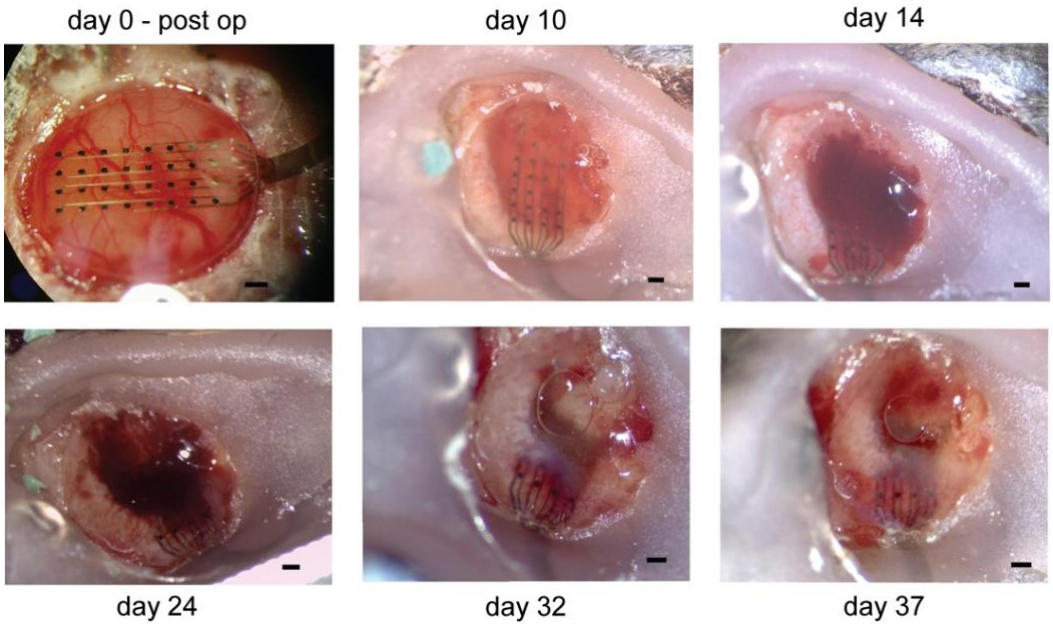

Figure 13 | *In vivo* progression of tissue growth around an epidural implanted µECoG array

Photographs were taken through a craniotomy glass coverslip window above the visual cortex of a Mongolian gerbil. During surgery, major blood vessels and the dura mater were not injured. From 10 days until 24 days after implantation, we observed bleeding and micro-hematoma above the µECoG array. After approximately 10 days, an opaque tissue started forming around the µECoG array, and the surrounding bone edge started growing, eventually closing the craniotomy window. Scale bar 500 µm. Adapted from Brosch et al. (2020).

We histologically analyzed brain sections, staining for two common markers: GFAP, a marker for astrocytes, and Iba1, a marker for activated microglia (Figure 14). We found a slight increase in GFAP fluorescence intensity in the implanted hemisphere (16.6% ± 4.86, mean ± SD) compared to the baseline intensity in the respective contralateral hemisphere (t-test, one-sided, p=.01, Figure 14a). No difference from baseline was observed for Iba1 (2% ± 1.5, mean ± SD) compared to the baseline intensity (t-test, one-sided, p=.22). The spatial distribution of both markers was different. Iba1 was more uniformly distributed across different layers of the cortex, whereas GFAP was predominantly observed in superficial layers (Figure 14b). In Nissl-stained slices, we did not observe any coarse cortical damage from array implantation (Figure 14c, middle, Nissl image).

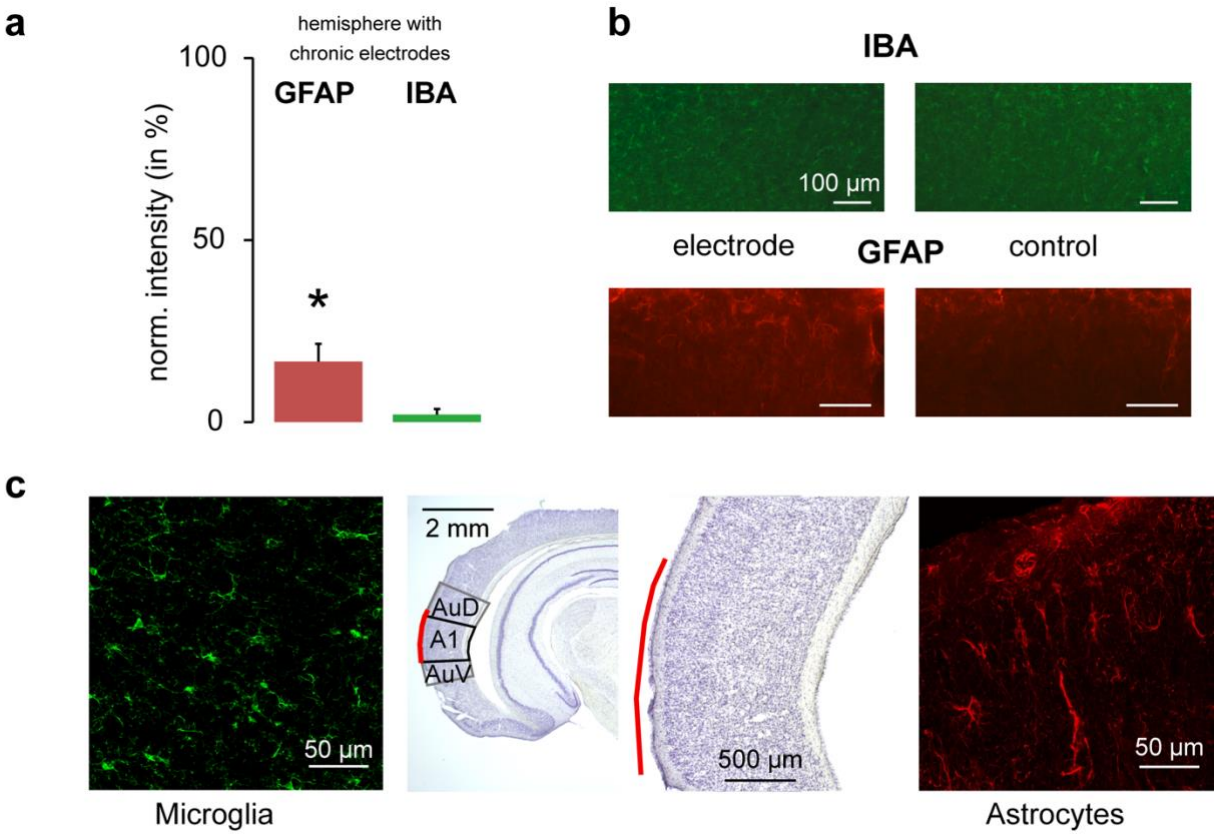

Figure 14 | Assessment of long-term implantation effects and neuroinflammation

a, GFAP and Iba1 fluorescence staining intensity in the auditory cortex in the implanted compared to the contralateral control hemisphere. GFAP is slightly increased in superficial layers below the array (n=8 slices per animal, 2 animals). **b**, Fluorescence micrographs of exemplary auditory cortical fields in the electrode implanted and control hemisphere. Iba1 staining is distributed across all cortical layers, whereas GFAP is located predominantly in superficial layers. **c**, left and right: Confocal imaging of microglia (Iba1) and astrocyte (GFAP) cell bodies in A1 below an implanted µECoG array. Middle: Nissl staining. The red line indicates the position and size of the µECoG array. dorsal auditory field (AuD), ventral auditory field (AuV), Adapted from Brosch et al. (2020).

2.2.4. Optogenetic stimulation through the µECoG array

Optogenetic methods are increasingly used to achieve a causal understanding of neuronal circuit function by exploiting the fact that defined populations of neurons can be selectively stimulated, and the consequences can be observed within the neural network. Due to the low transparency of PI in the blue spectral region, however, it is difficult to combine these methods with traditional PI-based electrode arrays. The improved blue light transmittance of the here presented array was demonstrated already in previous *in vitro* results (Figure 7c, Figure 8c). Here we tested transparency and light-evoked opsin activation *in vivo*.

We expressed the opsin ChR2(H134R) under the CamKIIα-promoter in the left visual cortex of the Mongolian gerbil, sensitizing the principal cells in this area to blue light (Figure 15a). We positioned the array (quadratic design, 500 µm spacing) over the visual cortex in an acute experiment. We applied laser stimulation through the transparent region between four contacts of the µECoG array (Figure 15b). Laser pulses induced ERPs in the opsin expressing hemisphere (peak amplitude: -511 ± 109.7 µV (mean ± SD), Figure 15c, upper panel). The induced electrical ECoG activity was locally concentrated around the stimulation site and decreased over distance (Figure 15c, top right panel). We observed only a minimal response in the contralateral, non-opsin expressing hemisphere (peak amplitude: -32 ± 14.19 µV, Figure 15c, lower panel).

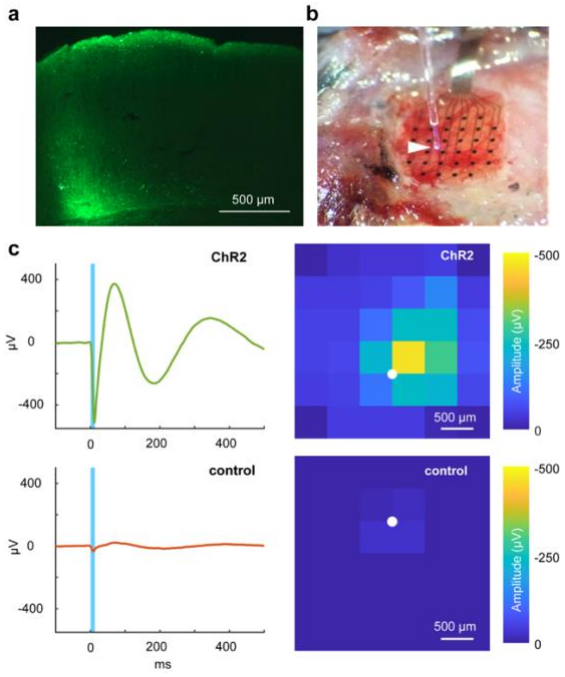

Figure 15 | *In vivo* optogenetic stimulation through the µECoG array

a, Channelrhodopsin 2 (ChR2) expression in the visual cortex. The virus injection site shows ChR2 expression at different depths of the cortical column. **b**, Stimulation procedure: a craniotomy above the visual cortex was performed, and the 32-channel array (quadratic design, 500 µm spacing) was applied on top of the intact dura mater. A fiber tip (105 µm) was positioned in-between four electrodes on top of the array (white arrow). **c**, Recorded ECoG signals during focal light pulses through the array. The channel showing the highest amplitude from ChR2 stimulation (473 nm, 10 ms, 20 mW mm-2, blue bar) in the opsin expressing hemisphere (top left) and the control hemisphere (bottom left). Right column: Spatial distribution of maximal N1 response amplitude across the ECoG array. The strongest response is located close to the stimulation site (white circle) and decreases with distance. (n=1). Scale bars: 500 µm. Adapted from Brosch et al. (2020).

2.2.5. Light-induced artifact

Light artifacts are a common problem in optophysiological experiments (Mikulovic et al., 2016). By choosing our strategy of using opaque metal electrodes as opposed to transparent graphene or ITO electrodes, we might experience a higher degree of the photovoltaic artifact. This subsection investigates if our array is suitable for combined electrophysiology and optogenetic stimulation or experiences significant artifacts that interfere with the neural signal.

Light artifacts can be caused by physical and physicochemical processes such as the Becquerel-effect; however, similar phenomena are also caused simply by the passive, light-gated opsin current, which precedes the active spiking response of the cell (Xiong et al., 2015, section: 1.5. Abiotic properties of signal quality, subsection: 1.5.5. Light-induced artifacts and damage).

To dissociate physical and biological factors, we evaluated light-induced artifacts *in vivo* (Figure 15) and *in vitro* (Figure 16). *In vivo* application did not result in a significant photovoltaic artifact as observed in recordings during light stimulation of the non-opsin expressing hemisphere (Figure 15c, lower panel). We observed strong light-induced artifacts in our arrays only when an electrode site was directly illuminated (blue light, 473 nm, 10 ms pulses, Figure 16d: left, channel 1). Already in neighboring electrodes, the artifact is small to absent (channel 2, 3). Illumination in the clear piece of the PI substrate, between four electrodes, did not show artifacts in three of the four surrounding electrodes, even for high-intensity stimulation (50 mW mm^{-2}, Figure 16d: right, channel 1, 2, 3). One electrode showed a small artifact when it was hit by stray light from the fiber tip (Figure 16d: right, channel 4).

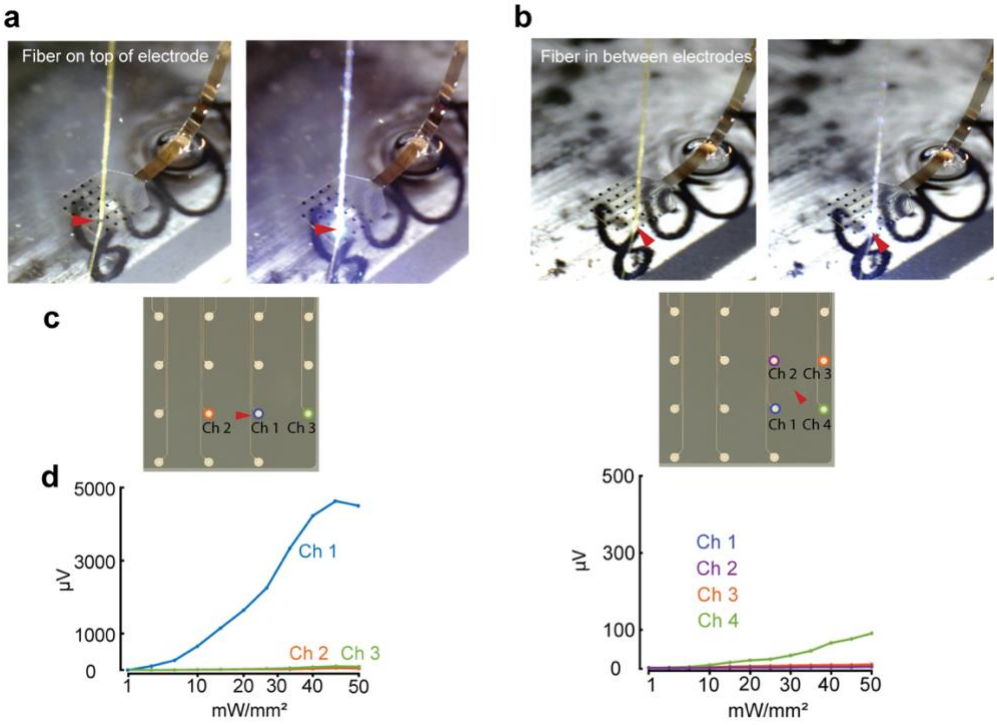

Figure 16 | *In vitro* light artifact characterization

a, Optical fiber (red arrow) placed directly above an electrode site of a quadratic ECoG array (500 µm spacing) immersed in PBS (left: laser off, right: laser on). **b**, The same configuration as in (**a**) but with the fiber was placed between electrode sites. **c**, Illustration of the spatial orientation of analyzed electrodes in relation to the fiber tip as depicted in photographs (red arrow),

Left: Channel 1 is exposed directly (left side), channels two and three are neighboring channels. Right: optical fiber tip is placed in between four channels. **d**, Artifact amplitudes in relation to laser pulse intensity for direct (left) and indirect (right) light exposure conditions. Adapted from Brosch et al. (2020).

2.2.6. Voltage-sensitive dye imaging through the µECoG array

Here we demonstrate the use of our array in combined electrophysiological and imaging experiments. The focus of the dissertation is the advancement of neural devices that incorporate both modalities. Each modality has its limitations, but a combined approach allows more accurate interpretations. We performed simultaneous µECoG array recording and VSD imaging. VSD imaging allows high-resolution imaging of membrane voltage at millisecond fidelity. While the transparency of the array has been shown to be sufficient, the electrode or electrodes shadows could obstruct the cortical areas used for imaging analysis. Such possible complications were tested in this subsection.

The imaging field of view covered an area of 4x4 electrodes of the µECoG array (quadratic design, 800 µm spacing). A 17x11 pixel ROI and the four surrounding electrodes on the rat's visual cortex were to directly compare optical and electrophysiological signals in response to a light flash to the contralateral eye (Figure 17a). The first major negative deflection (N1) in the electrical signal corresponds to an increase in the VSD fluorescence signal (P1) with similar peak latency (159.27 ± 12.87 ms versus 135.04 ± 24.58 ms, Figure 17b). The transparent µECoG array allows imaging the spatial distribution of evoked activity without being obscured by electrode shadows. For example, the delayed spread of posterior visual activity to medial anterior visual activity is visible in the imaging data (Figure 17c). The early onset posterior region occurred 80 ms post-stimulus onset and likely correspondents to the primary visual cortex (V1). Late anterior medial area activation occurred after 110 ms post-stimulus onset, likely corresponding to the medial secondary visual cortex area (Figure 17c, d: $P1_{VSD}$). This spread is also partially observable in the electrical recording data (Figure 17d: $P1_{ECoG}$, $N1_{ECoG}$). Activity remained confined mainly to visual areas, with the parietal association area showing only a slight activation (Figure 17c, d).

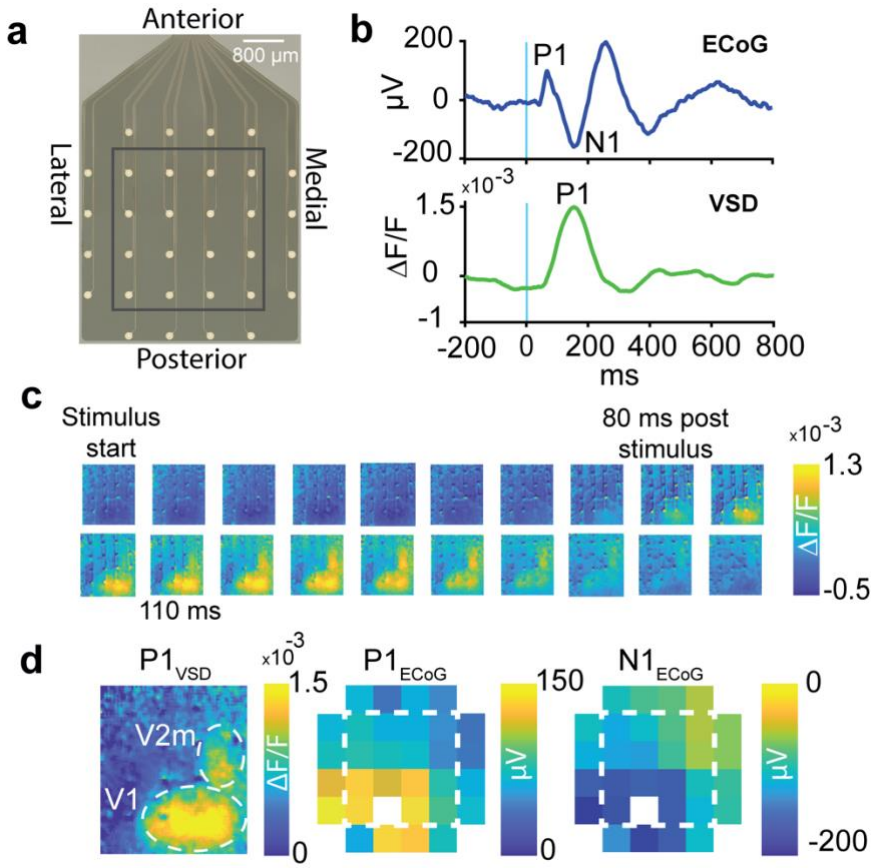

Figure 17 | VSD imaging through the µECoG array in rat visual cortex

a, Orientation of the epidural, 32-channel ECoG array relative to the orientation of the rat (quadratic design, 800 µm inter-electrode spacing). The solid square represents the field of view of the VSD camera. **b**, ECoG and VSD responses to a short light pulse (5 ms, blue bar) delivered to the contralateral eye. Averaged ECoG voltage signal from four electrodes (blue line, stimuli: n=24) and averaged VSD signal above the visual cortex (green line, stimuli n=24). **c**, Spatial and temporal distribution of the cortical activation imaged by the VSD signal. After stimulus onset, the posterior field depolarizes first (80 ms post-stimulus), followed by a delayed activation of the medial area (110 ms post-stimulus) and a return to baseline. Each image corresponds to a 10 ms interval. **d**, Spatial maps of peak amplitudes from different VSD and ECoG signal components. Left: optical VSD P1 activation V1 and the medial secondary visual area. Middle: ECoG P1 component. Right: ECoG N1 component. VSD field of view is marked with a white dashed line within the ECoG P1 and N1 components. One broken channel was excluded (marked white). Orientation of all response maps in **c**, **d** is as shown in **a**. n=1. Adapted from Brosch et al. (2020).

2.3. Discussion

2.3.1. Transparent electrodes versus opaque metal electrodes

Different approaches for neural devices combining electrical recording and optical modulation/ imaging exist. Previous studies have described transparent µECoG devices using ITO and graphene. We use opaque chrome-gold-platinum electrodes. Our device is transparent only because of the thin transparent PI layers. By using metal electrodes, we keep the excellent recording features of traditionally used metal electrodes. This subsection discusses electrical parameters, fabrication, and light transmittance between previously published transparent ITO and graphene electrodes and our opaque metal electrodes. This subsection highlights that most technical parameters are improved in metal electrodes. The transparency of ITO and graphene electrodes is lower than expected and comes with tradeoffs.

Sheet resistance and impedance

Opaque metal electrodes and traces have a higher conductivity compared to transparent electrodes. ITO and graphene, at transparent thicknesses, have sheet resistances in the range of tens to hundreds of Ω/sq. (Ledochowitsch et al., 2011b; Park et al., 2014; Kunori and Takashima, 2015). In contrast, our metal layer has a sheet resistance of approximately two to three orders of magnitude less. A low sheet resistance reduces the loss of transported charge.

In addition, we observed much lower impedances relative to electrode surface area compared to graphene (Park et al., 2014, 2016; Lu et al., 2018b; Thunemann et al., 2018). The micro-roughness of the metal electrodes on the plasma-roughened PI substrate might be one explanation. An improved graphene array from Park et al. (2018) has impedances comparable to ours. However, the surface area is four times larger in comparison to ours. Transparent electrodes often need additional surface modifications to reach comparable impedances. Liu et al. (2018) used nitrogen-doped graphene to lower impedances. However, the used nitric acid negatively affected the longevity of the array.

The introductory subsection 1.5.4. Noise: Impedance reduction (in section 1.5. Abiotic properties of signal quality), described the importance of impedance. If impedances are significantly below the headstage impedance, then the signal loss is insignificant. Fabrication of graphene electrodes with the same surface area as our electrodes would result in high impedances. Those would exceed the critical threshold of the voltage divider effect and lead to significant signal loss. In comparison, reduced sheet resistance and impedance in our µECoG array attenuate electric interference and noise.

Fabrication

The detailed fabrication is handled by the engineers and is not the focus of this dissertation. All other technical measurements in this thesis were performed by us. A short discussion of the complications during graphene and ITO array fabrication is nevertheless depicted in this paragraph.

Graphite is one of the strongest, lightest, most flexible materials with a high electrical and thermal conductivity (Geim and Novoselov, 2007; Lee et al., 2008; Geim, 2009). Graphene as a single atomic monolayer of graphite reduces this stability but results in the needed high transparency. Graphene electrodes depend on monolayer stacking. This requires complicated wet processes, making the fabrication less reliable (Zátonyi et al., 2020). The transfer of graphene from the growing material onto the substrate material often results in monolayer cracks (Kuzum et al., 2014; Park et al., 2014). Thunemann et al. (2018) developed crack-free techniques that include the reduction of organic residues after photoresist removal. However, the more complicated fabrication steps impair the uniformity of the graphene µECoG array.

ITO is easily sputtered and patterned lithographically (Ledochowitsch et al., 2011b). It is used commercially as a transparent conductor in smartphone touchscreens or for defrosting airplane windshields. The distributed applications make ITO a rare and expensive resource. Miniaturization, rough handling, small radius bending, and chronic application in ionic wet environments make the use of ITO in rodent research difficult. ITO electrodes suffer from isolator adhesion problems, limited strain resistance, brittleness, cracking, and other long-term related stability issues (Chen et al., 2001; Alzoubi et al., 2011). Interconnecting wires within the array are exposed to much higher bending stress. Because of ITO's brittleness, interconnects are made from metal. This complicates the fabrication process and limits the overall transparent area (Ledochowitsch et al., 2011b; Kwon et al., 2013). Only in µECoG arrays designs for acute recordings interconnects are ITO-based (Kunori and Takashima, 2015).

Overall the fabrication of our metal-based µECoG arrays is less expensive, requires less complicated processes, and has an increased reliability.

Light transmittance

Our electrodes are fabricated from chrome, gold, platinum and are therefore opaque. They block light transmittance of small areas of the cortex. To what extent that is problematic for optical imaging is discussed later. This paragraph discusses the limitations and tradeoffs of using transparent graphene and ITO electrodes.

The average transmittance of ITO electrodes is ≈ 80% (Park et al., 2014). However, ITO electrodes do not have a flat transmittance in the visible light spectrum (Ledochowitsch et al., 2011b). Additionally, the transmittance in the near-infrared wavelengths is decreased (Lee et al., 2016; Park et al., 2016).

Graphene monolayers allow for a broad-wavelength transmittance above 90% with a flat transmittance spectrum (Bae et al., 2010; Park et al., 2014). The used electrode insulator material influences the actual transmittance of both graphene and ITO µECoG arrays.

Graphene electrode arrays are often not produced from graphene monolayers. Since monolayers have poor electric properties and show substrate cracking during the transfer process. Adding layers comes with a tradeoff in transparency in that each added monolayer of graphene decreases the transmittance by ≈ 2.3% (Park et al., 2016). The sheet resistance improved from 152 Ω/sq. of monolayer graphene to 76 Ω/sq. of four-layer graphene. However, transmittance is reduced by 10% (Park et al., 2014). The sheet resistance is still two orders of magnitude higher than our platinum

electrode array. Surface modifications of graphene electrodes like platinum nanoparticles can improve the recording quality but degrade the transmittance by ≈ 50% (Lu et al., 2018b).

Here we saw that the transparency of graphene and ITO comes with tradeoffs. ITO electrodes are not translucent to all wavelengths used for optical imaging/stimulation. The need for multiple layers of graphene reduces transmittance significantly.

2.3.2. Light artifacts

Light artifacts appear as transients or oscillations in the recorded signal. The artifact overlays the actual signal, challenging further analysis. This subsection compares light-induced artifacts between our electrode array and previously proposed transparent µECoG arrays. In many applications, graphene (Kuzum et al., 2014; Park et al., 2014; Thunemann et al., 2018) and ITO (Kunori and Takashima, 2015; Ledochowitsch et al., 2015) electrodes promise artifact-reduced or even artifact-free recordings during electrode illumination. Since we have opaque metal electrodes, it is expected that the photovoltaic artifact would be increased.

We quantified the photovoltaic artifact *in vitro and in vivo. In vitro* tests allow dissociating between the physical photovoltaic artifact and biochemical artifacts, such as ChR2 currents introduced in the subsection: 1.5.5. Light-induced artifacts and damage.

We have demonstrated that direct laser illumination of the metal electrodes indeed created a significant light artifact. Illumination of the transparent PI insulator area between electrodes is almost artifact-free. This robustness against light artifacts might be partially supported by a residual metal ring around the electrode's opening, shielding the exposed conductor optically. *In vivo* optogenetic stimulation through the transparent PI of the array did also not show a significant light artifact.

Artifacts of graphene electrodes

Park et al. (2014) observed light intensity and light pulse length dependent artifacts on graphene µECoG arrays. Artifact amplitudes were the same as in simultaneously tested platinum electrodes. Thereby, already a low laser intensity (13.8 mW mm^{-2}, 473 nm) and stimulation time (3 ms) evoked a considerable artifact (>100 µV) on the graphene electrodes. The graphene µECoG array can only be artifact-free with reduced light energy. This allows, for example, only imaging techniques that use a low laser power and long-wavelengths like infrared light. However, optogenetic stimulation and two-photon imaging with increased light intensities induce significant artifacts. For these reasons, the graphene array from Park et al. (2014) has no advantage concerning artifact reduction.

Another graphene µECoG array shows partially artifact-free recordings (Thunemann et al., 2018). The number of stacked graphene monolayers can explain this finding. Park et al. (2014) used four-layer graphene electrodes. This multilayer results in higher absorption of photons. Therefore, an occurring photovoltaic effect is natural. Thunemann et al. (2018) used monolayer graphene electrodes. The light-induced artifacts in monolayers will be significantly less. The tradeoff is a high electrode impedance (> 1MΩ) and lower implantation longevity.

A second explanation is light directionality. Park et al. (2014) demonstrated light-induced artifacts while directly illuminating graphene electrodes via an optical fiber. In contrast, Thunemann et al.

(2018) illuminated the insulator right next to the graphene electrodes and observed no artifacts. However, the supplementary data reveals that direct light illumination of the graphene electrode does result in a considerable artifact. The artifact is reduced compared to metal electrodes but still considerably large. We observed a similar difference between direct and indirect light directionality with our metal electrodes.

The inherent appearance of light-induced artifacts in graphene can be explained as follows. The electronic band gap of a solid material defines the energy difference between the valence and the conduction band. In metals, the valence and conduction band overlap, whereas insolating materials have large band gaps. Electrons can leave the valence band and reach the conduction band through applied photon light energy. The electrons are now not anymore bound to their atom in the valence band. They carry a charge and are contributing to an electric potential resulting in the artifact.

Materials like glass are transparent and have a high band gap. Photons of visible light pass through glass without much absorption or reflection. In contrast, the small band gap of metals makes them susceptible to the photovoltaic effect. Graphene has a zero band gap and therefore is susceptible to the photovoltaic effect (Geim and Novoselov, 2007). It can be produced as an extremely thin monolayer, making graphene transparent despite its zero band gap. Strong covalent carbon atom bonds make graphene more mechanically resilient than thin metal layers. However, the disadvantage of graphene monolayers is their low electric conductivity and susceptibility to cracking.

Artifacts of ITO electrodes

ITO conduction is mediated by oxygen vacancies, which result in a larger band gap than that of metals and graphene (Mryasov and Freeman, 2001). Therefore, ITO is less susceptible for electrons to jump from the valence to the conduction band. ITO electrodes using long-wavelength red light in VSD imaging (Kunori and Takashima, 2015) and short-wavelength blue light (Ledochowitsch et al., 2015) do not show significant light-induced artifacts.

However, ITO electrodes are not entirely free from light-induced artifacts. An ITO array developed by Zátonyi et al. (2020) revealed light-induced artifacts during *in vitr*o two-photon microscopy. This could be the result of a focal plane close to the electrode and high laser intensities. The artifact was less significant compared to control opaque gold electrodes. Kwon et al. (2013) observed light-induced artifacts during *in vivo* recordings in an ITO µECoG array. An explanation is the direct illumination of metal interconnects towards the ITO electrodes.

Opaque gold traces are also an inherent problem of graphene µECoG arrays. All graphene-based µECoG arrays need gold traces for stable connection towards the EIB (Kuzum et al., 2014; Park et al., 2014, 2016; Liu et al., 2018; Thunemann et al., 2018). These opaque interconnects limit the total surface transparency and restrict the field of view.

µECoG array advancements in light artifact reduction

Transparent electrodes were seen as a valuable option to reduce the photovoltaic artifact for combined optophysiology in µECoG devices.

Overall, graphene and ITO electrodes exhibit a low light-induced artifact. The artifact amplitude is comparable to our array during indirect light stimulation. Light passes through the transparent PI, and electrodes are only indirectly illuminated. During direct electrode illumination, graphene electrodes, similarly to our metal electrodes, have a significant artifact. The artifact can only be reduced by monolayer graphene applications. Monolayers, however, result in low electric conductivity and possible cracks. ITO is a valuable option for direct electrode illumination because of its wider band gap. It is a brittle material, and therefore, not suitable for chronic experiments.

The light-induced artifact in our µECoG electrode design is reduced with increasing surface area of PI. Widefield cortical surface calcium imaging results in direct metal electrode illumination (Mohammed et al., 2016; Cramer et al., 2019). A significant light artifact would be the result. If the field of view is restricted, artifact-free imaging is possible. Thunemann et al. (2018) used a 50 µm x 100 µm field of view during two-photon imaging in graphene arrays. The electrode-free PI surface of our array is sufficient for such an imaging area (350 x 350 µm electrode free area between four electrodes, array design: 500 µm electrode site spacing). Therefore, the light artifact in our array is, in many applications, not increased.

However, the electrode-free surface area is limited for smaller rodents. Mice require lower electrode spacing for a comparable spatial sampling.

2.3.3. Substrate and isolation material

This subsection first discusses why we chose PI as an insulator for the µECoG array over other materials. Further, the transparency of our PI array is compared to other µECoG arrays made from PI. Especially the low blue light transmittance needed for optogenetics is problematic in previous approaches of PI-based arrays. Lastly, the thin-film interference effect observed during transparency measurements is discussed. Overall, this subsection highlights that the here used PI is a suitable material for transparent neural devices in terms of fabrication, durability, and transparency.

Insulator types

Substrates such as Parylene C, PI, Parylene HT, PDMS, and PET are typically used for optical transparent neural implants. Transparency depends highly on the material thickness.

Substrate types have different overall transparency. A Parylene HT µECoG array has the highest transparency that exceeds 90% for wavelengths between 400-900 nm (Zátonyi et al., 2020). Parylene C (Zátonyi et al., 2020) and PDMS (Renz et al., 2020) µECoG arrays have a lower transmittance between 85% and 90%. PI (Kuzum et al., 2014; Zátonyi et al., 2018a) and PET (Thunemann et al., 2018) µECoG arrays have transparency closer to 80%. The transmittance of PI is significantly lower for blue light (< 500 nm). While Parylene C is colorless, PI has a slight amber color.

The choice of a suitable insulator is not solely dependent on transparency. For example, Parylene C offers good long-term stability and high biocompatibility (Stark, 1996). However, the material is more fragile in thin films (Schmidt et al., 1988; Hassler et al., 2011) and has limited thermal stability (Von Metzen and Stieglitz, 2013; Li et al., 2019). PDMS is soft and thus highly tissue compatible but

challenging in combination with small electrodes (Henle et al., 2008). In PDMS arrays, the mismatch between conductor and polymer elasticity requires special processing methods or sandwich systems (Henle et al., 2011). PET needs to be applied in a more complicated foil-transfer process, leading to thicker and stiffer implants and lacks heat resistance (Thunemann et al., 2018).

We choose PI because of its high mechanical and thermal stability, good biocompatibility, and favorable processing characteristics. These features make PI one of the most popular materials in neural probe manufacturing (Yeager et al., 2008; Rubehn and Stieglitz, 2010; Hassler et al., 2011; Viventi et al., 2011; Ji et al., 2018).

Thin-film polyimide transmittance

Here we developed a PI-based µECoG array that achieves blue light transparency. Thin substrate layers result in an overall thickness of only 6.5 µm. At this thickness, PI transmits blue light (450-490 nm) with around 80% transparency.

Blue light illumination is required for typical optogenetics and calcium imaging methods. PI µECoG arrays at thicknesses of 25 µm and 50 µm are, however, almost opaque to blue light illumination. Only a few studies characterized PI µECoG arrays transparency (Kuzum et al., 2014; Zátonyi et al., 2018a). The PI-based µECoG array from Kuzum et al. (2014) used a 25 µm thick PI substrate with a transmittance of less than 20% in the blue-light wavelength. They also tested a PI thickness of 12.5 µm, which resulted in a transmittance of 30% in the blue-light wavelength. Kuzum et al. (2014) had to use a laser power four times higher than usual for confocal imaging through the PI array. Zátonyi et al. (2018a) produced an 8 µm thick PI-based µECoG array with an improved transmittance of approximately 70% at a wavelength of 473 nm. Other thin-film PI arrays did not reach similar transmittance or document optical parameters (Yeager et al., 2008; Rubehn et al., 2009; Kuzum et al., 2014; Zátonyi et al., 2018b, 2018a).

Here we could demonstrate that the optimized PI array with a low thickness can achieve similar optical parameters as other commonly used transparent substrates. The transparency is comparable or improved in comparison to previous PET or Parylene C µECoG arrays (Kwon et al., 2013; Lu et al., 2018b; Thunemann et al., 2018).

Thin-film interference

Thin-film interference is a phenomenon that can be observed by light reflection resulting in colorful oil films but also appears in thin polymer layers. The thin-film effect describes the interference of light reflected on the top and bottom of the surface. This reflection is dependent on material thickness and light wavelength. We showed that the interference effect of our thin PI material results in minor sinusoidal fluctuation of transmittance across wavelengths. Based on our recorded transmittance spectrum, a narrowband laser with a wavelength at one of the transmission interference peaks could result in a transmission of over 90%.

2.3.4. Optical imaging

The aim of this dissertation is to fabricate neural devices which combine electrophysiology and optophysiology. Therefore, we tested if optical imaging through our transparent µECoG array will be successful. The first paragraph discussed the usage of VSD imaging in this study instead of the more often used imaging of calcium signals. The following paragraph compares our imaging results to that of other transparent µECoG arrays, highlighting that opaque electrodes, as used in this study, do not exclude successful optical imaging. The last paragraph of this subsection discusses the differences between the electric and optic signal origin, highlighting that future mesoscopic neural investigations should optimally include both modalities.

Voltage versus calcium sensors

We applied VSD imaging through the transparent PI substrate. VSD imaging visualizes neuronal population activity of large cortical areas with a high spatial sub-columnar and temporal resolution in the millisecond range (Grinvald and Hildesheim, 2004). The temporal resolution is comparable to *in vivo* electrophysiology. However, calcium indicators are the more prominently used sensor. This paragraph discusses the pros and cons of both neural indicator types. It also highlights why VSD imaging is not an outdated technology and a suitable imaging technique within this work.

Both optical imaging methods have common phenomena like bleaching and phototoxicity. Despite those, there are also some major differences. The main problem of calcium indicators is the deconvolution of the indirect calcium signal into the voltage changes. If this problem is put aside, calcium sensors like GCaMP do indeed offer some advantages. The most prominent one is the cell-type specificity. In contrast, VSDs bind to many cell types, including non-neuronal glial cells (Chemla and Chavane, 2010). Chronic imaging with VSDs requires repeated staining of the cortex. The viral expression of calcium indicators is long-lasting. Fluorescence signals from calcium indicators come from the cytosol. In contrast, VSDs fluorescence originates from the plasma membrane. The plasma membrane only allows a limited amount of indicators compared to the cytosol (Kulkarni and Miller, 2017). The disadvantage of calcium indictors is the slow response function. The fast action potential kinetics of VSDs allows superior temporal resolution.

Optical imaging with GCaMP calcium indicators results in larger signal amplitudes ($\frac{\Delta F}{F_0}$) than VSDs. First, the fast kinetics of VSDs limit the number of photons delivered to the detector. Second, VSDs label internal and plasma membranes. Internal labeled membranes increase the resting fluorescence but do not contribute to signal changes (Scanziani and Häusser, 2009).

VSDs might be more widely used if cell specificity and low signal amplitudes are improved. Newer rhodamine voltage dyes have larger signal amplitudes but are slower in response time. This results from a mechanism that depends on voltage-dependent accumulation (Deal et al., 2016). The improvements of classic electrochromic fast dyes result in higher signal amplitude (Miller, 2016). Next-generation imaging will use the fast temporal volage indicator resolution and the genetically

specific expression of calcium indicators. Genetically encoded voltage dyes are becoming more and more available (Bando et al., 2019; Zhu et al., 2021).
VSD widefield imaging is classically performed in head-fixed anesthetized animals. Imaging setups for freely moving awake imaging also exist (Ferezou et al., 2006).

Voltage-sensitive dye imaging through µECoG arrays

We performed cortical VSD imaging through a PI-based µECoG array with opaque metal electrodes, which has not been performed previously. The question arises if opaque electrodes and interconnects themselves or their shadows prevent successful optical imaging.

We demonstrated that during VSD imaging, a fully transparent µECoG array is unnecessary. Platinum electrodes and gold traces in our array occlude only a minimal surface area. However, experiments requiring trans-illumination of electrode sites, such as two-photon imaging, might require transparent electrode materials.

The optical signal added additional features of the cortical activity distribution. Electrophysiological recordings are extended by another modality. We observed a gradual shift of the spatially localized activity from V1 to the secondary visual cortex. The spatial resolution of that shift was higher in the optical than in the simultaneously recorded ECoG data. The ROI for post-imaging analysis was targeted to the areas between the opaque electrodes. The transparent PI surface area allowed sufficient amounts of pixels. The electrodes were visible in the widefield view, but the electrodes or shadows did not obstruct the cortical spread of the signal. The excitation wavelength of the VSD is 630 nm, and the peak emission is near the infrared range. In this range, PI has a transmittance close to a 100%. VSD imaging did not cause optically induced artifacts. The used emission light has a long wavelength with lower energy.

Imaging through a different µECoG array with opaque platinum electrodes revealed difficulties. Park et al. (2018) showed altered widefield fluorescence calcium signals imaged with opaque electrodes compared to transparent graphene electrodes. Imaging through an array with opaque platinum electrodes revealed blocked calcium signal peak responses. However, the ROI was focused on a surface area of three electrodes. Compared to our electrode size, the diameter of the platinum electrodes used by Park et al. (2018) was nine times larger. An array with smaller-sized opaque platinum electrodes like ours could prevent the peak signal shielding. It is wise to skip laser scanning on top of opaque electrodes. This would reduce the induced artifact.

Kunori and Takashima (2015) performed VSD imaging through a fully transparent ITO electrode µECoG array. ITO electrode shadows were visible in the fluorescent images but did not prevent the detection of fluorescence changes below electrode sites. This is of an advantage compared to our opaque electrodes. However, there are also difficulties with ITO transmittance. The transmittance of the used PET substrate is above 80% for wavelengths of 480 nm – 680 nm. Kunori and Takashima (2015) used RH 795 as a VSD with an excitation peak close to 500 nm but a fluorescence emission peak at 700 nm. ITO transmittance degrades at near-infrared wavelengths (Lee et al., 2016; Park et

al., 2016). Therefore, transparent ITO electrodes are overall not suited to be used with red-shifted opsins (Zhang et al., 2008; Chuong et al., 2014) or infrared imaging techniques (Bruns et al., 2017; Shemetov et al., 2021). Additionally, the used RH 795 dye by Kunori and Takashima (2015) was shown to be more susceptible to the hemodynamic response. This results in a pulsation artifact, which distorts the signal quality (Shoham et al., 1999; Lippert et al., 2007).

Correlation of optical and electrophysiological signal

In this paragraph, the temporal relationship of the ECoG signal and the optical VSD signal are discussed. Due to their different origins, it makes sense to fabricate neural devices that allow to record both signal types and thus make more informed interpretations. Both showed a similar onset time. Additionally, the VSD signal peak amplitude correlated with the N1 component of the ECoG signal.

The origin of the VSD signal depends on the cortical dye staining depth and light penetration depth. VSD staining is mainly limited to supragranular layers (layers I-III, Kleinfeld and Delaney, 1996; Petersen et al., 2003; Ferezou et al., 2006). We stained the cortex through the intact dura mater. Lippert et al. (2007) showed that transdural staining reduces pulsation artifacts. Staining through the intact dura mater results in a supragranular dye distribution similar to staining after durotomy (Kleinfeld et al., 1994; Petersen et al., 2003; Ferezou et al., 2006).

ECoG signal and VSD signal revealed similar signal onset latencies. VSDs are organic small membrane-bound molecules. Their chromophore changes fluorescence absorbance in relation to LFPs. This is mediated by the redistribution of the dye. The dye molecules move in or out of the membrane depending on the membrane potential (Konnerth and Orkand, 1986; Shoham et al., 1999). The change in absorbance happens in a sub-microsecond timescale (Peterka et al., 2011). Therefore, VSD signal onset is only minimally delayed to ECoG signal onset.

The reason for the different shapes is the origin of either signal: VSD signal is a change in membrane voltage in the supragranular layers. In contrast, the LFP/ECoG signal is a complex overlay of different current sinks along the cortical depth. The two methods are complementary due to their different origin.

VSD signal peak amplitude occurs at the latency of the ECoG N1 peak amplitude. This relationship can be explained as follows. From laminar current source density analysis, it is known that the P1 ECoG component arises from early sinks in the granular and infragranular layers (Mitzdorf, 1985; Castro-Alamancos and Oldford, 2002; Jellema et al., 2004). The epidural ECoG array captures those signals through mainly return currents or so-called volume conduction. Supragranular layer I also gets widespread monosynaptic input from thalamocortical projections (Rubio-Garrido et al., 2009).

The N1 ECoG component originates mainly from intracortical projections. These projections originate from layer IV thalamocortical input. They are further relayed intracortically to supragranular layers (Mitzdorf, 1985; Sukov and Barth, 1998).

The early phase of the N1 is similar to that of P1, purely modulated by excitatory activity (Bruyns-Haylett et al., 2017). This finding was performed by pharmacological blockage with bicuculline across different laminar profiles. However, the late phase of the N1 components is inhibition-modulated (Bruyns-Haylett et al., 2017). This was evaluated by $GABA_A$ antagonist cortical injections.

The VSD signal rises and reaches its peak with the excitatory post-synaptic modulated P1 and early N1 component. VSD fluorescence decreases with the beginning of intracortical inhibitory post-synaptic modulation of the late N1 phase.

Kunori et al. (2015) observed the same correlation of the VSD peak and ECoG N1 peak. They used different experimental parameters like different VSD and cortical area. The exact laminar origin of both the VSD signal and the ECoG components is still under debate (Herreras, 2016; Bruyns-Haylett et al., 2017). Therefore, an ultimate explanation for both signal origins is still pending.

2.3.5. Optogenetic stimulation

Besides optical imaging, neural devices for combined electrophysiology and optophysiology should also allow optogenetic modulation of the recorded neurons. The low blue light transmittance of regular PI makes it an unfavorable choice for optogenetic applications. Our thin-film µECoG array has improved blue light transmittance. This subsection focuses on the *in vivo* application by activating ChR2 expressing neurons in the visual cortex by light stimulation through the array's PI substrate.

This subsection first discusses if optogenetic stimulation directly through the area of transparent electrodes is needed or if the recorded neurons can also be modulated by our approach where light enters through the transparent substrate right next to the electrode. The last paragraph discusses the origin of the small signal observed during light exposure of a non-opsin expressing area.

Optogenetic stimulation through transparent electrodes

Transparent electrodes allow neural modulation via light pulses directly through the electrode surface. Optical stimulation through transparent electrodes was previously shown for graphene (Park et al., 2016) and ITO electrodes (Kwon et al., 2013). The accessibility of the volume directly beneath the electrode can be an advantage for imaging studies. It allows *in vivo* imaging of glia cells and collagen formation underneath the electrode. These new insights can help in understanding the immunological response.

However, the necessity of optogenetic stimulation through the electrode surface is unclear. It promises modulation of spatially confined opsin only near one electrode. We clearly show that the light stimulation through the transparent substrate induced spatially confined activity on mainly one channel. Therefore, opaque electrodes do not prevent modulation of an electrode's localized neuronal population. Similar to light stimulation through transparent electrode surface (Kwon et al., 2013; Park et al., 2016).

Opaque electrodes and nearby light stimulation are also used in penetrating electrodes. Fiber-coupled acute recordings through the substrate polymer induced spatially localized signals (Richner et al., 2014; Minev et al., 2015; Brodnick et al., 2019). These studies, however, did not investigate the suitability of a PI thin film.

Activating a small subset of neurons near one electrode can be further improved by the following experimental parameters. Light power significantly affects the spread of the light-evoked activity (Park et al., 2016). The extent of opsin expression can be limited via neuron-type promoters or Cre/*loxP* specificity (Nagy, 2000). Additionally, light stimulation can be performed in projection terminals of opsin expressing neurons (Yizhar et al., 2011). We used viral expression restricted to excitatory neurons with the CamKIIα promoter sequence. Lower fiber diameter and low NA restrict the light spread further.

Overall, light stimulation next to opaque electrodes allows optogenetic modulation of spatially localized neuronal populations. Such localized activations are needed for future optogenetic brain-machine interfaces. Rarely, ECoG arrays with mounted µLEDs have been combined. Due to the thermal restrains, these were or only acutely tested *in vivo.* Ji et al. (2018) used a µECoG array in combination with µLEDs that were placed on the insulating substrate between opaque electrodes. Other options are stacked optrodes. Optical waveguides are embedded in alignment with opaque electrodes and evoked spatially confined signals (Yamagiwa et al., 2015).

We ruled out pure light artifact-related signals first by *in vitro* light simulation of the µECoG array. Targeting the PI layer between metal electrodes did not produce considerable artifacts. Second, we stimulated optogenetically through the array in the non-opsin expressing contralateral hemisphere. This did not result in a large-amplitude response. However, a small response occurred, which is discussed in the following paragraph.

Optogenetic response in the non-viral injected contralateral hemisphere

We observed a small response in the contralateral non-injected ChR2 hemisphere. Two possibilities explain that response:
1.) A small contribution of light-induced artifacts by stray light onto electrodes. 2.) Long-range ChR2 expression of projection neurons into the contralateral visual cortex.

The viral vector carrying the opsin was injected into three different depths. The result was an expression across all cortical layers. However, the expression is not only restricted to the somata at the injection site. The adeno-associated virus serotype we used also results in an anterograde ChR2 expression in axons and terminals (Haery et al., 2019). The amount of expression at axon terminals is usually much lower than at the injection site. Lower expression results in a significantly reduced ECoG signal amplitude.

Small cortical temperature changes have been shown to modulate neural activity (Owen et al., 2019). However, the stimulation length and power were too low in our experiments for a relevant light-induced temperature change (Arias-Gil et al., 2016).

2.3.6. Reduced thickness increased conformability

The reduced array thickness not only increases transparency for optical access but potentially improves structural biocompatibility. That is, if the µECoG array's mechanical properties result in enhanced conformability towards the neural tissue. The signal quality of neural devices can be improved by close contact of electrodes and neurons. Further, enhanced structural biocompatibility

can reduce neural damage. In the case of a µECoG array, an easy adaption and adherence to the curvature of the cortex are advantageous. Therefore, conformability is an important factor to consider for advanced neural recording devices.

Our array spontaneously adhered to the cortex. However, flexibility and conformability are difficult to quantify chronically *in vivo*. Therefore, this subsection discusses a simplified thin-film elasto-capillary conformability model. It allows calculating the necessary array thickness to adhere and conform to a defined brain curvature. The model allows comparing our array conformability to that of similar PI-based arrays.

Conformability can be described by the extent of the array's surface area in contact with the brain tissue. Most chronically implanted µECoG arrays need externally applied pressure to conform to the brain tissue. This pressure leads to mechanically induced cortical tissue depression (Minev et al., 2015; Degenhart et al., 2016; Vomero et al., 2020). Thicker µECoG arrays showed increased cortical depression (Vomero et al., 2020). Most graphene and ITO transparent µECoG arrays have an increased array thickness ≥ 25 µm (Kunori and Takashima, 2015; Park et al., 2016; Thunemann et al., 2018). Therefore, they need externally applied pressure for conformability.

Elasto-capillary model

Vomero et al. (2020) used an elasto-capillary model to predict the PI thickness needed to achieve conformability with the cortex. Elasto-capillarity describes the bending of a thin film elastic sheet. Bending occurs in the presence of a wetting liquid only through surface tension and capillary forces.

A simplified cylinder covered with liquid is used as a cortical surface reference. The surface tension of the liquid bends a thin polymer film. As a result, the presence of the deformed thin-film sheet reduces the contact area of the liquid with air. Therefore, the surface energy is decreased (Berthier, 2013). This makes it now an energetically favorable and stable state. Energetic gain through surface energy reduction must compete with the bending energy costs. The energetic gain of surface energy reduction must be larger than the costs of the elastic bending energy. Only then spontaneous wrapping of the µECoG array occurs.

The cylindric radius (r) of the cortex must be equal to or larger than the elasto-capillary length (L_{EC}). In that case, surface tension effectively bends the elastomer.

$$r \geq \frac{L_{EC}}{\sqrt{2}}$$

The elasto-capillary length (L_{EC}) is defined by the square root from the fracture of bending stiffness (B) and surface tension of the liquid (γ).

$$L_{EC} = \sqrt{\frac{B}{\gamma}}$$

The formula for the cylindric radius (r) can be rewritten as:

$$r = \sqrt{\frac{B}{2\times\gamma}} \text{ with } B = \frac{E \times t^3}{12\times(1-v^2)}$$

The equation can be solved for the unknown critical thickness t allowing spontaneous bending of the array around a given radius r. The following variables are known: E the Young's Modulus of PI, v the Poisson's ratio of PI, and γ the CSF surface tension value.

Solving the equation reveals that only a PI array thickness of a maximum of 10 µm adheres to the mouse cortex (estimated with a bending radius of r= 3 mm, Thunemann et al., 2018; Vomero et al., 2020). Above the critical thickness, additional external forces are needed. The elasto-capillary energy is not enough to induce enough bending energy. Ji et al. (2018) bent PI arrays with a thickness of 5 µm or 10 µm around a cylinder. The 5 µm array bent successfully without external forces around a radius cylinder of a minimum of 2 mm. The 10 µm array bent to a minimum radius of 3 mm.

Our array with a thickness of 6.5 µm is below the critical thickness to bend spontaneously around cortical curvature in mice. Therefore, it is also suitable for larger brain curvature radii in gerbils and rats. We purposely did not reduce the thickness of the µECoG array below 6.5 µm. Thinner substrates show increased optical thin-film interference effects. Additionally, lower thicknesses develop foil wrinkles and kinks.

We developed a PI-based µECoG array with a high conformability that is improved from previous ones. PI array with similar thickness was developed for macaques and not rodents (Rubehn et al., 2009). A rodent array design had a thickness of 25 µm with an additional SU-8 protective layer (Yeager et al., 2008). This top layer limits its conformability and flexibility. An 8 µm thick rodent PI array is close to the here achieved thickness. However, it uses brittle ITO electrodes and misses chronic *in vivo* stability evaluation (Zátonyi et al., 2018a).

The described flexibility and conformability do not consider high Young's modulus of platinum electrodes. Those could corrupt the flexibility. However, it can be neglected since the total surface area of the stiffer metal is low compared to the PI. Additionally, the chrome-gold-platinum electrode layer is only 450 nm thick. Other factors like the array's footprint and geometry play a more critical role (Vomero et al., 2020).

2.3.7. Cortical depression through plugging forces

The focus of cortical depression usually lies on arrays with high bending stiffness. They require externally applied pressure to conform to the brain and induce cortical depression (Minev et al., 2015; Degenhart et al., 2016; Vomero et al., 2020). Another often neglected component of the head implant is the EIB connector. This subsection highlights that advancements of neural devices go beyond modifications of direct electrode-tissue interactions, a factor we considered during the advancement of the µECoG array.

The pre-amplifier / headstage is plugged onto the EIB of the implanted µECoG array. This is repeated before and after each recording session. The plugging induces substantial mechanical forces onto the dental acrylic head cap. Interestingly, Vomero et al. (2020) revealed that the plugging forces of the electric connector are translated through the dental acrylic headcap, thereby increasing cortical depression. Implanted test arrays without a connector resulted in a lower degree of cortical depression. The interconnects from the EIB to the array can translate the tethering forces (Subbaroyan et al., 2005).

We used headstage connectors that act as zero-insertion force connectors. This type of connector reduces the overall needed plugging force and a secure connection. Often used Omnetics pin connectors need higher plugging forces. Our connectors additionally direct the force sideways instead of vertical onto the head. As a result, we did not observe cortical depression above the implanted auditory cortex.

2.3.8. *In vivo* impedance

This subsection discusses the initial high impedance variability after implantation and the long-term stability of the impedance. Chronic *in vivo* impedances can provide information about the electrode-tissue interactions but also about potential technical failures like delamination. An assessment is therefore indispensable for chronic evaluations of implanted neural devices.

We observed increased *in vivo* impedance values for the first days after implantation compared to *in vitro* saline measurements before implantation. Acute inflammation and craniotomy-induced damage are possible explanations. We observed hematomas due to µECoG implantation. Sealing the craniotomy with a glass coverslip allowed to exemplary show this effect in an animal. A similar phenomenon was reported by Schendel et al. (2013). Hematomas can change tissue conductivity and explain the higher impedance variability in the acute implantation stage.

Impedances decreased and stabilized after two weeks until the end of the experiments. The following factors are possible contributions to the impedance drop: changes in electrode surface chemistry, degradation of electrode adhered proteins picked up during surgery, and changes in the surrounding dura.

Vomero et al. (2020) showed that thick PI µECoG devices (12 µm) after three weeks of implantation showed increased *in vivo* impedance. Arrays with a thinner PI substrate showed lower values (8 µm). The thicker substrate was also more likely to flatten and detach from the brain surface. Chronically we observed low and stable impedances, which leads to two interpretations. First, the array adherence to cortical tissue allowed a stable connection. Second, the flexible thin-film PI array

prevented major chronic inflammation and glial encapsulation. Chronic inflammation is discussed more intensively in a later subsection: 2.3.10. Neuroinflammation within this discussion section.

In a PBS *in vitro* aging soak test, we did not observe impedance changes after prolonged soaking. Therefore, we excluded delamination and shortening of the electric contacts as a cause of impedance lowering. Impedance values were for most but not all electrode sites below 1-2 MΩ for longer than the depicted three-month period (data not shown). Even higher impedance values in the MΩ range are to some extent acceptable. Because of the voltage divider effect, the signal loss is insignificant. This phenomenon was introduced in the subsection: 1.5.4. Noise: Impedance reduction of the introductory section: 1.5. Abiotic properties of signal quality.

2.3.9. Chronic recording stability

This subsection discusses the chronic recording capability of different µECoG arrays: first, using transparent ITO and graphene, followed by more similar arrays to ours. Chronic recording stability is of major importance for neural devices intended to record during long-lasting behavioral learning experiments. Ultimately, knowledge gained from rodent research can be used for chronic human brain-machine interfaces.

Some components of the chronically recorded ERP might change more significantly over time than others. The last paragraph of this subsection discusses the origin of the more prominent changes of the late ERP components. This highlights that chronic signal changes are not necessarily related to the impact of the electrode itself.

Transparent electrode signal quality

Previous transparent µECoG electrodes show limitations in long-term *in vivo* studies. The longest published recording time for graphene is 70 days (Park et al., 2014). ITO electrodes are limited to acute recordings or implantations in the range of days (Kwon et al., 2013; Kunori and Takashima, 2015; Zátonyi et al., 2018a). Therefore, our transparent metallic µECoG array surmounts alternative transparent µECoG array designs.

Chronic signal amplitude of polyimide metal arrays

The P1 to N1 peak amplitude of the tone evoked ECoG signal was ≈ 70% after three months. Biocompatibility and signal quality cannot exclusively be attributed to the array design. However, technical parameters like Young's modulus and bending stiffness have a significant influence on the long-term recording success. Many other variations in surgical procedures, model animals, implantation location, post-surgery pharmacological treatment make a comparison of signal amplitude across studies difficult. The same µECoG array can be implanted for longer durations if all biological parameters are optimized. Electrode failure, corrosion, EIB damage, and insulator delamination can be pinpointed to array design failures. We did not observe such failures after µECoG array explantation.

Chronic signal stability is defined arbitrarily across studies. The ratio between background noise and distinctive neural response is defined as the SNR. This ratio is defined arbitrarily, and its

calculation differs between studies. Therefore, a universal comparison is not possible. In this subsection, only an approximate comparison of chronic signal quality across µECoG arrays is discussed.

Durations of *in vivo* recordings of rodent µECoG arrays range from weeks up to a year (Henle et al., 2011; Slutzky et al., 2011; Toda et al., 2011; Khodagholy et al., 2015; Woods et al., 2018).
It is essential to distinguish between the accelerated *in vitro* lifetime test of an µECoG array and the *in vivo* lifetime. Accelerated *in vitro* aging revealed lifetimes of between 4-7 years for PI-based arrays (Woods et al., 2018). Young's modulus of PI increased only slightly within 20 months (Rubehn and Stieglitz, 2010).
Epidural rodent PI-based µECoG arrays were recorded for up to three months in the auditory cortex (Yeager et al., 2008) and somatosensory cortex (Vomero et al., 2020). Subdural implantation in Rhesus monkeys allowed signal quality to be stable for 3.5 months (Rubehn et al., 2009).

Overall, our µECoG array chronic signal stability is in the range of previously published PI arrays. The chronic recording is significantly improved compared to transparent ITO and graphene electrodes.

Variations of the late ECoG components

We observed a change in ECoG response shape early in time. For example, the P2 component of the ERP declined considerably. Both P2 and N2 components revealed a higher variability across recording sessions.

We and others observed an apparent difference between the early P1/N1 components and the late P2/N2 components. Early P1/N1 components showed a clear focal tonotopy for pure tone frequencies. The later P2/N2 components did not reveal such clear tone representation at different electrode locations. This difference in components was described previously (Ohl et al., 2000a). It is also evident in the visual systems. The N1 component is sensitive to properties like contours and orientation, whereas the P2 is not (Machilsen et al., 2011). Devonshire et al. (2010) also observed a higher P2/N2 amplitude variability in acute recordings.

The neural origin can explain the higher variability of the late P2/N2 components. Current source density analysis and topographic recordings revealed the thalamocortical origin of the P1 component (Ohl et al., 2000a; Castro-Alamancos and Oldford, 2002). The thalamic neurons onto pyramidal neurons of the granular and infragranular layers. Volume conduction through extracellular space allows epidural ECoG recording of this deeper layer thalamocortical input (Bruyns-Haylett et al., 2017).

The later P2/N2 components are also hypothesized to reflect input from thalamocortical connections. However, studies show a large contribution of corticocortical microcircuits as well (Shaw, 1988; Barth and Di, 1990; Brett et al., 1996). This stronger corticocortical influence on later components can result in a larger variability.

These short and long-range intracortical circuits are crucial for spectral integration (Happel et al., 2010). Auditory current source density analysis revealed their importance, especially for neighboring tone frequency representations (Happel et al., 2010). The different origins of early and late ECoG

components are supported by the fact that P1/N1 components are centered on A1. In contrast, P2/N2 components spread to A1 and the secondary auditory cortex (Barth et al., 1993).

Overall, the response shape change of the late P2/N2 components can be explained by a change in intracortical processing. Intracortical processing can be changed over time due to behavioral adaption to the repeatedly exposed passive listening paradigm. Other possible reasons include neural damage and inflammation of superficial cortical layers.

2.3.10. Neuroinflammation

The chronic implantation of an electrode results in a continuous foreign body response. Advanced neural devices should optimally reduce this response. This subsection focuses on the evaluation of chronic glial response.

We evaluated the inflammatory response after chronic µECoG array implantation. Thereby we observed an increase in astrocytic GFAP signal but not microglial Iba1 staining. This finding is in agreement with previous reports with similar time scales (Xie et al., 2014). A thin-film µECoG array also induced only an elevated GFAP but not an Iba1 response (Schendel et al., 2014).

The different temporal patterns of glial activation can be explained as follows. Microglia are active during acute inflammation. They also contribute to the glial scar developing around implanted devices (Salatino et al., 2017). The thickness of the glial scar can be up to hundreds of micrometers. Within hours after implantation, pro-inflammatory microglia secrete cytokines and chemokines (Gulino et al., 2019). This process recruits other immune cells.

Astrocytes are activated in a time-delayed fashion within days and change their morphology. The GFAP is a marker for that change. Astrogliosis is generally longer lasting and contributes to the glial scar. Astrocytes secrete regulatory factors. Those sent negative feedback to microglia, stopping the acute immune response (Min et al., 2006).

The low microglial response reveals the absence of an ongoing acute inflammatory process. The increased astrocytic response shows the presence of chronic glial scarring. Its origin is likely related to the surgery and foreign body response. Reactive astrocytes have upregulated intermediate filaments like GFAP. They are found in the glial scar surrounding the electrode even after years (Schendel et al., 2014; Kozai et al., 2015; Salatino et al., 2017).

We attribute these processes also to a large extent to the craniotomy itself and not exclusively to the presence of the µECoG array. We could, however, not dissociate between surgical and foreign body immune responses. The influence of craniotomy becomes apparent in studies performing craniotomy without electrode placement. Xu et al. (2007) observed glial activation during a craniotomy window surgery but not in a thinned skull preparation. Schendel et al. (2013) observed connective tissue growth and micro-hematomas after craniotomy surgeries without array placement.

2.3.11. µECoG array tonotopic mapping

We intended to use the µECoG array for chronic high-resolution tonotopy mappings. If successful, the µECoG array could be used for studies investigating cortical topographic map reorganization during learning experiments. Such an assessment does not exist and is usually performed by time-

consuming and tissue disruptive recordings with penetrating electrodes, limited to a single evaluation instead of continuous tracking.

This subsection discusses to which extent our µECoG array can be useful for topographic recordings. It discusses the fact that chronic tonotopic resolution degraded despite the array's proven long-term functioning and signal quality. This subsection explicitly highlights the impact of the large craniotomy necessary for µECoG implantations. Therefore, showing that neural device advancements must be accompanied by improved surgical methods.

Acute and chronic tonotopy mapping

The spatial organization of vertebrate sensory neurons is preserved from lower to higher projections. These so-called topographic maps include areas that encode for similar sensory features. All afferent sensory systems and the efferent motor system have topographic maps (Weinberg, 1997). The focus of this work lies in auditory tonotopic maps.

This study aims to use the µECoG array for acute tonotopic mapping that assists the precise localization of the auditory cortex. Additionally, we aimed to use the µECoG array to evaluate chronic sensory map plasticity.

We successfully demonstrated acute epidural recordings of localized auditory frequency bands. We also were able to distinguish A1 from AAF. Cortical representations of nearby tone frequencies overlapped partially. Future smaller electrodes can record activity from a more localized volume.

Chronically, we observed a general trend in tonotopy resolution degradation. A discrete scaling for each recording instead of a uniform scaling over sessions restored the tonotopy. However, in all animals, the evoked signal amplitude of all channels became similar. Tonotopic resolution vanished over time.

µECoG recordings of the auditory cortex did not evaluate tonotopic maps or comment on their long-term stability (Escabí et al., 2014; Ledochowitsch et al., 2015; Insanally et al., 2016; Konerding et al., 2018). This missing chronic tonotopy assessment hints at possible recording difficulties.

Tonotopic mapping was performed previously by many penetrating electrodes in one terminal recording (Polley et al., 2007; Hui et al., 2009; Hackett et al., 2011; Bieszczad and Weinberger, 2012). Penetrating electrodes are highly invasive and damage the blood-brain barrier. Rodent auditory cortex sampling needs up to 100 penetrating wires, which is a slow process that can take up more than 12 hours (Polley et al., 2007). This entails a severe constraint and does not allow chronic tonotopic recordings of awake and behaving animals. Instead, we were able to map tonotopic maps with reduced invasiveness over many sessions.

Chronic tonotopic map recordings are of importance for learning-induced changes of tonotopic maps. The role of the auditory cortex in learning-related changes and cognitive functions is described in the introductory subsection: 1.4.3. µECoG applications: Tonotopic auditory cortex mapping. This subsection discusses several possible hypotheses for tonotopy degradation during chronic recordings.

The impact of craniotomy on topographic map stability

Mapping somatotopy through a thinned skull preparation resulted in longer-lasting chronic stability. Somatotopic maps of forelimb and hindlimb stimulation were recorded up to 38 days post-implantation in rats (Brodnick et al., 2019). This shows much longer chronic stability than our tonotopy.

The thinned skull preparation is less invasive but reveals some difficulties. The signal amplitude is ten times lower compared to epidural recordings. Thereby minor external noise sources will result in severe degradation of the signal quality. Specific *post hoc* referencing strategies were needed. Several other experimental conditions are different compared to our recordings. Somatosensory maps were recorded in a sedated state instead of awake. The somatotopy map recorded by Brodnick et al. (2019) only includes two distinctive sensory inputs that revealed largely overlapping cortical representations. In contrast, we used an array with a higher channel count, smaller inter-electrode distance, and more sensory modalities. Therefore, a topographic degradation becomes easily visible in our recordings of spatially distinctive maps. The degradation of overlapping somatotopy of only two stimuli types is less visible.

However, this dataset points out that the craniotomy's invasiveness has a significant impact. This hypothesis is supported by a lower fluctuation of *in vivo* impedance in the thinned skull preparation. Additionally, GFAP immunoreactivity and dura thickening were not observed during the thinned skull preparation (Brodnick et al., 2019).

Another study adds additional evidence for the surgical impact. Hosp et al. (2008) recorded epidural somatosensory maps in rats during fore- and hindlimb stimulation. They observed similar somatosensory map representations as Brodnick et al. (2019). However, somatotopy map stability was validated only for eight days. This result is identical to our epidural tonotopy recordings.
Another epidural µECoG recording of somatosensory evoked potentials confirmed stability for one month (Gierthmuehlen et al., 2014). They describe a relatively small craniotomy. 3D MRI modeling before surgery allowed precise craniotomy planning. Many possible biological factors and µECoG array design features can impact the topographic map stability. The discussed studies hint towards a craniotomy-related explanation.

Craniotomy induced cerebral edema

A craniotomy results in brain swelling. The primary cause is an abnormal accumulation of intra- and extracellular water, described as cerebral edema. The cerebral edema can only expand within the limited volume of the cranium or closed craniotomy (cranioplasty). The increased intracranial pressure leads to cortical damage.

Several factors contribute to the emergence of cerebral edema. Neural tissue is irritated by the transmission of heat and vibration from the drill tip (Shoffstall et al., 2018). Hemorrhages occur during drilling and µECoG array placement. The large craniotomy window, necessary for µECoG placement, additionally increases swelling. A large exposed cortical area dries out, causing meningeal damage and ultimately neuronal death. The uneven thickness and curvature of the skull above the temporal cortex make drilling difficult.

One hypothesis is that the tonotopic mapping was performed in the already intraoperatively swollen brain tissue. Usually, cerebral edema starts appearing intraoperatively and peaks within a few days. The swelling decreases within a week and goes back to normal within two weeks (Cheng Mei et al., 1959; Venkatasubramanian et al., 2011). The progressive reduction of swelling within approximately a week can cause a temporary detachment or movement of the µECoG array. The cerebral edema changes brain radius and, therefore, adhesive-capillary forces. Brain swelling after large craniotomies ranges from tens of micrometers to 500 µm (Vomero et al., 2020).

We did not evaluate the degree of brain swelling across different time points of implantation. However, the progressive change of the cerebral edema can be one explanation of the relatively fast tonotopic degradation. The time scale of the progressive cerebral edema reduction following the occurrence of tonotopy blurring. The often-observed tissue growth underneath the array and glial encapsulation occur in longer time intervals (Schendel et al., 2013, 2014; Chen et al., 2017b).

Alternative hypotheses for the tonotopy degradation

Other explanations could contribute at least partially to tonotopy degradation. Subdural recordings can acutely result in higher data quality but are susceptible to a more significant chronic damage and inflammation because of their invasiveness. In contrast, currents can spread in epidural placed arrays, leading to highly correlated signals of even distant channels (Insanally et al., 2016). This spread can be led by the dura mater of CSF.

Another contributing factor can be the animal's behavioral state. Animals passively listened to the same set of auditory stimuli over many thousands of trials. Stimuli-specific adaption is a well-demonstrated effect describing the decrease in neural response to repetitive stimuli across very different time scales (Ulanovsky et al., 2003; Von Der Behrens et al., 2009; Taaseh et al., 2011). Adaption, in general, reduces neural activity and attention.

A passive listening task compared to a reinforced learning task could reduce attention and motivation. The influence of cognitive factors like attention on auditory processing has been demonstrated early by Hubel et al. (1959), and similar dependencies have been shown in later studies (Miller et al., 1980; Benson et al., 1981).

This factor would be less important if we would have recorded chronically from anesthetized animals. Anesthesia can create a more coherent synchronized state of neural processing. Such an effect was demonstrated in ketamine anesthesia (Pachitariu et al., 2015; Deane et al., 2020).

Another explanation could be of technical nature. Moisture uptake by the array's substrate leads to cross-links and thus highly correlated signals. We excluded array insulation failures through an *in vitro* soak test. This test showed no significant impedance changes. After removing the *in vivo* electrode array, microscopy pictures did not reveal any apparent cracks or failures of the array.

Rodent auditory research requires a flat frequency response from the speakers. We used a specialized pre-amplifier and speaker for free-field acoustic tone presentation. This approach requires sound waves traveling larger distances through the air. The animal's ears constantly moving and can be directed away from the sound source. A reflected sound wave by the setup wall can already differ in frequency. Thus, a closed-speaker system calibrated to the hearing curve of the individual animal could lead to higher quality stimulations.

2.3.12. Future µECoG array design and recording advancements

We showed several improvements in ECoG recordings with our newly developed µECoG array. This subsection highlights possible future advancements of upcoming versions and also discusses possible surgical adaptions which could increase the chronic recording resolution of the tonotopy.

Electrode transparency and size

Transparency and high electrode density will be important for the future of ECoG devices. Thin metal electrodes provide transparency and good electrical properties. They could be a future direction. Gold nanomesh µECOG electrodes are a promising path that allows sufficient transparency (Seo et al., 2017; Qiang et al., 2018). A transparent bilayer consists of a thin nanomesh gold layer and the conductive polymer PEDOT:PSS. It allowed a light transmittance of around 70% at 550 nm (Qiang et al., 2018). The impedance is approximately one order of magnitude better than ITO and graphene electrodes. The electrode size is also significantly smaller in the range of single-neuron-sized electrodes. In contrast, graphene and ITO electrodes do not allow such a downscaling of the electrode size. They possess conductivity and capacitive limitations (Kwon et al., 2013; Park et al., 2016, 2018; Zátonyi et al., 2020). Transparent nanomesh metals or other ultrathin metal electrodes (Klauk et al., 2000; O'Connor et al., 2008; Yun, 2017) might be a good compromise for future µECoG electrodes. These materials allow miniaturized electrodes. Further, they can incorporate established advantages of conducting metals and transparency. A general reduction in electrode size would be beneficial. A small electrode diameter will be advantageous to achieve a higher sampling of the cortical surface. Additionally, it allows cortical multi- and single-unit recordings (Khodagholy et al., 2015; Bockhorst et al., 2018).

A newer generation of our µECoG array is in development and involves electrodes with a 3D structure. This design minimizes volume conduction and increases the SNR (Deckert et al., 2016a). However, the fabrication process needs optimization and *in vivo* studies need to be performed.

A higher channel count would increase spatial resolution. However, the channel number is limited by the existent pre-amplifier headstages. Otherwise, the array needs to be fabricated as an active multiplexed array with on-site digitization. Such an array was previously described with 360 channels (Viventi et al., 2011). However, it does not fit our flexibility and transparency aim.

Array flexibility

Thinner µECoG arrays are more flexible and reduce the mismatch between the stiffer implants and soft brain tissue. However, reducing the thickness of our µECoG array resulted in unfavorable wrinkles and kinks. Flexibility comes with the tradeoff in mechanical strength. The long-term reliability of thinner substrates is reduced (Ji et al., 2018). Extremely thin substrates are more applicable in acute recordings.

Flexible µECoG arrays developed for rodents can also be an advantage for human applications. The gyrification of the human cortex causes small radii structures. Flexible µECoG arrays that are already developed for such small radii would be beneficial (Baek et al., 2014). Similar flexible arrays

are found in retina (Segev et al., 2004) or spinal cord implants (Minev et al., 2015). Therefore, different designs and inter-electrode spacings of our array can be developed in the future.

Array substrate footprint

Circular holes in the array's substrate can further improve the tissue-array interaction. Vomero et al. (2020) developed an open fenestrated array with a perforated footprint. This µECoG array substrate results in a reduction of cortical depression. Schendel et al. (2013) observed that blood vessels grow through the holes in the array's substrate. In chronic implantations, connective tissue has grown on top of the array instead of below. This effect reduced chronic *in vivo* impedance. Holes also allow drainage of collected blood and fluids below the array. Overall fenestrated array substrates can improve signal quality and longevity. Holes in the substrate would also allow a full light transmittance and insertion of additional penetrating electrodes.

The here developed µECoG array is, however, intended as a precursor of µLED array. Therefore, we aimed to improve structural biocompatibility in a close substrate footprint. This allows the future placement of µLEDs, as previously attempted in different rodent array designs (Kwon et al., 2013; Ji et al., 2018).

Future array modalities

Light can be delivered wirelessly. The µECoG array is a precursor of a future µLED integrated array. Others developed such light integrated µECoG rodent array designs (Kwon et al., 2013; Yoshimoto et al., 2016; Ji et al., 2018). This advancement involves several difficulties. It is not trivial to erase capacitive stimulation artifacts (Deckert et al., 2016b). Tissue heating caused by the mounted µLEDs must be carefully managed and be evaluated *in vivo* (Kwon et al., 2013).

Signals can be recorded wirelessly. A wireless implant would benefit freely moving animal experiments (Chen et al., 2017b; Keramatzadeh et al., 2020). The tethering forces of moving cables act on the acrylic head implant. The wireless recording could prevent these forces and reduce cortical depression (Vomero et al., 2020). The term wireless is misleading since a rodent cannot carry a heavy transmitter. The wired transmitter would be placed near the animal. The implant communicates wirelessly with the wired transmitter. A fully wireless implant like a wearable human brain-computer interface would consist of a wireless implant and transmitter (Luan et al., 2020).

Inflammation reduction

Pharmacological treatment could be a potential solution to reduce neuroinflammation. Microglia activation can be reduced. An adenosine triphosphate hydrolyzing enzyme apyrase and antibiotic minocycline showed promising results (Hayn et al., 2017).

Glia response reduction does not necessarily result in better signal quality (Purcell et al., 2009). Reactive astrocytes of the glial scar are neurodegenerative. However, more recently, reactive astrocytes have also demonstrated neuroprotective effects (Becerra-Calixto and Cardona-Gómez, 2017).

Cerebral edema reduction

A large craniotomy window results in cerebral edema that potentially causes tonotopy degradation. A decompression surgery releases intracranial pressure and is often used in clinical settings. Rodent surgeries often use corticosteroid therapy with dexamethasone to reduce brain swelling. Systemic administration of dexamethasone has an immune suppressive effect leads to a higher risk of infectious spread. However, dexamethasone coated neural probes showed promising results (Zhong and Bellamkonda, 2007).

A cisterna magnum puncture could release intracranial pressure through CSF leakage. It is difficult to learn and, if performed wrong, induces more harm than benefit.

Reduction of the surgery invasiveness

The craniotomy and brain tissue manipulation cause cerebral edema and inflammation processes. Instead, sliding the array through a slit in the cranium would reduce the induced damage drastically. Improved signal quality could be the result. However, this approach does not allow array placement based on vascular or physiological markers. A large craniotomy window is indispensable if the exact location of A1 is required. In the Mongolian gerbil, characteristic vascular markers are used for differentiation between A1 and AAF. We experienced that those anatomical markers did not correlate with the individual tonotopy maps. Factors like age, weight, and prolonged inbreeding play a considerable role. We did not evaluate the A1 position systematically. However, we observed a higher variability of previously described A1 coordinates in the Mongolian gerbil (Thomas et al., 1993; Ohl and Scheich, 1996; Budinger et al., 2000).

Acute subdural recordings result in a better ECoG recording quality (Insanally et al., 2016). It is questionable if subdural placement would advance chronic signal quality. They are more invasive and impose a higher risk for negative implant-host interactions and a disruption of the cortical area. Because rodent meninges are very, the arachnoid and sometimes pia mater are also often accidentally cut during a durotomy.

Machine learning classification of µECoG data

We could not successfully record tonotopic maps with our µECoG array for more than a week. However, machine learning could potentially find patterns to resolve the tonotopic gradient from ECoG time series even after a visible signal degradation. Artificial intelligence algorithms could

potentially help classify tones based on the ECoG data. These approaches are also of major importance for the development of brain-computer interfaces.

Our ECoG data set was analyzed on a side project in collaboration with the faculty of computer science of the Otto-von-Guericke University Magdeburg (Prof. S. Stober, Sina Meier). The computer scientists aimed for an improved prediction of auditory stimuli based on the µECoG time series.

A baseline support vector machine learning algorithm did not result in a successful chronic classification above the duration of tonotopy stability. Similar low classification accuracy of auditory ECoG signals was observed in supervised linear classifiers from other groups (Insanally et al., 2016; Woods et al., 2018). Accuracy in those classifiers dropped drastically within the first days of epidural awake implanted animals.

Analyzing our dataset with two different deep learning models did also not allow an improved stimulus classification after tonotopy degradation. This is highly attributed to the limitations of the ECoG datasets. Current deep learning algorithms depend on extensive datasets for training. However, in neuroscience, the number of animals and training sessions is limited. Additionally, the tonotopic ECoG data has high inter-subject variability. The exact placement of the array results in significant varying patterns, which are difficult for model learning. However, a temporal introspection revealed that a parallel convolutional recurrent network but not a cascade convolutional recurrent network algorithm focused on time series pattern at the tonotopic P1 and N1 waves of the ECoG time series. The parallel convolutional recurrent network model prediction more often resembled the recorded tonotopic activation. These insights can help for future improvements of deep learning algorithms for ECoG datasets.

3. Part 2: A CUSTOM MADE OPEN-SOURCE MULTI-TETRODE MICRODRIVE FOR COMBINED ELECTROPHYSIOLOGY AND OPTOPHYSIOLOGY

Parts of this microdrive chapter are published in the journal of neural engineering (Brosch et al., 2021) and extended by a more detailed description of the setup and application of the custom-made head-fixed behavior setup.

3D printing files, detailed step-by-step assembly description, parts and, material list, cost estimation, and further information are available at the TetrODrive GitHub repository: https://github.com/MarcelMB/TetrODrive.

Overall, this chapter includes work that started from scratch by developing the neural recording device and the behavioral setup. It includes developing details like a head-fixation plate, testing behavioral setup components like finding the right solenoid for water reward delivery, testing transgenic mouse lines, and many details that arise in establishing a new device and behavioral setup.

3.1. Materials and Methods

3.1.1. Tetrodes and optical fibers

Approximately 40 cm of tungsten wire (12.5 µm diameter, HFV insulation, California Fine Wire Company) were twisted into a tetrode using an Arduino-based twister (Open Ephys). The twisted wires were heat-fused by a heat gun (temperature: 220 °C) from three sides. Eight of these tetrodes were attached to a custom-made EIB (design files in the GitHub repository) with gold pins (Neuralynx). As electrical connectors we use Hirose DF12 plugs on the EIB (Figure 18g). Since they are plugged sideways, they act as zero insertion force connectors, avoiding any plugging forces in the direction of the head. An adapter to convert the Hirose DF12 plug to Omnetics NPD headstage plugs is provided in the GitHub repository together with the adaptor's EIB files. A thin layer of silicone was used as a conformal coating (3140 RTV Coating, Dow Corning Inc.). Following assembly, the electrode tips of the assembled microdrive were lowered into a cyanide-free gold plating solution (31 g l^{-1}, SIFICO ASC) and plated to 150 kΩ (plating current: -0.015 µA, 1 s, 30 runs, NanoZ, Multi Channel Systems).

Two different types of optical fibers were used: regular silica fiber for optogenetic stimulation (100 µm core, 0.22 NA, UM22-100, Thorlabs) and low-autofluorescence fiber for fiber photometry (200 µm core, 0.5 NA, FP200URT, Thorlabs). The fiber was connected to ceramic (optotagging) or steel (fiber photometry) ferrules (1.25 mm diameter) using UV glue (Loctite 4305). The fiber was inserted into a thin furcation tubing with Kevlar fibers (FT900KY, Thorlabs).

3.1.2. 3D printing

The TetrODrive contains two 3D printed polymer parts: the main body (lower part) and the head (upper part). The TetrODrive was printed on a low-cost desktop printer using LCD technology (Photon, Anycubic). This printer hardens successive layers of resin (Cherry, HarzLabs) by transilluminating an LCD panel (50 µm resolution) with UV light (405 nm). The layer thickness was 50 µm. The layer cure time was 90 s for the six bottom layers and 16 s for the rest. The pieces were printed orthogonally to the build plate and on thin supports. During one run (approximately two hours), the printer can print dozens of microdrive parts in parallel. Given the design of the parts, they can be printed on virtually any current resin printer. Filament-based FDM printers are unsuitable, however, due to their low resolution. If no printer is locally available, online 3D print services can be used, or a milling machine can be used. Following printing, parts were briefly washed in isopropanol (<1 min). It is critical to limit dwell time in the isopropanol as it facilitates stress cracking later. Residual liquid was removed from the parts and holes using compressed air. The parts were post cured for 15 min under a UVA lamp and two hours of heating in an oven (50 °C). Design files, 3D files, and complete sliced printer files are available in the GitHub repository.

3.1.3. Animals

All animal experiments were conducted according to the guidelines of the European Community (EUVD 6 86/609/EEC) and approved by a local ethics committee of the State of Sachsen-Anhalt. For electrophysiology and optotagging in combination with classical Pavlovian conditioning, we used four adult male and female (15-25 g) hemizygous C57/B6.SJL-Slc6a3tm1.1(cre)Bkmn/J x C57/B6.129S-Gt(ROSA)26Sortm32(CAG-COP4*H134R/eYFP)Hze/J mice (Jackson laboratory, 006660 DAT-Cre crossed with 012569 Ai32). In these animals, ChR2 is expressed under the control of the dopamine transporter (DAT), labeling dopaminergic neurons (Tritsch et al., 2014; Coddington and Dudman, 2018). For fiber photometry, we used adult DAT-Cre mice (C57/B6.SJL-Slc6a3tm1.1(cre)Bkmn/J). All animals were housed under a twelve-hour light/dark cycle (light on at 6:00 AM). Food and water were provided *ad libitum*, except during the training period when water was restricted to 1 ml per day (Guo et al., 2014), keeping body weight at around 85% of its initial value.

At the end of the experiments, animals were killed with an overdose of pentobarbital and perfused with formaldehyde in 0.1 M PBS (4%). Brains were extracted and cryo-sectioned into 50 µm coronal slices. Slices were mounted in polyvinyl alcohol mounting solution (Mowiol®), and fluorescence images of the recording sites in the VTA were taken.

3.1.4. Microdrive implantation

Anesthesia was induced by 3% isoflurane vaporized in air, followed by an intraperitoneal injection of sodium pentobarbital (60 mg kg^{-1}). Local anesthesia at the surgery site was provided by an injection of bupivacaine hydrochloride (0.25%, 0.2 ml). Mice underwent stereotactic surgery with implantation of a TetrODrive into the left VTA (anterior-posterior: 3.5 mm, medial-lateral: -0.5 mm, dorsal-ventral: 3.9 mm). The microdrive was slowly (100 µm in one minute) lowered within a small craniotomy window (<500 µm diameter) until it reached its final position. Then, a silicone protection

layer was applied around the insertion site, and dental cement was used to form a head cap. Two skull screws were implanted for stability and a custom-made head plate embedded in the dental acrylic for the head fixation during behavioral training. Two reference electrodes (chlorinated silver wires) were placed adjacent to the microdrive insertion site, and two silver ground wires were implanted above the occipital lobe. The EIB was fixated next to the microdrive, mechanically decoupling it from the microdrive body and allowing the plugging of the electrical and optical connectors without bending the drive mechanism and potentially disturbing the electrodes or fiber. Dental cement was applied until it covered most of the lower body of the microdrive. Care was taken to avoid dental cement reaching the metal cannulas or screw, as this would prohibit proper electrode movement. Parafilm® was wrapped around the microdrive, tetrode wires, and EIB for protection. We found this to be a suitable lightweight alternative to a 3D-printed enclosure in mice. Larger rodents may require a sturdier enclosure for the head-mounted parts. We did not use any electrical shielding during recordings apart from the grounded Faraday cage surrounding the setup. Animals recovered for at least one week.

3.1.5. Fiber photometry

The mice underwent surgical procedures, as described above. Before inserting the microdrive, we injected 600 nl of an adeno-associated virus at a rate of 50 nl min^{-1} through a pulled glass pipette (Nanoliter 2000, World Precision Instruments), coding for the fluorescent calcium indicator GCaMP6f (AAV.Syn.Flex.GCaMP6f.WPRE.SV40, $1x10^{13}$ vg ml^{-1}, Addgene) into the left VTA (anterior-posterior: -4.2 mm, medial-lateral: -0.5 mm, dorsal-ventral: 4.2 mm). During the same surgery, the TetrODrive was implanted slightly above the left VTA (anterior-posterior: -3.5 mm, medial-lateral: -0.5 mm, dorsal-ventral: 3.5 mm). Fiber photometry recordings started after three weeks of indicator expression. For recordings, the mouse was placed in the conditioning setup, and a custom-made, pre-bleached, low-autofluorescence fiber optic cable was connected to the ferrule. Excitation light for GCaMP6 was generated by a FiberOptoMeter (NPI Electronic), which also measured the returning fluorescence. The excitation light was modulated with a 66 Hz sine wave using a waveform generator (DG4102, Rigol), and the fluorescence signal was demodulated with a lock-in amplifier (SR510, Stanford Research Systems) to reject ambient light changes. The resulting GCaMP6 signal was digitized at 1 kS s^{-1} using a biosignal recording system (RHD2000, Intan Technologies) and analyzed in MATLAB (The MathWorks). The signal was detrended and filtered with a phase-neutral 20 ms sliding average filter to remove high-frequency noise. The fluorescence was calculated as $\Delta F/F$, where F denotes the average pre-trial baseline fluorescence (1 s before trial start) and ΔF the difference between this resting light intensity and the ongoing signal.

3.1.6. Electrophysiological recordings and data analysis

Broadband signals (0.1-20 kHz, at 30 kS s^{-1}) of head-fixed mice were recorded via the RHD recording system (RHD2132 headstage, Intan Technologies) in a sound-attenuated and electrically shielded chamber. The spikes were detected and sorted using template matching with Kilosort2 (Pachitariu et al., 2016b, 2016a). We used the default Kilosort2 configuration parameters, except for high-pass

filtering, which was changed to 600 Hz, and spike-detection thresholds, which were reduced by half (Kilosort2 threshold setting: [5 2]). Bad channels, which show artifacts rather than neuronal signals due to issues like wire insulation damage, were manually removed. In chronic experiments, no more than two channels per animal were removed. Sorted spikes were manually curated using a python-based graphical user interface (GUI) for electrophysiological data (https://github.com/cortex-lab/phy, Cyrille Rossant, International Brain Laboratory).

The data were analyzed further with MATLAB (MathWorks). We quantified the quality of the chosen single units using isolation distance (separation from neighboring clusters, measure for false-positive spikes) and L-ratio (cluster spread, measure for false-negative events, Schmitzer-Torbert et al., 2005). L-ratio threshold was 0.1 and isolation distance 20 for a cluster to be considered well isolated. Peristimulus time histograms were calculated using 1 ms bins. Histograms were convolved with a function resembling a postsynaptic potential $R(t) = (1 - e^{-t}) \times e^{\left(\frac{-t}{20}\right)}$ (Thompson et al., 1996). Spike waveforms shown in the figures and used for cross-correlation calculation were band-pass filtered (300-6000 Hz). We calculated the peak width of the average waveforms of the highest negative amplitude deflection at half maximum amplitude. These points are more easily identified than the total spike length but naturally result in smaller absolute values. Non-identified units were only used for comparison if also optotagged units were found to ensure comparison in the same subregion. Each trial consisted of a CS (tone) and an US (reward). CS-US ratios were calculated as $CS - US_{ratio} = \frac{CS-US}{CS+US}$. The CS and US ratio values are the difference between the peak firing rate (till 1 s after CS or US onset) and baseline firing rate.

3.1.7. Optotagging

ChR2 expressing dopamine neurons were optogenetically identified by delivering short light pulses and analyzing the latency-locked, light-evoked spikes (Lima et al., 2009; Cohen et al., 2012). Laser light was provided by a blue diode laser (LightHUB-4®, Omicron). Before and after a behavioral session, light pulses (40 repetitions, 5 ms duration, 473 nm) of 5-40 mW were delivered to elicit single opto-evoked spikes. The light intensity was adjusted to keep light-induced artifacts below a threshold of 1 mV and to ensure that the opto-evoked waveform was not distorted in comparison to the spontaneous spikes. We used various criteria to identify dopaminergic neurons, similar to what was applied previously (Cohen et al., 2012): more than 50 percent of light pulses must evoke a light-induced spike, which has occurred in a time window of less than 10 ms post light onset. The cross-correlation of the spontaneous and light-evoked spike waveforms had to exceed r=0.9 to be considered as stemming from the same unit. The energy of the light-evoked spikes is defined as the integral of the squared voltage over time $E = \int v^2 \, dt$. If we did not find optotagged units in a recording session, we advanced the microdrive ventrally by approximately 60 µm and recorded on the following day.

3.1.8. Behavioral task

The behavior setup, water deprivation protocol, training protocols, and training software were established during the period of the dissertation. Water-deprived mice were handled and habituated

to the head-fixation setup for three days without experiencing any reward in the setup. During the head fixation, mice could run on a circular treadmill. Following habituation, the mice underwent a Pavlovian auditory trace-conditioning task. The trial structure consisted of a CS (pure tone, 60 dB, 5 ms onset/offset ramp, 500 ms, 16 kHz) delivered free-field (UltraSoundGate Player 116, Ultrasonic Dynamic Speaker Vifa, Avisoft Bioacoustics) and a 1.5 s delayed US (water reward, 5 µl, 2 s delay for fiber photometry). The tone was quieter than the previously reported tones eliciting dopamine neuron salience responses in primates (Fiorillo et al., 2013b). The water was dispensed by a solenoid valve (The Lee Company) and placed outside the sound attenuated setup in its own sound absorbing enclosure. The lick spout was a blunted syringe needle (gauge 20). Licks were detected through the breakage of an infrared beam in front of the lick spout. If the animal licked within a one second time window right before tone onset, the trial was aborted, and a new trial was initiated. This procedure prevents random licking. The intertrial intervals were computed from a randomly permuted exponential distribution (mean of 10 s, for fiber photometry 20 s). One session typically consisted of 100 to 150 total trials. In ten percent of trials maximum, the US was omitted, and in an additional maximum of ten percent, the US was given without a CS. In selected trial blocks with incorporated CS- or US-omitted trials, the number of those trials never exceeded 30% and never occurred consecutively. If the animals received less than 1 ml water within the session, additional water was given after the session in the home cage to maintain the desired body weight. We controlled our behavioral setup with an Arduino, running a custom code based on previous work (Micallef et al., 2017). The responses were visualized live using a custom MATLAB (MathWorks) interface. Timestamps generated by the Arduino were recorded by the RHD2000 recording system to synchronize behavior and electrophysiology.

3.2. Results

3.2.1. Simplified microdrive construction

This subsection introduces the general design and specific features of the microdrive. It highlights how this microdrive contributes to the overall aim of developing neural recording devices that can find widespread use.

The simple design of the TetrODrive consists of only two 3D-printed parts (head and body) and a few readily available workshop parts (Figure 18a), which makes it producible in any laboratory. It allows to carry up to 8 simultaneously driven tetrodes with one movable fiber in a lightweight (<1.5 g including EIB, electrodes and fiber, Figure 18a, g) and low footprint (27.2 mm^2) design. The assembly takes less than 15 minutes.

The small footprint and light weight allow recordings of juvenile mice, as shown in the following results section. The 3D printing design is open and can therefore be optimized for individual experimental conditions. Parameters like part dimensions or drivable distance (in the current design= 5 mm, Figure 18g) can be modified. Design files of the TetrODrive and EIB are readily available in the GitHub repository (https://github.com/MarcelMB/TetrODrive).

In addition, our system addresses a prominent issue of current microdrives: mechanical coupling of the implant and the preamplifier/headstage at the start of an experiment, which can lead to significant plugging forces transmitted to the implant. This micromovement induces neuronal damage immediately prior to recording, reducing the likelihood of continuously recording the same units across multiple sessions. When the optical and electrical connectors are separated from the microdrive body, plugging and unplugging have no influence on the movable electrodes and fibers (Figure 18h, Figure 19a).

3D printing allows for low material costs. A low-cost desktop resin printer with 50 µm resolution costs around 200 €, which is less than one piece of most commercial microdrives. It can simultaneously produce at least 36 parts in one print, at less than 0.5 € for the two drive parts. The total cost of the fully assembled TetrODrive, which includes the EIB, tetrodes, and optical fiber, does not exceed 20 €. A step-by-step guide for the assembly of the TetrODrive and fiber/tetrode loading as depicted in Figure 18 b-f can be found more detailed in the appendix: 4.1. TetrODrive fabrication.

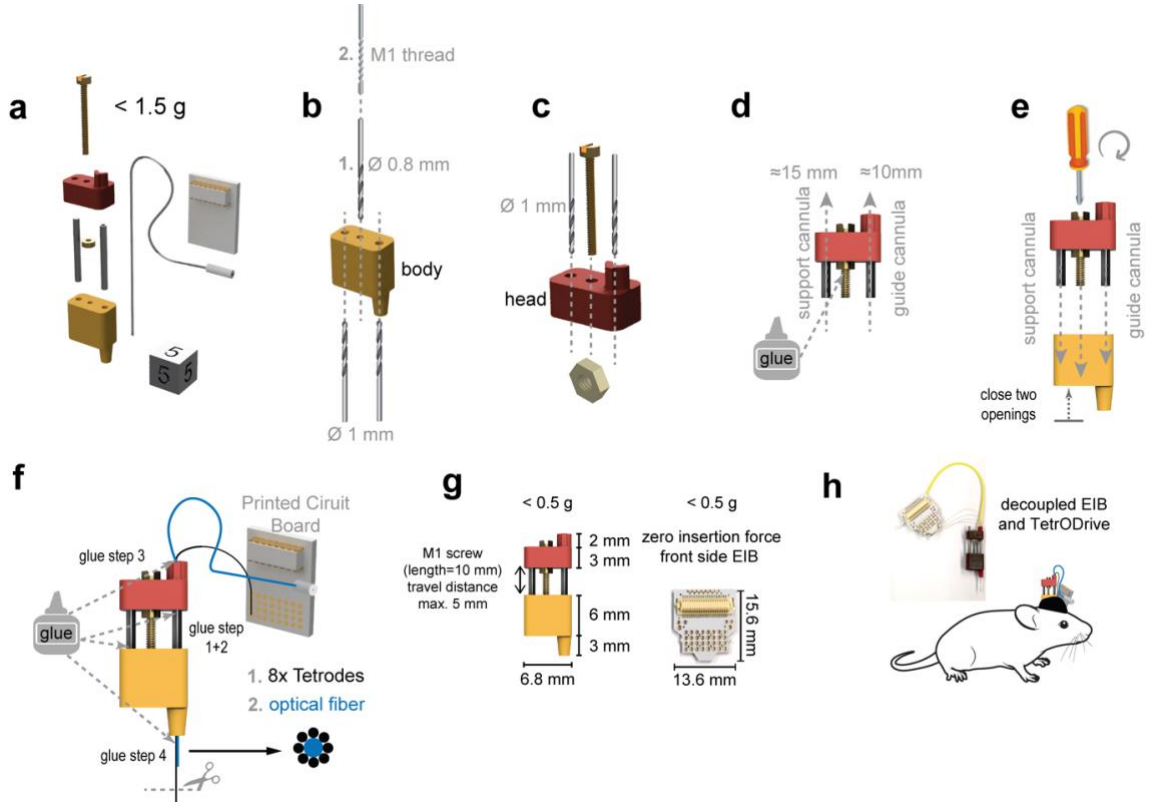

Figure 18 | Assembly and loading of the TetrODrive

a, The TetrODrive consists of two 3D printed parts, one screw, a nut, and two steel cannulas. **b**-**f**, Summarized assembly step. **b**, Holes in the body part are drilled to fit a 1 mm cannula size, and a thread is cut for the screw. **c**, Holes in the microdrive head are enlarged. A screw is inserted and fixed with a nut from the bottom. **d**, The nut is fixed with glue to the screw, and cannulas are inserted from the bottom. **e**, The microdrive head is connected to the body and the screw is turned several turns. The support cannula and screw holes need to be blocked with tape. **f**, The guide cannula for fibers and tetrodes is glued to the head and the support cannula is glued to the body part (glue step 1+2). Tetrodes and fiber are glued to the protrusion on the microdrive head (glue step 3). The tetrodes are fixed with glue to the fiber (glue step 4). Tetrodes are cut to length with sharp, carbide-tipped scissors and later gold plated. **g**, Dimensions of the TetrODrive. The length of the screw determines the dorsoventral travel distance. **h**, Illustration of the TetrODrive implanted in a mouse. Microdrive and EIB are mechanically isolated from each other. Mouse illustration adapted from SciDraw.io. Figure adapted from Brosch et al. (2021).

Mechanical and electrical shielding are important features of chronic implants. A thin layer of Parafilm® was a sufficient and lightweight protection against mechanical damage of the microdrive's outside lying tetrode wires and the optical fiber during unsupervised times (Figure 19b). Electrical noise shielding during electrophysiological recordings was not necessary since the behavior setup was placed in a Faraday cage (Figure 19c).

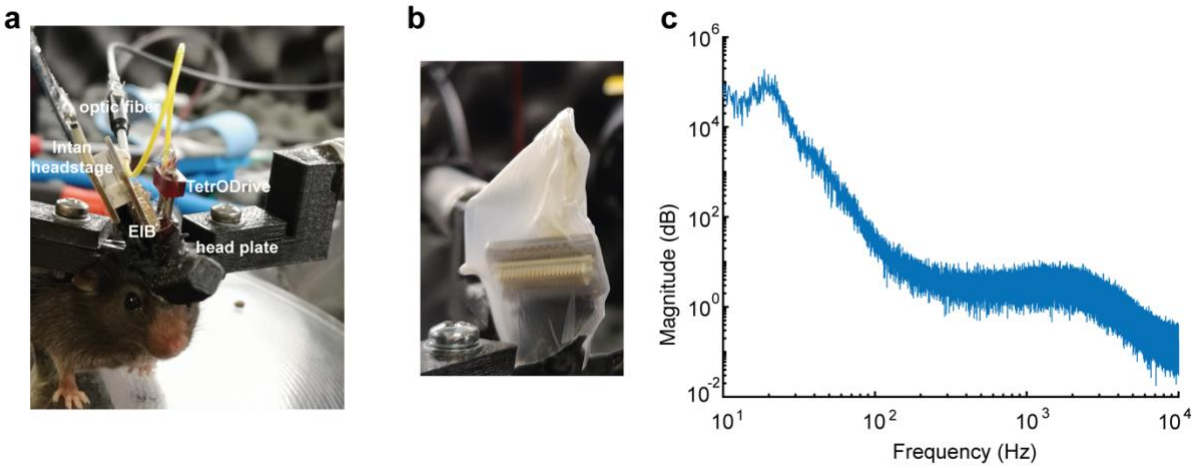

Figure 19 | *In vivo* application of the TetrODrive

a, Frontal view of the implant in the head-fixed behavior setup. The EIB, which carries the connector for the Intan headstage and the ferrule for the optic fiber, is placed adjacent to the microdrive. Mechanical stress from plugging only impacts the EIB, not the body of the microdrive. Both connections are facing to the side or backward to allow lick spout placement in the front. Black dental cement fixates the lower part of the EIB with silicone-covered gold pins and the body part of the microdrive. The head plate protrudes laterally and is clamped to the fixation setup. **b**, The Parafilm® protects the optic fiber loop and tetrode wires from damage. It can be easily removed and reapplied after each recording. **c**, Electric noise floor in a typical *in vivo* recording session. Welch's power spectral density of the unfiltered signal reveals no interference at 50 Hz line frequency or harmonics. This low level of interference is due to the electrical shielding surrounding the setup and careful ground layout. Adapted from Brosch et al. (2021).

3.2.2. Chronic single-unit recordings

The dissertation's focus is to develop neural recording devices with chronic stability of recorded signals. The tetrode microdrive should allow chronic recordings of distinct single units if the tetrodes are advanced continuously but also if tetrodes are stationary.

We recorded single units from tetrodes implanted in the VTA. Exemplary units, sorted in Kilosort2, are depicted in Figure 20a. Auto-correlograms show a clear refractory period, and cross-correlograms have no common refractory period (Figure 20b). Mean waveforms are depicted in Figure 21a, session II-VI, with the same color coding). An average of 5 ± 1 (mean ± SEM) well-isolated units per tetrode and recording session (n= 3 animals, 7 sessions) were found. Units could be recorded for many weeks, particularly if the tetrodes were continuously advanced (Figure 20c). To test long-term recording quality without electrode movement, we recorded from a preparation in which the microdrive had not been moved for six weeks (total implantation time ten weeks). Under these conditions, we still found clear single units, showing large spikes with amplitudes in the millivolt-range (Figure 20d). These large spikes were rather an exception, compared to the typically observed spike amplitudes of 1 mV and below during regular recordings. We find that, if units are lost, moving

tetrode tips forward for about 100 µm ($^1/_2$ turn) results in many new units (Figure 20e). We found it beneficial to advance the electrodes a day before recording, allowing the tips to settle. Particularly due to the relatively thick glass fiber, tissue movement can require some time (Bakhurin et al., 2020). However, this settling period may vary with implantation depth, fiber thickness, and structure of interest and should be experimentally determined for each preparation.

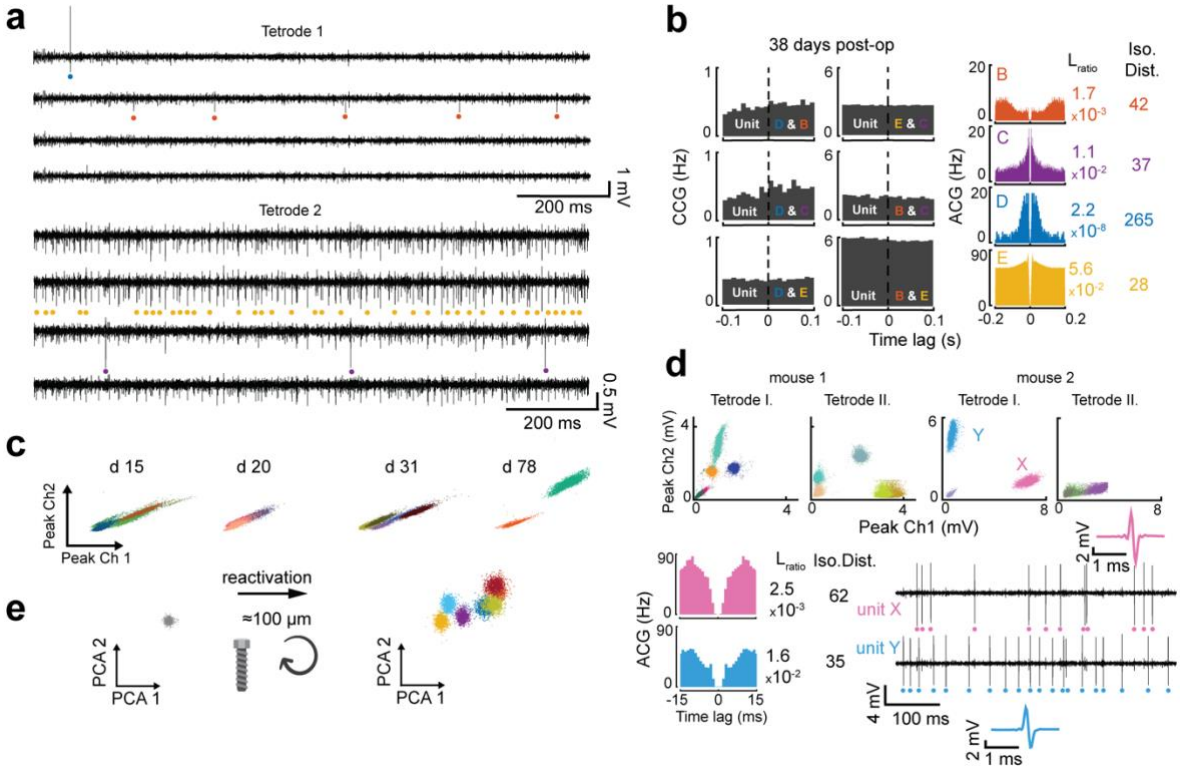

Figure 20 | Chronic single-unit recordings with and without microdrive depth adjustments

a, Band-pass filtered signal from two tetrodes 38 days post-op. Spikes from four detected single unit clusters are color-coded. **b**, Unit quality assessment of spikes in **a**. Only units with low L-ratio and sufficient isolation distance (iso. dist.) were included. Autocorrelations (ACG) for each unit and cross-correlations (CCG) between units demonstrate single-unit separation quality. **c**, Discrimination of single unit clusters during four different time points with microdrive movement between recording sessions. Peak amplitudes of two channels from the same tetrode. **d**, Exemplary remaining single unit clusters in the absence of microdrive movements after 42 days (72 days post-op) for two mice. Band-pass filtered signal, auto-correlogram and mean waveform for two exemplary spike clusters. **e**, Tetrodes that do not show active units after a prolonged time (1 unit / 3 tetrodes) at one position can be reactivated by turning the microdrive screw (7 units /3 tetrodes). (n=3). Adapted from Brosch et al. (2021).

3.2.3. Single-unit stability

It is advantageous for many experimental approaches to record from the same single units for multiple recording sessions and observe firing rate changes while animals learn a task. Therefore, the following results demonstrate the single-unit stability of the TetrODrive across sessions.

The fine thread of the screw and the mechanical decoupling allow precise movement of the electrode tips in the brain and resistance to plugging forces. Figure 21a depicts the two identical units from two tetrodes as Figure 20a and b but shows their evolution across recording sessions. For five consecutive recordings sessions, these units could be followed (Figure 21a, session II – session VI). Waveform correlations remain above r> 0.9 for most units for 5 days (session II - session VI). For example, unit B shows high intra-session and inter-session amplitude stability (Figure 21c, session III and IV). A stable coefficient of variation for interspike intervals (C_v) was an additional measure for unit stability over the recording session (e.g., unit $B_{1\text{-}5}$ and $E_{1\text{-}5}$, Figure 21a). These results demonstrate that TetrODrive can be used to record stable units across multiple days, even if the fiber is plugged and unplugged several times.

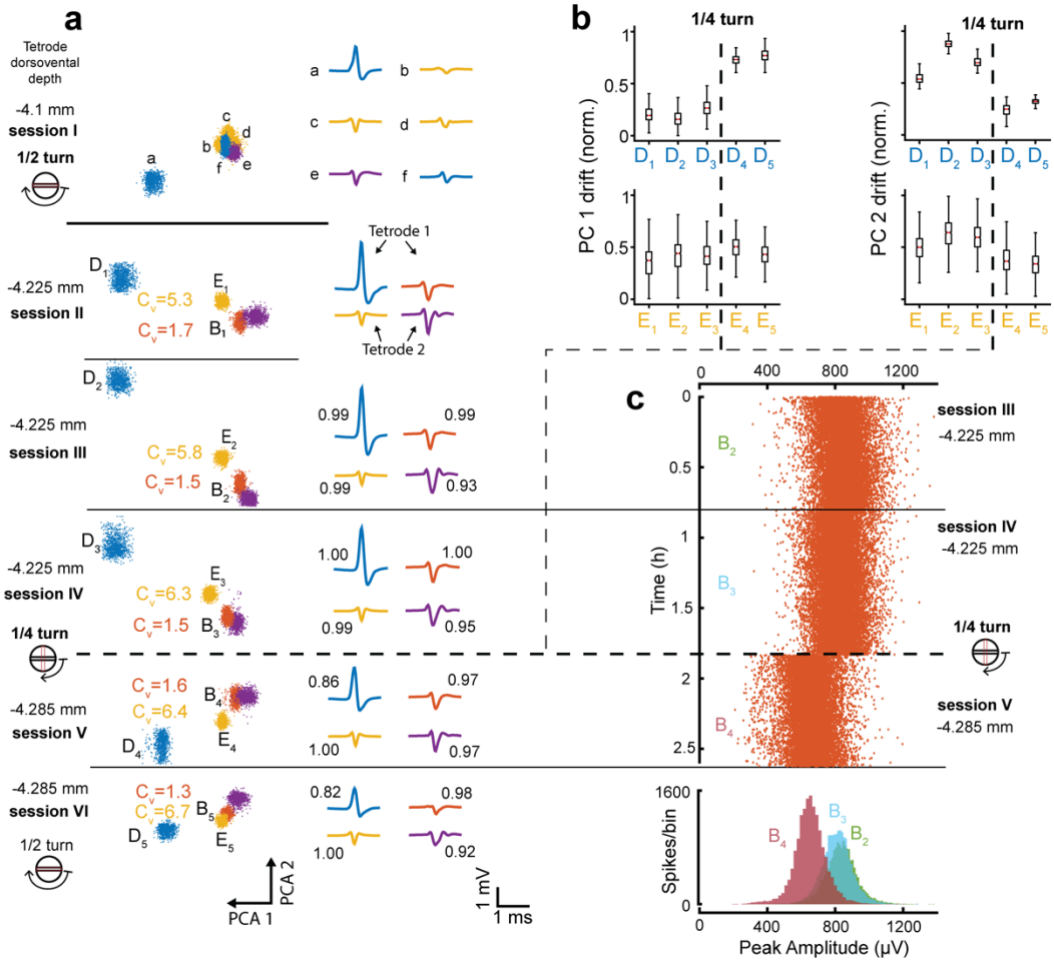

Figure 21 | Precise *in vivo* driving mechanism of the TetrODrive

a, Single-unit stability over consecutive recording sessions (plugging/unplugging connectors) and unit changes due to microdrive movement of four exemplary units. Principal components (PC) 1 and 2 and mean waveform (with cross-correlation of the similar unit from the previous session) of exemplary units. New units were acquired due to depth adjustments of more than 125 µm (1/2 turn) from -4.1 mm to -4.225 mm. Units at depth -4.255 mm were stable over three consecutive recording sessions. An adjustment of less than 60 µm (1/4 turn) resulted in an amplitude shift of the same units without losing them (depth -4.285 mm). **b**, Drift of PC 1 and 2 of unit D and unit E due to 1/4 microdrive turn (60 µm). **c**, Spike amplitudes from

unit B for three consecutive sessions (recording sessions III to V). A 1/4 turn resulted in a slight shift of the spike peak amplitudes on the best channel. (n=1). Adapted from Brosch et al. (2021).

3.2.4. Fine tetrode depth adjustments

The main function of a microdrive is to advance electrodes precisely. This subsection highlights that the TetrODrive is capable of such precise movements.

1/2 screw turn (>125 µm) resulted in new sets of single units (Figure 21a, session I – II). A 1/4 screw turn (<60 µm, session IV – V) moved the electrodes minimally that most units could still be followed with only slight shifts in mean waveform (Figure 21a). The fact that the tip did indeed moved is demonstrated by the change in the principal components of unit D (shift in PC components 1 + 2, Figure 21b, unit D, upper panel) and unit B amplitude change (Figure 21c, session IV – V). For unit E, this shift in principal components is more subtle and only observed in the principal component 2 (Figure 21b, lower panel). These results demonstrate that the TetrODrive is stable enough to keep units over days but can move precisely enough to allow fine, continuous movement through the tissue to find new single units.

3.2.5. Optogenetic identification of dopaminergic midbrain neurons

The development of neural devices combining electrophysiology and optophysiology, as already highlighted in the µECoG array chapter, is a major goal of this dissertation. In this subsection, optogenetic stimulation of the integrated optical fiber in the microdrive is used in combination with single-unit recordings.

We demonstrate the ability of TetrODrive to perform chronic optotagging in the VTA. We expressed ChR2 in dopaminergic cells (Figure 22e) and optogenetically stimulated these cells with blue (473 nm) laser pulses. In dopaminergic cells, this stimulation leads to a single, short-latency spike after the light onset (Figure 22a). Characteristically, such neurons can follow only low stimulation frequencies (Figure 22b). We plotted the correlative relationship between average spontaneous waveform and average optogenetically evoked waveform (Figure 22c) against the light-evoked voltage response, which revealed responsive (blue) and non-responsive (gray) units (Figure 22d). Interestingly, we observed units that showed changes in their response latency to the laser pulse when comparing it between before and after Pavlovian conditioning (unit 1, Figure 22c). Identified dopaminergic units had an average firing rate of 4.8 Hz (range: 1.9 - 9.4 Hz). Mean peak width was 151.6 µs (range: 81.2 - 261.30 µs, full width half maximum). Optogenetically non-responsive single units had higher mean firing rates of 24.9 Hz (range: 0.5 - 71.7 Hz) but similar mean peak width of 150.5 µs (range: 81.8 - 401.45 µs). Non-responsive units were only included in sessions that had at least one confirmed dopaminergic unit to ensure the correct localization of the electrodes.

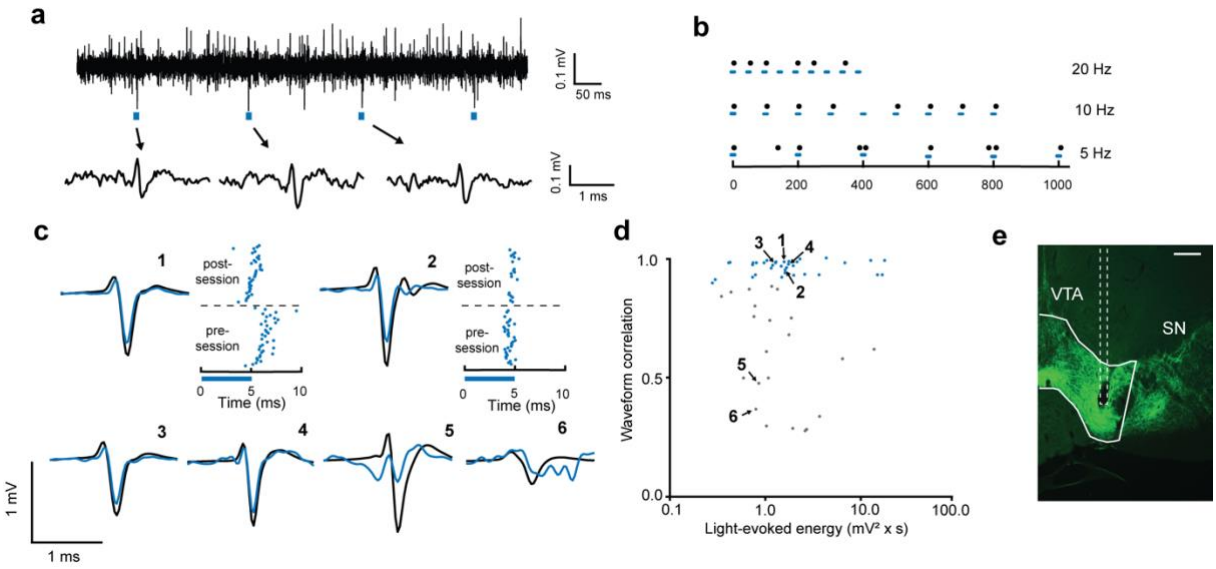

Figure 22 | Identifying dopaminergic neurons in the VTA

a, Continuous band-pass filtered signal. Short light pulses (blue square, 5 ms) elicited a single time-locked light-evoked spike. **b**, Response from an optotagged neuron for 5, 10, and 20 Hz light stimulation. Black dots represent spikes. Blue squares represent light pulses. **c**, Correlation of average spontaneous spike waveforms (black) and average light-evoked waveforms (blue). Raster plot of spikes around laser onset (0 ms) before and after a reward conditioning session. The onset latency of identified units has shifted during conditioning. **d**, Cross-correlation of spontaneous and light-evoked waveform against the light-evoked spike energy. Blue: identified dopaminergic units. Grey: unidentified and non-responsive units. **e**, Exemplary histological slice of fiber and tetrode position in the VTA (green: DAT specific ChR2-eYFP expression). Anatomical structures based on Paxinos and Franklin (2001). Scale bar= 200 µm. (n=4). Adapted from Brosch et al. (2021).

3.2.6. Open-source rodent head-fixed behavior setup

This subsection introduces the development of a custom-built behavior task. We aimed to demonstrate the usability of the TetrODrive in recordings of dopamine neurons during a classical reward conditioning task and focus future research on the RPE. For this reason, a new behavior task had to be established in our working group. The behavior task follows the open-source concept of this chapter. The Arduino code is a modified version of an open-source behavioral task (Micallef et al., 2017). The behavior task can be easily reproduced and modified.

I developed and established an appetitive mouse head-fixed behavior task. The task is primarily intended for auditory Pavlovian reward conditioning but also allows detection and discrimination learning. Behavioral data is shown in the following subsection.

I chose a head-fixation task over a task with freely moving animals for the following reason. In free-moving tasks, reward delivery timing is accurate but the reward consumption is not. In a head-fixed task, reward delivery results in immediate reward consumption. Therefore, reward consumption can be precisely correlated with electrophysiological recordings.

Ensuring recording quality and natural mouse behavior requires a careful setup design (Figure 23b). The behavioral setup was placed in a closed box. The box acts as a Faraday cage, electrically shielding recordings and attenuates environmental sounds. Circuits placed inside the box were

battery-powered, eliminating 50 Hz interference originating from the power grid connection. Acoustic pyramid foam prevented reflection of auditory stimuli.
Many components of the setup are customized by 3D printing or milling. This includes a micromanipulator for lick detector placement, head-fixation clamps, and a circular treadmill. Electronic control circuits for water solenoids and LED indicators are custom-built. Mice were allowed to run on a circular treadmill. All components were fixated with Thorlabs rods which are originally intended to be used for the arrangement of laser setups. This system allowed flexible and stable placement of individual setup components.

The high data throughput electrophysiological acquisition system was connected to a different computer than the one running the behavioral control software (Figure 23a). This reduces central processing unit workload and prevents data stream errors. An Arduino microcontroller is the central hub (Figure 23a). It sends output transistor-transistor logic (TTL) pulses to behaviorally relevant devices like speaker and water solenoid and receives input from the lick sensor. The Arduino software is a modified version of an open-source code released by Micallef et al. (2017). All trial- and behavior-relevant timestamps are sent to the Intan RHD data acquisition board and allow correlation with the electrophysiological data. The Arduino code can be updated by a bidirectional computer communication. Trial parameters can be easily changed, and live executions of the code can be followed. To overcome the limited GUI of the Arduino, I developed a MATLAB GUI. This GUI allows live behavior data monitoring and quick adjustments of all trial parameters. Thereby the core code of the Arduino code script does not need any modifications.

A typical trial structure consists of a pre-trial interval, stimulus, delay time, reward, and consumption time window (Figure 24a). If the animal licks in a period of 1 s before the trial start, a new trial will be initiated after a short waiting time. This prevents random licking. Auditory stimuli are played, and after a short delay, a reward is delivered. Accurate water reward volumes are delivered through solenoid openings. Animals can collect water from a blunt syringe positioned in front of them. Licks are counted as crossings of an infrared light beam.

Mice have a shifted hearing curve towards high frequencies (Gleich and Strutz, 2012). Therefore, I used specialized audio amplifiers and speakers for reliable high-frequency playback (Avisoft Bioacoustics). Arduino-triggered tones revealed a playback jitter of several hundred microseconds. As a result, every trial would have a variant duration. The jitter was mainly related to the inbuild circuit of the Avisoft-UltraSoundGate amplifier. I changed the Arduino code to trigger a sound and wait for a feedback signal. Only when the tone is played does the regular trial structure start. I further tested and modified my custom Arduino code in many iterations. The trial duration varies less than a few milliseconds, ensuring temporal precision.

The Arduino triggered the reinforcement. In the conditioning task, a solenoid allows water flow. The solenoid opening time was calibrated to be equivalent to ≈5 µl. For aversive reinforcement, solenoid opening enables a flow of compressed air. Solenoids were placed outside the setup inside

a separate sound-attenuated chamber. The reinforcement could have been otherwise predicted by solenoid opening click sounds.

Behavioral monitoring included lick detection and video recordings. Lick detection was initially performed by capacitive lick detection. This method produced significant artifacts on the electrophysiological data. The solution was the usage of an infrared beam pointed at a photodetector. The lick detector was carefully calibrated to detect every lick but avoid detection of water droplets or whisker movements.
Event LEDs were invisible for mice but in the camera's field of view. The LED signals allow offline synchronization within recorded video files.

I used laser stimulation for optogenetic tagging of dopaminergic neurons. A National Instruments acquisition board was controlled via a custom LabView GUI (Figure 23a).
The setup was designed to allow easy modifications for future experiments. The Arduino sends signals to the National instruments acquisition board. Therefore, the laser stimulus could be easily integrated into the trial structure. *In vivo* light activation of ChR2 expressing neurons can be used as a cue or reward. In a follow-up detection task, optogenetic stimulation of projections neurons from the lateral geniculate nucleus to V1 acts as a stimulus. Randomly licking is controlled for during no-cue catch trials. The laser stimulation detection task was already further modified towards a discrimination task with two different opsins and lasers.

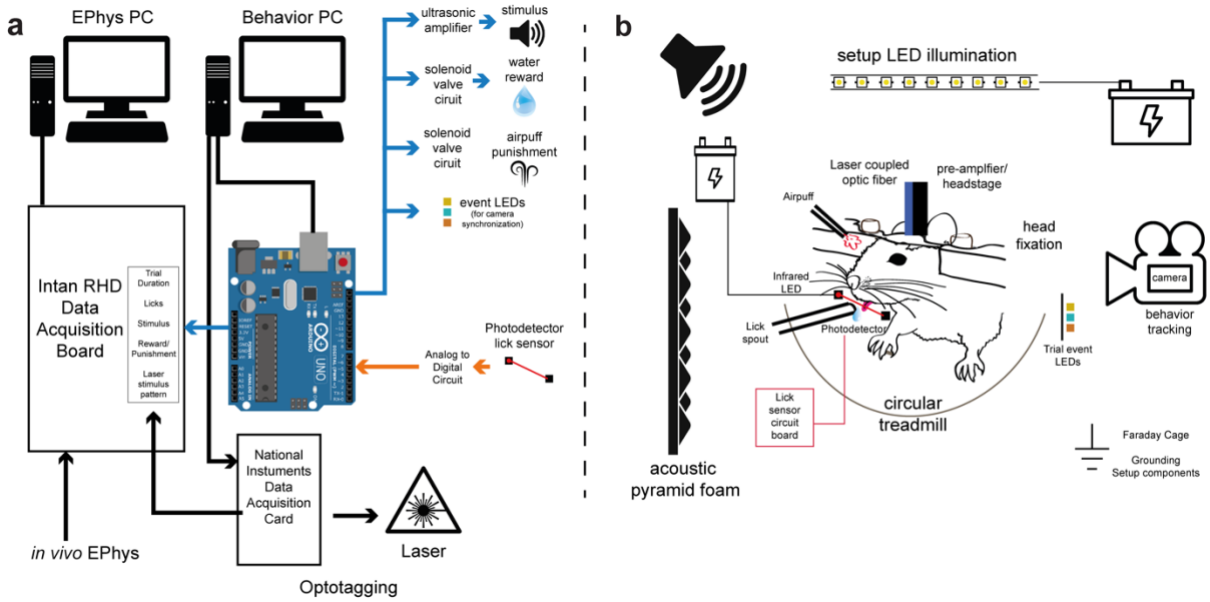

Figure 23 | Mouse head-fixed behavioral setup.

a, Wiring diagram of the Arduino controlled setup. The Arduino receives input (orange) and controls output TTL pulses (blue). It is connected via two-way communication with the computer. A custom MATLAB GUI allows live monitoring of the Arduino commands and adjustments to the trial structure. In this diagram, the laser is controlled by the labview software on the computer. However, it can also be controlled by the Arduino via a National instruments board and, therefore be integrated into the trial structure. All relevant digital time stamps are sent to the Intan Data acquisition recording system. **b**, Lick detection and behavioral setup components. The lick spout is directly placed in front of the mouse. An infrared beam detects single licks. The custom head fixation allows for natural movements. The mouse is allowed to run on a horizontal circular treadmill.

3.2.7. Head-fixed behavior task: Behavioral data

Behavioral data of the mainly used condition paradigm and some pilot experiments towards an operant discrimination task are depicted in this subsection. It highlights that the custom-built behavioral setup can and was already modified to adapt for future scientific questions.

Conditioning

My main aim was to establish a classical Pavlovian reward conditioning task (Figure 24a). During behavioral training, the animals increasingly licked towards the auditory stimulus (anticipatory licking, Figure 24b, c). Anticipatory licking is defined as licking within the time window after tone onset but before reward consumption.

I used trace conditioning instead of delay conditioning. A trace period allows us to observe a shift of dopaminergic activity in the VTA. In the RPE theory, dopaminergic activity shifts from reward towards the reward predicting stimulus.

Operant discrimination

The main behavioral task used within the dissertation is the reward trace conditioning task. Nevertheless, I explored operant behavioral training. I performed initial experiments on an auditory and visual detection task and an auditory Go/No-Go discrimination task.

The initial operant discrimination experiments revealed that an appetitive only approach (reward for successful Go and NoGo) does not allow a good discrimination performance. Instead, a combination of appetitive and aversive reinforcement was successful (Figure 24d). Licking during Go trials results in a water reward, whereas not licking has no reinforcement outcome. Licking during NoGo trials results in an air puff, whereas a correct rejection has no reinforcement outcome. Without the false alarm air puff or an additional reward to the correct rejection, animals licked continuously (learning curves not displayed). In contrast, appetitive reinforcement for the correct Go trial and aversive reinforcement for incorrect NoGo trials resulted in a balanced licking response.

The discrimination task required several pre-training steps, which are described in the appendix 4.2. Pre-training steps of operant discrimination. Subsequently, animals showed a learning performance >60 % in less than ten sessions (Figure 24e).

I used a pseudorandomized Gellermann trial list (Gellermann, 1933). Auditory stimuli consisted of up- or downward frequency-modulated tones (5-25 kHz). Frequency modulated tones produce overlapping cortical representations in the auditory cortex (Ohl et al., 2000b). Unlike pure tones, frequency-modulated tones are auditory cortex-dependent during discrimination learning (Ohl et al., 1999). The task included a trace period between action and reinforcement outcome. Delayed feedback is more likely to involve higher cognitive functions and attention than immediate reinforcement feedback (Han et al., 2003; Leal-Campanario et al., 2006). This made learning considerably more difficult.

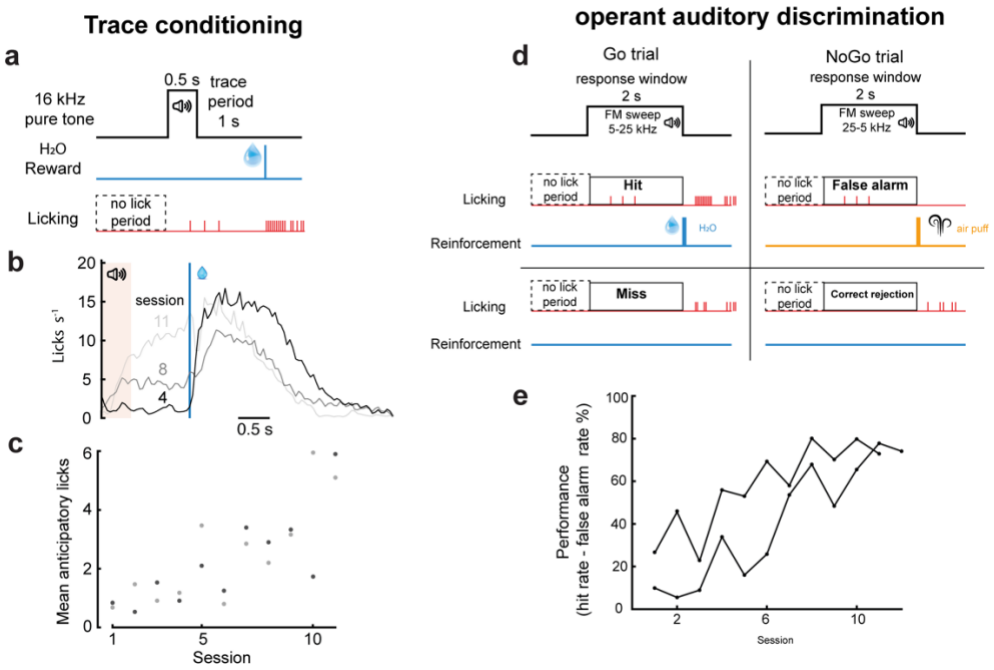

Figure 24 | Reward-based head-fixed behavior

a-**c**, Pavlovian trace conditioning paradigm. **d**-**e**, Operant auditory discrimination task. **a**, Conditioning trial structure. Lick in the no lick period initiates a new trial. **b**, Mean licking to the auditory cue and water reward for the same mouse in three different training sessions. **c**, Mean anticipatory licks (tone onset until reward delivery) for two mice during behavioral training. **d**, Operant discrimination paradigm. During a Go trial, animals can make a hit and receive a water reward or a miss without any consequences. During a NoGo trial, animals can make a correct rejection without any consequences or perform an incorrect false alarm resulting in an air puff. **e**, Learning performance of the discrimination task for two exemplary animals. Performance is defined by hit rate - false alarm rate. Performance over 60% for more than three consecutive sessions is considered good performance.

3.2.8. Reward prediction error in midbrain dopaminergic neurons

The development of the TetrODrive and the behavior task allowed us to assess the RPE of VTA dopamine neurons. This subsection highlights an application of the microdrive and its capability in combining electrophysiology with the imaging of calcium indicators.

Following previous works, we recorded the change in response to anticipated and surprising US (water reward) in the VTA during Pavlovian conditioning (Schultz et al., 1993; Bayer and Glimcher, 2005; Roesch et al., 2007; Cohen et al., 2012). Recording of the same identified dopaminergic single unit over four consecutive conditioning sessions showed an increased response strength to CS but a more diverse response strength to anticipated US (Figure 25a). After the presentation of an unpredicted US, dopaminergic neurons responded strongly (Figure 25b, positive RPE). The omission of a predicted US resulted in a firing rate decrease at the time of the anticipated US, best observed in the raster plot (Figure 25c, negative RPE). We generally observed high diversity of identified dopaminergic unit responses, with some units responding strongly to the US, to the CS, or both, even after extended conditioning (Figure 25d, f). Despite the observed response diversity of dopaminergic units, overall, we observed a shift of response strength from the US towards CS throughout conditioning sessions (Figure 25e, $r= 0.66$, $P<0.001$). The increase in the CS response was less pronounced ($r= 0.52$, $p<0.01$) than the decrease in US response ($r= 0.28$, $p=0.17$, Figure 25f).

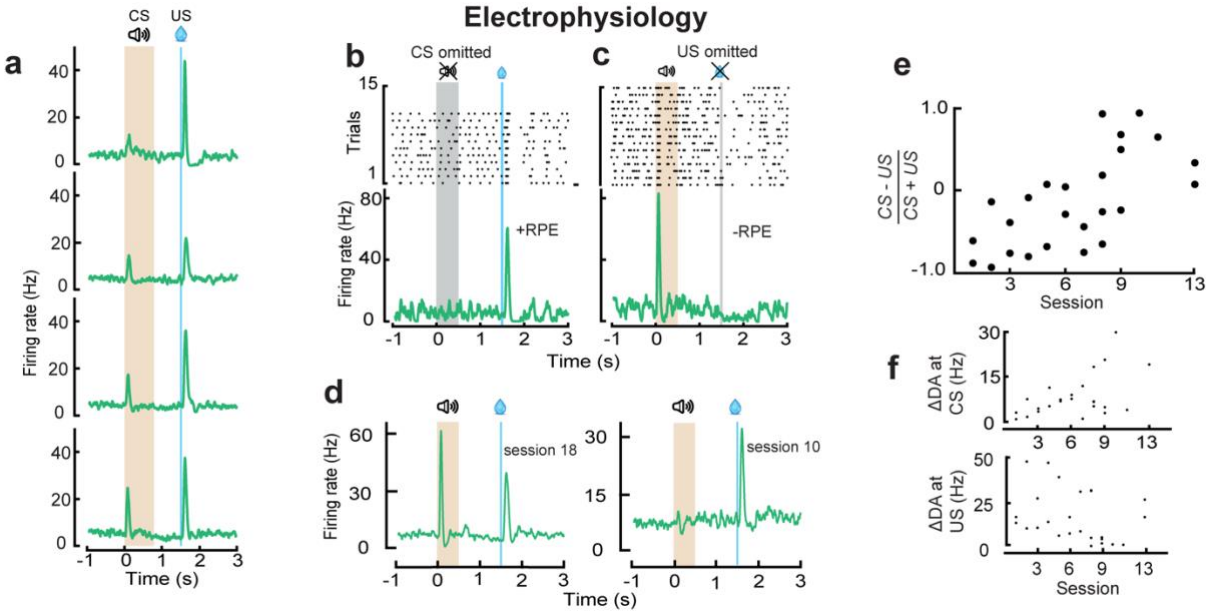

Figure 25 | Single-unit recordings of optotagged dopamine reward prediction error signals

a, Average responses of the same dopaminergic unit over four consecutive sessions. The response to the CS increases over time, whereas the response to the US is not extinguished. **b**, Positive reward prediction error (+RPE) response can be seen following the unpredicted US. **c**, Following extensive training (>18 training sessions with a total of over 2000 trials), cells respond to the CS tone but show a negative reward prediction error (-RPE) at the time of an omitted US. **d**, Average session response of dopaminergic units in two late behavioral training sessions not following traditional RPE. Session 18: Response to the US is still pronounced. Session 10: Response to the CS is not developed yet. **b**, **c**, **d**, depict responses of different neurons. **e**, CS-US ratios for dopaminergic units over the behavioral training. General shift of the response from US to CS. **f**, The average session response firing rate (minus baseline activity) for different identified dopaminergic units at the time of the CS and US as a function of behavioral sessions. (n=3). Adapted from Brosch et al. (2021).

For fiber photometry, we replaced the regular optical fiber in our TetrODrive with a low-autofluorescence fiber. At the initial implantation depth above the VTA, no reward-related fluorescence response could be detected (Figure 26a, position 1). The response magnitude to unexpected water rewards increased the further ventral the fiber was moved (Figure 26a). Once we reached an optimal depth for fluorescence recording, we started the Pavlovian reward conditioning task. In this task, similarly to the electrophysiological experiments, we found a RPE error response to unexpected US (Figure 26b) and a negative RPE response to the omitted US (Figure 26d). In trials with both CS and US presentation, dopamine cells were active (Figure 26c). All photometry findings are compatible with RPE coding.

However, the response to the US was present even after many conditioning sessions and did not shift gradually to the CS. A general response of dopamine neurons towards novel or salient stimuli was tested with neutral tones that were never associated with a reward and did not evoke a response (Figure 26f).

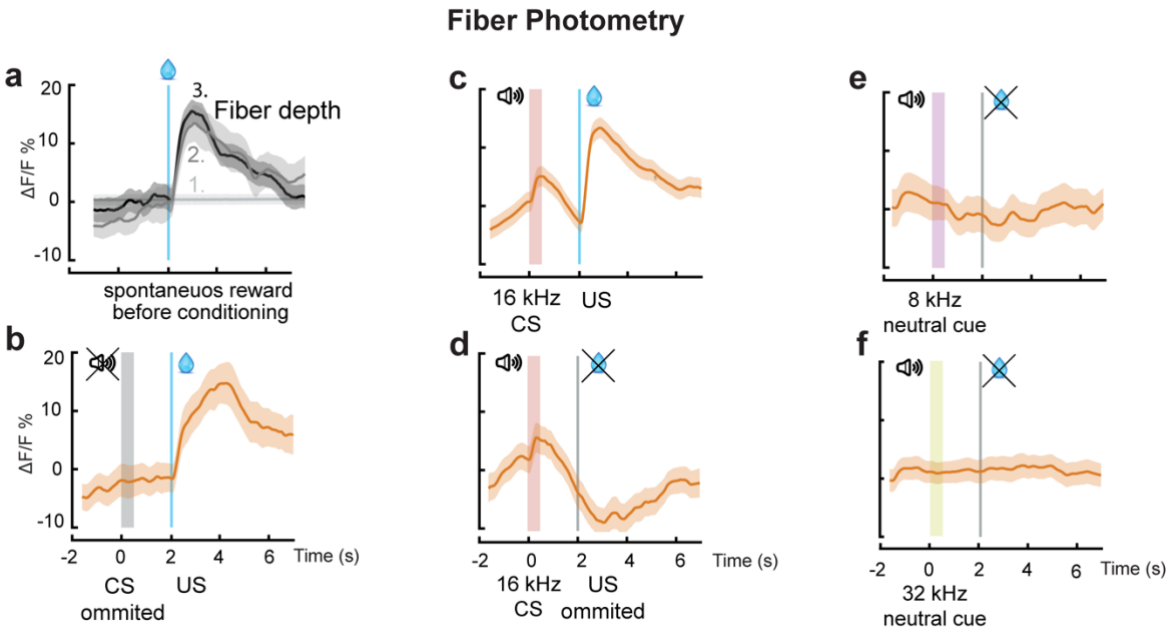

Figure 26 | Fiber photometry of dopaminergic bulk fluorescence revealing reward prediction error

a, Adjusting the fiber tip position can be used to optimize fiber photometry signal amplitude. **b**, Positive RPE in trials with unpredicted US in a trained animal. **c**, Response to the CS and the US in a trained animal. **d**, Negative RPE in trials with a CS, but omitted the US in a trained animal. **e**, Response to an 8 kHz and f, 32 kHz neutral. n=1, data represented as mean ± s.e.m. Adapted from Brosch et al. (2021).

3.3. Discussion

3.3.1. 3D-printed multi-tetrode microdrives

This and the following two subsections (3.3.1, 3.3.2, 3.3.3) discuss the main aims of the dissertation to develop neural recording devices for rodents, which have a simplified production, practical use and allow recordings with improved signal stability.

We developed a 3D-printed multi-tetrode microdrive for combined electrophysiology and optophysiology in mice. The TetrODrive is manufactured from two main 3D printed parts at a low cost (<20 €). The straightforward design allows fabrication in virtually any laboratory. It is compact, lightweight, and provides mechanical decoupling of all connectors from the movable microdrive parts. A movable fiber allows optogenetic stimulation as well as fiber photometry. All design resources are open source.

Most existing microdrives are developed for rats (Keating and Gerstein, 2002; Lansink et al., 2007; Kloosterman et al., 2009; Billard et al., 2018; Lu et al., 2018a; Ma et al., 2019). The body weight of rats is approximately ten times larger, allowing heavier implants. The weight of a head implant should be less than 10% of the animals' weight (Buzsáki et al., 2015).

3D printing has enabled easy customization and allows the incorporation of optical fibers. Optogenetics-enabled 3D printed microdrives for mice fall into two categories: hyperdrives and single-carrier microdrives.

(a) large, complex, and heavy hyperdrives allow the individual manipulation of each electrode (Brunetti et al., 2014; Freedman et al., 2016; Liang et al., 2017; Voigts et al., 2020).
Hyperdrive fabrication and electrode loading take up to several days. Our design is assembled within 15 min. Hyperdrive weight and dimensions can impact the animal's natural head movement and complicate post-surgery recovery.

(b) The TetrODrive is a single-carrier microdrive that drives electrodes simultaneously.
Our design intentionally reduced complexity and, therefore, the ability to drive individual tetrodes. Recordings in the VTA do not require relative movements between individual electrodes. The distance between tetrodes and optical fiber can be pre-defined during fabrication.
However, the TetrODrive will be less useful in hippocampus recordings. Positioning of individual electrodes in such thin cell layer structures is advantageous for a good unit yield (Ulanovsky and Moss, 2007; Pfeiffer and Foster, 2013).

Before 3D-printed parts existed, mouse microdrives were made from customized metal parts. This process needs specialized fabrication equipment and results in heavy designs (Fee and Leonardo, 2001; Korshunov, 2006; Anikeeva et al., 2012). The TetrODrive is the first lightweight 3D-printed single-carrier microdrive with a movable optic fiber.

Previous attempts to incorporate optical fibers complicated the microdrive design. Other mouse 3D-printed designs lack movable fibers (Headley et al., 2015; Kim et al., 2020). A design with a

movable fiber had a significantly increased weight of 4.4 g compared to 0.5 g of the TetrODrive (Delcasso et al., 2018). Juvenile mice have a low weight carrying threshold. Microdrives impair natural head movements needed for eating. Our lightweight design was successfully implanted in juvenile mice.

3.3.2. Driving mechanism precision

An ideal microdrive design moves the electrodes precisely in the micrometer range. Fine electrode movements are dependent on the drive mechanism. On the other hand, electrodes should also remain steady in one position. Stationary electrode stability depends on the resistance to externally applied forces.

3D printed microdrive movement precision

Microdrives should advance electrodes reliably in macro-steps (100-200 µm) and micro-steps (30-100 µm). We recorded single units in the VTA. We showed that $^1/_4$ screw turns resulted in fine adjustment, keeping the same single unit. Only slight changes in action potential amplitude were visible. In contrast, $^1/_2$ screw turns resulted in an acquisition of new single units.

Kim et al. (2020) presented a 3D printed single-carrier microdrive comparable to ours. In this microdrive, new units were acquired after $^1/_8$ screw turns. The drive mechanism is based on a M1.6 screw with a pitch of 350 µm per turn. Thus, a $^1/_8$ screw turn resulted in a travel distance of ≈140 µm less than $^1/_2$ screw turn in the TetrODrive. In other words, Kim et al. (2020) acquired new units with a smaller tetrode displacement. One possible explanation is the different neuronal cell density distribution. Recordings from Kim et al. (2020) occurred in the medial prefrontal cortex. Neuron density in the frontal cortex is estimated to be on average 121.000 ± 52.000. In contrast, we recorded in the VTA with a mean of 14.500 ± 100 neuronal cells (Keller et al., 2018).

The drive mechanism of single-carrier microdrives is similar across different designs. A screw is moved into a threaded hole. The electrode carrier is fixated to the screw and prevented from rotation. This results in a linear up and down motion.

However, the screw, the preparation of the thread, and the mechanism preventing electrode carrier rotation are different for each microdrive (Headley et al., 2015; Delcasso et al., 2018; Kim et al., 2020). Thus, it can result in a different actual travel distance for the same estimated distance. 3D printing resolution does not allow precise thread printing. It leads to variations of linear electrode advancements (Headley et al., 2015). The thread needs to be cut with a tap. However, this process also has its limitations. Successful thread cutting depends on the used printing material. Resin 3D prints must be hardened. Different hardness impacts thread perpetration. The thread is unprecise if the tap is advanced too fast and resin debris is not removed regularly.

A backlash while screw turning leads to an inaccurate linear electrode motion. Inaccurate threads can move electrodes sideways, causing neuronal damage and inflammation. A different but related

phenomenon is observed during changes of drive direction. Hysteresis is a slack in electrode advancement that occurs if the direction of the drive mechanism is reversed. The ShuttleDrive, a hyperdrive design, calculated 0.5–1 screw turns as hysteresis (Voigts et al., 2020).

We validated precise linear movements of the TetrODrive *in vivo*. Small turns result in a shift of single unit amplitude while retaining the neuron. In contrast, larger electrode advancements resulted in new single units.

The accuracy of microdrives can be additionally evaluated with several strategies. Such measurements could additionally be performed with the TetrODrive. Ma et al. (2019) developed a 3D-printed hyperdrive for rats. The error rate of the drive mechanism after 5, 10, or 15 full M1 screw turns is ± 50 µm. A different 3D printed hyperdrive evaluated electrode placement in histological slices. Estimated travel distance and *in vivo* tetrode tracks showed a discrepancy of 200-300 µm (Battaglia et al., 2009). Such a large error rate is critical for use in mice.

Single-unit reactivation

Microdrive adjustments allow recording of new single units even after prolonged stationary phases. We demonstrated that tetrodes that lost the ability to record single units over prolonged implantation time could be reactivated. Recovered recording quality was also observed in other microdrive designs (Voigts et al., 2013; Kim et al., 2020)

Single-unit loss over prolonged implantation times is the result of several factors. The motion between soft brain tissue and rigid electrodes is reinforced through breathing and vascular pulsation. This motion changes the location of neurons relative to the electrode (Gilletti and Muthuswamy, 2006). Additionally, such motion results in neuronal cell death and glial cell proliferation around the electrode (Polikov et al., 2005). Glial cells isolate the electrode from neurons. Glial cell proliferation and migration result in an altered cell distribution around the electrode (Eroglu and Barres, 2010).

The amount of glial sheath around electrode tips was reported to be as thick as 150 µm (Wang et al., 2018). Repositioning of the electrodes allows moving the electrodes out of a glial migration zone. This enables new single units even after several months at a stationary location.

3.3.3. Chronic unit stability

Decoupling of the optical and electric connector

Electrode micromotions make it challenging to record chronically from the same individual neuron. Physiologically induced electrode micromotions are caused by respiration and heartbeat. An important consideration in our approach is the existence of the optical fiber. Tetrodes were glued to the optical fiber and protruded only several hundred micrometers. The optical fiber has a diameter of ≈100 µm and is two times thicker than the tetrode. Tetrodes glued to an optical fiber are less transversely flexible compared to long free-floating wires. The motion between rigid electrodes and soft brain tissue does not allow to keep the same single unit over time.

Externally applied forces can cause interferences at the electrode-tissue interface. The optical fiber connector is typically attached directly to the microdrive. Connecting a light source coupled fiber introduces mechanical forces that translate onto the drive mechanism. Therefore, repeated plugging moves electrode tips. Similarly, the connection of the headstage results in electrode micro-movements. The impact of connector plugging is demonstrated experimentally (Chung et al., 2017). Spike waveforms changed after the electrical connector plugging. The waveforms were stable during recordings, excluding intrinsic neuronal property changes.

A possible solution is the decoupling of the electric connector. We placed the electric connector next to the microdrive and fixated it with dental acrylic. In a different approach, the electric connector was decoupled by placing it in a 3D-printed protective enclosure (Ma et al., 2019). This approach was performed in rats and allowed a large footprint enclosure. Such an approach is difficult in mice which allow only a small footprint and low-weight implants. Similar to other approaches, we used zero insertion force connectors. Those reduce the plugging force and allow horizontal instead of vertical plugging (Freedman et al., 2016). Almost no net plugging force is exerted vertically onto the head.

Decoupling of the optical connector is more complicated. Permanently fixating the optical connector at a distance does not allow fiber mobility. We have fixated the optical connector apart from the microdrive. The fiber is still movable since a thin optical fiber can be placed in a loop. This gives enough clearance to the fiber to be moved. A different microdrive design resolved this issue by developing a mechanical switch (Chung et al., 2017). Optical fibers are secured in a separate enclosure fixed to the skull. After plugging the optical connectors, screws can be loosened, allowing the fiber to move in concert with the electrodes. However, this approach requires a more complicated assembly process and has a larger footprint.

Chronic tracking of individual neurons

Some research questions require continuous recording of the same neurons across sessions. We showed stability of single units for several sessions even when the drive is advanced by micro-movements (< 60 µm, $^1/_4$ screw turn). We demonstrated the stability of the same single units for more than one month if electrodes were kept stationary.

Spike amplitude, spike waveform auto- and cross-correlation, principal components, inter-spike interval coefficient, and firing rate are used to define single-unit stability across sessions. However, spike waveforms (Emondi et al., 2004; Dickey et al., 2009) and firing rates (Hromádka et al., 2008; Mizuseki and Buzsáki, 2013) of the same neuron can be variable across time. Therefore, single neuron tracking can be challenging.

Single-unit stability of other multi-tetrode single-carrier microdrives varies. Such chronic stability depends on many factors and not exclusively on the microdrive design. Factors like surgical perpetration, tetrode material, electrical connector types, recording area play an important role.

Mouse microdrives in a hyperdrive designs show stable recordings for several days (Battaglia et al., 2009; Voigts et al., 2013).

A recently described 3D-printed single-carrier microdrive shows single-unit stability for a maximum of two consecutive sessions (Kim et al., 2020). Other microdrives of this type did not evaluate single unit stability across sessions (Headley et al., 2015; Delcasso et al., 2018).
A different microdrive design shows sample recording with six weeks of continuous single-unit tracking (Anikeeva et al., 2012). The single-carrier microdrive is, however, not 3D printed and has a different drive mechanism where tetrodes are inside a vented screw.

Many microdrives do not allow extended stability. However, microdrives must ensure stable recordings at least within a recording session. This is particularly challenging for freely-moving animals and long-lasting recordings (Anikeeva et al., 2012; Headley et al., 2015).

Single-unit tracking is not the primary use of microdrives. Electrodes fixed to a movable drive mechanism are more sensitive to micro-movements than permanently implanted electrodes. Stationary wire electrode arrays possess longer chronic recordings from the same neurons. However, they do not allow electrode readjustment if previously recorded units are lost.
In macaques, individual neurons could be tracked for weeks up to several months (Tolias et al., 2007; Krüger et al., 2010; Fraser and Schwartz, 2012; McMahon et al., 2014). In rodents, single-units were tracked for several weeks to months (Williams et al., 1999; Freire et al., 2011).

3.3.4. Identification of dopaminergic neurons in the VTA

Subsections 3.3.4 and 3.3.5 discuss one of the dissertation's main aims to develop recording devices that combine electrophysiology and optophysiology. They highlight the necessity of incorporating a movable optical fiber into a microdrive design. In this subsection, the optical fiber enabled optogenetic identification of the recorded neuron types. This subsection discusses the problematic identification of identifying a recorded neurons type. It discusses the benefits, limitations, and possible improvements of optogenetic identification of the recorded single units.

Electrophysiological markers

Characteristic electrophysiological markers are used to define single units as dopaminergic, but the identification of dopaminergic units is unambiguous. Unfiltered waveforms of VTA dopaminergic neurons have a slow firing rate (2-10 Hz) and long spike duration (>2 ms, Ungless and Grace, 2012). The waveform is biphasic and has a distinct negative peak.

High-pass filtering alters the waveform shape. Digital filters process data unidirectional or phase-neutral in forward and reverse directions. Filter frequencies vary between studies. Different filters affect amplitude and waveform (Ungless and Grace, 2012). Filtered waveforms are considered dopaminergic in origin if the spike duration is ≥1.1 ms from waveform start to negative peak (Ungless et al., 2004; Ungless and Grace, 2012). Several studies first identified dopaminergic neurons based on juxtacellular labeling. Alternatively, labeling is performed via antibody staining against the main dopamine limiting synthesis enzyme tyrosine hydroxylase (TH).

Action potentials of identified dopamine neurons display a diverse range of electrophysiological markers that do not fit the above-mentioned criteria (Ungless et al., 2004; Luo et al., 2008; Brischoux et al., 2009; Mileykovskiy and Morales, 2011). The insufficiency of electrophysiological markers has been further demonstrated *in vivo* (Ungless and Grace, 2012) and *ex vivo* in brain slices (Margolis et al., 2006). Therefore, alternative methods for targeting dopaminergic neurons in the VTA are needed.

Optotagging

An alternative to electrophysiological markers to identify dopaminergic units is optotagging. Neurons are optically tagged with cell-specific opsin expression (Lima et al., 2009). Light pulses elicit short-latency spikes. Only dopaminergic neurons show time-locked spikes to the light stimulation. Optotagging became a standard procedure to identify dopaminergic neurons in the VTA (Cohen et al., 2012; Chen et al., 2017a; Mohebi et al., 2019).

The decoupling of the fiber and electric connector allowed stable recordings. As a result, we could record from the same optotagged units for multiple consecutive sessions. Previous studies advanced electrodes during optotagging of dopaminergic neurons after each recording session (Pan et al., 2013; Eshel et al., 2015; Tian et al., 2016; Mohebi et al., 2019; Kremer et al., 2020).

Our optotagging experiments revealed firing rates of <5 Hz for identified dopaminergic units. This finding matches the low firing rate used as an electrophysiological marker (Ungless and Grace, 2012). Surprisingly, the width of the distinctive negative peak in dopaminergic neurons is similar to units of unknown identity. This challenges the assumption that dopaminergic neurons have exclusively long-duration action potentials.

Others observed similar waveform diversity of optotagged dopaminergic single units (Cohen et al., 2012). Optotagged units show a wide range of waveform durations (Mohebi et al., 2019; Hughes et al., 2020). Similar to our finding, the firing rate of dopaminergic units is consistently low.

Our optotagging results, in combination with other studies, confirm that waveform duration is an insufficient dopaminergic electrophysiological marker. In contrast, the average firing rate is consistent. However, the firing rate alone cannot ultimately define a unit as dopaminergic.
Activity is driven mainly by afferents, thus firing rates are state-dependent and variable. For instance, the type of anesthesia changes the firing rates significantly (Marinelli and McCutcheon, 2014).

The firing rate can in theory be used to differentiate GABAergic units with high firing rates (Cohen et al., 2012; Morales and Margolis, 2017). However, glutamatergic neurons have a wide range of firing rates (Root et al., 2018).

Optotagging limitations

Optotagging includes false-negative or false-positive identifications (Lima et al., 2009).

False-negative classification could occur due to low viral expression or insufficient amount of light. The laser power output of the fiber can be decreased by protein adherence or non-visible fiber cracks. Light pulse length and laser power determine light penetration depth and, therefore, opsin activation.

False negatives can be reduced by using the characteristic peak width and firing rate of optotagged cells. Those criteria can be used to mark light insensitive units with similar peak width and firing rate as dopaminergic (Hughes et al., 2020). However, such a classification can be misleading. As previously discussed, the peak width is not a reliable criterion.

False-positive classifications could occur during spike sorting. The photovoltaic artifact can produce artifacts that look similar to spikes and are added during unsupervised spike sorting to certain units. A result is a unit that appears light-sensitive to optotagging but is artifact contaminated.

Additionally, false-positive cells can occur due to low cell-type specificity. TH-Cre promotor lines showed considerable expression in non-dopaminergic (TH-immunonegative) neurons (Lammel et al., 2015). Therefore, we used DAT-Cre mice. Moreover, optogenetically activation of neurons induces postsynaptic action potentials of different cell types. Such polysynaptic activation is expected for excitatory cell identification. Analysis of light-evoked spike latency can reveal such polysynaptically activated cells.

Dopamine neuron diversity

Optotagging cannot dissociate between neurons that co-release different neurotransmitters. Co-release of dopamine and glutamate from distinctive compartments within the same cell (Zhang et al., 2015) or co-release of dopamine and GABA within the same vesicle (Berrios et al., 2016) are known phenomena.

The current cell specificity relies on genetic targeting of DAT or TH. The literature of recent years indicates the existence of many different dopamine neuron subtypes. Single-cell gene expression profiling revealed at least seven different dopamine neuron types (Poulin et al., 2020). This diversity has also been shown in dopamine neurons physiology and connectivity (Bromberg-Martin et al., 2010; Watabe-Uchida et al., 2012; Roeper, 2013; Lammel et al., 2014). Optotagging currently does not allow the differentiation between these subtypes.

Optotagging yield

Surprisingly, we observed a low yield of optotagged units despite sufficient expression of ChR2, which was assessed by an overlap of ChR2-eYFP expressing cells an TH staining. A similar low yield was observed in other studies.

Cohen et al. (2012) found on average four optotagged single units in each DAT-cre mouse during reward conditioning. Less than two dopaminergic optotagged units per animal were found by Kremer et al. (2020). The variability can be as high as 5 ± 4 identified dopaminergic units per mouse (Matsumoto et al., 2016). Similarly, the yield in rats was not more than six optotagged units per animal (Mohebi et al., 2019). The number of recording sessions and electrode channels differed between studies. However, the yield was constantly low.

Increasing optotagging yield

In order to increase the overall surviving yield of animals, optrode implantation should be performed laterally from the bregma-lambda midline. Otherwise, the sagittal sinus can be ruptured with sharp electrode tips, leading to a high mortality rate. We have identified several other experimental parameters for an increased optotagging yield.

We initially performed optotagging by viral injection of ChR2 flanked with double *loxP* sites into DAT-Cre mice (Cohen et al., 2012; Matsumoto et al., 2016; Kremer et al., 2020).
Later we used a double transgenic mouse line that endogenously expresses opsins. Cross-breeding of DAT-internal ribosomal entry site (IRES)-cre mice and Ai32 mice results in the double transgenic mouse line. Their dopamine specificity has been demonstrated previously (Tritsch et al., 2014; Coddington and Dudman, 2018).

We observed a slightly higher yield in transgenic compared to virus-injected mice. Hughes et al. (2020) used the same mouse line and successfully optotagged 15% of all recorded single units. This is a higher rate than the previously mentioned viral vector-injected animals. However, the yield was, similarly to our recordings, inconsistent across animals. Similar large intersubject variability was observed in juxtacellular recordings of the transgenic mouse line (Coddington and Dudman, 2018).

Specific caution must be taken during implantation and successive depth adjustments of the microdrive. Large diameter fibers compress the tissue and destroy a large portion of the neural volume. Thus, optrode implantation must be performed slowly for a deep area like the VTA (≈ 100 µm/min, slower if close to VTA). The optrode should be not lowered to its final position but rather a few hundred micrometers above and then lowered in minimal steps on consecutive days. This very slow lowering is the key to a good SNR (Bakhurin et al., 2020).
Stice and Muthuswamy (2009) showed that initial implantation of electrodes to the final depth increased GFAP levels compared to a stepwise lowering. Debris like the pial membrane, vascular tissue could be already cleared and induce less damage while driving down (Bjornsson et al., 2006).

Optotagged neurons will not appear directly after optrode implantation. Neurons are sensitive to the initially introduced neural damage. Shortly after the electrode implantation, neurons are often silent (Shoham et al., 2006). Activity slowly recovers from the initial insertion trauma over the following weeks to months (Eles et al., 2018). Optotagging is rarely successful if electrodes were advanced on the same day. Therefore, electrodes are driven the latest ≈24 h before recording.

Several light stimulation parameters are crucial. Only light pulse durations >1 ms elicit a reliable time-locked single-unit response for each light stimulus (Mohebi et al., 2019; Bakhurin et al., 2020). We used 5 ms light pulses. Very short pulses (0.1 ms) do not obscure the spike waveform with the light artifact but are insufficient. The laser power must be adjusted for each animal to avoid spike waveform distortions. The electrodes should not exceed the fiber tip by more than 300-500 µm.

3.3.5. Reward prediction error

The microdrive enabled the combination of electrophysiological recordings and optical imaging. Both techniques were used to assess the RPE coding of dopaminergic neurons during classical conditioning. This subsection discusses the dopamine activity we recorded, which is in part divergent from the classical RPE theory but in alignment with other studies. Overall, it highlights the usability and versatility of the TetrODrive for chronic deep brain recordings.

Two decades of research cannot explain how dopamine neurons calculate the RPE (Watabe-Uchida et al., 2017). We are not aiming to answer this question. Nevertheless, the observed dopamine responses are discussed in the light of the existing literature.
Dopamine research history shows a diverse set of dopamine neuron responses that are independent of pure reward predictions. Dopamine plays, for instance, not only play a role in reward-seeking but further in learning behavioral strategies to avoid aversive stimuli (Ilango et al., 2012), since avoidance of a negative outcome itself acts as a reward.

Dopamine neurons fire to stimuli that do not predict a reward. These stimuli are, for instance, loud sounds above 90 dB. Dopamine neurons code a salience response (Fiorillo et al., 2013a). They also respond to novelty: novel stimuli evoke phasic dopamine activity with decreasing responses to stimulus repetition (Ljungberg et al., 1992). Dopamine neurons respond to stimulus generalization. Stimuli that closely resemble previously rewarded stimuli can elicit dopamine firing (Mirenowicz and Schultz, 1996). Initially, all these dopaminergic neuron responses did not fit into the RPE hypothesis but were resolved later (Schultz, 2016).

Even though there is evidence for a significant overlap of dopamine neuron function in VTA and SNc (Ilango et al., 2014; Tian et al., 2016), there is also evidence for a large diversity within each anatomical defined subregion composted of dopamine subpopulations with specialized roles (Lammel et al., 2011; Parker et al., 2016).

Sustained response to the US

In general, our data is in alignment with the RPE theory. With the development of conditioning, the responses to the anticipated US gradually weaken, and responses to the CS grow. We observed, however, inhomogeneity in responses from the identified dopaminergic units. Many units will maintain a strong response to the US, even after prolonged conditioning. This response cannot be easily explained by salience or novelty. Novelty can be excluded by an extensive exposure of the trial components and the behavioral setup. The auditory stimuli were quieter than 70 dB tones that were reported eliciting a dopamine salience response (Fiorillo et al., 2013b; Coddington and Dudman, 2018).

Similarly, Cohen et al. (2012) observed a sustained response towards the US during classical conditioning. Coddington and Dudman (2018) observed a US response that increased initially over

time but decreased only minimally after many thousand trials. They conclude a contribution of movement-related dopamine response during reward consumption.
The sustained US response cannot be integrated into the current RPE theory. Previous data and computed models infer a direct shift from reward to an earlier predictive stimulus (Schultz et al., 1993, 1997; Suri and Schultz, 1999; Day et al., 2007). After repeated tone-reward pairings, the dopamine signal shifts entirely to the cue and disappears from the reward.

An explanation for the sustained US responses could be a long-lasting eligibility trace (Pan et al., 2005). This is one solution to the distal reward problem. An eligibility trace can be described as a form of a memory trace. This memory trace is used to form a link between the stimulus and the later occurring reward. The concept of an eligibility trace has its origin in temporal difference learning models. Responses from early trials remain eligible for the modification by prediction errors of continuous late trials.

In contrast, a short eligibility trace would only allow the reward dopamine response to go back in successive steps trial by trial. Physiologically, this would mean a limitation of learning from one trial to the next but not across a larger number of multiple trials. With long eligibility traces, the signal at the time point of the sensory cue remains eligible for many future steps of RPE signals at the reward outcome. This allows RPE learning over many trials and sessions. A sustained response at the US allows consecutively updating the CS response.

Occurrence of the reward prediction error

A related question is when, during behavioral training, the response shifts from the US to the CS. From the RPE theory, it is expected to co-occur with learning. An associative memory trace is formed between the reward predicting stimulus and the actual reward during learning.

Coddington and Dudman (2018) highlight that this shift of the response is not observed during learning but rather after learning occurred. Notably, several studies trained animals extensively before starting electrophysiological recordings (Hollerman and Schultz, 1998; Kawagoe et al., 2004; Roesch et al., 2007; Pan et al., 2013; Lak et al., 2016; Menegas et al., 2017). When recordings started, new cues or changing of the cue contingency allowed relatively fast learning and, therefore, a shift of dopamine response from US to CS. Dopamine responses can, for instance, adapt quite fast through stimulus generalization (Schultz, 2015).

If instead, naïve animals are used which never experienced an experimental reward, then this shift is not seen early in behavioral training. Coddington and Dudman (2018) observed significant responses at the time point of the CS after the animal learned the task and not in the initial trials. This finding is in agreement with our observations of training naïve animals. We observed responses to the CS over many sessions and never during the initial sessions. Responses like a negative RPE were generally only observed after excessive training and not during the initial sessions. However, we could not continuously track the RPE for each animal and all sessions.

One of our initial aims was to find several optotagged units per animal previous to starting behavioral training and record from those continuously over the length of the entire conditioning. This

would have allowed us to monitor the development of the RPE in the same cells rather than from different dopamine neuron populations as recorded previously. If animals showed optotagged neurons, we managed to record from at least one optotagged neuron over several sessions. However, since yield was low, most animals did not show optotagged neurons at all. Additionally, tracking of an identified dopaminergic neuron never allowed recording over a whole course of the conditioning.

If the RPE does not coincide with initial associative learning, another mechanism must mediate learning. Dopamine neurons get input from a wide range of areas (Watabe-Uchida et al., 2012) and code, for instance, movement initiation signals (Howe and Dombeck, 2016; Da Silva et al., 2018). This suggests a possible Hebbian teaching signal, where coinciding signals within the VTA get strengthened (Coddington and Dudman, 2018).

Limitations of our data

We did not evaluate the influence of motor responses. The influence of sensory motor-related processes on dopamine firing has been investigated extensively within the last years (Howe and Dombeck, 2016; Da Silva et al., 2018; Coddington and Dudman, 2019; Hughes et al., 2020). Phasic excitation occurs during movement initiation. It depicts an early reward-related response before the actual water consumption (Coddington and Dudman, 2018).

Interestingly, most *in vivo* recordings, including ours, aimed at lateral VTA recordings (Eshel et al., 2016; Matsumoto et al., 2016; Coddington and Dudman, 2019). This allows avoiding the medial sagittal sinus during probe insertion. Therefore, medial VTA dopamine neurons could show different responses. The medial VTA dopamine neurons are thought to be functionally more heterogeneous than the lateral ones (Lammel et al., 2014). Dopamine subpopulations differ along the dorsolateral and ventromedial VTA. Those different populations are proposed to mediate different behavioral responses such as salience vs. value coding (Bromberg-Martin et al., 2010). VTA dopamine neurons also have a differential lateromedial gene expression profile (Poulin et al., 2020).

The versatility of TetrODrive was demonstrated in recordings of optotagged dopamine neurons and fiber photometry during classical Pavlovian conditioning. The *in vivo* experiments are used a proof-of-concept in a limited number of animals. For that reason, interpretations concerning the RPE must be seen with caution.

Combining optophysiology and electrophysiology

A movable optical fiber offered some advantages over a stationary implanted fiber. The GCaMP fluorescence is high at the injection site. Fluorescence is more uniform if the fiber is not directly inside the high expression zone but slightly above (Cui et al., 2014). On the other side, if the fiber is placed too far, imaging will not be possible. The fiber can be slowly lowered more ventrally to find the optimal depth. The movable fiber also allows driving away from GCaMP fluorescence originating from already damaged cells, revealing distorted fluorescence transients.

In the fiber photometry calcium signal, we observed similar characteristics of the RPE coding. Those are responding to the CS and attenuated responses to omitted US. Again, we did not find a cessation of responding to anticipated US, even after prolonged conditioning. The fiber photometry data demonstrates the population-level characteristics. It hides, however, the diverse activity of electrophysiologically recorded individual dopaminergic units. For instance, some dopaminergic single units did not respond to the CS even after prolonged conditioning. Such responses cannot be seen in the fiber photometry data. Therefore, fiber photometry results should not be taken as representative for all units in a particular area but interpreted with caution.

3.3.6. Future improvements

The dissertation aims to provide neural devices that can be used readily. Nevertheless, there are always possible improvements. This subsection shows that improvements also concern other areas like developing improved specificity of genetically encoded opsin and gathering more behavioral relevant parameters.

The TetrODrive is a 3D printable, easy to assemble, and open-source microdrive. We provide detailed documentation of the fabrication with additional GitHub online resources with a step-by-step fabrication guide, recommended EIB manufacturing vendors, and all materials/tools. This reduces obstacles for laboratories with less experience in multi-tetrode microdrives. The TetrODrive allows simultaneous electrophysiology and optophysiology. Thus, it is bridging the gap between traditional unit recording and optical methods. The TetrODrive combines a simple design with reliable long-term performance.

Here, head-fixed used of the TetrODrive was preferred over freely moving to control the exact timing of stimulus presentation and reward consumption. Ultimately, the TetrODrive should be tested for recording in freely moving animals. The weight and dimensions are not larger than one-photon miniscopes devices for freely moving imaging (Aharoni and Hoogland, 2019; de Groot et al., 2020).

The open-source design allows everyone to make adaptions. Such modifications can be variations in footprint or dimensions. However, one can also integrate an additional optrode channel or a guide cannula for pharmacological experiments (Delcasso et al., 2018).

The drive manufacturing can be improved. The drive building time is considerably low but can be optimized. Manual tetrode twisting is a tedious process for every multi-electrode array. A new open-source microwire twister with an output of ≈70 tetrodes per hour can increase this process significantly (Newman et al., 2020).

We 3D print the microdrive with a desktop printer using LCD technology. Successive layers of liquid resin are hardened during UV light exposure. However, the repeated use of the screw thread can introduce drive failures. The material is too soft for multiple uses. We do not need reusable microdrives since the production cost and time are low. Expensive silicon probes benefit from a microdrive that allows probe retrieval. More recently, microdrives have been 3D printed with metal (Vöröslakos et al., 2021). Aluminum or stainless-steel microdrives would allow a more durable and long-lasting drive mechanism.

The drive design can be improved. The current footprint of the TetrODrive is 27.2 mm^2, which is comparable to other commercial and custom build microdrives (Vöröslakos et al., 2021). Currently, approximately two microdrives can be used per mouse. The EIB can be shared between microdrives. A smaller design allows the implantation of more microdrives (Headley et al., 2015).
Improved microdrive precision can be achieved with a remote drive mechanism. This includes using a miniature motor (Fee and Leonardo, 2001; Yamamoto and Wilson, 2008) or piezo crystals (Smith et al., 2020).

The drive can be better protected and shielded. Many microdrives use protection enclosures around the microdrive (Headley et al., 2015; Delcasso et al., 2018; Kim et al., 2020). We deliberately did not include a large enclosure to keep dimensions and weight low. Instead, we used parafilm to protect the tetrode wires and EIB. This protected the fragile parts for many months. If the drive is used in larger rodents, mechanical shielding must be developed. A mechanical shielding can also be helpful if stable recordings from the same neurons are required. It allows better protection against external forces that could introduce electrode micromotions.

Our recordings were performed in a Faraday cage, blocking electromagnetic fields. Additionally, care was taken to ground metallic devices, and technical equipment was battery operated. A noisy environment requires electrical shielding. The most lightweight solution is a thin layer of copper foil connected to the headstage ground (Ma et al., 2019).

Non-optotagged single units cannot be separated further. Optotagging could optimally be performed with several cell-specific opsins. For example, viral expression of ChR2 with double *loxP* sited in DAT-Cre mice versus Vgat-Cre mice allowed to compare dopaminergic neurons with GABAergic neurons (Cohen et al., 2012).

Behavioral setup improvements

Dopamine neurons signal movement initiation responses (Coddington and Dudman, 2019). Therefore, tracking movements is crucial. The behavioral setup could be equipped with an acceleration sensor on the circular treadmill. Optimally, movements should be distinguished between forward or backward. Recently, it was found that discrete dopamine neuron populations code for the direction of movement (Hughes et al., 2020). Some movements are not whole-body movements but instead are minor head adjustments. An open-source setup that measures head movements during head-fixed recordings became available recently (Bakhurin et al., 2020).

Further, pupillary reflex or whisker motion of recorded video sequences could be analyzed. Automated deep learning behavioral tracking software like DeepLabCut would assist in evaluating the animal's behavioral state (Mathis et al., 2018).

The discrimination task can be improved. Currently, the discrimination task allows animal's performance to increase without making an active decision every trial. During NoGo trials, correct rejections can simply occur through reduced attention or other distractions. A two-alternative forced-

choice task requires an active decision for every trial (Goltstein et al., 2018). The animal needs to lick on either a right or left spout. Correct performance due to not attending the task is excluded. Establishing such a task is not trivial and needs several pre-training steps. For instance, animals usually develop a bias towards one side. This needs to be counterbalanced by pseudo-randomized trials that favor rewards for the less biased site.

4. APPENDIX

4.1. TetrODrive fabrication

Assembly of TetrODrive

The assembly process requires the following steps: the middle hole of the printed microdrive body is widened with a 0.8 mm drill, followed by tapping for M1x0.25 thread (Figure 18b). Tapping must be done carefully to avoid destroying the fragile threads. The drill should be repeatedly removed to clear forming resin debris from the tap. The two holes holding the cannulas in the body must be widened completely with a 1 mm drill to achieve a precise gliding motion (Figure 18b). It is beneficial to test the drilling result with a piece of later used cannula for smooth movements. All drilling should be done by hand, holding the drill bit inside a small clamp in one hand and the microdrive part in the other.

Following the microdrives body's preparation, the microdrive head is assembled: First, the two outer holes are widened to 1 mm. Then, a 10-millimeter long M1 screw is fastened into the microdrives head's middle hole, and a nut is fastened against the lower side of the microdrive head (Figure 18c). The nut must be tight enough to prevent wiggling, but it must not unduly restrict the turning of the screw. The nut is then fixed to the screw with a tiny drop of UV glue (Figure 18d), Loctite 4305 UV glue). Stainless-steel cannula tubing (1 mm diameter, hollow inside) is prepared for the 10 mm long guide cannula and 15 mm long support cannula. A small grinder (Dremel or Proxonn) with a diamond disk is the preferred solution for cannula cutting. To prevent tetrode damage, cannula ends must be carefully deburred with the diamond disk from the outside and a slightly larger drill (e.g., 2 mm) on the inside. A drill that fits inside the opening can be used to check for remaining debris and obstructions. Both cannulas are inserted into the microdrive head (Figure 18d). We chose affordable and readily available materials for our implementation. Alternative materials can also be used to accommodate non-metric materials. The length difference between the guide and support cannulas is approximately the drivable distance for the TetrODrive (in this case, five mm).

The microdrive head with its guide and support cannulas is inserted into the microdrive body. The screw is carefully turned a few turns into the microdrive body, joining the two subassemblies (Figure 18e). Using a small amount of UV glue, the support cannula now has to be secured in the microdrive body and the guide cannula in the microdrive head (Figure 18f, glue step 1+2). This allows the guide cannula fixed to the head to move up and down using the fixed body support cannula. By turning the screw, thereby moving the head up and down, the correct assembly is confirmed.

The bottoms of the support cannula hole and the tapped screw hole should be blocked with a piece of tape against the ingress of fluids or glue during surgery (Figure 18e). The dimensions and low weight of the microdrive are designed for mice, including juvenile mice used in this study (Figure 18g, h).

Tetrode and fiber loading

Before loading, the tetrodes and fibers need to be prepared as described in the methods section. Tetrodes are inserted into the guide cannula until they protrude a few millimeters beyond the planned

initial implantation depth from the lower side of the microdrive body (Figure 18f). Care should be taken not to damage the tetrode insulation. Following tetrode loading, the prepared optical fiber is inserted into the guide cannula until it protrudes the planned initial implantation depth. The fiber and tetrodes are secured to the guide cannula at the microdrive head using UV glue (Figure 18f, glue step 3). The protruding electrodes are UV glued to the fiber and cut to length using carbide-tipped scissors (regular steel scissors are too soft and can lead to poor tetrode performance, shorts, and coating crosslinks, Figure 18f, glue step 4). We kept the distance between fiber and electrode tips in the range of 300 to 500 µm. Ideally, tetrodes should be equally spaced around the fiber tip and not clustered in one spot. UV glue must not touch the fiber's tip, and only small amounts should be used to keep the implant diameter low. In the last step, the ferrule at the end of the fiber is glued to the backside of the EIB (Figure 18f). The assembled microdrive is now ready for tetrode plating, sterilization, and implantation. Design files of the TetrODrive and EIB are available in the repository.

4.2.Pre-training steps of operant discrimination

After mouse handling and habituation to the head fixation, pre-training steps were necessary. The first train step is a session of a few lick-reward associations. First the animal is motivated to lick with a few releases of water droplets. Later the animal is rewarded for every five licks in a total time of five minutes. The second stage is the Go stimulus training, where the animal gets immediate water if it licked within a specific time window after the Go tone onset. The animals are only trained for maximum of 50 trials in this stage. The next training stage is the first discrimination step, where the tone is presented, and within a two-second response window, the animal's licks are counted. Here, 50% NoGo trials are included, and a false alarm lick results in an immediate air puff within the response window. The reward is delivered after the end of the response window. Only motivated animals are trained with a criterion that three consecutive misses result in a training session termination. If the animal over the session accomplishes 60% correct responses (Hit, Correct rejection), it is transferred to the final discrimination step. Here, the only difference is that the false alarm air puff is now also delivered at the end of the response window. Both reward and punishment are now delayed to the lick response of the animal.

5. BIBLIOGRAPHY

Abdul-Muneer PM, Chandra N, Haorah J (2015) Interactions of oxidative stress and neurovascular inflammation in the pathogenesis of traumatic brain injury. Mol Neurobiol 51:966–979.

Adelsberger H, Garaschuk O, Konnerth A (2005) Cortical calcium waves in resting newborn mice. Nat Neurosci 8:988–990.

Aharoni D, Hoogland TM (2019) Circuit investigations with open-source miniaturized microscopes: past, present and future. Front Cell Neurosci 13:141.

Alzoubi K, Hamasha MM, Lu S, Sammakia B (2011) Bending fatigue study of sputtered ITO on flexible substrate. IEEE J Disp Technol 7:593–600.

Anikeeva P, Andalman AS, Witten I, Warden M, Goshen I, Grosenick L, Gunaydin LA, Frank LM, Deisseroth K (2012) Optetrode : a multichannel readout for optogenetic control in freely moving mice. Nat Neurosci 15:163–170.

Aregueta-Robles UA, Enke YL, Carter PM, Green RA, Poole-Warren LA (2020) Subthreshold electrical stimulation for controlling protein-mediated impedance increases in platinum cochlear electrode. IEEE Trans Biomed Eng 67:3510–3520.

Arias-Gil G, Ohl FW, Takagaki K, Lippert MT (2016) Measurement, modeling, and prediction of temperature rise due to optogenetic brain stimulation. Neurophotonics 3:045007.

Bae S, Kim H, Lee Y, Xu X, Park JS, Zheng Y, Balakrishnan J, Lei T, Ri Kim H, Song Y Il, Kim YJ, Kim KS, Özyilmaz B, Ahn JH, Hong BH, Iijima S (2010) Roll-to-roll production of 30-inch graphene films for transparent electrodes. Nat Nanotechnol 5:574–578.

Baek DH, Lee J, Byeon HJ, Choi H, Kim IY, Lee KM, Pak JJ, Jang DP, Lee SH (2014) A thin film polyimide mesh microelectrode for chronic epidural electrocorticography recording with enhanced contactability. J Neural Eng 11:046023.

Bakhurin KI, Hughes RN, Barter JW, Zhang J, Yin HH (2020) Protocol for recording from ventral tegmental area dopamine neurons in mice while measuring force during head-fixation. STAR Protoc 1:100091.

Bando Y, Sakamoto M, Kim S, Ayzenshtat I, Yuste R (2019) Comparative evaluation of genetically encoded voltage indicators. Cell Rep 26:802–813.

Bao S, Chan VT, Merzenich MM (2001) Cortical remodelling induced by activity of ventral tegmental dopamine neurons. Nature 412:79–83.

Barrese JC, Rao N, Paroo K, Triebwasser C, Vargas-irwin C, Franquemont L, Donoghue JP (2013) Failure mode analysis of silicon-based intracortical microelectrode arrays in non-human primates. J Neural Eng 10:066014.

Barth DS, Di S (1990) Three-dimensional analysis of auditory-evoked potentials in rat neocortex. J Neurophysiol 64:1527–1536.

Barth DS, Kithas J, Di S (1993) Anatomic organization of evoked potentials in rat parietotemporal cortex: Somatosensory and auditory responses. J Neurophysiol 69:1837–1849.

Battaglia FP, Kalenscher T, Cabral H, Winkel J, Bos J, Manuputy R, van Lieshout T, Pinkse F, Beukers H, Pennartz C (2009) The Lantern: An ultra-light micro-drive for multi-tetrode recordings in mice and other small animals. J Neurosci Methods 178:291–300.

Bayer HM, Glimcher PW (2005) Midbrain dopamine neurons encode a quantitative reward prediction error signal. Neuron 47:129–141.

Becerra-Calixto A, Cardona-Gómez GP (2017) The role of astrocytes in neuroprotection after brain stroke: Potential in cell therapy. Front Mol Neurosci 10:88.

Becquerel E (1839) Memoire sur les effets electriques produits sous linfluence des rayons solaires. Comptes Rendus 9:561–567.

Beier KT, Steinberg EE, Deloach KE, Xie S, Miyamichi K, Schwarz L, Gao XJ, Kremer EJ, Malenka RC, Luo L (2015) Circuit architecture of VTA dopamine deurons revealed by systematic input-output mapping. Cell 162:622–634.

Benson DA, Hienz RD, Goldstein MH (1981) Single-unit activity in the auditory cortex of monkeys actively localizing sound sources: Spatial tuning and behavioral dependency. Brain Res 219:249–267.

Berényi A, Somogyvári Z, Nagy AJ, Roux L, Long JD, Fujisawa S, Stark E, Leonardo A, Harris TD, Buzsáki G (2014) Large-scale, high-density (up to 512 channels) recording of local circuits in behaving animals. J Neurophysiol 111:1132–1149.

Berrios J, Stamatakis AM, Kantak PA, McElligott ZA, Judson MC, Aita M, Rougie M, Stuber GD, Philpot BD (2016) Loss of UBE3A from TH-expressing neurons suppresses GABA co-release and enhances VTA-NAc optical self-stimulation. Nat Commun 7:10702.

Berthier J (2013) Droplet on deformable surfaces—elasto-capillarity and electro-elasto-capillarity. In: Micro-Drops and Digital Microfluidics, pp 439–445.

Bieszczad KM, Weinberger NM (2012) Extinction reveals that primary sensory cortex predicts reinforcement outcome. Eur J Neurosci 35:598–613.

Billard MW, Bahari F, Kimbugwe J, Alloway KD, Gluckman BJ (2018) The systemdrive: A multisite, multiregion microdrive with independent drive axis angling for chronic multimodal systems neuroscience recordings in freely behaving animals. eNeuro 5:e0261.

Biran R, Martin DC, Tresco PA (2005) Neuronal cell loss accompanies the brain tissue response to chronically implanted silicon microelectrode arrays. Exp Neurol 195:115–126.

Bjornsson CS, Oh SJ, Al-Kofahi YA, Lim YJ, Smith KL, Turner JN, De S, Roysam B, Shain W, Kim SJ (2006) Effects of insertion conditions on tissue strain and vascular damage during neuroprosthetic device insertion. J Neural Eng 3:196–207.

Bockhorst T, Pieper F, Engler G, Stieglitz T, Galindo-Leon E, Engel AK (2018) Synchrony surfacing: epicortical recording of correlated action potentials. Eur J Neurosci 48:3583–3596.

Brett B, Krishnan G, Barth DS (1996) The effects of subcortical lesions on evoked potentials and spontaneous high frequency (gamma-band) oscillating potentials in rat auditory cortex. Brain Res 721:155–166.

Brischoux F, Chakraborty S, Brierley DI, Ungless M a (2009) Phasic excitation of dopamine neurons in ventral VTA by noxious stimuli. Proc Natl Acad Sci U S A 106:4894–4899.

Brodnick SK, Ness JP, Richner TJ, Thongpang S, Novello J, Hayat M, Cheng KP, Krugner-Higby L, Suminski AJ, Ludwig KA, Williams JC (2019) µECoG recordings through a thinned skull. Front Neurosci 13:1017.

Bromberg-Martin ES, Matsumoto M, Hikosaka O (2010) Dopamine in motivational control: rewarding, aversive, and alerting. 68:815–834.

Brosch M, Deckert M, Rathi S, Takagaki K, Weidner T, Ohl FW, Schmidt B, Lippert MT (2020) An optically transparent multi-electrode array for combined electrophysiology and optophysiology at the mesoscopic scale. J Neural Eng 17:046014.

Brosch M, Vlasenko A, Ohl FW, Lippert MT (2021) TetrODrive: An open-source microdrive for combined electrophysiology

and optophysiology. J Neural Eng 18:046030.

Brovelli A, Ding M, Ledberg A, Chen Y, Nakamura R, Bressler SL (2004) Beta oscillations in a large-scale sensorimotor cortical network: Directional influences revealed by Granger causality. Proc Natl Acad Sci U S A 101:9849–9854.

Brunetti M, Wimmer RD, Liang L, Siegle JH, Voigts J, Wilson M, Halassa MM (2014) Design and fabrication of ultralight weight, Adjustable multi-electrode probes for electrophysiological recordings in mice. J Vis Exp 91:51675.

Bruns OT et al. (2017) Next-generation in vivo optical imaging with short-wave infrared quantum dots. Nat Biomed Eng 1:0056.

Bruyns-Haylett M, Luo J, Kennerley AJ, Harris S, Boorman L, Milne E, Vautrelle N, Hayashi Y, Whalley BJ, Jones M, Berwick J, Riera J, Zheng Y (2017) The neurogenesis of P1 and N1: A concurrent EEG/LFP study. Neuroimage 146:575–588.

Budinger E, Heil P, Scheich H (2000) Functional organization of auditory cortex in the Mongolian gerbil (meriones unguiculatus). III. Anatomical subdivision and corticocortical connections. Eur J Neurosci 12:2425–2451.

Buzsáki G (2004) Large-scale recording of neuronal ensembles. Nat Neurosci 7:446–451.

Buzsáki G, Penttonen M, Nádasdy Z, Bragin A (1996) Pattern and inhibition-dependent invasion of pyramidal cell dendrites by fast spikes in the hippocampus in vivo. Proc Natl Acad Sci U S A 93:9921–9925.

Buzsáki G, Stark E, Berényi A, Khodagholy D, Kipke DR, Yoon E, Wise KD (2015) Tools for probing local circuits: High-density silicon probes combined with optogenetics. Neuron 86:92–105.

Cai DJ et al. (2016) A shared neural ensemble links distinct contextual memories encoded close in time. Nature 534:115–118.

Campbell PK, Jones KE, Normann RA (1990) A 100 electrode intracortical array: structural variability. Biomed Sci Instrum 26:161–165.

Carandini M, Heeger DJ (2011) Normalization as a canonical neural computation. Nat Rev Neurosci 13:51–62.

Cardin J a, Carlén M, Meletis K, Knoblich U, Zhang F, Deisseroth K, Tsai L-H, Moore CI (2010) Targeted optogenetic stimulation and recording of neurons in vivo using cell-type-specific expression of Channelrhodopsin-2. Nat Protoc 5:247–254.

Carlson D, Carin L (2019) Continuing progress of spike sorting in the era of big data. Curr Opin Neurobiol 55:90–96.

Castro-Alamancos MA, Oldford E (2002) Cortical sensory suppression during arousal is due to the activity-dependent depression of thalamocortical synapses. J Physiol 541:319–331.

Ceballo S, Bourg J, Kempf A, Piwkowska Z, Daret A, Pinson P, Deneux T, Rumpel S, Bathellier B (2019) Cortical recruitment determines learning dynamics and strategy. Nat Commun 10:1479.

Chemla S, Chavane F (2010) Voltage-sensitive dye imaging: technique review and models. J Physiol Paris 104:40–50.

Chen G, Zhang Y, Li X, Zhao X, Ye Q, Lin Y, Tao HW, Rasch MJ, Zhang X (2017a) Distinct inhibitory circuits orchestrate cortical beta and gamma band oscillations. Neuron 96:1403–1418.

Chen R, Canales A, Anikeeva P (2017b) Neural recording and modulation technologies. Nat Rev Mater 2:16093.

Chen Z, Cotterell B, Wang W, Guenther E, Chua SJ (2001) A mechanical assessment of flexible optoelectronic devices. Thin Solid Films 394:201–205.

Cheng Mei S, Alvord EC, Berry RG (1959) Swelling of the brain following ischemic infarction with arterial occlusion. Arch Neurol 1:161–177.

Cheung KC, Renaud P, Tanila H, Djupsund K (2007) Flexible polyimide microelectrode array for in vivo recordings and current source density analysis. Biosens Bioelectron 22:1783–1790.

Chung J, Sharif F, Jung D, Kim S, Royer S (2017) Micro-drive and headgear for chronic implant and recovery of optoelectronic

probes. Sci Rep 7:2773.

Chung JE, Joo HR, Fan JL, Liu DF, Barnett AH, Chen S, Geaghan-Breiner C, Karlsson MP, Karlsson M, Lee KY, Liang H, Magland JF, Pebbles JA, Tooker AC, Greengard LF, Tolosa VM, Frank LM (2019) High-density, long-lasting, and multi-region electrophysiological recordings using polymer electrode arrays. Neuron 101:21-31.

Chuong AS et al. (2014) Noninvasive optical inhibition with a red-shifted microbial rhodopsin. Nat Neurosci 17:1123–1129.

Coddington LT, Dudman JT (2018) The timing of action determines reward prediction signals in identified midbrain dopamine neurons. Nat Neurosci 21:1563–1573.

Coddington LT, Dudman JT (2019) Learning from Action: Reconsidering Movement Signaling in Midbrain Dopamine Neuron Activity. Neuron 104:63–77.

Cohen JY, Haesler S, Vong L, Lowell BB, Uchida N (2012) Neuron-type-specific signals for reward and punishment in the ventral tegmental area. Nature 482:85–88.

Cole JT, Yarnell A, Kean WS, Gold E, Lewis B, Ren M, McMullen DC, Jacobowitz DM, Pollard HB, O'Neill JT, Grunberg NE, Dalgard CL, Frank JA, Watson WD (2011) Craniotomy: True sham for traumatic brain injury, or a sham of a sham? J Neurotrauma 28:359–369.

Cramer J V., Gesierich B, Roth S, Dichgans M, Düring M, Liesz A (2019) In vivo widefield calcium imaging of the mouse cortex for analysis of network connectivity in health and brain disease. Neuroimage 199:570–584.

Cui G, Jun SB, Jin X, Luo G, Pham MD, Lovinger DM, Vogel SS, Costa RM (2014) Deep brain optical measurements of cell type-specific neural activity in behaving mice. Nat Protoc 9:1213–1228.

Da Silva JA, Tecuapetla F, Paixão V, Costa RM (2018) Dopamine neuron activity before action initiation gates and invigorates future movements. Nature 554:244–248.

Dávalos A, Castillo J, Marrugat J, Fernandez-Real JM, Armengou A, Cacabelos P, Rama R (2000) Body iron stores and early neurologic deterioration in acute cerebral infarction. Neurology 54:156–1574.

Day JJ, Roitman MF, Wightman RM, Carelli RM (2007) Associative learning mediates dynamic shifts in dopamine signaling in the nucleus accumbens. Nat Neurosci 10:1020–1028.

de Groot A, van den Boom BJG, van Genderen RM, Coppens J, van Veldhuijzen J, Bos J, Hoedemaker H, Negrello M, Willuhn I, De Zeeuw CI, Hoogland TM (2020) Ninscope, a versatile miniscope for multi-region circuit investigations. Elife 9:49987.

Deal PE, Kulkarni RU, Al-Abdullatif SH, Miller EW (2016) Isomerically pure tetramethylrhodamine voltage reporters. J Am Chem Soc 138:9085–9088.

Deane KE, Brunk MGK, Curran AW, Zempeltzi MM, Ma J, Lin X, Abela F, Aksit S, Deliano M, Ohl FW, Happel MFK (2020) Ketamine anaesthesia induces gain enhancement via recurrent excitation in granular input layers of the auditory cortex. J Physiol 598:2741–2755.

Deckert M, Lippert M, Takagaki K, Brose A, Ohl F, Schmidt B (2016a) Fabrication of MEMS-based 3D-µECoG-MEAs. Curr Dir Biomed Eng 2:83–86.

Deckert M, Lippert M, Takagaki K, Brose A, Rathi S, Ohl F, Schmidt B (2016b) A 3D-capable, flexible, hybrid µECoG optrode. In: Front. Neurosci. Conference, 10th International Meeting on Substrate-Integrated Electrode Arrays.

Deckert M, Lippert MT, Krzemiñski J, Takagaki K, Ohl FW, Schmidt B (2017) Polyimide foil flip-chip direct bonding. In: EMPC 2017 - 21st European Microelectronics and Packaging Conference and Exhibition.

Degenhart AD, Eles J, Dum R, Mischel JL, Smalianchuk I, Endler B, Ashmore RC, Tyler-Kabara EC, Hatsopoulos NG, Wang

W, Batista AP, Cui XT (2016) Histological evaluation of a chronically-implanted electrocorticographic electrode grid in a non-human primate. J Neural Eng 13:046019.

Delcasso S, Denagamage S, Britton Z, Graybiel AM (2018) HOPE: Hybrid-drive combining optogenetics, pharmacology and electrophysiology. Front Neural Circuits 12:41.

Deng W, Goldys EM, Farnham MMJ, Pilowsky PM (2014) Optogenetics, the intersection between physics and neuroscience: Light stimulation of neurons in physiological conditions. Am J Physiol - Regul Integr Comp Physiol 307:1292–1302.

Denk W, Strickler JH, Webb WW (1990) Two-photon laser scanning fluorescence microscopy. Science 248:73–76.

Denk W, Svoboda K (1997) Photon upmanship: why multiphoton imaging is more than a gimmick. Neuron 18:351–357.

Desai SA, Rolston JD, Guo L, Potter SM (2010) Improving impedance of implantable microwire multi-electrode arrays by ultrasonic electroplating of durable platinum black. Front Neuroeng 3:5.

Devonshire IM, Grandy TH, Dommett EJ, Greenfield SA (2010) Effects of urethane anaesthesia on sensory processing in the rat barrel cortex revealed by combined optical imaging and electrophysiology. Eur J Neurosci 32:786–797.

Dickey AS, Suminski A, Amit Y, Hatsopoulos NG (2009) Single-unit stability using chronically implanted multielectrode arrays. J Neurophysiol 102:1331–1339.

Ding MC, Wang Q, Lo EH, Stanley GB (2011) Cortical excitation and inhibition following focal traumatic brain injury. J Neurosci 31:14085–14094.

Ekanadham C, Tranchina D, Simoncelli EP (2014) A unified framework and method for automatic neural spike identification. J Neurosci Methods 222:47–55.

Eles JR, Vazquez AL, Kozai TDY, Cui XT (2018) In vivo imaging of neuronal calcium during electrode implantation: Spatial and temporal mapping of damage and recovery. Biomaterials 174:79–94.

Emondi AA, Rebrik SP, Kurgansky A V., Miller KD (2004) Tracking neurons recorded from tetrodes across time. J Neurosci Methods 135:95–105.

Eroglu C, Barres BA (2010) Regulation of synaptic connectivity by glia. Nature 468:223–231.

Escabí MA, Read HL, Viventi J, Kim D-H, Higgins NC, Storace DA, Liu ASK, Gifford AM, Burke JF, Campisi M, Kim Y-S, Avrin AE, Spiegel Jan V, Huang Y, Li M, Wu J, Rogers JA, Litt B, Cohen YE (2014) A high-density, high-channel count, multiplexed μECoG array for auditory-cortex recordings. J Neurophysiol 112:1566–1583.

Eshel N, Bukwich M, Rao V, Hemmelder V, Tian J, Uchida N (2015) Arithmetic and local circuitry underlying dopamine prediction errors. Nature 525:243–246.

Eshel N, Tian J, Bukwich M, Uchida N (2016) Dopamine neurons share common response function for reward prediction error. Nat Neurosci 19:479–486.

Fee MS, Leonardo A (2001) Miniature motorized microdrive and commutator system for chronic neural recording in small animals. J Neurosci Methods 112:83–94.

Ferezou I, Bolea S, Petersen CCH (2006) Visualizing the cortical representation of whisker touch: voltage-sensitive dye imaging in freely moving mice. Neuron 50:617–629.

Ferguson J, Boldt C, Redish D (2009) Creating low impedance tetrodes by electroplating with additives. 156:388–393.

Fiorillo CD, Song MR, Yun SR (2013a) Multiphasic temporal dynamics in responses of midbrain dopamine neurons to appetitive and aversive stimuli. J Neurosci 33:4710–4725.

Fiorillo CD, Yun SR, Song MR (2013b) Diversity and homogeneity in responses of midbrain dopamine neurons. J Neurosci 33:4693–4709.

Fraser GW, Schwartz AB (2012) Recording from the same neurons chronically in motor cortex. J Neurophysiol 107:1970–1978.

Freedman DS, Schroeder JB, Telian GI, Zhang Z, Sunil S, Ritt JT (2016) OptoZIF Drive: A 3D printed implant and assembly tool package for neural recording and optical stimulation in freely moving mice. J Neural Eng 13:066013.

Freire MAM, Morya E, Faber J, Santos JR, Guimaraes JS, Lemos NAM, Sameshima K, Pereira A, Ribeiro S, Nicolelis MAL (2011) Comprehensive analysis of tissue preservation and recording quality from chronic multielectrode implants. PLoS One 6:23–27.

Fujita T, Yoshimine T, Maruno M, Hayakawa T (1998) Cellular dynamics of macrophages and microglial cells in reaction to stab wounds in rat cerebral cortex. Acta Neurochir (Wien) 140:275–279.

Geim AK (2009) Graphene: Status and prospects. Science 324:1530–1534.

Geim AK, Novoselov KS (2007) The rise of graphene. Nat Mater 6:183–191.

Gellermann LW (1933) Chance orders of alternating stimuli in visual discrimination experiments. Pedagog Semin J Genet Psychol 42:206–208.

Gierthmuehlen M, Wang X, Gkogkidis A, Henle C, Fischer J, Fehrenbacher T, Kohler F, Raab M, Mader I, Kuehn C, Foerster K, Haberstroh J, Freiman TM, Stieglitz T, Rickert J, Schuettler M, Ball T (2014) Mapping of sheep sensory cortex with a novel microelectrocorticography grid. J Comp Neurol 522:3590–3608.

Gilletti A, Muthuswamy J (2006) Brain micromotion around implants in the rodent somatosensory cortex. J Neural Eng 3:189–195.

Gleich O, Strutz J (2012) The mongolian gerbil as a model for the analysis of peripheral and central age-dependent hearing loss. In: Hearing Loss (Naz S, ed), pp 67–92. Regensburg.

Goldring S, Gregorie EM (1984) Surgical management of epilepsy using epidural recordings to localize the seizure focus. Review of 100 cases. J Neurosurg 60:457–466.

Goltstein PM, Reinert S, Glas A, Bonhoeffer T, Hübener M (2018) Food and water restriction lead to differential learning behaviors in a head-fixed two-choice visual discrimination task for mice. PLoS One 13:0204066.

Gothard KM, Skaggs WE, Moore KM, McNaughton BL (1996) Binding of hippocampal CA1 neural activity to multiple reference frames in a landmark-based navigation task. J Neurosci 16:823–835.

Gradinaru V, Mogri M, Thompson KR, Henderson JM, Deisseroth K (2009) Optical deconstruction of parkinsonian neural circuitry. Science 324:354–359.

Gray CM, Maldonado PE, Wilson M, McNaughton B (1995) Tetrodes markedly improve the reliability and yield of multiple single-unit isolation from multi-unit recordings in cat striate cortex. J Neurosci Methods 63:43–54.

Grienberger C, Konnerth A (2012) Imaging calcium in neurons. Neuron 73:862–885.

Grinvald A, Hildesheim R (2004) VSDI: a new era in functional imaging of cortical dynamics. Nat Rev Neurosci 5:874–885.

Guitchounts G, Markowitz JE, Liberti WA, Gardner TJ (2013) A carbon-fiber electrode array for long-term neural recording. J Neural Eng 10:046016.

Gulino M, Kim D, Pané S, Santos SD, Pêgo AP (2019) Tissue response to neural implants: The use of model systems toward new design solutions of implantable microelectrodes. Front Neurosci 13:689.

Guo Z V., Hires SA, Li N, O'Connor DH, Komiyama T, Ophir E, Huber D, Bonardi C, Morandell K, Gutnisky D, Peron S, Xu N, Cox J, Svoboda K (2014) Procedures for behavioral experiments in head-fixed mice Simon SA, ed. PLoS One 9:e88678.

Hackett T a (2011) Information flow in the auditory cortical network. Hear Res 271:133–146.

Hackett TA, Barkat TR, O'Brien BMJ, Hensch TK, Polley DB (2011) Linking topography to tonotopy in the mouse auditory thalamocortical circuit. J Neurosci 31:2983–2995.

Haery L, Deverman BE, Matho KS, Cetin A, Woodard K, Cepko C, Guerin KI, Rego MA, Ersing I, Bachle SM, Kamens J, Fan M (2019) Adeno-associated virus technologies and methods for targeted neuronal manipulation. Front Neuroanat 13:93.

Haiss F, Butovas S, Schwarz C (2010) A miniaturized chronic microelectrode drive for awake behaving head restrained mice and rats. J Neurosci Methods 187:67–72.

Hämmerle H, Kobuch K, Kohler K, Nisch W, Sachs H, Stelzle M (2002) Biostability of micro-photodiode arrays for subretinal implantation. Biomaterials 23:797–804.

Han CJ, O'Tuathaigh CM, Van Trigt L, Quinn JJ, Fanselow MS, Mongeau R, Koch C, Anderson DJ (2003) Trace but not delay fear conditioning requires attention and the anterior cingulate cortex. Proc Natl Acad Sci U S A 100:13087–13092.

Happel MFK, Jeschke M, Ohl FW (2010) Spectral integration in primary auditory cortex attributable to temporally precise convergence of thalamocortical and intracortical input. J Neurosci 30:11114–11127.

Hardung S, Alyahyay M, Eriksson D, Diester I (2017) A toolbox for optophysiological experiments in freely moving rats. Front Syst Neurosci 11:27.

Harris KD, Henze DA, Csicsvari J, Hirase H, Aki B, Kenneth D, Henze DA, Csicsvari J (2000) Accuracy of tetrode spike separation as determined by simultaneous intracellular and extracellular measurements. J Neurophysiol 81:401–414.

Harris KD, Hirase H, Leinekugel X, Henze DA, Buzsáki G (2001) Temporal interaction between single spikes and complex spike bursts in hippocampal pyramidal cells. Neuron 32:141–149.

Harris KD, Quiroga RQ, Freeman J, Smith SL (2016) Improving data quality in neuronal population recordings. Nat Neurosci 19:1165–1174.

Hassler C, Boretius T, Stieglitz T (2011) Polymers for neural implants. J Polym Sci Part B Polym Phys 49:18–33.

Hayn L, Deppermann L, Koch M (2017) Reduction of the foreign body response and neuroprotection by apyrase and minocycline in chronic cannula implantation in the rat brain. Clin Exp Pharmacol Physiol 44:313–323.

Headley DB, DeLucca M V., Haufler D, Paré D (2015) Incorporating 3D-printing technology in the design of head-caps and electrode drives for recording neurons in multiple brain regions. J Neurophysiol 113:2721–2732.

Heil P, Irvine DR (1998) The posterior field P of cat auditory cortex: coding of envelope transients. Cereb Cortex 8:125–141.

Henle C, Raab M, Cordeiro JG, Doostkam S, Schulze-Bonhage A, Stieglitz T, Rickert J (2011) First long term in vivo study on subdurally implanted micro-ECoG electrodes, manufactured with a novel laser technology. Biomed Microdevices 13:59–68.

Henle C, Schuettler M, Ordonez JS, Stieglitz T (2008) Scaling limitations of laser-fabricated nerve electrode arrays. In: Annu Int Conf IEEE Eng Med Biol Soc, pp 4208–4211.

Henze DA, Borhegyi Z, Csicsvari J, Mamiya A, Harris KD, Buzsáki G (2000) Intracellular features predicted by extracellular recordings in the hippocampus in vivo. J Neurophysiol 84:390–400.

Hermann JK, Lin S, Soffer A, Wong C, Srivastava V, Chang J, Sunil S, Sudhakar S, Tomaszewski WH, Protasiewicz G, Selkirk SM, Miller RH, Capadona JR (2018) The role of toll-like receptor 2 and 4 innate immunity pathways in intracortical microelectrode-induced neuroinflammation. Front Bioeng Biotechnol 6:113.

Herreras O (2016) Local field potentials: myths and misunderstandings. Front Neural Circuits 10:101.

Hill DN, Mehta SB, Kleinfeld D (2011) Quality metrics to accompany spike sorting of extracellular signals. J Neurosci 31:8699–8705.

Hill NJ, Lal TN, Schröder M, Hinterberger T, Wilhelm B, Nijboer F, Mochty U, Widman G, Elger C, Schölkopf B, Kübler A, Birbaumer N (2006) Classifying EEG and ECoG signals without subject training for fast BCI implementation: Comparison of nonparalyzed and completely paralyzed subjects. In: IEEE Trans Neural Syst Rehabil Eng., pp 183–186.

Hochberg LR, Serruya MD, Friehs GM, Mukand JA, Saleh M, Caplan AH, Branner A, Chen D, Penn RD, Donoghue JP (2006) Neuronal ensemble control of prosthetic devices by a human with tetraplegia. Nature 442:164–171.

Hodgkin AL, Huxley AF (1939) Action potentials recorded from inside a nerve fibre. Nature 144:710–711.

Hollerman JR, Schultz W (1998) Dopamine neurons report an error in the temporal prediction of reward during learning. Nat Neurosci 1:304–309.

Hong G, Lieber CM (2019) Novel electrode technologies for neural recordings. Nat Rev Neurosci 20:330–345.

Hosp JA, Molina-Luna K, Hertler B, Atiemo CO, Stett A, Luft AR (2008) Thin-film epidural microelectrode arrays for somatosensory and motor cortex mapping in rat. J Neurosci Methods 172:255–262.

Howe MW, Dombeck DA (2016) Rapid signalling in distinct dopaminergic axons during locomotion and reward. Nature 535:505–510.

Hromádka T, Deweese MR, Zador AM, Figs S (2008) Sparse representation of sounds in the unanesthetized auditory cortex. PLoS Biol 6:e16.

Hubel DH, Henson CO, Rupert A, Galambos R (1959) Attention units in the auditory cortex. Science 192:1279–1280.

Hubel DH, Wiesel TN (1959) Receptive fields of single neurones in the cat's striate cortex. J Physiol 148:574–591.

Hubel DH, Wiesel TN (1962) Receptive fields, binocular interaction and functional architecture in the cat's visual cortex. J Physiol 160:106–154.

Hubel H (1957) Tungsten microelectrode for recording from single units. Science 125:549–550.

Hughes RN, Bakhurin KI, Petter EA, Watson GDR, Kim N, Friedman AD, Yin HH (2020) Ventral tegmental dopamine neurons control the impulse vector during motivated behavior. Curr Biol 30:2681–2694.

Hui GK, Wong KL, Chavez CM, Leon MI, Robin KM, Weinberger NM (2009) Conditioned tone control of brain reward behavior produces highly specific representational gain in the primary auditory cortex. Neurobiol Learn Mem 92:27–34.

Ikemoto S (2007) Dopamine reward circuitry: two projection systems from the ventral midbrain to the nucleus accumbens-olfactory tubercle complex. Brain Res Rev 56:27–78.

Ilango A, Kesner AJ, Keller KL, Stuber GD, Bonci A, Ikemoto S (2014) Similar roles of substantia nigra and ventral tegmental dopamine neurons in reward and aversion. J Neurosci 34:817–822.

Ilango A, Shumake J, Wetzel W, Scheich H, Ohl FW (2012) The role of dopamine in the context of aversive stimuli with particular reference to acoustically signaled avoidance learning. Front Neurosci 6:132.

Im C, Seo JM (2016) A review of electrodes for the electrical brain signal recording. Biomed Eng Lett 6:104–112.

Insanally M, Trumpis M, Wang C, Chiang CH, Woods V, Palopoli-Trojani K, Bossi S, Froemke RC, Viventi J (2016) A low-cost, multiplexed μECoG system for high-density recordings in freely-moving rodents. J Neural Eng 116:1477–1490.

Jacobs J, Kahana MJ (2010) Direct brain recordings fuel advances in cognitive electrophysiology. Trends Cogn Sci 14:162–171.

Jeantet Y, Cho YH (2003) Design of a twin tetrode microdrive and headstage for hippocampal single unit recordings in

behaving mice. J Neurosci Methods 129:129–134.

Jellema T, Brunia CHM, Wadman WJ (2004) Sequential activation of microcircuits underlying somatosensory-evoked potentials in rat neocortex. Neuroscience 129:283–295.

Ji B, Guo Z, Wang M, Yang B, Wang X, Li W, Liu J (2018) Flexible polyimide-based hybrid opto-electric neural interface with 16 channels of micro-LEDs and electrodes. Microsystems Nanoeng 4:27.

Jiang Z, Huxter JR, Bowyer SA, Blockeel AJ, Butler J, Imtiaz SA, Wafford KA, Phillips KG, Tricklebank MD, Marston HM, Rodriguez-Villegas E (2017) TaiNi: maximizing research output whilst improving animals' welfare in neurophysiology experiments. Sci Rep 7:8086.

Jorfi M, Skousen JL, Weder C, Capadona JR, R. CJ (2015) Progress towards biocompatible intracortical microelectrodes for neural interfacing applications. J Neural Eng 12:583–592.

Joshua M, Adler A, Prut Y, Vaadia E, Wickens JR, Bergman H (2009) Synchronization of midbrain dopaminergic neurons is enhanced by rewarding events. Neuron 62:695–704.

Juavinett AL, Bekheet G, Churchland AK (2019) Chronically implanted neuropixels probes enable high-yield recordings in freely moving mice. Elife 8:e47188.

Jun JJ et al. (2017) Fully integrated silicon probes for high-density recording of neural activity. Nature 551:232–236.

Kamiński M, Ding M, Truccolo WA, Bressler SL (2001) Evaluating causal relations in neural systems: Granger causality, directed transfer function and statistical assessment of significance. Biol Cybern 85:145–157.

Kane SR, Cogan SF, Ehrlich J, Plante TD, McCreery DB, Troyk PR (2013) Electrical performance of penetrating microelectrodes chronically implanted in cat cortex. IEEE Trans Biomed Eng 60:2153–2160.

Kawagoe R, Takikawa Y, Hikosaka O (2004) Reward-predicting activity of dopamine and caudate neurons - a possible mechanism of motivational control of saccadic eye movement. J Neurophysiol 91:1013–1024.

Keating JG, Gerstein GL (2002) A chronic multi-electrode microdrive for small animals. J Neurosci Methods 117:201–206.

Keller D, Erö C, Markram H (2018) Cell densities in the mouse brain: a systematic review. Front Neuroanat 12:83.

Keramatzadeh K, Kiakojouri A, Nahvi MS, Khazaei Y, Feizi-nejad A, Maghami MH, Mohammadi R, Sharifshazileh M, Nasiri S, Akbari Boroumand F, Nadimi E, Rezaei M, Shojaei A, Mirnajafi-Zadeh J, Sodagar AM (2020) Wireless, miniaturized, semi-implantable electrocorticography microsystem validated in vivo. Sci Rep 10:21261.

Khan HN, Hounshell DA, Fuchs ERH (2018) Science and research policy at the end of Moore's law. Nat Electron 1:14–21.

Khodagholy D, Gelinas JN, Thesen T, Doyle W, Devinsky O, Malliaras GG, Buzsaki G (2015) NeuroGrid: recording action potentials from the surface of the brain. Nat Neurosci 18:310–315.

Khurram A, Seymour JP (2013) Investigation of the photoelectrochemical effect in optoelectrodes and potential uses for implantable electrode characterization. Proc Annu Int Conf IEEE Eng Med Biol Soc EMBS:3032–3035.

Kilgard MP, Merzenich MM (1998) Cortical map reorganization enabled by nucleus basalis activity. Science 279:1714–1718.

Kim CK, Adhikari A, Deisseroth K (2017) Integration of optogenetics with complementary methodologies in systems neuroscience. Nat Rev Neurosci 18:222–235.

Kim CK, Yang SJ, Pichamoorthy N, Young NP, Kauvar I, Jennings JH, Lerner TN, Berndt A, Lee SY, Ramakrishnan C, Davidson TJ, Inoue M, Bito H, Deisseroth K (2016) Simultaneous fast measurement of circuit dynamics at multiple sites across the mammalian brain. Nat Methods 13:325–328.

Kim H, Brünner HS, Carlén M (2020) The DMCdrive: practical 3D-printable micro-drive system for reliable chronic multi-tetrode recording and optogenetic application in freely behaving rodents. Sci Rep 10:11838.

Kim J, Adam Wilson J, Williams JC (2007) A cortical recording platform utilizing μECoG electrode arrays. Annu Int Conf IEEE Eng Med Biol - Proc 2721:5353–5357.

Kim JH, Kang G, Nam Y, Choi YK (2010) Surface-modified microelectrode array with flake nanostructure for neural recording and stimulation. Nanotechnology 21:85303.

Klauk H, Huang JR, Nichols JA, Jackson TN (2000) Ion-beam-deposited ultrathin transparent metal contacts. Thin Solid Films 366:272–278.

Kleinfeld D, Delaney KR (1996) Distributed representation of vibrissa movement in the upper layers of somatosensory cortex revealed with voltage-sensitive dyes. J Comp Neurol 375:89–108.

Kleinfeld D, Delaney KR, Fee MS, Flores JA, Tank DW, Gelperin A (1994) Dynamics of propagating waves in the olfactory network of a terrestrial mollusk: An electrical and optical study. J Neurophysiol 72:1402–1419.

Kloosterman F, Davidson TJ, Gomperts SN, Layton SP, Hale G, Nguyen DP, Wilson MA (2009) Micro-drive array for chronic in vivo recording: drive fabrication. J Vis Exp:1094.

Knierim JJ, McNaughton BL, Poe GR (2000) Three-dimensional spatial selectivity of hippocampal neurons during space flight. Nat Neurosci 3:209–210.

Konerding WS, Froriep UP, Kral A, Baumhoff P (2018) New thin-film surface electrode array enables brain mapping with high spatial acuity in rodents. Sci Rep 8:3825.

Konnerth A, Orkand RK (1986) Voltage-sensitive dyes measure potential changes in axons and glia of the frog optic nerve. Neurosci Lett 66:49–54.

Korshunov VA (2006) Miniature microdrive-headstage assembly for extracellular recording of neuronal activity with high-impedance electrodes in freely moving mice. J Neurosci Methods 158:179–185.

Kozai TDY, Jaquins-Gerstl AS, Vazquez AL, Michael AC, Cui XT (2015) Brain tissue responses to neural implants impact signal sensitivity and intervention strategies. ACS Chem Neurosci 6:48–67.

Kozai TDY, Vazquez AL (2015) Photoelectric artefact from optogenetics and imaging on microelectrodes and bioelectronics: new challenges and opportunities. J Mater Chem B 3:4965–4978.

Kozai TDY, Vazquez AL, Weaver CL, Kim SG, Cui XT (2012) In vivo two-photon microscopy reveals immediate microglial reaction to implantation of microelectrode through extension of processes. J Neural Eng 9:066001.

Kremer Y, Flakowski J, Rohner C, Lüscher C (2020) Context-dependent multiplexing by individual VTA dopamine neurons. J Neurosci 40:7489–7509.

Krüger J, Caruana F, Volta RD, Rizzolatti G (2010) Seven years of recording from monkey cortex with a chronically implanted multiple microelectrode. Front Neuroeng 3:6.

Kulkarni RU, Miller EW (2017) Voltage imaging: pitfalls and potential. Biochemistry 56:5171–5177.

Kunori N, Takashima I (2015) A transparent epidural electrode array for use in conjunction with optical imaging. J Neurosci Methods 251:130–137.

Kuzum D et al. (2014) Transparent and flexible low noise graphene electrodes for simultaneous electrophysiology and neuroimaging. Nat Commun 5:1–10.

Kwon KY, Sirowatka B, Weber A, Li W (2013) Opto-μECoG array: A hybrid neural interface with transparent μECoG electrode array and integrated LEDs for optogenetics. IEEE Trans Biomed Circuits Syst 7:593–600.

Lago N, Ceballos D, J Rodríguez F, Stieglitz T, Navarro X (2005) Long term assessment of axonal regeneration through polyimide regenerative electrodes to interface the peripheral nerve. Biomaterials 26:2021–2031.

Lak A, Stauffer WR, Schultz W (2016) Dopamine neurons learn relative chosen value from probabilistic rewards. Elife 5:18044.

Lammel S, Ion DI, Roeper J, Malenka RC (2011) Projection-specific modulation of dopamine neuron synapses by aversive and rewarding stimuli. Neuron 70:588–862.

Lammel S, Lim BK, Malenka RC (2014) Reward and aversion in a heterogeneous midbrain dopamine system. Neuropharmacology 76:351–359.

Lammel S, Steinberg EE, Földy C, Wall NR, Beier K, Luo L, Malenka RC (2015) Diversity of transgenic mouse models for selective targeting of midbrain dopamine neurons. Neuron 85:429–438.

Lansink CS, Bakker M, Buster W, Lankelma J, van der Blom R, Westdorp R, Joosten RNJMA, McNaughton BL, Pennartz CMA (2007) A split microdrive for simultaneous multi-electrode recordings from two brain areas in awake small animals. J Neurosci Methods 162:129–138.

Leach JB, Achyuta AKH, Murthy SK (2010) Bridging the divide between neuroprosthetic design, tissue engineering and neurobiology. Front Neuroeng 2:18.

Leal-Campanario R, Delgado-García JM, Gruart A (2006) Microstimulation of the sornatosensory cortex can substitute for vibrissa stimulation during Pavlovian conditioning. Proc Natl Acad Sci U S A 103:10052–10057.

Ledochowitsch P, Félus RJ, Gibboni RR, Miyakawa A, Bao S, Maharbiz MM (2011a) Fabrication and testing of a large area, high density, parylene MEMS μECoG array. In: Proceedings of the IEEE International Conference on Micro Electro Mechanical Systems (MEMS), pp 1031–1034.

Ledochowitsch P, Olivero E, Blanche T, Maharbiz MM (2011b) A transparent ECoG array for simultaneous recording and optogenetic stimulation. In: Proceedings of the Annual International Conference of the IEEE Engineering in Medicine and Biology Society, pp 2937–2940.

Ledochowitsch P, Yazdan-Shahmorad A, Bouchard KE, Diaz-Botia C, Hanson TL, He JW, Seybold BA, Olivero E, Phillips EAK, Blanche TJ, Schreiner CE, Hasenstaub A, Chang EF, Sabes PN, Maharbiz MM (2015) Strategies for optical control and simultaneous electrical readout of extended cortical circuits. J Neurosci Methods 256:220–231.

Lee C, Wei X, Kysar JW, Hone J (2008) Measurement of the elastic properties and intrinsic strength of monolayer graphene. Science 321:385–388.

Lee H, Kim M, Kim I, Lee H (2016) Flexible and stretchable optoelectronic devices using silver nanowires and graphene. Adv Mater 28:4541–4548.

Lefebvre B, Yger P, Marre O (2016) Recent progress in multi-electrode spike sorting methods. J Physiol Paris 110:327–335.

Li W, Rodger D, Menon P, Tai Y-C (2019) Corrosion behavior of parylene-metal-parylene thin films in saline. ECS Trans 11:1.

Liang L, Oline SN, Kirk JC, Schmitt LI, Komorowski RW, Remondes M, Halassa MM (2017) Scalable, lightweight, integrated and quick-to-assemble (SLIQ) hyperdrives for functional circuit dissection. Front Neural Circuits 11:8.

Lima SQ, Hromádka T, Znamenskiy P, Zador AM (2009) PINP: A new method of tagging neuronal populations for identification during in vivo electrophysiological recording. PLoS One 4:6099.

Lippert MT, Takagaki K, Xu W, Huang X, Wu JY (2007) Methods for voltage-sensitive dye imaging of rat cortical activity with high signal-to-noise ratio. J Neurophysiol 98:502–512.

Liu X, Lu Y, Iseri E, Shi Y, Kuzum D (2018) A compact closed-loop optogenetics system based on artifact-free transparent graphene electrodes. Front Neurosci 12:132.

Ljungberg T, Apicella P, Schultz W (1992) Responses of monkey dopamine neurons during learning of behavioral reactions. J Neurophysiol 67:145–163.

Llinás RR (1988) The intrinsic electrophysiological properties of mammalian neurons: Insights into central nervous system function. Science 242:1654–1664.

Lu L, Popeney B, Dickman JD, Angelaki DE (2018a) Construction of an improved multi-tetrode hyperdrive for large-scale neural recording in behaving rats. J Vis Exp:57338.

Lu Y, Liu X, Hattori R, Ren C, Zhang X, Komiyama T, Kuzum D (2018b) Ultralow impedance graphene microelectrodes with high optical transparency for simultaneous deep two-photon imaging in transgenic mice. Adv Funct Mater 28:1800002.

Luan L, Robinson JT, Aazhang B, Chi T, Yang K, Li X, Rathore H, Singer A, Yellapantula S, Fan Y, Yu Z, Xie C (2020) Recent advances in electrical neural interface engineering: minimal invasiveness, longevity, and scalability. Neuron 108:302–321.

Ludwig KA, Uram JD, Yang J, Martin DC, Kipke DR (2006) Chronic neural recordings using silicon microelectrode arrays electrochemically deposited with a poly(3,4-ethylenedioxythiophene) (PEDOT) film. J Neural Eng 3:59–70.

Luo AH, Georges FE, Aston-Jones GS (2008) Novel neurons in ventral tegmental area fire selectively during the active phase of the diurnal cycle. Eur J Neurosci 27:408–422.

Luo TZ, Bondy AG, Gupta D, Elliott VA, Kopec CD, Brody CD (2020) An approach for long-term, multi-probe neuropixels recordings in unrestrained rats. Elife 9:59716.

Ma J, Zhao Z, Cui S, Liu FY, Yi M, Wan Y (2019) A novel 3D-printed multi-drive system for synchronous electrophysiological recording in multiple brain regions. Front Neurosci 13:1322.

Machilsen B, Novitskiy N, Vancleef K, Wagemans J (2011) Context modulates the ERP signature of contour integration. PLoS One 6:25151.

Marg E, Adams JE (1967) Indwelling multiple micro-electrodes in the brain. Electroencephalogr Clin Neurophysiol 23:277–280.

Margolis EB, Lock H, Hjelmstad GO, Fields HL (2006) The ventral tegmental area revisited: is there an electrophysiological marker for dopaminergic neurons? J Physiol 577:907–924.

Marinelli M, McCutcheon JE (2014) Heterogeneity of dopamine neuron activity across traits and states. Neuroscience 282:176–197.

Mathis A, Mamidanna P, Cury KM, Abe T, Murthy VN, Mathis MW, Bethge M (2018) DeepLabCut: markerless pose estimation of user-defined body parts with deep learning. Nat Neurosci 21:1281–1289.

Matsumoto H, Tian J, Uchida N, Watabe-Uchida M (2016) Midbrain dopamine neurons signal aversion in a reward-context-dependent manner. Elife 5:17328.

Maxwell WL, Povlishock JT, Graham DL (1997) A mechanistic analysis of nondisruptive axonal injury: a review. J Neurotrauma 14:419–440.

Maynard EM, Fernandez E, Normann RA (2000) A technique to prevent dural adhesions to chronically implanted microelectrode arrays. J Neurosci Methods 97:93–101.

Maynard EM, Nordhausen CT, Normann RA (1997) The Utah intracortical electrode array: a recording structure for potential brain-computer interfaces. Electroencephalogr Clin Neurophysiol 102:228–239.

McConnell GC, Rees HD, Levey AI, Gutekunst CA, Gross RE, Bellamkonda R V. (2009) Implanted neural electrodes cause chronic, local inflammation that is correlated with local neurodegeneration. J Neural Eng 6:056003.

McHugh TJ, Blum KI, Tsien JZ, Tonegawa S, Wilson MA (1996) Impaired hippocampal representation of space in CA1-specific NMDAR1 knockout mice. Cell 87:1339–1349.

McMahon DBT, Jones AP, Bondar I V., Leopold DA (2014) Face-selective neurons maintain consistent visual responses across months. Proc Natl Acad Sci U S A 111:8251–8256.

McNaughton BL, O'Keefe J, Barnes CA (1983) The stereotrode: a new technique for simultaneous isolation of several single units in the central nervous system from multiple unit records. J Neurosci Methods 8:391–397.

Mechler F, Victor JD, Ohiorhenuan I, Schmid AM, Hu Q (2011) Three-dimensional localization of neurons in cortical tetrode recordings. J Neurophysiol 106:828–848.

Menegas W, Babayan BM, Uchida N, Watabe-Uchida M (2017) Opposite initialization to novel cues in dopamine signaling in ventral and posterior striatum in mice. Elife 6:21886.

Meyer RD, Cogan SF, Nguyen TH, Rauh RD (2001) Electrodeposited iridium oxide for neural stimulation and recording electrodes. IEEE Trans Neural Syst Rehabil Eng 9:2–11.

Micallef AH, Takahashi N, Larkum ME, Palmer LM (2017) A reward-based behavioral platform to measure neural activity during head-fixed behavior. Front Cell Neurosci 11:156.

Mikulovic S, Pupe S, Peixoto HM, Do Nascimento GC, Kullander K, Tort ABL, Leão RN (2016) On the photovoltaic effect in local field potential recordings. Neurophotonics 3:015002.

Mileykovskiy B, Morales M (2011) Duration of inhibition of ventral tegmental area dopamine neurons encodes a level of conditioned fear. J Neurosci 31:7471–7476.

Miller EW (2016) Small molecule fluorescent voltage indicators for studying membrane potential. Curr Opin Chem Biol 33:74–80.

Miller JM, Dobie RA, Pfingst BE, Hienz RD (1980) Electrophysiologic studies of the auditory cortex in the awake monkey. Am J Otolaryngol 1:119–130.

Min KJ, Yang MS, Kim SU, Jou I, Joe EH (2006) Astrocytes induce hemeoxygenase-1 expression in microglia: A feasible mechanism for preventing excessive brain inflammation. J Neurosci 26:1880–1887.

Minev IR et al. (2015) Electronic dura mater for long-term multimodal neural interfaces. Science 347:159–164.

Mirenowicz J, Schultz W (1996) Preferential activation of midbrain dopamine neurons by appetitive rather than aversive stimuli. Nature 379:449–451.

Mitzdorf U (1985) Current source-density method and application in cat cerebral cortex: investigation of evoked potentials and EEG phenomena. Physiol Rev 65:37–100.

Mizuseki K, Buzsáki G (2013) Preconfigured, skewed distribution of firing rates in the hippocampus and entorhinal cortex. Cell Rep 4:1010–1021.

Mohammed AI, Gritton HJ, Tseng HA, Bucklin ME, Yao Z, Han X (2016) An integrative approach for analyzing hundreds of neurons in task performing mice using wide-field calcium imaging. Sci Rep 6:20986.

Mohebi A, Pettibone JR, Hamid AA, Wong JMT, Vinson LT, Patriarchi T, Tian L, Kennedy RT, Berke JD (2019) Dissociable dopamine dynamics for learning and motivation. Nature 570:65–70.

Morales M, Margolis EB (2017) Ventral tegmental area: cellular heterogeneity, connectivity and behaviour. Nat Rev Neurosci 18:73–85.

Mryasov ON, Freeman AJ (2001) Electronic band structure of indium tin oxide and criteria for transparent conducting behavior. Phys Rev B 64:233111.

Muthuswamy J, Anand S, Sridharan A (2011) Adaptive movable neural interfaces for monitoring single neurons in the brain. Front Neurosci 5:94.

Nagy A (2000) Cre recombinase: the universal reagent for genome tailoring. Genesis 26:99–109.

Nair-Roberts RG, Chatelain-Badie SD, Benson E, White-Cooper H, Bolam JP, Ungless MA (2008) Stereological estimates of dopaminergic, GABAergic and glutamatergic neurons in the ventral tegmental area, substantia nigra and retrorubral field in the rat. Neuroscience 152:1024–1031.

Negi S, Bhandari R, Rieth L, Solzbacher F (2010) In vitro comparison of sputtered iridium oxide and platinum-coated neural implantable microelectrode arrays. Biomed Mater 5:15007.

Neto JP, Baião P, Lopes G, Frazão J, Nogueira J, Fortunato E, Barquinha P, Kampff AR (2018) Does impedance matter when recording spikes with polytrodes? Front Neurosci 12:715.

Newman JP, Voigts J, Borius M, Karlsson M, Harnett MT, Harnett MT, Wilson MA (2020) Twister3: a simple and fast microwire twister. J Neural Eng 17:026040.

Nicolelis MAL, Dimitrov D, Carmena JM, Crist R, Lehew G, Kralik JD, Wise SP (2003) Chronic, multisite, multielectrode recordings in macaque monkeys. Proc Natl Acad Sci U S A 100:11041–11046.

Nolte G, Bai O, Wheaton L, Mari Z, Vorbach S, Hallett M (2004) Identifying true brain interaction from EEG data using the imaginary part of coherency. Clin Neurophysiol 115:2292–2307.

Nunamaker EA, Kipke DR (2010) An alginate hydrogel dura mater replacement for use with intracortical electrodes. J Biomed Mater Res B Appl Biomater 95:421–429.

O'Connor B, Haughn C, An KH, Pipe KP, Shtein M (2008) Transparent and conductive electrodes based on unpatterned, thin metal films. Appl Phys Lett 93:223304.

O'Keefe J, Dostrovsky J (1971) The hippocampus as a spatial map. Preliminary evidence from unit activity in the freely-moving rat. Brain Res 34:171–175.

Obaid A, Wu Y-W, Hanna M, Jáidar O, Nix W, Ding J, Melosh N (2020) Ultra-sensitive measurement of brain penetration mechanics and blood vessel rupture with microscale probes. bioRxiv:306498.

Ohl FW, Scheich H (1996) Differential frequency conditioning enhances spectral contrast sensitivity of units in auditory cortex (Field AI) of the alert mongolian gerbil. Eur J Neurosci 8:1001–1017.

Ohl FW, Scheich H, Freeman WJ (2000a) Topographic analysis of epidural pure-tone-evoked potentials in gerbil auditory cortex. J Neurophysiol 83:3123–3132.

Ohl FW, Scheich H, Freeman WJ (2001) Change in pattern of ongoing cortical activity with auditory category learning. Nature 412:733–736.

Ohl FW, Schulze H, Scheich H, Freeman WJ (2000b) Spatial representation of frequency-modulated tones in gerbil auditory cortex revealed by epidural electrocorticography. J Physiol Paris 94:549–554.

Ohl FW, Wetzel W, Wagner T, Rech A, Scheich H (1999) Bilateral ablation of auditory cortex in mongolian gerbil affects discrimination of frequency modulated tones but not of pure tones. Learn Mem 6:347–362.

Ojemann GA, Ramsey NF, Ojemann J (2013) Relation between functional magnetic resonance imaging (fMRI) and single neuron, local field potential (LFP) and electrocorticography (ECoG) activity in human cortex. Front Hum Neurosci 7:34.

Owen SF, Liu MH, Kreitzer AC (2019) Thermal constraints on in vivo optogenetic manipulations. Nat Neurosci 22:1061–1065.

Pachitariu M, Lyamzin DR, Sahani M, Lesica NA (2015) State-dependent population coding in primary auditory cortex. J Neurosci 35:2085–2073.

Pachitariu M, Steinmetz N, Kadir S, Carandini M, Kenneth D. H (2016a) Kilosort: realtime spike-sorting for extracellular electrophysiology with hundreds of channels. bioRxiv:061481.

Pachitariu M, Steinmetz NA, Kadir SN, Carandini M, Harris KD (2016b) Fast and accurate spike sorting of high-channel count probes with KiloSort. In: Advances in Neural Information Processing Systems.

Pan W-X, Schmidt R, Wickens JR, Hyland BI (2005) Dopamine cells respond to predicted events during classical conditioning: evidence for eligibility traces in the reward-learning network. J Neurosci 13:900–913.

Pan WX, Brown J, Dudman JT (2013) Neural signals of extinction in the inhibitory microcircuit of the ventral midbrain. Nat Neurosci 16:71–78.

Park D-W, Schendel AA, Mikael S, Brodnick SK, Richner TJ, Ness JP, Hayat MR, Atry F, Frye ST, Pashaie R, Thongpang S, Ma Z, Williams JC (2014) Graphene-based carbon-layered electrode array technology for neural imaging and optogenetic applications. Nat Commun 5:5258.

Park D, Brodnick SK, Ness JP, Atry F, Krugner-higby L, Sandberg A, Mikael S, Richner TJ, Novello J, Kim H, Baek D, Bong J, Frye ST, Thongpang S, Swanson KI, Lake W, Pashaie R, Williams JC, Ma Z (2016) Fabrication and utility of a transparent graphene neural electrode array for electrophysiology, in vivo imaging, and optogenetics. Nat Protoc 11:2201–2222.

Park D, Ness JP, Brodnick SK, Esquibel C, Novello J, Atry F, Baek D, Kim H, Bong J, Swanson KI, Suminski J, Otto KJ, Pashaie R, Williams JC, Ma Z (2018) Electrical neural stimulation and simultaneous in vivo monitoring with transparent graphene electrode arrays implanted in GCaMP6f mice. ACS Nano 12:148–157.

Parker NF, Cameron CM, Taliaferro JP, Lee J, Choi JY, Davidson TJ, Daw ND, Witten IB (2016) Reward and choice encoding in terminals of midbrain dopamine neurons depends on striatal target. Nat Neurosci 19:845–854.

Patriarchi T, Cho JR, Merten K, Howe MW, Marley A, Xiong WH, Folk RW, Broussard GJ, Liang R, Jang MJ, Zhong H, Dombeck D, von Zastrow M, Nimmerjahn A, Gradinaru V, Williams JT, Tian L (2018) Ultrafast neuronal imaging of dopamine dynamics with designed genetically encoded sensors. Science 360:4422.

Patrick E, Orazem ME, Sanchez JC, Nishida T (2011) Corrosion of tungsten microelectrodes used in neural recording applications. J Neurosci Methods 198:158–171.

Paxinos G, Franklin K (2001) The mouse brain in stereotaxic coordinates, 2nd edition, (New York: Academic Press).

Penfield W, Steelman H (1947) The treatment of focal epilepsy by cortical excision. Ann Surg 126:740–761.

Peterka DS, Takahashi H, Yuste R (2011) Imaging voltage in neurons. Neuron 69:9–21.

Petersen CCH, Grinvald A, Sakmann B (2003) Spatiotemporal dynamics of sensory responses in layer 2/3 of rat barrel cortex measured in vivo by voltage-sensitive dye imaging combined with whole-cell voltage recordings and neuron reconstructions. J Neurosci 23:1298–1309.

Pfeiffer BE, Foster DJ (2013) Hippocampal place-cell sequences depict future paths to remembered goals. Nature 497:74–79.

Polikov VS, Tresco PA, Reichert WM (2005) Response of brain tissue to chronically implanted neural electrodes. J Neurosci Methods 148:1–18.

Polley DB, Read HL, Storace DA, Merzenich MM (2007) Multiparametric Auditory Receptive Field Organization Across Five Cortical Fields in the Albino Rat. J Neurophysiol 97:3621–3638.

Polley DB, Steinberg EE, Merzenich MM (2006) Perceptual learning directs auditory cortical map reorganization through top-down influences. J Neurosci 26:4970–4982.

Pommersheim J, Nguyen T, Zhang Z, Lin C (1995) Cation diffusion at the polymer coating/metal interface. J Adhes Sci Technol 9:935–951.

Poulin JF, Gaertner Z, Moreno-Ramos OA, Awatramani R (2020) Classification of midbrain dopamine neurons using single-cell gene expression profiling approaches. Trends Neurosci 43:155–169.

Prasad A, Xue QS, Dieme R, Sankar V, Mayrand RC, Nishida T, Streit WJ, Sanchez JC (2014) Abiotic-biotic characterization of Pt/Ir microelectrode arrays in chronic implants. Front Neuroeng 7:2.

Pupe S, Wallén-Mackenzie Å (2015) Cre-driven optogenetics in the heterogeneous genetic panorama of the VTA. Trends Neurosci 38:375–386.

Purcell EK, Thompson DE, Ludwig KA, Kipke DR (2009) Flavopiridol reduces the impedance of neural prostheses in vivo without affecting recording quality. J Neurosci Methods 183:149–157.

Qiang Y, Artoni P, Seo KJ, Culaclii S, Hogan V, Zhao X, Zhong Y, Han X, Wang PM, Lo YK, Li Y, Patel HA, Huang Y, Sambangi A, Chu JS V., Liu W, Fagiolini M, Fang H (2018) Transparent arrays of bilayer-nanomesh microelectrodes for simultaneous electrophysiology and two-photon imaging in the brain. Sci Adv 4:0626.

Quirk MC, Blum KI, Wilson MA (2001) Experience-dependent changes in extracellular spike amplitude may reflect regulation of dendritic action potential back-propagation in rat hippocampal pyramidal cells. J Neurosci 21:240–248.

Radtke-Schuller S, Schuller G, Angenstein F, Grosser OS, Goldschmidt J, Budinger E (2016) Brain atlas of the Mongolian gerbil (Meriones unguiculatus) in CT/MRI-aided stereotaxic coordinates. Brain Struct Funct 221:1–272.

Raducanu BC, Yazicioglu RF, Lopez CM, Ballini M, Putzeys J, Wang S, Andrei A, Rochus V, Welkenhuysen M, van Helleputte N, Musa S, Puers R, Kloosterman F, van Hoof C, Fiáth R, Ulbert I, Mitra S (2017) Time multiplexed active neural probe with 1356 parallel recording sites. Sensors (Basel) 17:2388.

Redgrave P, Gurney K (2006) The short-latency dopamine signal: A role in discovering novel actions? Nat Rev Neurosci 7:967–975.

Reece M, O'Keefe J (1989) The tetrode: a new technique for multi-unit extracellular recording. Soc Neurosci Abstr 15:1250.

Renz AF, Lee J, Tybrandt K, Brzezinski M, Lorenzo DA, Cerra Cheraka M, Lee J, Helmchen F, Vörös J, Lewis CM (2020) Opto-E-Dura: a soft, stretchable ECoG array for multimodal, multiscale neuroscience. Adv Healthc Mater 9:2000814.

Rescorla RA, Wagner AR (1972) A theory of pavlovian conditioning: variations in the effectiveness of reinforcement and nonreinforcement. In: Clasical conditioning II: current research and theory, pp 64–99. New York: Appleton-Century-Crofts.

Resendez SL, Jennings JH, Ung RL, Namboodiri VMK, Zhou ZC, Otis JM, Nomura H, McHenry JA, Kosyk O, Stuber GD (2016) Visualization of cortical, subcortical and deep brain neural circuit dynamics during naturalistic mammalian behavior with head-mounted microscopes and chronically implanted lenses. Nat Protoc 11:566–597.

Richner TJ, Brodnick SK, Thongpang S, Sandberg AA, Krugner-Higby LA, Williams JC (2019) Phase relationship between micro-electrocorticography and cortical neurons. J Neural Eng 16:066028.

Richner TJ, Thongpang S, Brodnick SK, Schendel AA, Falk RW, Krugner-Higby LA, Pashaie R, Williams JC (2014) Optogenetic micro-electrocorticography for modulating and localizing cerebral cortex activity. J Neural Eng 11:016010.

Roeper J (2013) Dissecting the diversity of midbrain dopamine neurons. Trends Neurosci 36:336–342.

Roesch MR, Calu DJ, Schoenbaum G (2007) Dopamine neurons encode the better option in rats deciding between differently delayed or sized rewards. Nat Neurosci 10:1615–1624.

Root DH, Estrin DJ, Morales M (2018) Aversion or salience signaling by ventral tegmental area glutamate neurons. iScience 2:51–62.

Rose T, Goltstein PM, Portugues R, Griesbeck O (2014) Putting a finishing touch on GECIs. Front Mol Neurosci 7:88.

Rossant C, Kadir SN, Goodman DFM, Schulman J, Hunter MLD, Saleem AB, Grosmark A, Belluscio M, Denfield GH, Ecker AS, Tolias AS, Solomon S, Buzski G, Carandini M, Harris KD (2016) Spike sorting for large, dense electrode arrays. Nat Neurosci 19:634–641.

Rousche PJ, Normann RA (1998) Chronic recording capability of the utah intracortical electrode array in cat sensory cortex. J Neurosci Methods 82:1–15.

Rousche PJ, Pellinen DS, Pivin DP, Williams JC, Vetter RJ, Kipke DR (2001) Flexible polyimide-based intracortical electrode arrays with bioactive capability. IEEE Trans Biomed Eng 48:361–370.

Rubehn B, Bosman C, Oostenveld R, Fries P, Stieglitz T (2009) A MEMS-based flexible multichannel ECoG-electrode array. J Neural Eng 6:036003.

Rubehn B, Stieglitz T (2010) In vitro evaluation of the long-term stability of polyimide as a material for neural implants. Biomaterials 31:3449–3458.

Rubio-Garrido P, Pérez-De-Manzo F, Porrero C, Galazo MJ, Clascá F (2009) Thalamic input to distal apical dendrites in neocortical layer 1 is massive and highly convergent. Cereb Cortex 19:2380–2395.

Salatino JW, Kale AP, Purcell EK (2019) Alterations in ion channel expression surrounding implanted microelectrode arrays in the brain. bioRxiv:518811.

Salatino JW, Ludwig KA, Kozai TDY, Purcell EK (2017) Glial responses to implanted electrodes in the brain. Nat Biomed Eng 1:862–877.

Salcman M, Bak MJ (1973) Design, fabrication, and in vivo behavior of chronic recording intracortical microelectrodes. IEEE Trans Biomed Eng BME-20:253–260.

Sauer I, Doerr C, Schanze T (2015) Spike sorting: the overlapping spikes challenge. Curr Dir Biomed Eng 1:42–45.

Saunders BT, Richard JM, Margolis EB, Janak PH (2018) Dopamine neurons create Pavlovian conditioned stimuli with circuit-defined motivational properties. Nat Neurosci 21:1072–1083.

Saxena T, Karumbaiah L, Gaupp EA, Patkar R, Patil K, Betancur M, Stanley GB, Bellamkonda R V. (2013) The impact of chronic blood-brain barrier breach on intracortical electrode function. Biomaterials 34:4703–4713.

Scanziani M, Häusser M (2009) Electrophysiology in the age of light. Nature 461:930–939.

Scheich H, Heil P, Langner G (1993) Functional organization of auditory cortex in the Mongolian Gerbil (Meriones unguiculatus) II. tonotopic 2-deoxyglucose. Eur J Neurosci 5:898–914.

Schendel AA, Nonte MW, Vokoun C, Richner TJ, Brodnick SK, Atry F, Frye S, Bostrom P, Pashaie R, Thongpang S, Eliceiri KW, Williams JC (2014) The effect of micro-ECoG substrate footprint on the meningeal tissue response. J Neural Eng 11:046011.

Schendel AA, Thongpang S, Brodnick SK, Richner TJ, Lindevig BDB, Krugner-higby L, Williams JC (2013) A cranial window imaging method for monitoring vascular growth around chronically implanted micro-ECoG devices. J Neurosci Methods 218:121–130.

Schmidt EM, Mcintosh JS, Bak MJ (1988) Long-term implants of Parylene-C coated microelectrodes. Med Biol Eng Comput 26:96–101.

Schmitzer-Torbert N, Jackson J, Henze D, Harris K, Redish AD (2005) Quantitative measures of cluster quality for use in extracellular recordings. Neuroscience 131:1–11.

Scholten K, Meng E (2015) Materials for microfabricated implantable devices: A review. Lab Chip 15:4256–4272.

Schultz W (1986) Responses of midbrain dopamine neurons to behavioral trigger stimuli in the monkey. J Neurophysiol

56:1439–1461.

Schultz W (2007) Multiple dopamine functions at different time courses. Annu Rev Neurosci 30:259–288.

Schultz W (2015) Neuronal Reward and Decision Signals: From Theories to Data. Physiol Rev 95:853–951.

Schultz W (2016) Dopamine reward prediction-error signalling: a two-component response. Nat Rev Neurosci 17:183–195.

Schultz W, Apicella P, Ljungberg T (1993) Responses of monkey dopamine neurons to reward and conditioned stimuli during successive steps of learning a delayed response task. J Neurosci 13:900–913.

Schultz W, Dayan P, Montague PR (1997) A neural substrate of prediction and reward. Science 275:1593–1599.

Schultz W, Stauffer WR, Lak A (2017) The phasic dopamine signal maturing: from reward via behavioural activation to formal economic utility. Curr Opin Neurobiol 43:139–148.

Schulz AL, Woldeit ML, Gonçalves AI, Saldeitis K, Ohl FW (2016) Selective increase of auditory cortico-striatal coherence during auditory-cued Go/NoGo discrimination learning. Front Behav Neurosci 9:368.

Segev R, Goodhouse J, Puchalla J, Berry MJ (2004) Recording spikes from a large fraction of the ganglion cells in a retinal patch. Nat Neurosci 7:1154–1161.

Seo KJ, Qiang Y, Bilgin I, Kar S, Vinegoni C, Weissleder R, Fang H (2017) Transparent electrophysiology microelectrodes and interconnects from metal nanomesh. ACS Nano 11:4365–4372.

Seshagiri C V., Delgutte B (2007) Response properties of neighboring neurons in the auditory midbrain for pure-tone stimulation: A tetrode study. J Neurophysiol 98:2058–2073.

Shaw NA (1988) The auditory evoked potential in the rat-a review. Prog Neurobiol 31:19–45.

Shemetov AA, Monakhov M V., Zhang Q, Canton-Josh JE, Kumar M, Chen M, Matlashov ME, Li X, Yang W, Nie L, Shcherbakova DM, Kozorovitskiy Y, Yao J, Ji N, Verkhusha V V. (2021) A near-infrared genetically encoded calcium indicator for in vivo imaging. Nat Biotechnol 39:368–377.

Shi J, Fang Y (2018) Flexible and implantable microelectrodes for chronically stable neural interfaces. Adv Mater 31:1804895.

Shoffstall AJ, Paiz JE, Miller DM, Rial GM, Willis MT, Menendez DM, Hostler SR, Capadona JR (2018) Potential for thermal damage to the blood-brain barrier during craniotomy: Implications for intracortical recording microelectrodes. J Neural Eng 15:034001.

Shoham D, Glaser DE, Arieli A, Kenet T, Wijnbergen C, Toledo Y, Hildesheim R, Grinvald A (1999) Imaging cortical dynamics at high spatial and temporal resolution with novel blue voltage-sensitive dyes. Neuron 24:791–802.

Shoham S, O'Connor DH, Segev R (2006) How silent is the brain: Is there a "dark matter" problem in neuroscience? J Comp Physiol A Neuroethol Sens Neural Behav Physiol 192:777–784.

Shokoueinejad M, Park D-W, Jung Y, Brodnick S, Novello J, Dingle A, Swanson K, Baek D-H, Suminski A, Lake W, Ma Z, Williams J (2019) Progress in the field of micro-electrocorticography. Micromachines 10:62.

Shuman T et al. (2020) Breakdown of spatial coding and interneuron synchronization in epileptic mice. Nat Neurosci 23:229–238.

Siegle JH, Carlen M, Meletis K, Tsai LH, Moore CI, Ritt J (2011) Chronically implanted hyperdrive for cortical recording and optogenetic control in behaving mice. In: Annu Int Conf IEEE Eng Med Biol Soc, pp 7529–7532.

Siegle JH, López AC, Patel YA, Abramov K, Ohayon S, Voigts J (2017) Open Ephys: An open-source, plugin-based platform for multichannel electrophysiology. J Neural Eng 14:045003.

Slutzky MW, Jordan LR, Lindberg EW, Lindsay KE, Miller LE (2011) Decoding the rat forelimb movement direction from epidural and intracortical field potentials. J Neural Eng 8:036013.

Smith RD, Kolb I, Tanaka S, Lee AK, Harris TD, Barbic M (2020) Robotic multi-probe-single-actuator inchworm neural microdrive. bioRxiv:338137.

Sridharan A, Rajan SD, Muthuswamy J (2013) Long-term changes in the material properties of brain tissue at the implant-tissue interface. J Neural Eng 10:066001.

Stark E, Roux L, Eichler R, Senzai Y, Royer S, Buzsáki G (2014) Pyramidal cell-interneuron interactions underlie hippocampal ripple oscillations. Neuron 83:467–480.

Stark NJ (1996) Literature in review: biological saftey of Parylene C. Med Plast Biomater 3:30–35.

Steinmetz NA et al. (2021) Neuropixels 2.0: A miniaturized high-density probe for stable, long-term brain recordings. Science 372:4588.

Steinmetz NA, Koch C, Harris KD, Carandini M (2018) Challenges and opportunities for large-scale electrophysiology with Neuropixels probes. Curr Opin Neurobiol 50:92–100.

Stevenson IH, Kording KP (2011) How advances in neural recording affect data analysis. Nat Neurosci 14:139–142.

Stice P, Muthuswamy J (2009) Assessment of gliosis around moveable implants in the brain. J Neural Eng 6:046004.

Stieglitz T (2009) Development of a micromachined epiretinal vision prosthesis. J Neural Eng 6:065005.

Stiller AM, Black BJ, Kung C, Ashok A, Cogan SF, Varner VD, Pancrazio JJ (2018) A meta-analysis of intracortical device stiffness and its correlation with histological outcomes. Micromachines (basel) 9:443.

Stringer C, Pachitariu M, Steinmetz N, Reddy CB, Carandini M, Harris KD (2019) Spontaneous behaviors drive multidimensional, brainwide activity. Science 364:7893.

Stuart G, Spruston N, Sakmann B, Häusser M (1997) Action potential initiation and backpropagation in neurons of the mammalian CNS. Trends Neurosci 20:125–131.

Subbaroyan J, Martin DC, Kipke DR (2005) A finite-element model of the mechanical effects of implantable microelectrodes in the cerebral cortex. J Neural Eng 2:103–113.

Sukov W, Barth DS (1998) Three-dimensional analysis of spontaneous and thalamically evoked gamma oscillations in auditory cortex. J Neurophysiol 79:2875–2884.

Suri RE, Schultz W (1999) A neural network model with dopamine-like reinforcement signal that learns a spatial delayed response task. Neuroscience 91:871–890.

Sutton RS, Barto AG (1981) Toward a modern theory of adaptive networks: expectation and prediction. Psychol Rev 88:135–170.

Szostak KM, Grand L, Constandinou TG (2017) Neural interfaces for intracortical recording: requirements, fabrication methods, and characteristics. Front Neurosci 11:655.

Taaseh N, Yaron A, Nelken I (2011) Stimulus-specific adaptation and deviance detection in the rat auditory cortex. PLoS One 6:23369.

Tang-Schomer MD, Johnson VE, Baas PW, Stewart W, Smith DH (2012) Partial interruption of axonal transport due to microtubule breakage accounts for the formation of periodic varicosities after traumatic axonal injury. Exp Neurol 233:364–372.

Theis L, Berens P, Froudarakis E, Reimer J, Román Rosón M, Baden T, Euler T, Tolias AS, Bethge M (2016) Benchmarking spike rate inference in population calcium imaging. Neuron 90:471–482.

Thelin J, Jörntell H, Psouni E, Garwicz M, Schouenborg J, Danielsen N, Linsmeier CE (2011) Implant size and fixation mode strongly influence tissue reactions in the CNS. PLoS One 6:16267.

Thomas H, Tillein J, Heil P, Scheich H (1993) Functional organization of auditory cortex in the mongolian gerbil (Meriones unguiculatus). I. electrophysiological mapping of frequency representation and distinction of fields. Eur J Neurosci 5:882–897.

Thompson KG, Hanes DP, Bichot NP, Schall JD (1996) Perceptual and motor processing stages identified in the activity of macaque frontal eye field neurons during visual search. J Neurophysiol 76:4040–4055.

Thunemann M, Lu Y, Liu X, Kılıç K, Desjardins M, Vandenberghe M, Sadegh S, Saisan PA, Cheng Q, Weldy KL, Lyu H, Djurovic S, Andreassen OA, Dale AM, Devor A, Kuzum D (2018) Deep 2-photon imaging and artifact-free optogenetics through transparent graphene microelectrode arrays. Nat Commun 9:2035.

Tian J, Huang R, Cohen JY, Osakada F, Kobak D, Machens CK, Callaway EM, Uchida N, Watabe-Uchida M (2016) Distributed and mixed information in monosynaptic inputs to dopamine neurons. Neuron 91:1374–1389.

Tian J, Uchida N (2015) Habenula lesions reveal that multiple mechanisms underlie dopamine prediction errors. Neuron 87:1304–1316.

Toda H, Suzuki T, Sawahata H, Majima K, Kamitani Y, Hasegawa I (2011) Simultaneous recording of ECoG and intracortical neuronal activity using a flexible multichannel electrode-mesh in visual cortex. Neuroimage 54:203–212.

Tolias AS, Ecker AS, Siapas AG, Hoenselaar A, Keliris GA, Logothetis NK (2007) Recording chronically from the same neurons in awake, behaving primates. J Neurophysiol 98:3780–3790.

Tóth A, Petykó Z, Máthé K, Szabó I, Czurkó A (2007) Improved version of the printed circuit board (PCB) modular multi-channel microdrive for extracellular electrophysiological recordings. J Neurosci Methods 159:51–56.

Tritsch NX, Oh WJ, Gu C, Sabatini BL (2014) Midbrain dopamine neurons sustain inhibitory transmission using plasma membrane uptake of GABA, not synthesis. Elife 3:01936.

Ulanovsky N, Las L, Nelken I (2003) Processing of low-probability sounds by cortical neurons. Nat Neurosci 6:391–398.

Ulanovsky N, Moss CF (2007) Hippocampal cellular and network activity in freely moving echolocating bats. Nat Neurosci 10:224–233.

Ungless MA, Grace AA (2012) Are you or aren't you? Challenges associated with physiologically identifying dopamine neurons. Trends Neurosci 35:422–430.

Ungless MA, Magill PJ, Bolam JP (2004) Uniform inhibition of dopamine neurons in the ventral tegmental area by aversive stimuli. Science 303:2040–2042.

Venkatasubramanian C, Mlynash M, Finley-Caulfield A, Eyngorn I, Kalimuthu R, Snider RW, Wijman CA (2011) Natural history of perihematomal edema after intracerebral hemorrhage measured by serial magnetic resonance imaging. Stroke 42:73–80.

Verharen JP, Zhu Y, Lammel S (2020) Aversion hot spots in the dopamine system. Curr Opin Neurobiol 64:46–52.

Vezzani A, Viviani B (2015) Neuromodulatory properties of inflammatory cytokines and their impact on neuronal excitability. Neuropharmacology 96:70–82.

Viventi J et al. (2011) Flexible, foldable, actively multiplexed, high-density electrode array for mapping brain activity in vivo. Nat Neurosci 14:1599–1605.

Voigts J, Newman JP, Wilson MA, Harnett MT (2020) An easy-to-assemble, robust, and lightweight drive implant for chronic tetrode recordings in freely moving animals. J Neural Eng 17:026044.

Voigts J, Siegle J, Pritchett DL, Moore CI (2013) The flexDrive: An ultra-light implant for optical control and highly parallel chronic recording of neuronal ensembles in freely moving mice. Front Syst Neurosci 7:8.

Vomero M, Porto Cruz MF, Zucchini E, Ciarpella F, Delfino E, Carli S, Boehler C, Asplund M, Ricci D, Fadiga L, Stieglitz T (2020) Conformable polyimide-based µECoGs: bringing the electrodes closer to the signal source. Biomaterials 255:120178.

Von Der Behrens W, Bäuerle P, Kössl M, Gaese BH (2009) Correlating stimulus-specific adaptation of cortical neurons and local field potentials in the awake rat. J Neurosci 29:13837–13849.

Von Metzen RP, Stieglitz T (2013) The effects of annealing on mechanical, chemical, and physical properties and structural stability of Parylene C. Biomed Microdevices 15:727–735.

Vöröslakos M, Petersen PC, Vöröslakos B, Buzsáki G (2021) Metal microdrive and head cap system for silicon probe recovery in freely moving rodent. Elife 10:65859.

Wang L, Huang K, Zhong C, Wang L, Lu Y (2018) Fabrication and modification of implantable optrode arrays for in vivo optogenetic applications. Biophys Reports 4:82–93.

Wang D V, Tsien JZ (2011) Conjunctive processing of locomotor signals by the ventral tegmental area neuronal population. PLoS One 6:16528.

Wang X-J (2010) Neurophysiological and computational principles of cortical rhythms in cognition. Physiol Rev 90:1195–1268.

Watabe-Uchida M, Eshel N, Uchida N (2017) Neural circuitry of reward prediction error. Annu Rev Neurosci 40:373–394.

Watabe-Uchida M, Zhu L, Ogawa SK, Vamanrao A, Uchida N (2012) Whole-brain mapping of direct inputs to midbrain dopamine neurons. Neuron 74:858–873.

Weale RA (1951) A new micro-electrode for electro-physiological work. Nature 167:529–530.

Weinberg RJ (1997) Are topographic maps fundamental to sensory processing? Brain Res Bull 44:113–116.

Weinberger NM (2007) Associative representational plasticity in the auditory cortex: a synthesis of two disciplines. Learn Mem 14:1–16.

White RL, Gross TJ (1974) An evaluation of the resistance to electrolysis of metals for use in biostimulation microprobes. IEEE Trans Biomed Eng BME-21:487–490.

Williams JC, Rennaker RL, Kipke DR (1999) Stability of chronic multichannel neural recordings: Implications for a long-term neural interface. Neurocomputing 26–27:1069–1076.

Williams PR, Marincu BN, Sorbara CD, Mahler CF, Schumacher AM, Griesbeck O, Kerschensteiner M, Misgeld T (2014) A recoverable state of axon injury persists for hours after spinal cord contusion in vivo. Nat Commun 5:5683.

Wilson MA, McNaughton BL (1993) Dynamics of the hippocampal ensemble code for space. Science 261:1055–1058.

Wilson MA, McNaughton BL, Stengel K (1991) A high-density miniature microdrive array for chronic stimulation and recording of patterned multiple single-unit activity in the rat hippocampus. Soc Neurosci Abstr 17:1395.

Wise KD, Angell JB, Starr A (1970) An integrated-circuit approach to extracellular microelectrodes. IEEE Trans Biomed Eng 17:238–247.

Wise RA (2004) Dopamine, learning and motivation. Nat Rev Neurosci 5:483–494.

Wolf JA, Stys PK, Lusardi T, Meaney D, Smith DH (2001) Traumatic axonal injury induces calcium influx modulated by tetrodotoxin-sensitive sodium channels. J Neurosci 21:1923–1930.

Woods V, Trumpis M, Bent B, Palopoli-Trojani K, Chiang CH, Wang C, Yu C, Insanally MN, Froemke RC, Viventi J (2018) Long-term recording reliability of liquid crystal polymer µECoG arrays. J Neural Eng 15:066024.

Xie C, Lin Z, Hanson L, Cui Y, Cui B (2012) Intracellular recording of action potentials by nanopillar electroporation. Nat

Nanotechnol 7:185–190.

Xie Y, Martini N, Hassler C, Kirch RD, Stieglitz T, Seifert A, Hofmann UG (2014) In vivo monitoring of glial scar proliferation on chronically implanted neural electrodes by fiber optical coherence tomography. Front Neuroeng 7:34.

Xiong Q, Znamenskiy P, Zador AM (2015) Selective corticostriatal plasticity during acquisition of an auditory discrimination task. Nature 521:348–351.

Xu HT, Pan F, Yang G, Gan WB (2007) Choice of cranial window type for in vivo imaging affects dendritic spine turnover in the cortex. Nat Neurosci 10:549–551.

Yamagiwa S, Ishida M, Kawano T (2015) Flexible optrode array: Parylene-film waveguide arrays with microelectrodes for optogenetics. In: Transducers-18th International conference on solid-state sensors, actuators and microsystems, pp 277–280. Anchorage, AK, USA.

Yamamoto J, Wilson MA (2008) Large-scale chronically implantable precision motorized microdrive array for freely behaving animals. J Neurophysiol 100:2430–2440.

Yang W, Miller J eun K, Carrillo-Reid L, Pnevmatikakis E, Paninski L, Yuste R, Peterka DS (2016) Simultaneous multi-plane imaging of neural circuits. Neuron 89:269–284.

Yarrow S, Razak KA, Seitz AR, Seriès P (2014) Detecting and quantifying topography in neural maps. PLoS One 9:e87178.

Yeager JD, Phillips DJ, Rector DM, Bahr DF (2008) Characterization of flexible ECoG electrode arrays for chronic recording in awake rats. J Neurosci Methods 173:279–285.

Yizhar O, Fenno LE, Davidson TJ, Mogri M, Deisseroth K (2011) Optogenetics in Neural Systems. Neuron 71:9–34.

Yoshida Kozai TD, Langhals NB, Patel PR, Deng X, Zhang H, Smith KL, Lahann J, Kotov NA, Kipke DR (2012) Ultrasmall implantable composite microelectrodes with bioactive surfaces for chronic neural interfaces. Nat Mater 11:1065–1073.

Yoshimoto S, Araki T, Uemura T, Nezu T, Sekitani T, Suzuki T, Yoshida F, Hirata M (2016) Implantable wireless 64-channel system with flexible ECoG electrode and optogenetics probe. In: Proceedings - IEEE Biomedical Circuits and Systems Conference (BioCAS). Shanghai, China.

Yun J (2017) Ultrathin metal films for transparent electrodes of flexible optoelectronic devices. Adv Funct Mater 27:1606641.

Zátonyi A, Borhegyi Z, Srivastava M, Cserpán D, Somogyvári Z, Kisvárday Z, Fekete Z (2018a) Functional brain mapping using optical imaging of intrinsic signals and simultaneous high-resolution cortical electrophysiology with a flexible, transparent microelectrode array. Sensors Actuators, B Chem 273:519–526.

Zátonyi A, Brodsky JL, Andrews DW (2020) Transparent, low-autofluorescence microECoG device for simultaneous Ca2+ imaging and cortical electrophysiology in vivo. J Neural Eng 17:016062.

Zátonyi A, Li X, Demartino GN (2018b) In vitro and in vivo stability of black-platinum coatings on flexible, polymer microECoG arrays. J Neural Eng 15:054003.

Zhang F, Prigge M, Beyrière F, Tsunoda SP, Mattis J, Yizhar O, Hegemann P, Deisseroth K (2008) Red-shifted optogenetic excitation: A tool for fast neural control derived from Volvox carteri. Nat Neurosci 11:631–633.

Zhang S, Qi J, Li X, Wang HL, Britt JP, Hoffman AF, Bonci A, Lupica CR, Morales M (2015) Dopaminergic and glutamatergic microdomains in a subset of rodent mesoaccumbens axons. Nat Neurosci 18:386–392.

Zhong Y, Bellamkonda R V. (2007) Dexamethasone-coated neural probes elicit attenuated inflammatory response and neuronal loss compared to uncoated neural probes. Brain Res 1148:15–27.

Zhu MH, Jang J, Milosevic MM, Antic SD (2021) Population imaging discrepancies between a genetically-encoded calcium indicator (GECI) versus a genetically-encoded voltage indicator (GEVI). Sci Rep 11:5295.

Declaration of Honor

„I hereby declare that I prepared this thesis without impermissible help of third parties and that none other than the indicated tools have been used; all sources of information are clearly marked, including my own publications.

In particular I have not consciously:

- fabricated data or rejected undesired results
- misused statistical methods with the aim of drawing other conclusions than those warranted by the available data
- plagiarized external data or publications
- presented the results of other researchers in a distorted way.

I am aware that violations of copyright may lead to injunction and damage claims of the author and also to prosecution by the law enforcement authorities.
I hereby agree that the thesis may be reviewed for plagiarism by mean of electronic data processing.

This work has not yet been submitted as a doctoral thesis in the same or a similar form in Germany or in any other country. It has not yet been published as a whole."

_____ _____

(Place, Date) (Signature)